ISSN: 0128-7680

Pertanika Journal of

SCIENCE & TECHNOLOGY

VOLUME 12 NO.2
JULY 2004

A scientific journal published by Universiti Putra Malaysia Press

Pertanika Journal of Science & Technology

About the Journal

Pertanika, the poineer journal of UPM, began publication in 1978. Since then, it has established itself as one of the leading multidisciplinary journals in the tropics. In 1992, a decision was made to streamline Pertanika into three journals to meet the need for specialised journals in areas of study aligned with the strengths of the univeristy. These ara **(i) Pertanika Journal of Tropical Agricultural Science, (ii) Pertanika Journal of Science and Technology (iii) Pertanika Journal of Social Science and Humanities.**

Aims and Scope

Pertanika Journal of Science and Technology welcomes full papers and short communications in English or Bahasa Melayu in the fields of chemisty, physics, mathematics and statistics, engineering, environmental control and management, ecology and computer science. It is published twice a year in January and July.

Articles must be reports of research not previously or simultaneously published in other scientific or technical journals.

Communications are notes of a significant finding intended for rapid publication. It should not exceed five double-spaced typerwritten pages and must be accompanied by a letter from the author justifying its publication as a communication.

Reviews are critical appraisals of literature in areas that are of interest to a broad spectrum of scientists and researchers. Review papers will be published upon invitation.

Submission of Manuscript

Three complete clear copies of the manuscript are to be submitted to

The Chief Editor
Pertanika Journal of Science and Technology
Universiti Putra Malaysia
43400 UPM Serdang, Selangor Darul Ehsan
MALAYSIA
Tel: (603) 89468855 Fax (603) 89416172

Proofs and Offprints

Page proofs, illustration proofs, the copy-edited manuscript and an offprint order form will be sent to the author. Proofs must be checked very carefully within the specified time as they will not be proofread by the Press editors.

Authors will receive 20 offprints of each article. Additional copies can be ordered from the Secretary of the Editorial Board by filling out the offprint order form.

Published by Universiti Putra Malaysia Press
ISSN No.: 0128-7680

Pertanika Journal of Science & Technology

Volume 12 No. 2, 2004

Contents

ISSN: 0128-7680
Pertanika J. Sci. & Technol. 12(2): 173 - 188 (2004)

Modeling of Evaporation Rates in an Arid Region Using Artificial Neural Networks

Abdel-Azim, M. Negm & Abdulmohsen Alshaikh
Civil Engineering Department, College of Engineering
King Saud University
P.O. Box 800, Riyadh 11421
Saudi Arabia

Received: 8 May 2003

ABSTRAK

Satu komponen kitar hidrologi yang penting ialah penyejatan. Kadar penyejatan adalah satu fungsi suhu, kelembapan relatif, radiasi solar dan kelajuan angin. Data sejarah faktor-faktor tersebut boleh digunakan untuk menjangka kadar penyejatan dengan menggunakan teknik-teknik yang berlainan seperti pemodelan siri masa, analisis regresi berganda dan rangkaian neuron buatan (ANN). Dalam kertas kerja ini, ANN digunakan untuk menjangka kadar penyejatan dalam kawasan gersang dikenali sebagai faktor iklim asas. Data yang dikumpulkan untuk Wilayah Bisha, Saudi Arabia digunakan untuk melatih, mengesahkan dan menguji rangkaian tersebut. Juga, kaedah linear berganda dan regresi bukan linear digunakan untuk membangunkan model jangkaan untuk menjangka kadar penyejatan dalam hal faktor iklim yang sama. Hasil keputusan model ANN dibandingkan dengan model regresi linear berganda (MLR) yang terbaik. Analisis keputusan menunjukkan bahawa jangkaan ANN boleh dibandingkan dengan kaedah regresi dan ANN adalah alat perjanjian untuk data penyejatan pemodelan. Analisis sensitiviti menunjukkan bahawa suhu udara mempunyai kesan utama ke atas kadar penyejatan manakala faktor lain mempunyai kesan yang kurang.

ABSTRACT

One important component of the type hydrologic cycle is evaporation. Evaporation rate is a function of temperature, relative humidity, solar radiation and wind speed. Historical data of these factors could be used to predict the evaporation rates by using different techniques such as time series modeling, multiple regression analysis and artificial neural networks (ANN). In this paper, The ANNs are used to predict the evaporation rates in an arid region knowing the basic climate factors. The collected data for Bisha Province, Saudi Arabia is used to train, validate and test the network. Also, multiple linear and nonlinear regression methods are used to develop prediction models for predicting evaporation rates in terms of the same climatic factors. The results of the ANN model are compared to the best multiple linear regression (MLR) model. The analysis of the results indicated that the predictions of ANN are comparable to those of the regression methods and that ANN is a promising tool for modeling evaporation data. Sensitivity analysis indicated that the air temperature has a major effect on the evaporation rates while other factors have less effects.

Keywords: Evaporation, artificial neural network, regression, climatic factors

INTRODUCTION

Evaporation is the process whereby the liquid is converted to water vapor by the transfer of water molecules to the atmosphere. The net result is that visible water is converted into invisible water vapor resulting in a significant reduction of the available amount of free surface fresh water. High evaporation rates in arid regions such as Saudi Arabia are a major problem because it reduces the very limited amount of the available fresh water. Evaporation in some regions of Saudi Arabia may reach 3500 mm per year while the average annual precipitation is only about 90 mm (MOAW 1984). Hence, evaporation rates should be estimated to account their impact on the different water resource projects and to consider their effect on water resource planning. Accurate estimation of evaporation requires precise information on the factors affecting it. Different researchers in the field of hydrology listed different factors affecting the evaporation process. Factors affecting evaporation are given by Linsely *et al.* (1958), Chow *et al.* (1988), Gupta (1992) and Singh (1992). The most important of factors affecting evaporation are air temperature (AT), relative humidity (RH), solar radiation (SR) and wind speed (WS). Tahir and (1998) and Alshaikh (1998) found that the correlation coefficients between evaporation and these factors for Riyadh city, Saudi Arabia (Riyadh station R001) are 0.92, -0.86, 0.72 and 0.42 respectively.

Prediction of evaporation using different theories and techniques were investigated by numerous researchers, some of them are Morton (1979), Anderson and Jobson (1982), Omar and Elbakry (1985), Singh and Xu (1997) and Alshaikh (1998). Accurate estimation of evaporation using water-budget, energy budget, mass transfer and combination of energy and mass transfer needs large amounts of data which might be not available. Regression techniques using fewer numbers of variables may lead to inaccurate estimation. Fortunately, a relatively new technique called artificial neural networks was recently developed which is capable of predicting evaporation using less detailed data and even incomplete records. Recent studies on hydrological modeling were proved that artificial neural network is a powerful technique in predicting and estimating hydrologic process and parameters. Daniel (1991), Karunanithi *et al.* (1994), Anmala and Jobseon (1995), Hsu *et al.* (1995), Ichiyanagi (1995), Smith and Eli (1995), Raman and Chandramouli (1996), Mason *et al.* (1996), Minns (1996), Poff *et al.* (1996), Tawfik *et al.* (1997), Thirumalaiah and Deo (1998), Jain and Srivastava (1999), Jung *et al.* (2000) and Tingsanchali and Gautam (2000) are examples of such studies.

Artificial neural networks (ANN) were successfully applied by Tahir (1997) to predict the evaporation in Riyadh City (Riyadh Station R001) knowing the AT, RH, SR and WS. A correlation coefficient of 0.97 between ANN prediction and observed data based on four input factors (AT, RH, SR and WS) against 0.93 using the best representative regression model (Alshaikh 1998) was obtained. These results encourage the authors to carry out the present study to apply the ANN to predict the evaporation rates at Bisha Province, Saudi Arabia to confirm the ability of the ANN to provide accurate prediction of evaporation

in arid regions such as Saudi Arabia. Also, results of regression models will be compared to those of the developed ANN.

Description of the Study Area and Collection of Data

The study area is Bisha Province, Saudi Arabia (SA). It is located at an altitude of 1020 m from mean sea level within Asseer region south-east of Saudi Arabia and 11000 km from Riyadh City. Climatic conditions of this district is arid as most of Saudi Arabia. A major dam with multi-purpose reservoir was recently constructed at Bisha Wadi to store 325 million cubic meters of rainfall water and to prevent the area from being flooded. The stored water will be used to feed the groundwater aquifer and to supply water treatment plant that yields 4000 m^3 of treated water daily. This dam is the Custodian of the Two Holy Mosques King Fahd Ibn Abdul-Aziz dam which is 103 m high from foundation level, 80 m thick at bottom where the width is 507 m.

The data are collected from two stations, MOAW (1996). Both of them are far 30 km and away from Bisha Dam by the second station (B005) is a 15 km away from Bisha and Mouteka station. Information of both stations is given in Table 1.

The collected data covered a period of 22 years from 1975 to 1996. The monthly values of the evaporation rate in mm/day and the four climatic factors (AT, RH, SR and WS) are considered. However, the wind speed was not recorded for the last three years. This is overcome by using the average value of the corresponding months from the previous 19 years. Table 2 shows the basic statistics of the collected data. It should be mentioned that any single observation is the result of the average of the corresponding observations at the stations shown in Table 1.

Basics of Artificial Neural Networks

Since many literatures is available now in the ANN such as Schalkoff (1997), only the very basic information will be introduced here. Artificial neural networks or simply neural networks are a new way of analyzing data. They have a unique ability to learn complex patterns and trends in the data simulating the human ability to solve complicated problems. Therefore, neural computing is based on the way that biological systems, such as the human brain, works. The human brain is made up of many neurons. Each of the brain cells is connected

TABLE 1
Basic information of the climatic stations

Station Name	No.	Code	Altitude, m	Latitude	Longitude
Bisha & Mouteka	64	B004	1020	20 01	42 36
Hefa & Mouteka	65	B005	1090	19 52	42 32

to many others in a network that adopts and changes as the brain learns. In neural computing, processing elements (PE) replace the neurons and these PEs are linked together to form neural networks. Each PE performs a simple task. It is the connections between the PEs that give neural networks the ability to learn patterns and interrelationship in data through the certain weights associated to the connecting PEs. The most important tool of ANN applied in this study is the multi-layer perceptrons (MLP) which is a neural network modeling tool that is optimized for prediction and forecasting applications (Neural Connection 1998). The MLP learns from examples by providing the data to the neural network through and input tool or input layer which consists of a number of PEs equaling the number input variables of fields such that each PE represents one variable or one field. These data are processed in a second layer called hidden layer because all the processing and computations through this core layer are hidden from the users. More than one hidden layer could be used depending on the complexity of the application (if no hidden layer is used, it is a simple perception). The processed data are sent to the output layer that consists of a number of PEs equal to the number of targets (or number of desired outputs) in the application. All the PEs or neurons of each layer are connected to the PEs of the preceding and following layers by links or connections without feedback (therefore they are MLP foreword networks) but not to other neurons within the layer. A typical network of this type of size 4-3-1 is shown in *Fig. 1*. The network consists of three layers. An input layer of 4 neurons (or 4PEs) is to represent the variables AT, RH, SR and WS. An output layer is to represent the single output variable EV. The hidden layer between the input and the output layer is to receive the input, to perform the computations and to send the outputs to the output layer. The hidden layer uses a transfer or activation function to modify the input to the neuron. The transfer function maybe linear, sigmoid or tansh. Sigmoid or tansh are smooth nonlinear functions and one of them is normally chosen because the learning algorithm requires a response function with a continuous, single-valued first derivatives. Building the MLP network is known as training.

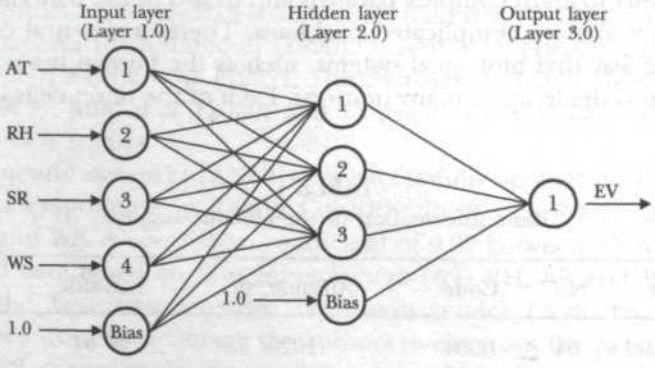

Fig. 1: The developed network of size 4-3-1 to predict the evaporation rates at Bisha, (SA)

Training proceeds in the following way. First, the weights and biases in the network are initialized, usually to small random values. A training patter is then applied to the input layer and the activation of neurons in the first hidden layer is calculated. The output produced by these neurons via the transfer function is then fed to the neurons of the following layer. This forward pass process is repeated at each layer until an output signal from the neurons of the output layer is obtained. The difference between the actual (target) and the desired output values is measured, and the network model connection strength is modified such that the desired output from the network becomes more close to the actual values. This is achieved by a backward pass during which connection modifies are propagated back through network, starting with the connections to the output layer and ending with those at the input layer (from which comes the name back-propagation neural network). The connection strengths is modified according to the produced output of the network. If the network output is correct, no change in the weights takes place. If the network output is larger than the desired output at any neuron, then the connection weights between this neuron and all the input neurons are decreased and vice versa. It should be noted that the training algorithm should be run from many different starting values to find a good optimum solution (lower minimum mean square error). This is because the gradient descent used by the algorithm finds only the nearest local minimum in the mean square error from any given set of initial connection values. In terms of mathematics, the following steps summarise the network training processes based on back-propagation learning algorithm (Neural Connection 1998 and Negm 2001).

a) The values of the weights are set to initial random values.
b) The normalized input pattern X_p (AT, RH, SR and WS) and the normalized target pattern (T_p (EV) are shown to the network.
c) The output (O) from each node in a layer is calculated. The output from a node j in the second layer is given by:

$$O_j = \phi\left(\sum_{i=1}^{n} w_{ij} x_i + b\right) \tag{1}$$

In which is the activation or transfer function of the node. The activation function in the present application is the hyperbolic tangent function (tansh) and b_j is the bias weight of the node j.

d) The weights (w) between nodes are adjusted, starting from output layer and working backwards as follows:

$$w_{ij}(S+1) = w_{ij}(S) + \eta \delta_{pj} O_{pj} \tag{2}$$

in which $w_{ij}(S)$ is the weight between nodes i and j at step S before adjustment while $w_{ij}(S+1)$ is the same weight after adjustment, O_{pj} is the output value at node j, δ_{pj} is the error of pattern p at node j and η is the learning rate. The error δ_{pj} is given by

$$\delta_{pj} = O_{pj}(1 - O_{pj})\ (T_{pj} - O_{pj}) \quad (3)$$

e) The steps from b) to d) are repeated until the error between the desired and the neural network output reaches a global minimum.

Effect of Climatic Factors on Evaporation

Figs. 2a, 2b, 2c and *2d* show the variations of EV and the four climatic factors (AT, RH, SR and WS) with the month of the year to indicate the seasonal effect on the EV. It could be observed that the evaporation is higher during the months of March to October and low from November to February. This is attributed to the effect of EV while RH follows a reverse trend to that EV. *Figs. 3a, 3b, 3c* and *3d* present the variations of EV with AT, RH, SR and WS for the 22 years from 1975 and 1996. Clearly, the evaporation increases in general with the increase in AT, SR and WS and decreases with increase in RH. High scatter in the data is observed specially in SR, this may be attributed to changing the instrument measuring SR in 1979. The minimum and maximum values of EV, AT, RH, SR and WS are shown in Table 2. Units of variables in all tables and figures are as shown in Table 2.

Results of Statistical Modeling

The correlation matrix is computed and the evaporation is found to be correlated to the AT, RH, SR and WS as follows 0.89, -0.66, 0.39 and 0.60 respectively. This indicates that air temperature has a major effect on the evaporation, followed by relative humidity, wind speed and solar radiation.

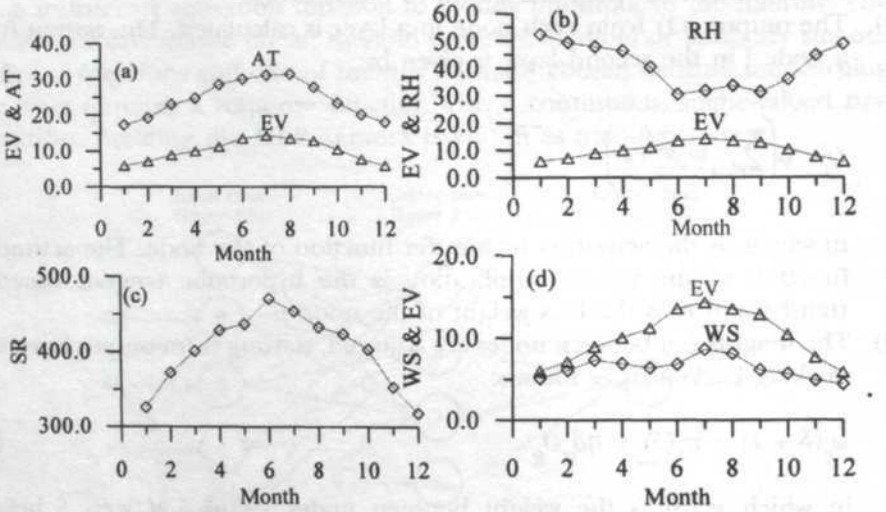

Fig. 2: Monthly variation of average values of EV, AT, RH, SR and WS

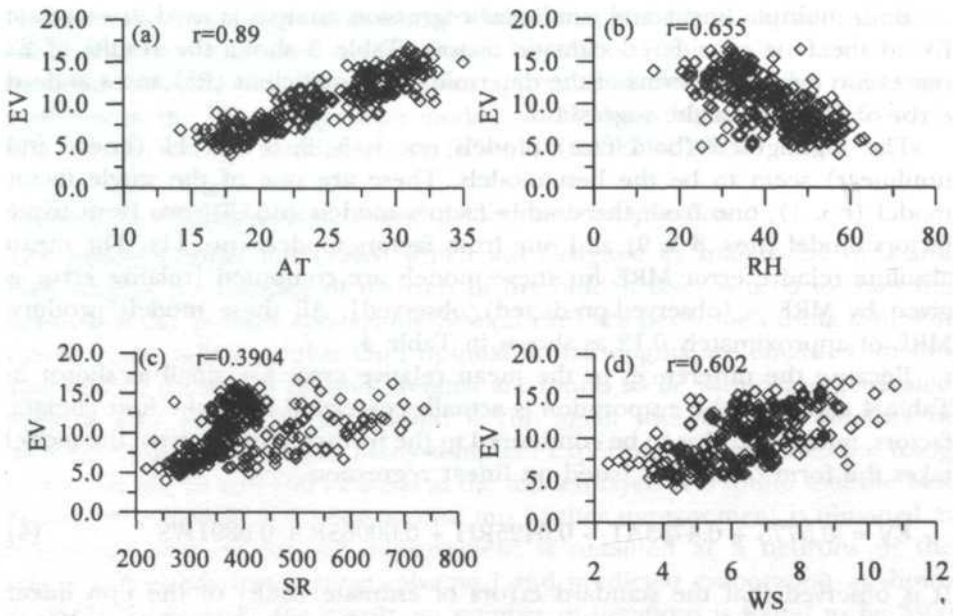

Fig. 3: Variations of EV with (a) AT, (b) RH, (c) SR and (d) WS

TABLE 2
Basic statistic of the used data in the present study

Month	EV(mm/d)	AT(°C)	RH(%)	SR(Cal/cm²/s)	WS(km/h)
Jan.	6.00	17.30	52.40	326.10	5.10
Feb.	7.10	19.20	49.40	372.30	6.10
March	9.00	23.00	47.80	401.30	7.30
April	10.00	24.70	46.30	428.60	6.90
May	11.20	28.50	40.30	436.90	6.40
June	13.60	30.40	30.50	470.20	6.80
July	14.30	31.10	31.70	453.40	8.60
Aug.	12.90	27.70	31.20	423.50	6.10
Sept.	12.86	27.74	31.16	423.54	6.12
Oct.	10.40	23.30	35.90	402.90	5.70
Nov.	7.70	20.00	44.50	353.10	4.90
Dec.	5.90	18.00	48.60	318.10	4.40
Mean of 22 yrs	10.18	24.45	40.47	409.34	6.40
STD of 22 yrs	3.11	5.11	9.74	102.96	1.50
CV of 22 yrs	4.80	14.20	14.10	233.80	2.40
Max of 22 yrs	16.70	32.90	63.30	737.00	10.80

Both multiple linear and nonlinear regression analysis is used to correlate EV to the four considered climatic factors. Table 3 shows the results of 22 regression models in terms of the determination coefficient (R^2) and standard error of estimate of the regression.

The highlighted (bold face) models no. 1, 5, 8, 9 and 11 (linear and nonlinear) seem to be the best models. These are one of the single factor model (no. 1), one from the double factors models (no. 5), two from triple factors model (nos. 8 & 9) and one from factors models (no. 11). The mean absolute relative error MRE for these models are computed [relative error is given by MRE = (observed-predicted)/observed]. All these models produce MRE of approximately 0.12 as shown in Table 4.

Because the differences in the mean relative error are small as shown in Table 4 and since the evaporation is actually correlated to all the four climatic factors, model no. 11 is to be considered in the forthcoming analysis, the model takes the form of Eq. (4) based on linear regression.

$$EV = -0.5775 + 0.4753AT - 0.0425RH + 0.0006SR + 0.0891WS \quad (4)$$

It is observed that the standard errors of estimate (SEE) of the non linear regression models are always less than those of the linear regression models.

TABLE 3
Results of linear and nonlinear regression analysis

Model no.	Factors	Linear regression		Nonlinear regression	
		R2	SEE	R2	SEE
1	AT	0.79	1.43	0.79	1.17
2	RH	0.43	2.40	0.39	1.29
3	SR	0.15	2.91	0.23	1.35
4	WS	0.36	2.52	0.35	1.31
5	AT,RH	0.80	1.40	0.80	1.15
6	AT,WS	0.79	1.43	0.80	1.20
7	AT,WS	0.79	1.43	0.80	1.20
8	AT, RH, SR	0.80	1.40	0.80	1.15
9	AT, RH, WS	0.80	1.40	0.80	1.20
10	AT, SR, WS	0.79	1.44	0.80	1.20
11	AT, RH, SR, WS	0.80	1.40	0.80	1.15

TABLE 4
Mean absolute relative error (MRE) for model no. 1, 5, 8, 9 and 11

Regression	1	5	8	9	11
Linear	0.122	0.119	0.120	0.124	0.121
Non-linear	0.121	0.121	0.120	0.128	0.123

However, the linear regression models show better stability when the regression coefficients are estimated several times based on 70% of the data chosen randomly in each run. Also, using this approach of estimating the regression coefficients, the linear regression model no. 11 shows higher R^2 (R^2=0.804 & SEE = 1.4) than the nonlinear one (R^2=0.716 & SEE=1.20).

Building the Artificial Neural Network for the Present Application

The Neural Connection (1998) which was designed to analyze the data and then suggest the number of neurons of the hidden layer is used to train the network of the present application. Several runs are performed using different values of the initial weights until optimal initial weights are obtained. In this application, the initial random weights are found to be within ± 4 generated using a seed of 1. The application is run again with different number of neurons in the hidden layer. Many computer experiments are carried out using 1, 3, 6, 10, 20, 30 and 100 neurons at the hidden layer. It is found that the best results are obtained at 3 neurons and mp further improvement is obtained at 3 neurons and no further improvement is obtained at 3 neurons in the correlation coefficient between observed and predicted evaporation as shown in Table 5. Similarly, the maximum number of iterations is found to be 3300 (over a range of 4 to 20000 iterations). Very slight improvement is observed when the number of iterations is increased beyond 1600 to 3300 (Table 6). Further increase in the iterations to more than 3300 increases the validation system error and decreases the training system error. An over-training occurs in this case and the network which in turn loses the capability to generalize. Table 6 shows the results of testing the network for determining the best number of iterations.

TABLE 5
Effect of no. of neurons or the hidden on the output of the network

	(Number of iteration)						
Data set	1	3	6	10	20	30	100
Training	0.888	0.903	0.911	0.907	0.905	0.904	0.908
Validation	0.907	0.920	0.924	0.918	0.920	0.920	0.919
Test	0.946	0.923	0.926	0.935	0.935	0.934	0.937

Similar experiments are carried out to find the best learning rate and momentum coefficient for the different stages of learning. There is no hard and fast rule about what value the learning rate should have, it should be determined by trials. The learning rate weights the change in the connection. The momentum coefficient tends to alter the change in the connections in the direction of the average gradient to prevent the learning algorithm from being stopped in a local minimum than the global one. It is found that 0.9, 0.7, 0.5

TABLE 6
Effect of no. of iterations on the output of the network

Data set	(Number of iteration) 4	20	40	100	200	800	1600	3300
Training	0.846	0.887	0.890	0.982	0.892	0.897	0.903	0.903
Validation	0.881	0.906	0.908	0.908	0.908	0.910	0.919	0.920
Test	0.928	0.947	0.946	0.946	0.946	0.941	0.925	0.923

and 0.4 are suitable learning rates for the four stages of training while values of 0.1, 0.4, 0.5 and 0.6 are suitable for the momentum coefficient. It should be mentioned here that the steepest descent measures the gradient of the error surface after each iteration and changes the weights in the direction of the steepest gradient by a value; an amount equals the learning rate.

Stability of the Network

Once the structure of the network is determined, its stability is studied. Several computer experiments are conducted using the pre-determined structure of the network but in each case the data sets are chosen randomly in different ways. The results of six experiments using different seeds of 1, 2, 3, 4, 5, and 6 are shown in Table 7. Experiment 4 shows the best results, however, its results do not vary largely compared to the other experiments.

TABLE 7
Results of network stability

Data set	Exp. 1	Exp. 2	Exp. 3	Exp. 4	Exp. 5	Exp. 6
Training	0.899	0.899	0.906	0.903	0.911	0.928
Validation	0.905	0.918	0.914	0.920	0.890	0.879
Test	0.926	0.917	0.891	0.923	0.880	0.840

Effect of Data Normalization

The input and output data vectors are normalized according to three methods. The first two methods are based on maximum and minimum values (Tahir 1998). The third method is based on mean and standard deviation (Negm 2000).

1 - $Z=(X-X_{min})/(X_{max}-X_{min})$ to set the values in the range of 0 to 1.
2 - $Z=[(X-X_{min})/(X_{max}-X_{min})$ to set the values in the range of 0.1 to 1.
3 - $Z=(X-\mu) / \sigma$. to set the values in the range of -1 to 1.

The maximum, the minimum and the estimates of μ(mean) and σ(standard deviation) for the inputs and target are given in Table 2.

The network is re-trained using the normalized data based on the two methods 1 and 2. The results of the trained network are shown in Table 8. Better results are to the zero mean unit standard deviation normalization method (method 3). This is because most of the series of the present application (EV, AT and SR) have peaks and tails. In this case, the majority of values are mapped to a small range of values and hence the data is distorted, Neural Connection (1998). The third method is therefore adopted in this paper.

TABLE 8
Effect of data normalization method

Data set	Method-1	Method-2	Method-3
Training	0.894	0.892	0.903
Validation	0.888	0.887	0.920
Test	0.930	0.931	0.923

Results of the Trained Network 4-3-1

Figs. 4a, 4b, 4c and *4d* show the results of the trained network for training, validation, test and all data sets respectively. Fair agreement between observed and predicted evaporation is obtained.

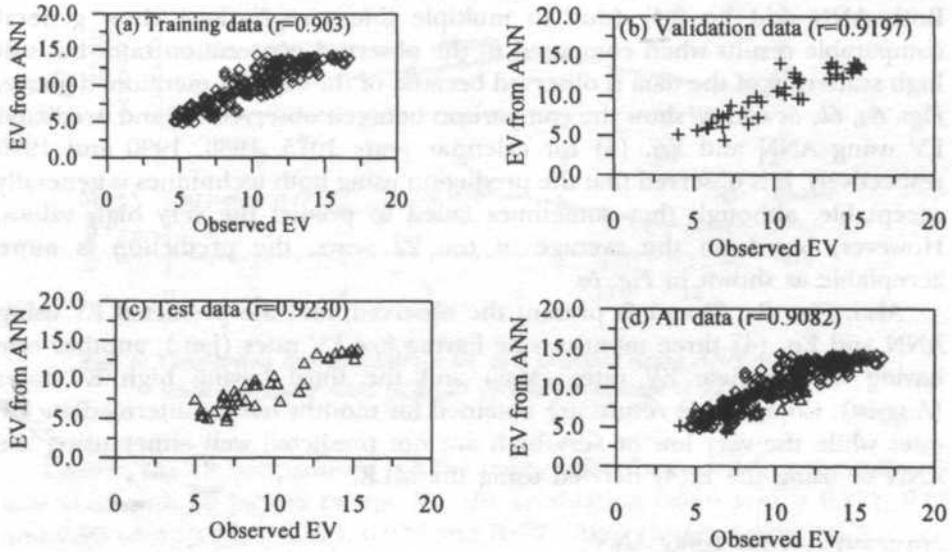

Fig. 4: Comparison between observed EV and predicted using ANN 4-3-1 model

The correlation coefficient between the observed and the predicted evaporation rates using ANN is still small compared to the excellent capabilities of the promising techniques. In a previous study conducted by Tahir (1998) based on evaporation in Central Saudi Arabia (Riyadh City Station), a correlation coefficient of 0.97 was obtained. One reason for the low correlation in the present study is the use of the average values of the data of two stations as shown in Table 1. Also, the high scatter in the SR data may be another reason. Alshaikh (1998) proved that the EV is highly correlated with SR (r=0.76) than do with WS (0.42) for Riyadh City (same data used by Tahir 1998). These values are (r=0.39) and (r=0.60) for Bisha which are contradicting with those of Alshaik (1998). Also, he obtained higher correlation between EV & AT as (r=0.29) and between EV & RH as (r=-0.86) compared to (r=0.89) and (r=-0.66) in the present study. In order to make sure that the software is performing well, the same network is used to handle the same data used by Alshaikh (1998) and Tahir (1998). Correlation coefficients of 0.946, 0.940 & 0.908 are found for training, validation and test data test respectively. The corresponding correlation coefficients of the regression model similar to Eq. (4) are 0.940, 0.964 and 0.933 for the same data sets. Hence, it is recommended that in order to obtain better results for Bisha region, it is advised to re-train the network using the data of each station of Table separately. Then the outputs of the two networks are averaged to obtain the values applied to Bisha province.

Comparisons

Figs. 5a and *4b* show the comparison between observed evaporation rates and the predicted values using both ANN and Eq. (4) for both and test data sets. Both ANN and Eq. (4) (due to multiple linear regression) show general comparable results when compared to the observed evaporation rates but still high scattering of the data is observed because of the reasons mentioned above. *Figs. 6a, 6b, 6c* and *6d* show the comparison between observed EV and predicted EV using ANN and Eq. (4) for calendar years 1975, 1980, 1990 and 1996 respectively. It is observed that the prediction using both techniques is generally acceptable, although they sometimes failed to predict the very high values. However, based on the average of the 22 years, the prediction is more acceptable as shown in *Fig. 6e.*

Also, *Figs. 7a, 7b* and *7c* present the observed, and the predicted EV using ANN and Eq. (4) three months, one having low EV rates (Jan.), another one having intermediate EV rates (May) and the third having high EV rates (August). Comparable results are obtained for months having intermediate EV rates while the very low or very high are not predicted well either using the ANN or using the E.(4) derived using the MLR.

Sensitivity Analysis Using ANN

The developed network is trained again using the data when one or more factor is excluded to study the effect of the different factors on the output of the neural network. The results of such analysis are presented in Table 9.

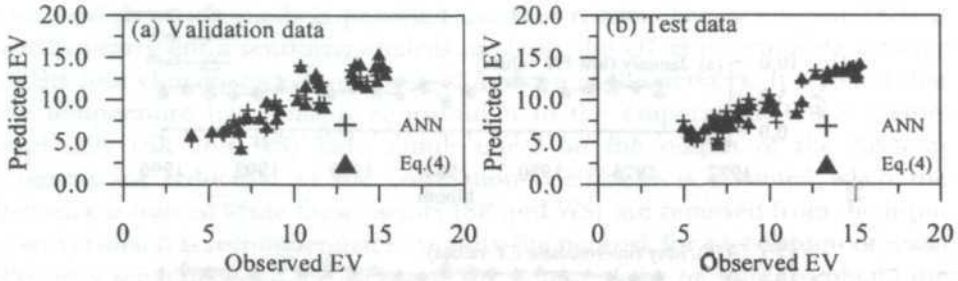

Fig. 5: Comparison between observed and predictions of ANN and Eq. (4) for (a) validation data and (b) test data

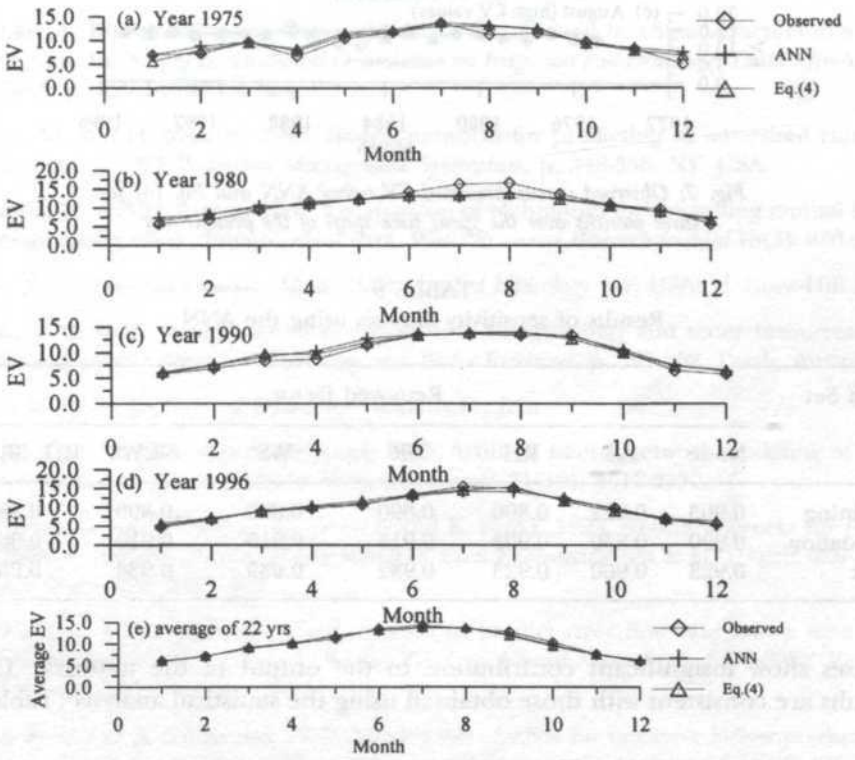

Fig. 6: Comparison between observed EV and predicted using ANN and Eq. (4) selected calendar years (a,b,c,& d) and for average of 22 yrs (e)

Clearly, the air temperature has the major effect because when the network is trained with all factors except AT, the correlation coefficient is 0.822, 0.83 and 0.90 compared to 0.903, 0.920 and 0/923 for training, validation and test data set. Also, when all factors are removed except AT, the network yields prediction with correlation coefficients which are close to those obtained when all factors are used (0.880, 0.905 & 0.934 versus 0.903, 0.920 & 0.923). Other

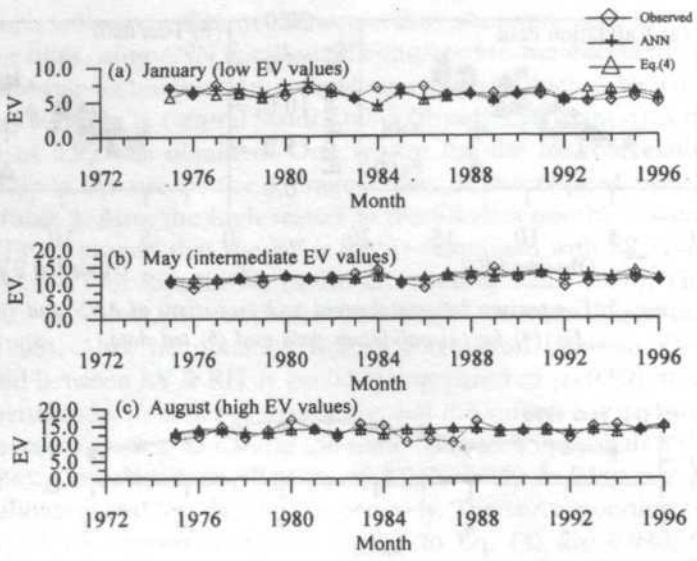

Fig. 7: Observed versus predicted EV using ANN and Eq. (4) for three months over the spent time span of the present day

TABLE 9
Results of sensitivity analysis using the ANN

Data Set	Removed factor						
	None	AT	RH	SR	WS	SR,WS	RH, SR, WS
Training	0.903	0.822	0.896	0.890	0.890	0.890	0.880
Validation	0.920	0.830	0.903	0.915	0.915	0.910	0.905
Test	0.923	0.900	0.925	0.932	0.939	0.934	0.934

causes show insignificant contribution to the output of the network. These results are consistent with those obtained using the statistical analysis (Table 3).

CONCLUSION

The average monthly time series data of evaporation at Bisha Province, Saudi Arabia, with a length of 22 years from 1975 to 1996 is analyzed and correlated to the basic climatic factors (air temperature, relative humidity, solar radiation and wind speed). Prediction models are developed using both statistical techniques (multiple linear and non-linear regression analysis) and artificial neural networks. The results of the developed models are compared with the observed data. The prediction of the artificial neural network is proven to be comparable to that of the regression models for the region under consideration. Different data normalization methods are tested and the zero mean unit

standard deviation method provided the best results. The developed ANN is used to carry out a sensitivity analysis to clarify the effect of removing a factor of the four climatic factors on the performance of the network. It is found that air temperature has a major contribution to the evaporation. Other factors especially (SR and WS) have minor effect on the output of the ANN as insignificant reduction in the correlation coefficient is obtained when the network is trained while these factors (SR and WS) are removed from the input data vectors. It is recommended to re-train the network for each station of Bisha Province separately and the averaging the output of the networks to obtain the evaporation rates applied to Bisha region.

REFERENCES

ALSHAIKH, A. 1998. Analysis of evaporation data has affected by climatic factors in a rid regions. In *Proc. of International Commission on Irrigation and Drainage, Tenth Afro-Asian Conf.*, p. A27.1-A-28.15. Bali.

ANMALA, M. and H. JOBSEON. 1995. Neural networks for predicting of watershed runoff. In *Proc. of 1995 Watershed Management Symposium*, p. 348-356. NY, USA.

ANDERSON, M. and H. JOBSON. 1982. Comparison of techniques for estimating annual lake evaporation using climatological data. *Water Resources Research Journal* **18(3)**: 630-636.

CHOW, V., D. MAIDMENT and L. MAYS. 1998. *Applied Hydrology*. NY, USA: McGraw-Hill Inc.

DANIEL, T.M. 1991. Neural networks applications in hydrology and water resources. In *Proc. of the Int. Symp. on Hydrology and Water Resources*, p. 797-802. Perth, Australia.

GUPTA, B. 1992. *Engineering Hydrology*. India: N.C., Jain.

HSU, K., V. H. GUPTA and S. SOROOSHIAN. 1995. Artificial neural network modeling of the rainfall-runoff process. *Water Resources Research* **31(10)**: 2517-2530.

KARUNAITHI, N., W. J. GRENNEY, D. WHITLEY and K. BOVEE. 1994. Neural networks for river flows prediction. *Journal of Computing in Civil Engineering* ASCE **8(2)** April: 201-219 and Discussion **9(5)**: 293.

ICHIYANAGI, A. 1995. Artificial neural network to predict river flow rate into a dam for hydropower plant. In *Proc. of the Int. Conf. on Neural Networks*, p. 2679-2682. Perth, Australia.

JAIN, S. K. and D. K. SRIVASTAVA. 1999. Application of ANN for reservoir inflow prediction and operation. *Journal of Water Resources Planning and Management* ASCE **125 (5)**: 263-271.

JUNG, J. S., K. S. KIM and J. H. LEE. 2000. Short-term prediction model of local rainfall. Proc. of abstracts and Papers (on CD ROM) of the *3rd Int. Conf. on Hydroscience and Engineering*, **4**, Seoul, Korea.

LINSLEY, R., M. KOHLER and J. PAULUS. 1958. *Hydrology for Engineers*. New York: McGraw-Hill Inc.

MASON, J. C., R. K. PRICE and A. TEM'ME. 1996. A neural network model of rainfall-runoff using radial basis functions. *J. of Hydraulic Research* **34:** 537-548.

MOAW. 1984. *Monthly Climatic Data for the Period 1964-1984*. Saudi Arabia: Ministry of Agriculture and Water.

MOAW. 1996. *Monthly Climatic Data for the Period 1975-1996*. Saudi Arabia: Ministry of Agriculture and Water.

MINNS, A. W. 1996. Extended rainfall-runoff modeling using artificial neural networks. In *Proc. of 2nd Int. Conf. on Hydroinformatics*, p. 207-213. Zurich.

MORTON, F. 1979. Climatological estimate of lake evaporation. *Water Resources Research Journal* **15(1):** 64-76.

NEGM, A. M. 2000. Prediction of hydraulic design parameters of expanding stilling basins using artificial neural networks. *Egyptian Journal of Engineering Science and Technology* EJEST **5(2)**: 1-18.

NEURAL CONNECTIONS. 1998. ANN Software and Manuals, Developed by SPSS/Recognition Systems LTD.

OMAR, M. and M. ELBAKRY. 1985. Evaporation from the Aswan high dam lake (Lake Nasser). WMO *Casebook on Operational Assessment of Areal Evaporation*: 11-15.

POFF, L. N., A. S. TOKAR and P. A. JOHNSON. 1996. Stream hydrological and ecological responses to climate change assessed eith an artificial neural network. *J. Limnol. and Oceanogr.* **41(5):** 857-863.

RAMAN, H. and V. CHANDRAMOULI. 1996. Deriving a general operating policy for reservoir using neural network. *Journal of Water Resources Planning and Management*, ASCE **122(5)**: 342-347.

SCHALKOFF, R.J. 1997. *Artificial Neural Networks. Computer Science Series*. New York: McGraw-Hill Co., Inc.

SINGH, V. 1992. *Elementary Hydrology*. NJ., USA: Prentice Hall Inc.

SINGH, V. and C. Y. XU. 1997. Evaluation and generalization of 13 mass-transfer equations for determining free water evaporation. *Journal of Hydrological Processes* **11(3)**: 311-323.

SMITH, J. and R. N. ELI. 1995. Neural network models of rainfall-runoff process. *Journal of Water Resources Planning and Management*, ASCE **121(6):** 499-508.

TAHIR, S. A. 1998. Estimating potential evaporation using artificial neural network. In *Proc. of International Commission on Irrigation and Drainage*, Tenth Afro-Asian Conf., p. A-28.1-A-28.12. Bali.

TAWFIK, M., A. IBRAHIM and H. FAHMY. 1997. Hysteresis sensitive neural network for modeling rating curves. *Journal of Computing in Civil Engineering*, ASCE **11(3):** 206-211 and Discussion **13(1):** 56-57.

THAIRUMALAIAH, K. and M.C. DEO. 1998. River stage forecasting using artificial neural networks. *Journal of Hydrologic Engineering*, ASCE **3(1):** 26-32.

TINGSANCHALI, T. and M. R. GAUTAM. 2000. Application of tank, NAM, ARMA, and neural network models to flood forecasting. *Hydrological Processes* **14(4)**: 2473-2487.

ISSN: 0128-7680
Pertanika J. Sci. & Technol. 12(2): 189 - 201 (2004)

A Planning Model of Optimal Development and Transportation of Recycled Waste Material

[1]L.A. Mohammed & [2]Leow Soo Kar
[1]Swinburne University of Technology
Jln Simpang Tiga
Kuching, Sarawak, Malaysia
E-mail:lmohammed@swinburne.edu.my
[2]Director of Research and Development
School of Information Technology
Monash University Malaysia
No. 2, Jalan Kolej, Bandar Sunway
46150 Petaling Jaya, Malaysia
E-mail: leow.soo.kar@infotech.monash.edu.my

Received: 30 November 2000

ABSTRAK

Pembuangan sisa pepejal bandaran merupakan masalah yang sering dihadapi oleh negara industri di seluruh dunia. Program kitar semula bahan sisa adalah suatu komponen kepada sistem pengurusan sisa pepejal bandaran. Kitar semula yang mempunyai impak signifikan boleh dikategorikan di bawah tiga bahagian besar: signifikan dari segi ekonomi, kesihatan dan alam sekitar dan sosial. Kesemua ini berupaya meringankan kemelesetan sumber, mengurangkan permintaan kawasan pembuangan dan umumnya melibatkan penjimatan penggunaan tenaga. Model pengoptimuman boleh memainkan peranan utama dalam perancangan keberkesanan kos secara berpanjangan bagi sistem ini. Pengangkutan adalah komponen penting yang memerlukan siasatan yang teliti. Substesen diperlukan untuk memastikan kuantiti bahan kitar semula dan seterusnya pengumpulannya oleh sistem pengangkutan ekonomi yang lain (lori atau kereta api). Kajian ini menumpukan siasatan ke atas penempatan substesen yang berkemungkinan di antara penjual dan pembeli untuk mengurangkan waktu pengangkutan di antara pusat pembekal dan permintaan supaya bahan kitar semula boleh dihantar terus ke pusat permintaan atau stesen.

ABSTRACT

Disposal of municipal solid waste is a problem commonly confronting all industrialized countries around the world. A waste material recycling program is one of the most visible components of municipal solid waste management systems. The significant impacts of recycling can be grouped under the following three broad areas: Economic significance, Environmental and Health significance, and Social significance. It mitigates resource scarcity, decreases demand for landfill space and generally involves savings in energy consumption. Optimization models play a prominent role in the long-term cost-effective planning of these systems. Transportation of the waste material from one location to another is an important component of these systems. To minimize the cost of transporting the waste materials from the collection points or areas

to the recycle center, there is the need to have substations at some strategic places to collect density the materials for economical transportation (e.g. by rail) to the center. This paper examines the possibility of locating substations between sellers or suppliers and demand centers to reduce the overall transportation costs.

Keywords: Facility location, integer programming, waste material recycling

INTRODUCTION

Recycling is widely assumed to be environmentally beneficial and conducive to sustainable economic development. The advantages of recycling can be classified as follows:

1. Economic advantages: these include reduction of cost of solid waste management, saving of energy in terms of electricity and fuel, reducing foreign importation, generation of employment, and reduction in health care costs and saving in cost for other public utilities.
2. Environment/Ecological advantages: these include landfilling, and soil/ other natural resources conservation such as control of erosion and soil moisture (it improves the external environment).
3. Social advantages: creating employment for scavengers, and cutting down littering.

Traditionally, solid waste management is mainly concerned with the removal of municipal wastes by hauling and dumping them out of the city boundaries. However, with more and more refuse being generated due to the expansion of urban centers, this has given rise to increased collection and transportation and disposal costs. To overcome this increased cost, recycling can be a viable approach to solid waste management. These problems are challenging in today's society. For instance, collection generally includes the gathering of recyclable materials and the hailing of these to a processing center, then to a transfer station, usually near a landfill and finally to the market destinations. If the distance from the location to the center is far, the transportation cost will go very high. Solving this problem is complicated because factors such as volume, weight, loading, cleaning, shipping costs for both rail and truck and fuel surcharges must be considered. This paper focuses on the optimal location of the facilities so that the overall transportation cost is minimized.

Historical background is introduced in the next section. Section 3 deals with problem formulation, and looks at the different constraints to be used when dealing with capacitated and incapacitated problems. Further, it analyzes and formulates an optimum location for a single facility. The practical implementation or the results are given at the last part of the section. The concept of Voting Process procedures is introduced. Finally, the conclusion section completes the paper.

A Brief Historical Perspective

The early work on location problems originated from Fermat in the 17th century. Others who contributed to this field include Weber in 1909 who introduced the concept of industrial location. In 1937, Weisfield presented the idea of iterative procedures for locating a new facility to minimize the sum of weighted Euclidean distances to any number of existing facilities. The advent of electronic computers in the 1970s brought about a new avenue for further research in iterative procedures. Since then, a lot of researchers have been using computers to implement these concepts in solving real world problems. Details of historical references may be found in Francis and Goldstein (1974). Some of the application areas include the use of Linear Programming models for waste material recycling program development. Khan (1987) employed a method of optimizing the cost of solid waste disposal. Kirca and Erkip (1988) proposed a mathematical programming model for selecting transfer station locations. A different approach was developed by Hansen and Thisse (1981). They investigated a Voting and Planning problem in relation to facility location. Constrained location and the Weber-Rawls problems have been considered by Hansen *et al.* (1990). Baeth and Neebe (1994) developed a mixed integer linear programming (MILP) model that was capable of determining the optimal recycling program development levels for individual recycling materials within an integrated waste management system. Konforty and Tamir (1997) addressed the problem of a single facility with minimum distance constraints. Recently, Chen (2001) developed an optimal location of a facility based on circular demand areas. Surveys of several location problem development were presented in Dearing (1985).

Problem Formulation

The choice of an appropriate model depends on the nature of the problem being investigated and the stage of the programmed solution. Some of the basic questions that can be addressed include:

- the number of facilities to be located and the cost involved
- the sites selection
- the sizes of the facilities
- which facility should serve which demand point

Generally, there are fixed costs for locating the facilities and transportation costs for distributing the commodities between the facilities and the clients (facility location problem). When each potential facility has a capacity, the problem is called the capacitated facility location problem, otherwise it is known as the incapacitated facility location problem.

The Capacitated and Incapacitated Facility Location Problem

First, we start with the incapacitated location problem. In this case, we are concerned with a set of locations.

$N = \{1,2.....m\}$

and the distance between them,'

c_{ij}, $\quad i, ,j = 1, ...m;$

We assume that there is a set $U \subseteq N$ of locations at which we may open a facility, and a subset $V \subseteq N$ of locations that must be assigned to some open facility. For each location $j \in V$, there is a positive integral amount of waste generated of simply *generation* say *di* that must be shipped to its assigned location. We also assign a non-negative cost *fi* of opening a facility at *i* for each location $i \in U$. The cost of assigning location *j* to an open facility at *i* is c_{ij} per unit of material shipped. Further we should assume that the costs are non-negative, symmetric, and also satisfy the triangle inequality, i.e $c_{ij} = c_{ji}$ for all $i,j = N$, and $c_{ij} + c_{jk} \geq c_{ik}$ for all $i, j, k \in$ N. The objective is that we want to find a feasible assignment of each location in *V* to an open facility so as to minimize the total cost incurred. The following integer programming can be used to solve the problem:

$$\text{Minimize} \sum_{i \in U} fiyi + \sum_{i \in U} \sum_{j \in V} djc_{ij}x_{ij} \tag{3.0}$$

Subject to

$$\sum_{i \in U} x_{ij} = 1 \qquad j \in V \tag{3.1}$$

$x_{ij} \leq y_i$ for each $i \in U$ and $j \in V$,
$x_{ij} \in \{0, 1\}$ for each $i \in U$ and $j \in V$,
$y_i \in \{0, 1\}$ for each $i \in U$,

It should be noted that $y_i \in \{0.1\}$ for each $i \in U$ indicates if a facility is opened at location *i*, and $x_{ij} \in \{0, 1\}$ for each $i \in U$ and $j \in V$ indicates if location *j* is assigned to a facility at *i*.

In the capacitated location problem, we need to impose an additional capacity constraint i.e. the amount of recycled materials that can be accommodated by the substations. This can be formulated as follows:

$$\sum_{j \in V} x_{ij} dj \leq Mi \tag{3.0*}$$

Where *Mi* is the maximum size of the stores used to keep and pack the materials before fetching them to the center. In the uncapacitated problem, if we know the value of *y*, then it is trivial to find the corresponding value of *x*: we simply assign each location $j \in V$ to the location *i* for which c_{ij} is the minimum among all possibilities where $y_i = 1$. In the capacitated case, the

situation is more complicated especially when each location can be assigned to more than one facility.

Optimum Solution for Single Facility Location

We will consider a single facility location problem where both the new facility location and the existing facility locations are treated as points, and where the demands and costs are known. From the classical Weber problem, the generalized problem can be formulated as:

$$\text{Min } Z = \sum_{j=1}^{n} Q_j lp(X,Y) \tag{3.2}$$

Alternatively, (for simplicity) let the objective function be given as follows:

$$\min \left\{ f(x,y) = \sum_{i=1}^{m} fi\big(di(x,y)\big) \right\} \tag{3.3}$$

Where fi is the weight of the i^{th} demand point located at (xi, yi), $di(x, y) = [(x - xi)^2 + (y - yi)^2]^{1/2}$ (for a straight line distance) are functions of the Euclidean distance $di(x, y)$ between point i and the point to be located. It is useful at this point in the discussion to introduce the concept of a *convex* function. A function $f(X)$ is said to be convex if the line segment between any two points, $[X^1, f(X^1)]$ and $[X^2, f(X^2)]$, on the graph of the function never lies below the graph (Love *et al.* 1988). Formally, this means $f(X)$ is convex if

$$f[\lambda x^1 + (1 - \lambda)x^2] \leq \lambda f(x^1) + (1 - \lambda) f(x^2)$$

for any two distinct points x^1 and x^2 in the domain of f and any $\lambda \in [0,1]$.

To solve equation (3.3), a single new facility must be located among the m existing ones on the plane so as the sum of weighted distances be minimized. As mentioned above, problem (3.3) is a classical Weber problem, and it has been shown to be a convex (Eilon *et al.* 1971). By direct differentiation, the condition for a local minimum can be obtained by considering the partial first derivatives of $f(x,y)$ in (3.4):

$$\frac{\partial f}{\partial x} = \sum_{i=1}^{m} \left\{ \frac{1}{di(x,y)} \frac{\partial fi}{\partial di} (x - xi) \right\} = 0, \tag{3.4}$$

$$\frac{\partial f}{\partial y} = \sum_{i=1}^{m} \left\{ \frac{1}{di(x,y)} \frac{\partial fi}{\partial di} (y - yi) \right\} = 0, \tag{3.5}$$

The necessary condition for a point (x,y) to be a solution of the problem is that both equation (3.4) and (3.5) must be 0. Now due to convexity, if such a point is found, then it is a global solution. Therefore we look for a point for which $\frac{\partial f}{\partial x} = \frac{\partial f}{\partial y} = 0$

Solving the equation implicitly leads to the following recursive relationship:

$$x = \frac{\sum_{i=1}^{m} \left\{ \frac{1}{di(x,y)} \frac{\partial fi}{\partial di} xi \right\}}{\sum_{i=1}^{m} \left\{ \frac{1}{di(x,y)} \frac{\partial fi}{\partial di} \right\}} \tag{3.6}$$

$$y = \frac{\sum_{i=1}^{m} \left\{ \frac{1}{di(x,y)} \frac{\partial fi}{\partial di} yi \right\}}{\sum_{i=1}^{m} \left\{ \frac{1}{di(x,y)} \frac{\partial fi}{\partial di} \right\}} \tag{3.7}$$

Since these equations cannot be solved in closed form, we use an iterative procedure or *Weiszfeld procedure* based on equation (3.6) and (3.7), i.e the n^{th} step in the iteration as follows:

$$x^{n+1} = \frac{\sum_{i=1}^{m} \left\{ \frac{1}{di(x^n,y^n)} \frac{\partial fi}{\partial di} xi \right\}}{\sum_{i=1}^{m} \left\{ \frac{1}{di(x^n,y^n)} \frac{\partial fi}{\partial di} \right\}} \tag{3.8}$$

$$y^{n+1} = \frac{\sum_{i=1}^{m} \left\{ \frac{1}{di(x^n,y^n)} \frac{\partial fi}{\partial di} yi \right\}}{\sum_{i=1}^{m} \left\{ \frac{1}{di(x^n,y^n)} \frac{\partial fi}{\partial di} \right\}} \tag{3.9}$$

The center of gravity point can be taken as:

$$x^0 = \frac{\sum_{i=1}^{m} \frac{\partial fi}{\partial di} xi}{\sum_{i=1}^{m} \frac{\partial fi}{\partial di}}, \quad y^0 = \frac{\sum_{i=1}^{m} \frac{\partial fi}{\partial di} yi}{\sum_{i=1}^{m} \frac{\partial fi}{\partial di}} \tag{3.10}$$

Ostresh (1978) pointed out that Weiszfeld's method is the steepest descent method with a stepsize determined by the denominator in equations (3.8) and (3.9). This can be seen when we consider Chen (1984), the step determined by two consecutive points in the iteration.

$$x^{n+1} - x^n = \frac{\sum_{i=1}^{m} \left\{ \frac{1}{di(x^n, y^n)} \frac{\partial fi}{\partial di} (xi - x^n) \right\}}{\sum_{i=1}^{m} \left\{ \frac{1}{di(x^n, y^n)} \frac{\partial fi}{\partial di} \right\}} \tag{3.11}$$

$$y^{n+1} - y^n = \frac{\sum_{i=1}^{m} \left\{ \frac{1}{di(x^n, y^n)} \frac{\partial fi}{\partial di} (yi - y^n) \right\}}{\sum_{i=1}^{m} \left\{ \frac{1}{di(x^n, y^n)} \frac{\partial fi}{\partial di} \right\}} \tag{3.12}$$

Morris (1981) shows the convergence of Weiszfeld procedure for a Weber problem with different distances (*generalized lp*). This assures that the iterations will converge to an optimal location, provided that neither an iterative nor an optimal new facility location is at an existing facility location.

RESULTS AND DISCUSSION

Assuming that the points or locations where recycled materials are collected in tons for transporting to the main recycle center are clustered some distance from the center, we are considering the best location on which to construct a sub-center that would receive the tons from the points and then transport them to the center in 10-ton modules. If we consider four points, their locations (A, B, C, D) are given in *Fig. 1* below and the amount of recycle materials they can generate per month in tons are 50, 40, 20, and 10 respectively. Let us further assume that the cost per module per mile is RM30.00 for transporting to the center and RM10.00 per ton per mile transporting from the points to the new sub-center. Now we have five existing facilities, including the center. The weights can calculated as in Table 1:

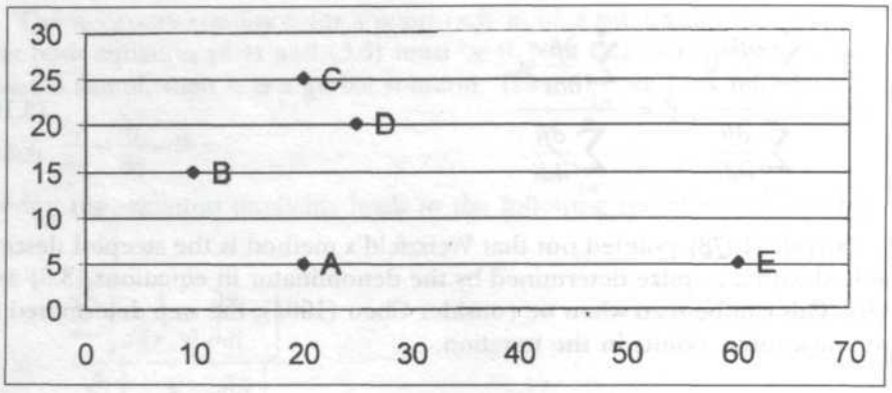

Fig. 1: Schematic of a facility location

TABLE 1
Calculating the weights

Points	*fi*
A	50 X 10 = 500
B	40 X 10 = 400
C	20 X 10 = 200
D	10 X 10 = 100
E	12 X 30 = 360

If for example $di(x,y) = [(x - xi)^{1.5} + (y - yi)^{1.5}]^{1/1.5}$ i.e if p = 1.5 in *lp*, then we have:

$$f(x,y) = 500\,(|x - 20|^{1.5} + |y - 5|^{1.5})^{1/1.5} + 400(|x - 25|^{1.5} + |y - 20|^{1.5})^{1/1.5} + 200(|x - 20|^{1.5} + |y - 25|^{1.5})^{1/1.5} + 100(|x - 10|^{1.5} + |y - 15|^{1.5})^{1/1.5} + 360(|x - 60|^{1.5} + |y - 5|^{1.5})^{1/1.5}$$

The problem is to find the location (x,y) that minimizes $f(x,y)$. This idea is shown in *Fig. 2.*

Rectangular Distance (p=1) is a best choice in solving this type of problem, their use simplifies many problems that cannot easily be handled with straight-line distances. For simplicity, let *fi* in Table 1 be 5, 4, 2, 1 for points A, B, C, D respectively. Using $p = 1$ equation (3.3) can be rewritten:

$$\text{Minimize } f(x,y) = f(X) + f(Y) \tag{3.13}$$

Where

$$f(X) = \sum_{i=1}^{m} fi|x - xi| \text{ and } f(Y) = \sum_{i=1}^{m} fi|y - yi|$$

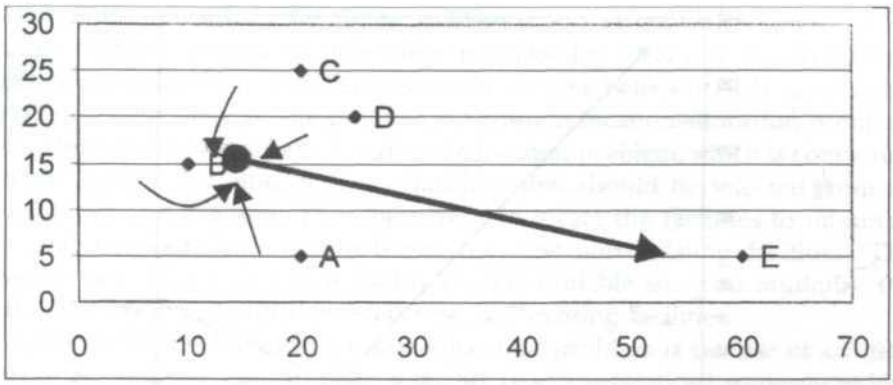

Fig. 2: Searching for the optimum location of sub center

Minimizing $f(x,y)$ is equivalent to separately finding an x that minimizes $f(X)$ and y that minimizes $f(Y)$. First, we must verify that $f(x,y)$ in (3.13) is a convex function. The result is obvious from the fact that the sum of convex functions is also a convex. To make things easier, we can combine the like terms of xi's and yi's to create a sequence of xi*'s and yi*'s that are strictly increasing in value. Example:

$$f(X) = 5|x - 20| + 4|x - 25| + 2|x - 20| + 1|x - 10| \text{ and}$$
$$f(X^*) = 7|x - 20| + 4|x - 25| + 1|x - 10|$$

As result we may have fewer values to deal with as shown in Table 2.

The graph for $f(X)$ and $f(Y)$ is given in *Fig. 3* and *Fig. 4* below.

From *Figs. 3* and *4*, it is easy to see that $f(X)$ has a minimum value of 30 at $xi^* = 20$, while the minimum value of $f(Y)$ is 95 at $yi^* = 15$. Hence, $f(x, y)$ has a minimum of 125 at (20,15). The new point N is at this point as shown in *Fig. 5*.

TABLE 2
New data entry

Points	Original Coordinates and Weights			Ordering the x Dimension		Ordering the y Dimension	
	xi	yi	fi	xi^*	fi^*	yi^*	fi^*
A	20	5	5	10	1	5	5
B	25	20	4	20	7	15	1
C	20	25	2	25	4	20	4
D	10	15	1			25	2

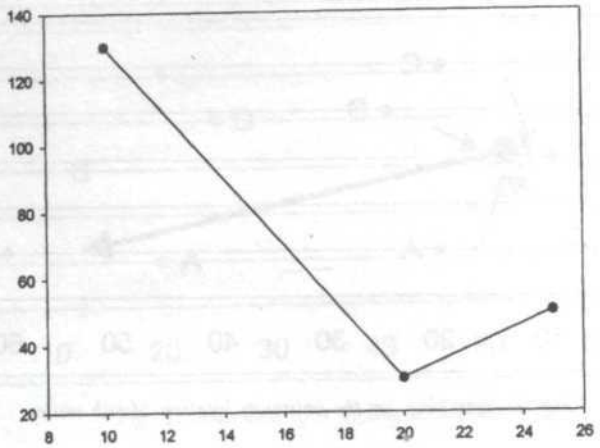

Fig. 3: Plot of f(X)

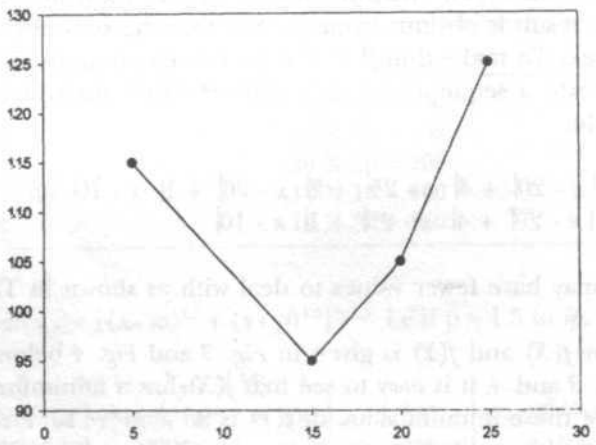

Fig. 4: Plot of f(Y)

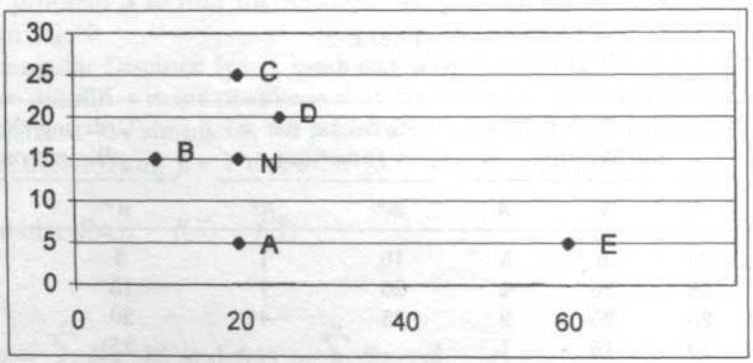

Fig.5: Optimum location of sub-center at 'N'

As mentioned earlier, the above problem is concerned with a single facility location. When we want to determine multi-facility locations of several new facilities simultaneously with the allocation of flow between each new facility and the existing facilities, the problem is known as location-allocation problem. It can alternatively be addressed as discrete location problem, which is concerned with the optimal location of p new facilities that should be selected from an available set of $q \geq p$ sites. The objective is to locate the facilities to minimize the total transportation cost between the new and existing facilities. The objective is to assign each new facility i to an available site j, to minimize the total cost of transportation between new and existing facilities.

An alternative solution to location-allocation problem is the use of a voting process. Suppose we want to place a facility (e.g. a substation) somewhere in a transportation network along the routes of which the users are established, and if the facility location is left up to the users. Given the assumption that the clients prefer to have the facility as close as possible to them, we know that since the population is spread over the space, it is impossible to meet simultaneously the wishes of all. In such situations a voting procedure is therefore required for choosing a particular location among the candidate locations. Let us assume that one substation is to be located for servicing a given set of clients, the voting problem consists of finding a location which is supported by a majority of the clients. Some of the solutions that can be used which address this problem are: *Plurality* solution, *Condorcet* solution, and *Simpson* solution as described in (Hansen and Thisse 1981) and (Carrizosa *et al.* (1997).

Before defining these terms, let's consider an undirected and connected network $N = (V.A)$, where $V = (v_1, v_2, \ldots v_n)$ is the set of vertices, and A as the set of arcs. The length of each arc $[v_i, v_j] \in A > 0$ when $i \neq j$. A point $n \in N$ may or may not be a vertex. The set of paths joining ni N and $n_j \in N$ is denoted by $P(n_i, n_j)$, a path in P in which the shortest distance in N between n_i and n_j is denoted by $d(n_i, n_j)$. Location of facility is allowed at any point along the route or at the vertices. We assume that there exists a finite set of clients 'U' and the cardinal of U is denoted by $|U|$. A client $u \in U$ is described by his location v_u N and by his utility function that reflects the desire of a client to have the facility locations n_i and n_j. We denote the number of clients who are closer to n_i than n_j as

$$|n_i < n| = \{u \in U : d(v_u, n_i) < d(v_u, n_j)\} \quad (3.14)$$

Moreover, for any $x \in N$ and any $\varepsilon > 0$, an ε-neighborhood of x is defined as the set

$$N(x;\varepsilon) = \{y \in N: d(x, y) \leq \varepsilon\} \quad (3.15)$$

A point $p \in N$ is said to be a Plurality point (PP) iff $|n < p| \leq |p < n| \forall\ n \in N$. Plurality point has more votes than any other point in N. A point $x \in N$ is called a local Plurality solution if

$|n < x| \leq |x < n| \forall\ n \in N(x;\varepsilon)$ for a given $\varepsilon > 0$ (3.16)

A point $c \in N$ is called condorcet point (CP) iff $|n < c| \leq |U| / 2\ \forall\ n \in$ N. CP is a point such that there exists no feasible n is strictly closer to an absolute majority of users, that is no more than 1/2 of the clients would prefer any other point on the network. A point $y \in N$ is said to be local Condorcet solution if

$|n < y| \leq |U| / 2$ for all $n \in N(y;\varepsilon)$ (3.17)

A point $s \in N$ is called a *Simpson point*, also called (1| 1)-*centroids* or *minimax Point* if $\max |y < s| \leq \max |y < x|$ for a particular $y \in N$, and $\forall x \in N$. Simpson solution is least objectionable locations, in the sense that any other feasible location will find a higher portion of users against. Note that if the score of Simpson point is less than or equal to $|U| / 2$, then it becomes a Condorcet point.

CONCLUSION

In this paper we addressed the problems of optimal location in general. Further, we applied the concept of a single facility location problem to develop a model for minimizing transportation costs which can play an important role in the planning of (municipal solid waste) MSW. An overview and economic importance of solid-waste management system has been highlighted. A very important new field of study in location theory known as Voting Process was also introduced. The paper shows that the voting process can be applied in deciding where to locate substations. However, there is a major difficulty in that the existence of solutions is not guaranteed, which further indicates the need for alternative solution concepts and further research in this field.

REFERENCES

BAETZ, B.W. and A.W. NEEBE. 1994. A planning model for the development of waste material recycling programs, *J. Operational Research Society* **45(12):** 1374-1384.

CARRIZOSA *et al.* 1997. Simpson points in planar problems with locational constraints. The round-norm case, *Mathematics of Operations Research* **22(2):** 276-290.

CHEN, R. 1984. Solution of location problems with radial cost functions. *Computer Maths. Applic.* **10(1):** 87-94.

CHEN, R. 2001. Solution of location of a single facility with circular demand areas, *Computer Maths. Applic.* 41, p. 1409-1061.

DEARING, P.M. 1985. Location problems. *Operations Research Letters* **4:** 95-98.

ELION, S. *et al.* 1971. *Distribution Management: Mathematical Modeling and Practical Analysis.* London: Griffin.

FRANCIS, R. L. and J.M. GOLDSTEIN. 1974. Location theory: a selective bibliography. *Operations Research* **22:** 400-410.

HANSEN, P. and J-F. THISSE. 1981. Outcomes of voting and planning: Condorcet, Wever and rawls locations. *Journal of Public Economics* **16:** 1-15.

HANSEN, P., J-F. THISSE and R. W. WENDELL. 1990. Equilibrium analysis for voting and competitive location problems. In *Discrete Location Theory*, ed. P. B. Mirchandi and F. L Richard, p. 479-500. John Wiley & Sons, Inc.

KHAN, A.M. 1987. Solid waste disposal with intermediate transfer stations: an application of fixed charge location problem. *J. of Operational Research Society* **38:** 31-37.

KIRCA, O. and N. ERKIP. 1988. Selecting transfer station location for large solid waste system. *European J. of Operational Research* **38:** 339-349.

LOVE, R., J.G. MORRIS and G.O. WESOLOWSKY. 1988. *Facilities Location Models and Methods.* North Holland.

MORRIS, J.G. 1981. Convergence of the Weiszfield algorithm for Weber problems using a generalised distance function. *Operations Research* **29:** 37-48.

OSTRESH, L. 1978. Convergence of a class of iterative methods for solving Weber location problem. *Operations Research* **26:** 597-609.

ZIPKIN, P. 2000. *Foundations of Inventory Management.* New York: McGraw Hill.

ISSN: 0128-7680
Pertanika J. Sci. & Technol. **12(2)**: 203 - 211 (2004)

Experimental Evaluation of H-Ometer Performance

H. Omar, M.S. Salsidu & M. Ratnasamy
Mountainous Terrain Development Research Centre, Faculty of Engineering, Universiti Putra Malaysia, 43400 UPM, Serdang, Selangor, Malaysia
E-mail: husaini@eng.upm.edu.my

Received: 15 October 2001

ABSTRAK

Terdapat beberapa jenis alatan yang dapat mengukur kekuatan tegangan tak langsung batuan di pasaran. Kebanyakannya adalah bersaiz besar dan mahal. Tetapi tidak semua alatan ini dapat digunakan untuk mengukur kekuatan tegangan tak langsung batuan lemah. Ini kerana batuan lemah adalah senang pecah semasa pensampelan. Untuk mengatasi dan menyenangkan ujian ke atas batuan lemah, satu alat yang kecil dan mudah alih yang efektif yang dipanggil H-Ometer telah direka cipta. Makalah ini membentangkan kajian analisis teori dan interpretasi praktik H-Ometer yang dapat digunakan secara efektif dalam penentuan kekuatan tegangan tak langsung batuan lemah.

ABSTRACT

There are several devices available in the market that can measure the indirect tensile strength of rocks. Most of them are bulky and costly. However, not many devices can be used to measure the indirect tensile strength of weak rock. This is attributed to the fact that weak rocks are easily broken during sampling. To facilitate and ease the process of testing weak rocks, a small and yet an effective portable device called H-Ometer was invented. This paper presents the theoretical analysis and practical interpretation of the H-Ometer that can be effectively used to determine the indirect tensile strength of weak rocks.

Keywords: Theoretical analysis, H-Ometer tests, indirect tensile strength, weak rocks

INTRODUCTION

H-Ometer is a portable indirect tensile strength measuring device designed specifically for testing weak rocks. It consists of a main body, head connector, H-Oring, tails, tubing and a control unit (Omar and Salsidu 2001). The basic schematic diagram of H-Ometer used by Omar (2001) is shown in *Fig. 1.*

The strength measuring devices like pressuremeters are primarily used to estimate the values of shear modulus, in-situ horizontal stress, undrained shear strength, and the coefficient of horizontal consolidation for clay deposits (Mair and Wood 1987). Traditionally, the testing is carried out within a pre-drilled vertical borehole or with the self-boring pressuremeter. A study showed that pressuremeter testing is quite commonly carried out in the laboratories, and most of the tests in the laboratory are for the research study.

According to Haberfield and Johnston (1990) the pressuremeter test has been modeled as the expansion of a long cylindrical cavity in a semi-infinite,

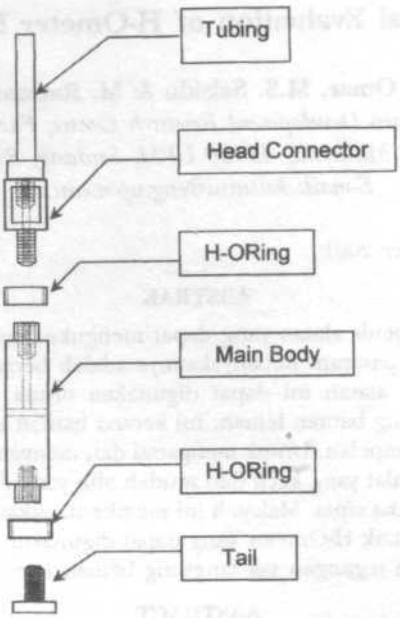

Fig. 1: The schematic diagram of H-Ometer

elasto-plastic medium, which was also illustrated by several earlier researchers. For the H-Ometer test, the expansion of the cylindrical cavity and the failure of the sample in tension are analysed using the Haberfield and Johnston (1990) model which assumes that the first crack or failure in tension will start at the cavity wall and propagate radially into the surrounding mass. The tensile failure of the test sample is therefore highly dependent on its relative tensile strength and the brittleness.

The weak rocks are often characterised by extreme difficulties in obtaining intact and competent samples for laboratory testing. Because of the difficulties in getting and sampling the specimens of weak rocks, the tests were carried out on the make-up samples (artificial rocks) using the model material recommended by Bandis (1980). The samples were then dried at a room temperature of 25°C and tested at different drying rates to get different tensile strengths of the specimens.

Theoretical Analysis

The first theory to analyse rocks using the pressuremeter test was proposed long time ago, by assuming that the rock mass is homogenous, isotropic, elastic and expected to undergo plain strain conditions. The above assumptions are very important to be incorporated in H-Ometer since it includes the effects of cracks that develop on the inside of the cavity walls. The basic development of radial tensile cracking during pressuremeter tests is represented in *Fig. 2*. The analysis seemed realistic in the sense that the rocks behaved as elastic-brittle masses.

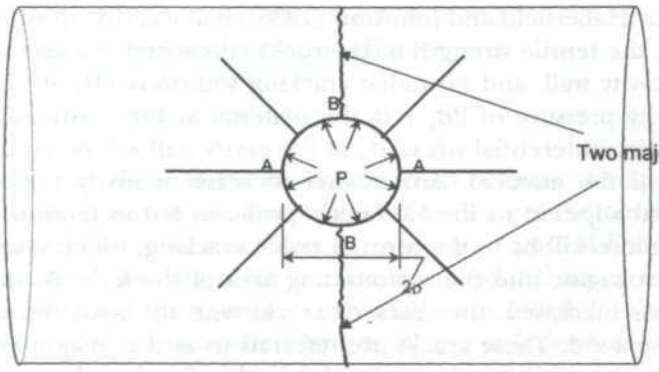

Fig. 2: Development of radial tensile cracking during pressumemeter tests

From the Mohr's circle of stress, during a pressuremeter test, it can be seen that there is a possibility of cracks existing or fissures being formed around the cavity during the test. As discussed by Mair and Wood (1987) during the elastic phase of test, the total radial stress, s_r, and the circumferential stress, s_q, change by equal and opposite amounts from the in-situ horizontal stress, s_h. When the cavity pressure, p, exceeds twice the in-situ horizontal stress, s_h, the circumferential stress, s_q, becomes zero. Thus, for the higher values of the cavity pressure, p, the circumferential stress, S_q becomes tensile stress. If the tensile value obtained through testing exceeds the tensile strength of the rock, s_t, cracks may develop radially from the cavity as indicated in *Fig. 2.*

The use of finite element model to describe the pressuremeter test in soft rocks was carried out by Haberfield and Johnston (1990). According to them, the propagation of crack through a finite element mesh involves three basic problems: the determination of the stress intensity factor at the crack tip, the direction and extent of crack propagation, and regeneration of the mesh as the crack tip moves. In general, the propagation of cracks through a finite element mesh has been divided into two groups: the crack zone approach and the discrete approach. The finite element simulations of the model pressuremeter tests were carried out at a cell pressure range of 0.02 to 0.4 MPa by Haberfield and Johnston (1990).

Model Assumptions

In H-Ometer tests, the H-Ometer probe is inserted into pre-drilled vertical holes of the core sample. The core sample is assumed to be much undisturbed. The core samples are also assumed to be homogenous and isotropic, therefore it contains no discontinuities. The cavity expansion is assumed to start when the applied pressure is equal to the in-situ horizontal stress, σ_h. The weak rock is considered to behave in an elastic manner. Initially as the pressure is increased, the response of the material surrounding the H-Ometer probe is assumed to be linearly elastic. This elastic response will continue until it fails in tension.

As discussed by Haberfield and Johnston (1986), if at a cavity pressure of $2\sigma_h + \sigma_t$, (where σ_t is the tensile strength of the rock) is reached, a shear failure is initiated at the cavity wall, and no radial cracking will occur. If, on the other hand, at the cavity pressure of $2\sigma_h + \sigma_t$ the material at the cavity wall is still elastic, then the circumferential stress, σ_θ, at the cavity wall will be equal to the tensile strength of the material. Any further increase in cavity pressure will cause the material adjacent to the H-Ometer probe to fail in tension.

The tensile failure will be in the form of radial cracking, which starts at the cavity wall and propagate into the surrounding area of the hole. As the cavity pressure is further increased, the crack or cracks with the least resistance to propagation will extend. These cracks are referred to as the 'major' cracks. A small number of major cracks are formed and these are distributed symmetrically around the cavity (Haberfield and Johnston 1989, 1990). The major cracks have been determined to occur at least in two directions in the H-Ometer test. *Fig. 2* illustrates the mode of failure of the specimen (Omar and Salsidu 2001) from the H-Ometer test. Laboratory analysis showed that the major cracks occur perpendicular to the longitudinal axis of the specimen. This could be due to the fact that the resistance from the transverse plane is much lower. As illustrated in *Fig. 2*, the cracks will propagate in a direction perpendicular to the maximum tensile stress in the radial direction, and the amount of extension will be governed by the fracture mechanic theory (Haberfield and Johnston 1990).

However the conditions shown in *Fig. 2* are assumed to be applicable for the H-Ometer test. Radial cracks start at the cavity wall and propagate until it fails in tension. Clarke (1995) shows that the radial and circumferential stresses are equal to the in-situ horizontal stress, σ_h, at the start of the test. When the cracks start at the cavity wall, the pressure at failure, P_f, will be equal to two times the horizontal stress plus the tensile stress. The above can be represented as in the following equation:

$$P_f = 2\sigma_h + \sigma_t \qquad (1)$$

where

P_f = pressure at failure
σ_h = horizontal stress
σ_t = tensile strength

Thus, this formula is quite applicable to an infinitely large block of isotropic and homogenous material with a hole and at the same formula can be also applied to H-Ometer tests for indirect tensile analysis up to rupture. Because the tensile failure starts in the annulus immediately around the cavity, the H-Ometer cannot tell the difference. From Equation (1) the tensile strength of weak rocks using H-Ometer can be interpreted as:

$$\sigma_{t,HO} = P_f - 2\sigma_h \qquad (2)$$

where

$\sigma_{t,HO}$ = Tensile strength using H-Ometer
P_f = Pressure at failure
σ_h = Horizontal stress

In this case there is no deviatoric stress because the specimens or core samples were tested in the unconfined state. To get the tensile strength from Equation (2), the horizontal stress, σ_h, is required from H-Ometer tests. For the H-Ometer test, the failure in tension occurred before it reached the limit pressure (P_L), and the pressure at this failure is called P_f. From Equation (2) it is also found that the tensile strength, $\sigma_{t,HO}$, is independent but P_f depends on the horizontal stress, σ_h. The horizontal stress, σ_h, can be estimated from H-Ometer test as discussed later in this paper.

Most of the tests were carried out on the specimens with minimum length equal to two times of diameter. This size of material is chosen because the tensile strengths are equal to the tensile principal stress which met over a finite distance in the annulus. As discussed by Mellor and Hawkes (1971), in the annulus, only a very small volume of material is subjected to tensile stress which approached the peak stress of the critical point, and the simple Griffith conditions for the tensile strength to be equal to the tensile principal stress are met over a finite distance in the annulus. Most of the H-Ometer test with this dimension failed in tension.

Failure Criteria

In H-Ometer tests, failure in tension was found right after the elastic phase (*Fig. 3*). The distance of the rupture point from the end-zone of the elastic phase seemed to largely depend on the material type and property. In principal, for tensile stress condition, failure involves both a crack initiation and a crack propagation criterion. Crack initiation is assumed to occur when the minor principal stress exceeds the tensile strength of the material. Crack propagation is determined by the linear elastic fracture mechanics theory, which means that once the crack has been initiated, it will propagate in a direction normal to the minor principal stress direction if the stress intensity at the crack tip exceeds the fracture toughness of the material (Haberfield and Johnston 1990).

According to Clarke (1995), it is considered that the minimum value of circumferential stress, σ_m, is less than the tensile strength, σ_t, in order to initate the crack. It is assumed that for the H-Ometer tests, the radial cracks start at the cavity wall, at least in two major directions and propagate with the minor cracks to the surrounding area of the material until it completely fails in tension.

The failure in tension or radial cracks in H-Ometer tests is based on the radial expansion of the H-Ometer. Upon the application of pressure at an increment, minor cracks may occur radially in the cavity wall and the migration of the cracks may take place over the weaker transverse plane which causes the sample split diametrically.

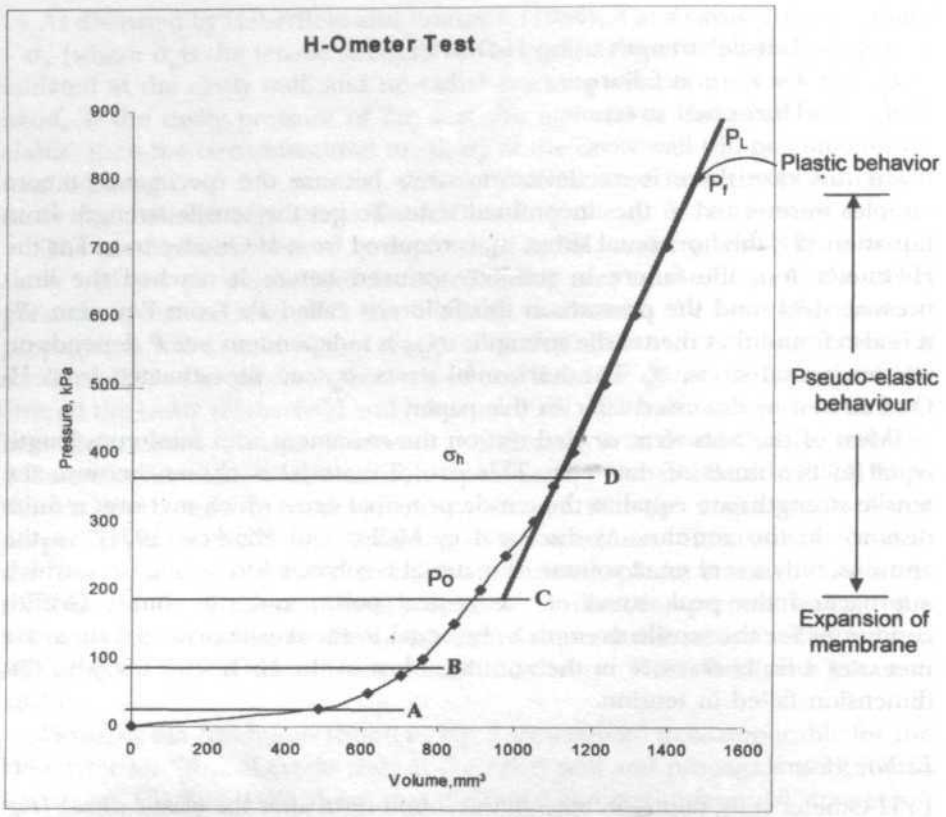

Fig. 3: A typical result from H-Ometer

Estimating Horizontal Stress Using Curve Fitting Method

As mentioned earlier, the cavity expansion is assumed to start when the applied pressure is equal to the in-situ horizontal stress, σ_h. But it is difficult to identify the reference datum or origin of the H-Ometer test. The H-Ometer test is similar to Pre-Bored Pressuremeter (PBP) test. According to Clarke (1995), it is difficult to identify the datum on a PBP test curve. The horizontal stress cannot be identified directly from a push-in pressuremeter (PIP) test curve. This is because of increased stress acting on the membrane during installation of the PIP (creating its test pocket is similar to the expansion of a cavity). So, the applied pressure during loading always exceeds the horizontal stress. The self-boring pressuremeter test is considered the best small-displacement method to determine the horizontal stress in-situ. However, the effects of boring disturbance, equipment characteristics and variations in test procedure cause problems in the interpretation of horizontal stress, σ_h (Mair and Wood 1897). However, further study is in progress to look into the development of the radial strain levels using radial strain gauges that may give a better correlation.

For the H-Ometer test (*Fig. 3*), the pressure is increased until, at A, where the expands with slightly increase in pressure until B. At the point C, where the slope of the curve becomes linear, is taken to be the point at which the membrane reaches the pocket wall. P_o is the pressure at this point but it is not equal to horizontal stress, σ_h, since the pocket wall was unloaded during drilling. There is some point at D, where $P_d > P_o$, at which the pressure is equal to the horizontal stress, σ_h, and that is the reference datum.

Based on the above assumption, the horizontal stress, σ_h, from H-Ometer test is determined by fitting the straight line to the corrected H-Ometer curve. The intersection of the H-Ometer curve with the straight line at the bottom is taken as a horizontal stress, σ_h, (*Fig. 3*). The data from H-Ometer test on weak rocks are analysed using the curve fitting method to get the horizontal stress, σ_h. The correlation is made on initial pressure and horizontal stress. It is found that the initial pressure, P_o, is half of the horizontal stress, σ_h. This is shown in *Fig. 4*. Based on the correlation it is summarized that:

$$P_o = 0.5\ \sigma_h \tag{1}$$

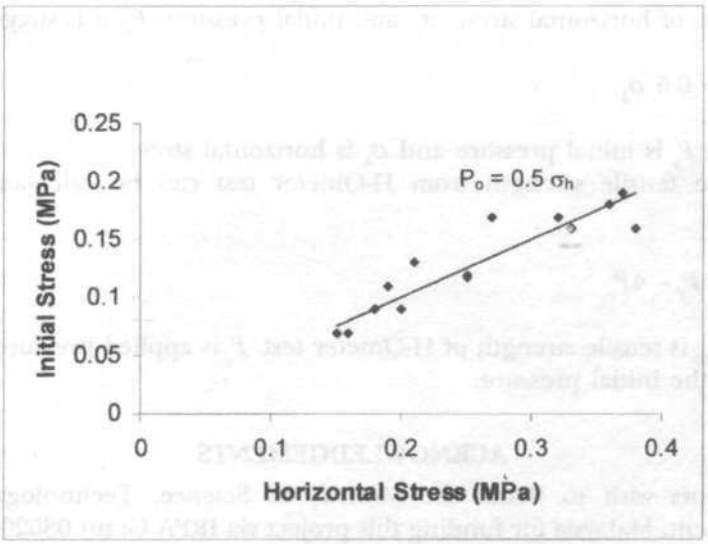

Fig. 4: The correlation of horizontal stress and initial pressure from H-Ometer tests

From Equation (3), the tensile strength from H-Ometer test, $\sigma_{t,HO}$ can be simplified by replacing horizontal stress, σ_h, to the initial pressure, P_o.

$$\sigma_{t,HO} = P_f - 2\sigma_h \tag{2}$$

$$P_o = 0.5\ \sigma_h \tag{3}$$

$$\therefore\ \sigma_h = 2P_o \tag{4}$$

So, the tensile strength of H-Ometer test,

$$\sigma_{t,HO} = P_f - 4P_o \quad (5)$$

By using Equation (5), the tensile strength of weak rocks can be calculated without getting the horizontal stress, σ_h. Based on Equation (5), the tensile strength of H-Ometer tests was calculated.

DISCUSSION AND CONCLUSIONS

In the theories of cavity expansion, it is assumed that the probe is installed into the test pocket without much disturbance. In H-Ometer test, there is some disturbance during the installation although it is small but in interpretation, this must be considered. Thus the initial pressure, P_o, is not equal to the horizontal stress, σ_h. There is a point at which the pressure is equal to the horizontal stress, σ_h, and this point is the *reference datum*. The reference datum is estimated by using the curve-fitting method, where the straight line is fitted to the test curve and the intersection at the bottom is chosen as a reference datum. This reference datum is taken as the horizontal stress, σ_h. From the correlation of horizontal stress, σ_h, and initial pressure, P_o, it is suggested that:

$$P_o = 0.5\ \sigma_h$$

where, P_o is initial pressure and σ_h is horizontal stress.

So, the tensile strength from H-Ometer test can be calculated by the formula:

$$\sigma_{t,HO} = P_f - 4P_o$$

where $\sigma_{t,HO}$ is tensile strength of H-Ometer test, P_f is applied pressure at failure and P_o is the initial pressure.

ACKNOWLEDGEMENTS

The authors wish to thank the Ministry of Science, Technology and the Environment, Malaysia for funding this project via IRPA Grant 0302040083 and MTD-RC staff for their support given throughout this study.

REFERENCES

BAGUELIN, F., J.F. JEZEQUEL and D.H. SHIELDS. 1978. *The Pressuremeter and Foundation Engineering*. Germany: Trans Tech Publications.

BANDIS, S. 1980. Experimental studies of scale effects on shear strength and deformation of rock joints. Ph.D Thesis, University of Leeds, U.K.

CLARKE, B.G. 1995. *Pressuremeters in Geotechnical Design*. Glasgow: Blackie Academic & Professional.

HABERFIELD, C.M. and I.W. JOHNSTON. 1986. Concepts for pressuremeter interpretation in soft work. In *Special Geomech. Symp. on Interpretation of Field Testing for Design Parameters,* p. 65-69. Adelaide, Canberra: I.E. Aust.

HABERFIELD, C.M. and I.W. JOHNSTON. 1990. A numerical model for pressuremeter testing in soft rock. *Geotechnique* **40(4):** 569-580.

MAIR, R.J. and D.M. WOOD. 1987. *Pressuremeter Testing – Methods and Interpretation.* London: Butterworth.

MELLOR, M. and I. HAWKES. 1971. Measurement of tensile strength by diametral compression of discs and annuli. *Eng. Geol.* **5:** 173-225.

OMAR, H. and M.S. SALSIDU. 2001. A new indirect tensile strength measuring device for weak rock. *Geotechnical Engineering Journal of the Southeast Asian Geotechnical Society* **32:** 75-81.

OMAR, H. 2001. The interpretation of H-Ometer test in weak rock – theoretical analysis. In *Proceedings of UPM Engineering Research Seminar,* p. 110-117, 2-3 Oct., Selangor.

ISSN: 0128-7680
Pertanika J. Sci. & Technol. **12(2)**: 213 - 224 (2004)

Design, Development and Calibration of a PTO Shaft Torque Transducer for an Agricultural Tractor

Azmi Yahya, A. F. Kheiralla & T. C. Lai
Department of Biological and Agricultural Engineering
Faculty of Engineering, Universiti Putra Malaysia
43400 UPM Serdang, Selangor, Malaysia

Received: 16 April 2002

ABSTRAK

Kertas ini menerangkan tentang reka bentuk, pembangunan serta penentukuran sebuah penderia bersepadu untuk mengukur keluaran daya kilas PTO bagi sebuah traktor pertanian. Reka bentuk penderia ini adalah hasil daripada pengubahsuaian yang telah dibuat ke atas aci pemacu PTO traktor komersial. Tolok terikan rintangan elektrik telah dilekatkan pada permukaan lilitan aci pemacu untuk mengukur terikan yang terjadi disebabkan oleh putaran daya kilas aci PTO. Tolok terikan diatur untuk membentuk litar titi *wheatstone* and disambungkan kepada sistem perolehan data dalam traktor melalui unit gelang gelincir. Penderia telah direka bentuk untuk daya kilas maksimum 1000 Nm dengan kepekaan bersamaan 0.1390 μStrain/Nm. Ujian penentukuran statik ke atas penderia memberikan kelelurusan serta kejituan pengukuran yang tinggi dengan pekali sekaitan atau R^2 yang masing-masing bersamaan 0.9942 dan 0.9945. Histerisis bagi pengukuran statik untuk penderia didapati tidak bererti. Kejituan pengukuran penderia tidak melebihi 6.65% dan 1% daripada magnitud daya kilas yang terukur dalam pengukuran statik dan pengukuran dinamik. Ujian demonstrasi ladang ke atas penderia dan sistem perolehan data menunjukkan keputusan yang amat memuaskan. Sistem perolehan data berjaya mengimbas serta merakam isyarat penderia seperti diprogramkan. Penderia yang dibangunkan ini adalah sebahagian daripada sistem peralatan lengkap dalam traktor Massey Ferguson 3060 yang akan digunakan dalam pembangunan pangkalan data yang menyeluruh darihal keperluan kuasa dan tenaga bagi traktor dan alat pertaniannya dalam ladang.

ABSTRACT

This paper describes the design, development, and calibration of an integrated transducer unit for measuring the input torque of a tractor's PTO driven agricultural implements. The transducer design is as a result of modifications made to a standard commercial tractor's PTO drive shaft. Electrical resistance strain gauges are mounted to the circumferential surface of the drive shaft to measure strain caused by the turning torque of the PTO shaft. The strain gauges are arranged into a wheatstone bridge circuit and interfaced to a data acquisition system on board the tractor via a slip ring. The transducer has been designed for a maximum torque of 1000 Nm with a sensitivity of 0.1390 μStrain/Nm. Static calibration tests on the transducer were excellent both in measurement linearity and measurement accuracy with coefficient of correlation or R^2 equal to 0.9942 and 0.9945, respectively. The hysteresis for static measurement with the transducer is found to be not significant. The transducer measurement errors are not more than 6.65% and 1% of the measured torque magnitudes under static and simulated dynamic measurements, respectively.

Field demonstration tests on the transducer and data acquisition system showed favorable results. The data acquisition system is able to scan and record the transducer signals as programmed. The developed transducer is part of the complete instrumentation system in the Massey Ferguson 3060 tractor to be used in the generation of a comprehensive database on the power and energy requirements of the tractor and its working implement in the field.

Keywords: Tractor, implement, instrumentation, transducer, PTO torque

INTRODUCTION

Measurements of tractor PTO shaft torque have received considerable attention in tractor-implement performance studies to determine the power requirements of various PTO driven agricultural implements working under normal field conditions for agricultural database. Instrumentation that measures the tractor PTO shaft torque and angular velocity would enable the power requirement of the drive PTO shaft agricultural implement to be calculated. Although there are a number of commercial torque transducers available in the market, they are still expensive and sometimes cannot fulfill the requirements of the researchers. Hoki *et al.* (1988) developed a PTO torque transducer using strain gauge and slip ring. The torque of the PTO was measured by applying strain gauge to the surface of the circular section shaft near the universal joint connected to the tractor PTO. The rotation of the shaft was measured by fixing a reflection type photo sensor closed to the PTO torque. The reflected light by the reflector plate on the revolving PTO shaft generated a current pulse for every revolution, which was recorded by a data recorder. Wilkinson and Rose (1990) developed an appropriate technology torque meter, which was low cost, simple and could be constructed with basic shop tools. The torque meter used a heavy coil spring, a section of large pipe, and a PTO shaft. A standard automotive ignition timing light had been modified slightly and was used as a strobe light to read rotational torque displacement of the PTO shaft under load. The shaft rotational speed was measured using a suitable tachometer, and shaft power was easily calculated using the rpm and torque load. Brassert and Dahlstrand (1996) developed an in-line torque meter for use with an absorption dynamometer in which the twist of a rotating PTO shaft was measured by a single sensor on the adjacent stationary structure.

The intended transducer is part of an additional instrumentation system to complement with the ready built-in tractor instrumentation for the purpose of providing comprehensive information on tractor-implement field performance for various agricultural field operations in Malaysia for the development of a useable agricultural machinery management database. The new developed transducers include drawbar pull at the tractor drawbar point, wheel torque at both tractor rear wheels, PTO torque at the tractor PTO output, and both horizontal and vertical forces at the tractor three-point hitches (Kheiralla and Azmi 2001).

This paper describes the design, development, calibration and demonstration of a tractor's shaft PTO torque transducer.

MATERIALS AND METHODS

General Descriptions

The design of PTO shaft torque transducer is as a result of the modifications made to a standard commercial tractor's PTO drive shaft (see *Fig. 1*). The free end of the female PTO shaft is provided with a raised collar, a screw bracket and a lock nut to position a 9E06-S1-3B NEC slip ring while the outer end is welded to a universal joint. Two sets of KFG-5-120-D16-11-L1M-2S Kyowa, 90° rosette, 120 Ohm, 2.1 gauge factor strain gauges are bonded at 45° shear planes at the two opposing positions on the outer surface of the female PTO drive shaft. The bonded strain gauges on the female PTO shaft are connected in a full bridge configuration. A 2.5 mA constant current excitation source is supplied from data acquisition system to the shaft transducer via the slip ring. The block diagram shown in *Fig. 2* illustrates the PTO torque transducer and its associated data acquisition system for the PTO torque measurement.

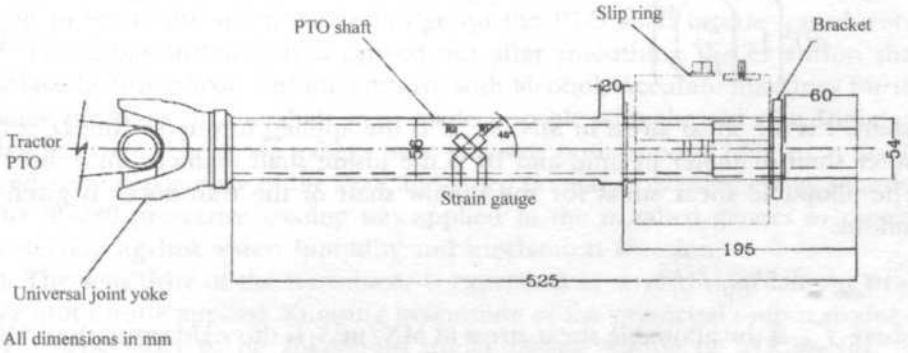

Fig. 1: Detail of the PTO shaft torque transducer

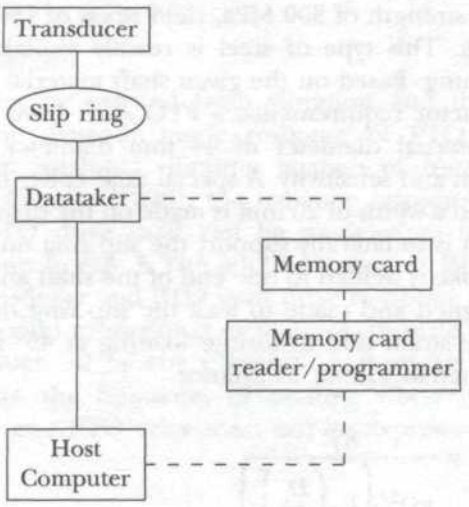

Fig. 2: Block diagram of PTO shaft torque transducer measurement

PTO Shaft Design

The expected PTO drive shaft torque, which the transducer is designed to measure, is estimated from tractor PTO output power. The maximum torque is calculated using the following formula:

$$P = \frac{2\pi NT}{60 \times 10^3} \tag{1}$$

where P is power output in kW, N is PTO speed in rpm, and T is torque in Nm.

A Massey Furgeson 3060 tractor having a PTO output power of 53 kW operating at standard PTO speed of 540 rpm would produce a maximum torque of 937.23 Nm on its PTO drive shaft.

The maximum shear stress in the hollow shaft of the transducer is subjected to a torque load which is given as follows:

$$\tau = \frac{16T}{\pi D_0^3 \left(1 - \left(\frac{D_i}{D_0}\right)^4\right)} \tag{2}$$

where τ is the shear stress in MN/m^2, T is the applied torque in Nm, D_0 is the outer shaft diameter in mm, and Dl is the inside shaft diameter in mm.

The allowable shear stress for the hollow shaft of the transducer is given as follows:

$$\tau_{allow} = 0.57 S_{yt} / f_s \tag{3}$$

where τ_{allow} is the allowable shear stress in MN/m^2 S_{yt} is the yield strength in MN/m^2, and f_s is the dimensionless safety factor.

The material used for the PTO shaft is mild steel SAE 1020 having ultimate tensile strength of 300 MPa, yield stress of 180 MPa, and modulus of rigidity of 82 GPa. This type of steel is readily available locally and provides for easy machining. Based on the given shaft material strength, slip ring bore diameter and tractor requirements, a PTO shaft having external diameter of 56.6 mm and internal diameter of 44 mm diameter is selected to meet transducer strength and sensitivity. A special raise collar having an outer diameter of 62.40 mm and a width of 20 mm is made on the drive shaft. The purpose of this collar portion is to laterally support the slip ring on the PTO drive shaft. A universal joint yoke is welded to one end of the shaft and a special mild steel screwed nut is designed and made to lock the slip ring on the other end of the shaft.

The strain due to torque loading at 45° location to shaft axis is given by Timoshenko (1990) as follows:

$$\varepsilon_{45^0} = \frac{8T}{\pi D_0^3 G \left(1 - \left(\frac{D_i}{D_0}\right)^4\right)} \tag{4}$$

where ε_{45° is the output strain in μStrain, T is the applied torque in Nm, D_o is outer shaft diameter in mm, D_i is inside shaft diameter in mm, and G is the material modulus of rigidity in GPa.

Having the applied torque equal to 937.23 Nm, inside and outer shaft diameters equal to 44 mm and 56.6 mm, torque magnitude of 937.23 Nm, and material modulus of rigidity of 82 GPa, the predicted maximum strain ε_{45° is calculated to be 257μStrain.

Strain Gauges Configuration

The PTO shaft torque sensing element design had 2 sets of Kyowa KFG-5-120-D16-11-L1M-2S 90° rossette strain gauges installed on opposite sides of extension axle shaft and positioned at 45° to axle axis to give the maximum sensitivity to torsional strains. The selected gauges have gauge resistance of 120 Ohm, gauge factor of 2.1, and provided with one-meter length lead wires. The available 4 gauges are wired to a constant current full wheatstone bridge configuration. A full bridge 2.5 mA constant current supply from the data acquisition system is used to excite the strain gauge bridge on the PTO shaft torque transducer.

The gauge installation is carried out after smoothing the extension shaft surface by fine silicon carbide abrasive with alcohol. Accurate markings for the gauge locations on the shaft were made possible with the aid of a Digimetic Height gauge. The strain gauges were precisely positioned at 180° apart on the predetermined surface of the shaft and glued permanently using epoxy adhesive. The SG280 protective coating was applied to the installed gauges to provide protection against water, humidity and mechanical abrasion.

The sensitivity of the transducer is expressed in terms bridge output strain per unit torque applied. Knowing magnitude of the predicted output strains of PTO drive shaft to be 257μStrain under design torque of 937.23 Nm, the predicted channel sensitivity for the data acquisition system is calculated to be 0.2731 μ Strain/kNm.

Natural Frequency and Dynamic Response

The designed transducer cannot be isolated from vibration and therefore should be able to measure the dynamic mode response of PTO torque measurements. Based on earlier torsional vibration analysis of tractor and implement PTO drive shaft by Corolla (1978), the dynamic response of the PTO torque transducer and PTO drive shaft can be modeled as torsional vibration of two mass shafts shown in *Fig. 3*. The applied torque at PTO shaft ends causes the PTO torque transducer and PTO shaft drive to vibrate and the complete transducer unit to respond to torsional oscillations. In order for the recorded torque to be not influenced by any vibration motions, its natural frequency should be larger than the frequency of exciting vibrations. The natural frequency of transducer and PTO drive shaft can be expressed as:

$$f = \frac{1}{2\pi}\sqrt{\left(k_t \frac{J_1 + J_2}{J_1 J_2}\right)} \qquad (5)$$

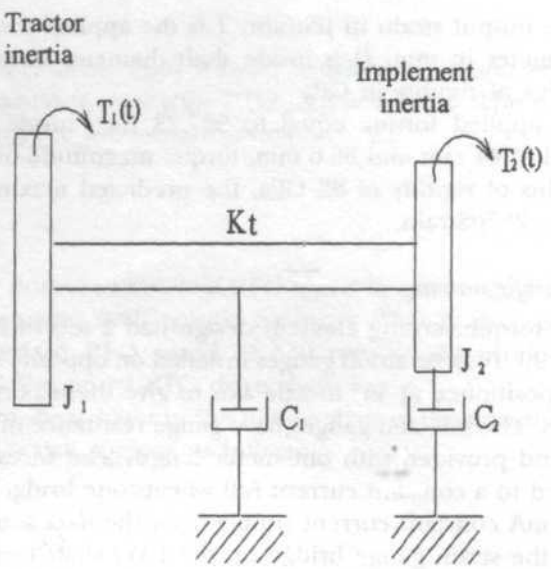

Fig. 3: Transducer PTO shaft modeled as torsional vibration of two mass shafts

$$\text{with} \quad k_t = \frac{\pi G\left(D_1^4 - D_0^4\right)}{32L}$$

where f is the natural frequency in Hz, J_1 is the equivalent engine inertia kgm^2, J_2 is the equivalent implement inertia, kgm^2, k_t is the stiffness in Nm/rad, D_o is the outer shaft diameter in mm, D_i is the inside shaft diameter in mm, L is the shaft length in m, and G is the modulus of rigidity in GPa.

The equivalent inertia for the tractor and implement are estimated to be 2 kgm^2 and 34 kgm^2 on the basis of the example mentioned by Crolla (1978). Knowing PTO drive shaft transducer diameters of 44 mm and 56.6 mm, shaft modulus of rigidity of 82 GPa and shaft drive line length of 1.54 m, the shaft stiffness is calculated to be 31868 Nm/rad. Finally, the natural frequency of the transducer and PTO drive shaft is calculated to be 21 Hz. This estimated value is conservative because the PTO drive shaft is assumed to be one uniform piece element and the presence of universal joint, overload clutch and non-linearity are being ignored.

Calibration

Static calibration tests of the PTO shaft torque transducer are carried out to determine linearity between the applied torque with measured output strain and accuracy between the applied torque with the measured torque. The calibration tests are performed by subjecting known torque loadings to the PTO shaft torque transducer and recording the respective measured output strains or the measured torque by the data acquisition system. Special calibration beam

and stand are developed to calibrate the PTO shaft torque transducer. The calibration beam is made from a hollow section of 1 meter length with a male spline in one end and a fitted chain on the other end. The male spline of the calibration beam is fitted to the PTO drive shaft of the tractor, where the chain on its other end is used to hang dead weights. The calibration stand consists of two steel angle bars welded vertically to a base plate and adjustable horizontal beam. The stand is used to support the PTO shaft while it is being calibrated. One end of the PTO shaft is installed to the tractor PTO unit and the other end with female spline was supported on the calibration stand. Ten dead weight, each having mass of 10 kg is added at increment to the maximum torque loading of 1000 Nm. DeCipher Plus program code is written for the data acquisition system to scan and record the output strain from the PTO shaft torque transducer. The transducer is calibrated under two modes of loading (i.e. loading and unloading) and two modes of loading directions (i.e. clockwise and anticlockwise). Each measurement of these treatment combinations is repeated four times with three measurements for each applied torque loading. A similar test was conducted to obtain the relationship between the measured torque by the data acquisition system and the applied torque for the purpose of checking the measurement accuracy of the transducer. The involved test was only conducted to clockwise loading direction mode and the test procedure was similar to the one before.

Statistical Analysis

A two-way factorial statistical design that consists of 2 modes of loading (i.e. loading and unloading), 2 modes of loading direction (i.e. clockwise and anticlockwise), 11 levels of applied torque and 4 replications is employed in the calibration test of the PTO shaft transducer. The linear additive model for this design is expressed as follows:

$$Y_{ijk} = \mu + \alpha_i + \beta_j + (\alpha\beta)_{ij} + \varepsilon_{ijk}. \begin{cases} i = 1,2,\ldots a \\ j = 1,2,\ldots b \\ k = 1,2,\ldots r \end{cases} \quad (6)$$

The collected calibration data is analyzed using General Linear Model procedure in PC SAS software package (SAS 1996).

Demonstration Test

Field demonstration test of PTO shaft torque transducer on the Massey Ferguson 3060 tractor is conducted at the University's farm. The prepared plot for the demonstration test is slashed once by a rotary slasher to remove any available undergrowth. The plot has a sandy clay loam soil classification texture. The tractor is equipped with data acquisition system and mounted with 36-1550 HOWARD HR39 rotary tiller for the field demonstration test. The demonstration test is conducted at different gear combinations to check on the effect tractor forward speed on the PTO torque and power with rotary tiller. The tractor is

operated at standard PTO speed of 540 rpm and rotor speed of 200 rpm. At the end of the field test, the stored data in memory card is downloaded into the hard disk of the host computer for analysis on the recorded data measurements by the PTO Torque transducer and its associated data acquisition system.

RESULTS AND DISCUSSION

The ANOVA on the calibration for PTO shaft torque transducer in Table 1 shows that the entire tested main effects and interactions with the exception of applied torque had no significant ($P>0.05$) effects on measured output strain. The insignificance of rotation implies no differences on the measured output strain between clockwise and anticlockwise wheel rotation. The insignificance of loading indicates no hysteresis effect on the measured output strain under loading and unloading modes. All these obtained findings supported the use of one calibration equation for wheel torque transducer measurement.

TABLE 1
ANOVA on the calibration for PTO shaft torque transducer

Source of variation	SS	MS	F-value
Replication	123.90	61.95	8.59NS
Rotation	171.91	171.91	23.84NS
Loading	0.83	0.83	0.12NS
Torque	246712.51	22428.41	3110.82**
Rot. × Load.	11.57	11.57	1.61NS
Rot. × Torq.	69.98	6.36	0.88NS
Load. × Torq.	64.11	5.82	0.81NS
Rot. × Load. × Torq.	63.47	5.77	0.80NS
Error	591.20	7.20	

** Significant at 1% probability level
NS Not Significant

Fig. 4 shows the plot of output strain versus applied load resulting from the measurement linearity determinations. Regression analysis show a high degree of linearity between applied torque and measured output strain with coefficient of correlation or R^2 equal to 0.9942. The linearity equation is best expressed as follows:

$$S = 0.1270T \quad \text{with} \quad R^2 = 0.9942 \tag{7}$$

where S represents the measured output strain in (Strain and T is the applied torque in Nm. Equation 7 is employed in the programming of Datataker 605 to read the measured output strain from the tractor's PTO shaft in Nm. The measured transducer sensitivity was 0.1390 μStrain/Nm. This value was 0.51 times lower than earlier computed theoretical sensitivity (i.e 0.2731μStrain/

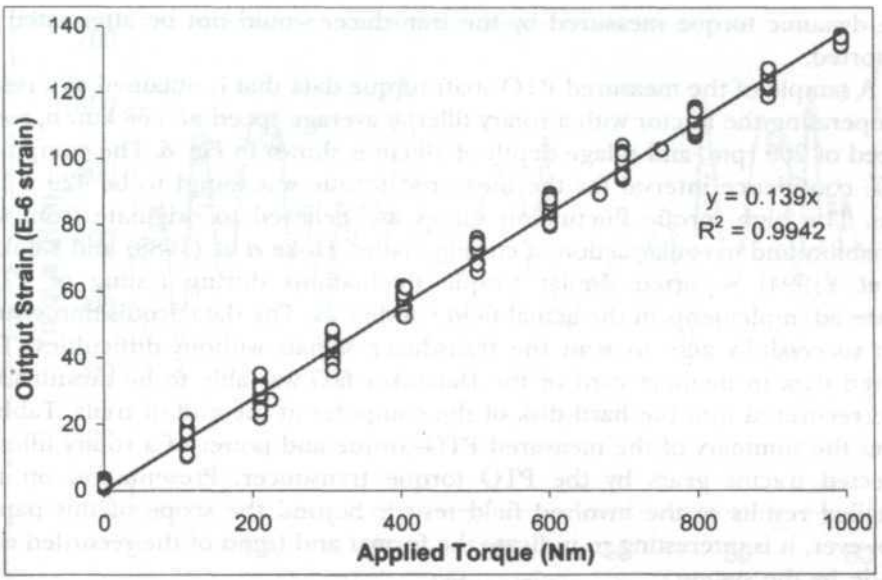

Fig. 4: Calibration curve for PTO torque transducer

Nm). Again, this difference was due to gain multiplier effect that was automatically set during autoranging by the Datataker 605.

Fig. 5 shows the plot of applied torque versus measured torque resulted from the measurement accuracy determinations. Regression analysis shows a high degree of linearity between applied torque and measured torque with coefficient of correlation or R^2 equal to 0.9945. The linearity equation is best expressed as follows:

$$T_M = 1.0665 \quad \text{with} \quad R^2 = 0.9945 \tag{8}$$

where T_M represents the measured output torque in N_m and T is the applied torque in Nm. The 6.6% measurement error is within the acceptable limit and is believed to be slight distortion effects of the cylindrical tubing on which the torsional stress is measured when it is subjected to torsional load. The obtained calibration factor is used for computing and documenting the measured output torque by the transducer.

The natural frequency of PTO shaft torque transducer based on torsional vibration of two mass shaft systems is estimated to be 21 Hz while the working frequency of a typical tractor operating in the field as indicated by Claar *et al.* (1982) and Erickson and Larsen (1983) was around 2 Hz. Fortunately, this frequency ratio of less than 0.1 (i.e. 0.0952 to be exact) resulted with a transmissibility value of less than 1.01 and torque measurement error of no more than 1% of the excitation torque (James *et al.* 1989; Timoshenko *et al.* 1990). Consequently, the conducted static calibration on the transducer was acceptable for dynamic torque measurement. Besides that, it also ensured that

the dynamic torque measured by the transducer would not be attenuated or distorted.

A sample of the measured PTO shaft torque data that is obtained as a result of operating the tractor with a rotary tiller at average speed of 5.68 km/h, rotor speed of 200 rpm, and tillage depth of 10 cm is shown in *Fig. 6.* The computed 95% confidence interval for the measured torque was found to be 429 ± 182 Nm. The high torque fluctuation values are believed to originate from soil variability and irregular action of cutting blades. Hoke *et al.* (1988) and Salokhe *et al.* (1994) reported similar torque fluctuations during testing of PTO-powered implements in the actual field conditions. The data acquisition system was successfully able to scan the transducer signals without difficulties. The stored data in memory card of the Datataker 605 was able to be downloaded and recovered into the hard disk of the computer at the end of trials. Table 2 gives the summary of the measured PTO torque and power of a rotary tiller at selected tractor gears by the PTO torque transducer. Presentation on the detailed results of the involved field tests is beyond the scope of this paper. However, it is interesting to indicate the format and trend of the recorded data made by the system.

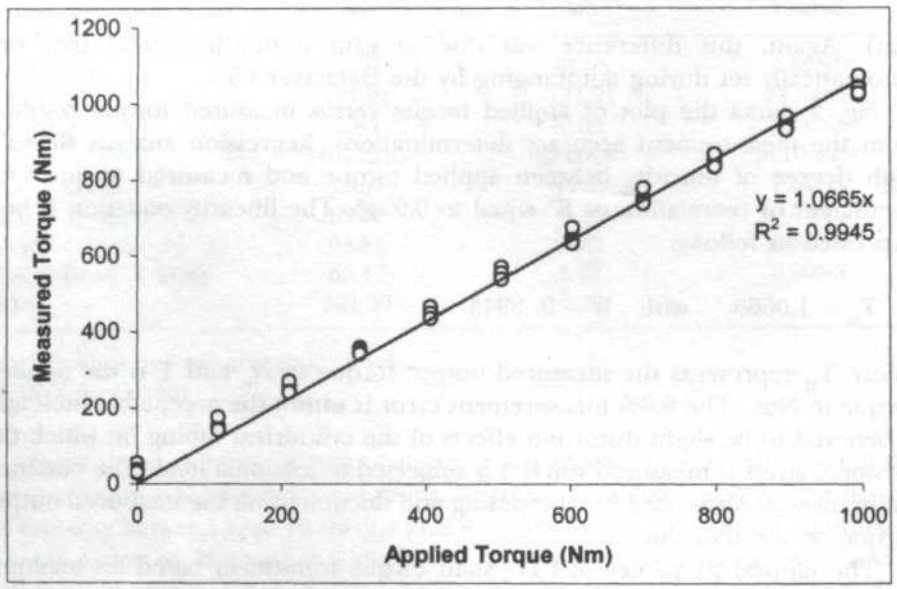

Fig. 5: Verification curve for measurement accuracy of PTO torque transducer

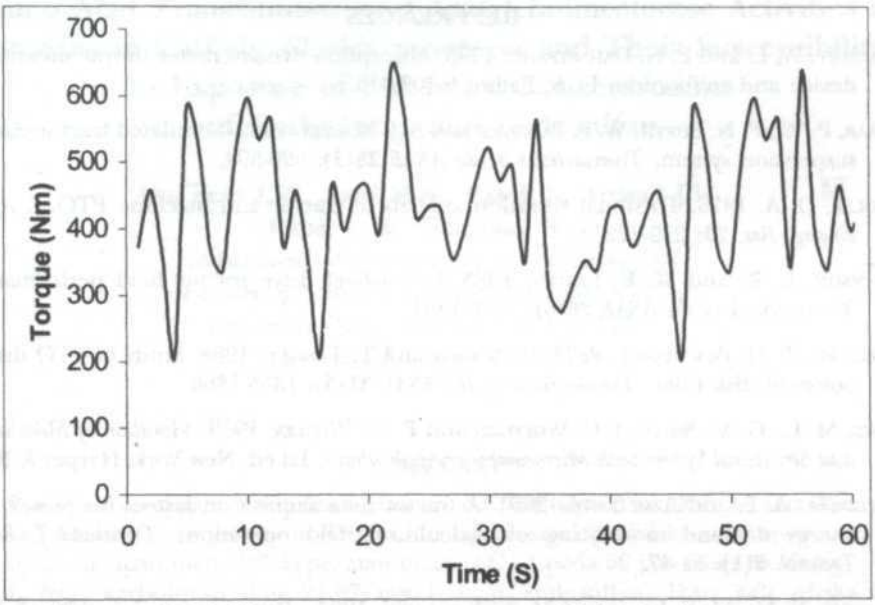

Fig. 6: Torque measurement at tractor's PTO drive shaft

CONCLUSIONS

A PTO torque transducer had been successfully designed, developed, and calibrated to measure tractor's PTO torque output up to 1000 Nm at a sensitivity of 0.1390 μStrain/Nm. The transducer design is as a result of modifications made to a standard commercial tractor's PTO drive shaft. Static calibration of the transducer revealed excellent linearity between applied torque with output strain with coefficient of correlation equal to 0.9942 and acceptable measurement accuracy between applied load with measured torque with coefficient of correlation equal to 0.9945. Natural frequency of the transducer is estimated to be 21 Hz by modeling the complete system as a torsional vibration of two mass-shafts. The static and dynamic responses of the transducer are within the acceptable measurement error limits. Field demonstration trials on the transducer and acquisition system were satisfactory. The data acquisition system was able to scan and record the signal measured by the transducer. The stored data in the memory card of the acquisition system as this demonstration was able to download into the hard disk of computer successfully.

ACKNOWLEDGEMENTS

This research project is classified under RM7IRPA Project No. 01-02-04-0138. The authors are very grateful to the Malaysian Ministry of Science, Technology, and the Environment for granting the funds.

REFERENCES

BRASSERT, W. L. and P. N. DAHLSTRAND. 1996. Absorption dynamometer torque measuring device and calibration. U. S. Patent 5,509,315.

CLAAR, P. W., P. N. SHETH, W. F. BUCHELE and S. J. MARLEY. 1982. Simulated tractor chassis suspension system. *Transactions of the ASAE* **25(3):** 590-594.

CROLLA, D. A. 1978. Torsional vibration analysis of tractor and machine PTO. *J. Agric. Engng. Res.* **23:** 259-272.

ERICKSON, L. R. and W. E. LARSEN. 1983. Four-wheel drive tractor field performance. *Transactions of the ASAE* **26(6):** 1346-1351.

HOKI, M., T. H. BURKHARDT, R. H. WILKINSON and T. TANOUE. 1988. Study of PTO driven powered disk tiller. *Transactions of the ASAE* **31(5):** 1355-1360.

JAMES, M. L., G. M. SMITH, J. C. WOLFORD and P. W. WHALEY. 1989. *Vibration of Mechanical and Structural System with Microcomputer Applications.* 1st ed. New York: Harper & Row.

KHEIRALLA, A. F. and AZMI YAHYA. 2001. A tractor data acquisition system for power and energy demand monitoring of agricultural field operations. *Pertanika J. Sci.& Technol.* **9(1):** 51-67.

SALOKHE, V. M., M. S. ISLAM and M. N. SAKALAINE. 1994. Power spectral density of draft and torque fluctuations of a PTO powered disk tiller. *J. Agric. Engng. Res.* **31(3)**: 163-171.

SAS. 1996. *SAS User's Guide: Statistics.* North Carolina: Statistical Analysis System Inc.

TIMOSHENKO, S. and J. M. GERE. 1990. *Mechanics of Materials.* 3rd ed. New York: Van Nostrand Reinhold.

TIMOSHENKO, S., D. H. YOUNG and W. WEAVER, JR. 1990. *Vibration Problems in Engineering.* 5th ed. New York: John Wiley and Sons.

WILKINSON, R. H. and K. J. ROSE. 1990. An appropriate technology torque meter. Paper presented in the *Asia-Pacific Regional Conference on Engineering for Development of Agriculture,* June 5-7th, Kuala Lumpur, Malaysia.

Pertanika J. Sci. & Technol. 12(2): 225 - 233 (2004)
ISSN: 0128-7680

Amino Acid Transaminase and Acetylcholinesterase Activities in the African Catfish, *Clarias gariepinus* and Their Susceptibility to Exposure of Sub-lethal Concentrations of Carbofuran and Endosulfan

Abu Zeid I.M., Syed M.A., Ramli J., Arshad J.H., Omar I. & *Shamaan N.A.

Department of Biochemistry and Microbiology
Faculty of Science and Environmental Studies
Universiti Putra Malaysia, 43400 UPM,
Serdang, Selangor, Malaysia

Received: 18 July 2002

ABSTRAK

Penilaian ketoksikan karbofuran dan endosulfan telah dilakukan ke atas ikan keli Afrika, *Clarias gariepinus*. Daripada analisis secara probit ke atas keputusan ujian, didapati nilai 50% kepekatan maut (LC_{50}) pada 96 jam ialah 10.42 mg/L bagi karbofuran dan 21.67 mg/L bagi endosulfan. Ikan keli Afrika kemudiannya didedahkan kepada dos submaut (50% daripada nilai LC_{50} iaitu 5.2 mg/L karbofuran dan 10.8 mg/L endosulfan) untuk tempoh 20 hari. Aktiviti enzim transaminase glutamat-oksaloasetat (GOT), transaminase glutamat-piruvat (GPT) dan asetilkolinesterase dipantau dalam hati ikan tersebut selepas didedahkan kepada racun perosak tersebut selama 3 jam (0 hari), 4, 8, 12, 16 dan 20 hari. Kedua-dua aktiviti GOT dan GPT meningkat secara signifikan ($P<0.05$) tetapi aktiviti enzim asetilkolinesterase direncat. Kedua-dua aktiviti GOT dan GPT meningkat secara perlahan ke tahap maksimum selepas 16 hari. Endosulfan meningkatkan aktiviti GOT dan GPT lebih daripada karbofuran manakala karbofuran lebih berkesan daripada endosulfan dalam merendahkan aktiviti asetilkolinesterase. Eraman secara *in vitro* karbofuran dan endosulfan dalam ekstrak hati ikan normal mengakibatkan perencatan aktiviti asetilkolinesterase tetapi meningkatkan secara signifikan kedua-dua aktiviti GOT dan GPT. Endosulfan pula mengakibatkan peningkatan aktiviti GPT lebih daripada karbofuran sementara tidak memberi kesan ke atas aktiviti GOT. Karbofuran didapati lebih merencat aktiviti asetilkolinesterase daripada endosulfan secara *in vitro*.

ABSTRACT

Toxicity evaluations of carbofuran and endosulfan were conducted on the African catfish, *Clarias gariepinus*. From probit analysis of the results obtained, the 96 h LC_{50} values were calculated to be 10.42 mg/L for carbofuran and 21.67 mg/L for endosulfan. The African catfish were then exposed to a sublethal dose (50% LC_{50} values i.e. 5.2 mg/L carbofuran and 10.8 mg/L endosulfan) of the insecticides for over 20 days. Glutamate-oxaloacetate transaminase (GOT), glutamate-pyruvate transaminase (GPT) and

* Corresponding author

acetylcholinesterase activities were monitored in the liver after 3 h exposure (0 day), 4, 8, 12, 16 and 20 days. Both GOT and GPT activities were increased significantly ($P<0.05$) but acetylcholinesterase activity was inhibited. Both GOT and GPT activities were increased gradually to a maximum over 16 days. Endosulfan elicited higher GOT and GPT activities than carbofuran. Carbofuran attenuated acetylcholinesterase activity more than endosulfan. *In vitro* incubation of carbofuran and endosulfan in normal fish liver extracts inhibited acetylcholinesterase activity but sigficantly increased both GOT and GPT activities. Endosulfan caused a higher increase in GPT activity than carbofuran but there was no difference for GOT activity. Carbofuran seemed to inhibit acetylcholinesterase activities *in vitro* more than endosulfan.

Keywords: African catfish, toxicity evaluation, carbofuran, endosulfan, transaminases, acetylcholinesterase

INTRODUCTION

Carbofuran (Furadan) and endosulfan (Thiodan) are two insecticides extensively used for pest control in rice fields in Malaysia. These pesticides were found to be highly toxic to freshwater fishes, resulting in a decline in fish production and a significant loss of subsistence income for the rice growers (Liong *et al.* 1988). A similar situation occurred in Botswana, Africa. Following extensive application of endosulfan for tsetse fly control in Botswana, about one percent of the freshwater fish in the area were killed due to the toxicity of endosulfan (Mathiessen and Roberts 1982).

Carbofuran and endosulfan have been reported to affect protein and amino acid metabolism (Murty and Devi 1982; John and Jayabalan 1993; Singh and Sharma 1998). Protein concentration in organs and tissues was significantly reduced in fish exposed to carbofuran and endosulfan. The effect is dependent on the dose and time of exposure to the insecticides. Activities of serum glutamate-oxaloacetate (GOT) and glutamate-pyruvate transaminases (GPT) were found to be significantly elevated in fish exposed to insecticides at sub-lethal concentrations (Verma *et al.* 1981; Samuel and Sastry 1989). The increase in transaminase activities after exposure to insecticides may reflect tissue damage and stress. The increase in transaminase activities coupled with the reduction of protein content in organs and tissues may provide an explanation for the reduced growth rate in the catfish, *Clarias batrachus* exposed to a sublethal dose of carbofuran (Mukhopadhyay *et al.* 1982).

Both carbofuran and endosulfan exert their effect by inhibiting cholinesterase activity in fish (Trotter 1991). Inhibition of cholinesterase activities by insecticides in fish both *in vivo* and *in vitro* have been widely reported and is one of the major causes of mortality in fish (Sur and Ghose 1978; Gill *et al.* 1990).

We report the toxicity evaluations of carbofuran and endosulfan in the African catfish *Clarias gariepinus*, a fish that was introduced in Malaysian rice fields and also on the effect of these insecticides at sub-lethal concentrations on amino acid transaminase and acetylcholinesterase activities *in vivo* and *in vitro*.

MATERIALS AND METHODS

Technical grade carbofuran (99.1% purity) and endosulfan (99.3% purity) were obtained from Ehrenstorfer GmbH, Germany. The African catfish, *Clarias gariepinus* was obtained from the university hatchery. The fish used in this study were 14-16 cm long, 28-32g body weight, maintained in aquaria containing dechlorinated water and aerated. The fish were fed fish pellet and the water maintained at 27-29°C, pH 7.5-7.9, dissolved oxygen at 5.6-7.8 mg/L and 0.4-1.4 mg/L ammonia.

Toxicity Evaluations

Carbofuran and endosulfan were used at concentration range of 8.5 - 12.5 mg/L and 16.0 - 30.0 mg/L respectively, in toxicity evaluations. The fishes were acclimatised for 14 days in a glass aquarium containing 25 L of aerated dechlorinated water at 27-29°C before being put into test aquaria. The fish were fasted for 24 h before exposure to the insecticides. Carbofuran or endosulfan were applied to the aquaria containing 10 fishes each and monitoring of mortality started 3 h later. Subsequent monitoring was carried out at 24 h intervals for 3 days. After every 24 h, the water was replaced with fresh water and insecticide to ensure the insecticide concentration is kept constant. The fish were fed daily with fish pellet. Mortality was considered as either moribund, loss of equilibrium, lack of response to prodding, frequent surfacing for air, erratic swimming, or death. The results obtained were converted into probit values and the LC_{50} values for each insecticide determined.

After determining the 96 h LC_{50} values for both carbofuran and endosulfan, the African catfish were then exposed to a sublethal dose of the insecticides at 50% of LC_{50} values calculated; 5.2 μg/L and 10.8 μg/L for carbofuran and endosulfan, respectively over a 3 week period. The fish were kept in a glass aquarium containing 25L dechlorinated water and maintained under conditions stated previously. The fish were sacrificed at 0 (3 h), 4, 8, 12, 16 and 20 days and the liver excised immediately. Controls were maintained in dechlorinated water without insecticides.

Assays for Enzyme Activities

Fish liver was homogenised in cold 0.25M sucrose (1 g liver to 3 mL sucrose solution) and centrifuged at 10,000g for 20 min. The homogenate obtained after centrifugation was filtered in muslin cloth and the resulting filtrate used in assays of glutamate-oxaloacetate transaminase (GOT), glutamate-pyruvate transaminase (GPT) and acetylcholinesterase activities. GOT and GPT activities were assayed following the method of Reitman and Frankel (1957) while acetylcholinesterase was assayed according to the method of Ellman *et al.* (1961). Enzyme activities were expressed as mmol per min per mg protein. Protein concentration was determined by the Biuret method.

Effect of Carbofuran and Endosulfan on Enzyme Activities In Vitro

The liver of control fish was excised and the homogenate prepared as described above. Sublethal doses of carbofuran and endosulfan (5.2 mg/L and 10.8 mg/L, respectively) were added to the homogenate and incubated at 27-29°C over time. Aliquots of the homogenate treated with the insecticides were taken and assayed for enzyme activity.

RESULTS

Toxicity Evaluations

Toxicity evaluations were carried out for carbofuran and endosulfan. The percentage mortality observed was converted to probits. The plot of probits against log concentration of carbofuran yielded a straight line with a gradient of $y = 16.109x - 11.399$ ($R^2 = 0.9786$) and for endosulfan, $y = 7.788x - 5.4026$ (R2 = 0.9249). The 96 h LC_{50} values calculated for carbofuran was 10.42 mg/L and endosulfan 21.67 mg/L, respectively. No mortality was recorded at carbofuran and endosulfan concentrations of less than 8.5 mg/L and 16 mg/L, respectively. However, 90% mortality was reached at a concentration of 12.51 mg/L carbofuran and 31.62 mg/L endosulfan after 96 h. The LC_{50}:LC_{90} ratio for carbofuran was 1:1.20 and endosulfan 1:1.46.

Effect of Sublethal Dose of Carbofuran and Endosulfan on Enzyme Activities

After the LC_{50} values were determined, the effect of sublethal doses of carbofuran and endosulfan on transaminase and acetylcholinesterase activities in the liver of the fish was investigated. The fishes were maintained at 50% of the LC_{50} values calculated previously (5.2 mg/L carbofuran and 10.8 mg/L endosulfan) and the liver enzyme activities monitored over 20 days (Table 1). Liver GOT and GPT activities were increased significantly ($P<0.05$) after exposure to carbofuran and endosulfan, compared against controls. The enzyme activities peaked after 16 days. Endosulfan registered a higher percentage change than carbofuran for both GOT and GPT activities. Endosulfan also effected an immediate increase in enzyme activities compared to after 4 days for carbofuran.

Acetylcholinesterase activities were significantly lowered in fish exposed to carbofuran and endosulfan. Attenuation of liver acetylcholinesterase activity was immediate for carbofuran but after 8 days for endosulfan. Generally, carbofuran showed greater attenuation of acetylcholinesterase activity than endosulfan. Also, attenuation of acetylcholinesterase activities by carbofuran and endosulfan seemed to be time-dependent.

In Vitro Effect of Carbofuran and Endosulfan on Enzyme Activities

Both GOT and GPT activities were significantly increased after 20 min. and 10 min incubation respectively, by carbofuran and endosulfan compared with normal controls (*Fig. 1*). Endosulfan was observed to elicit higher GPT increase than carbofuran after 10 min. incubation.

TABLE 1

Effect of sublethal doses of carbofuran and endosulfan on enzyme activities in the liver of the African catfish. Values shown are mean ± standard deviation, n= 9. * $P < 0.05$ compared against control. One unit of enzyme activity is expressed as mmol/min/mg protein. Values shown in brackets are percentage change in enzyme activities compared with controls

Treatment/Days	0	4	8	12	16	20
GOT (x 10^{-3} U/mg)						
Control	17.6 ± 1.5	17.7 ± 0.13	17.9 ± 1.3	17.8 ± 1.1	17.5 ± 0.9	17.9 ± 0.7
+ Carbofuran	18.2 ± 1.2 (+3)	21.0 ± 0.15* (+19)	29.7 ± 1.7* (+66)	41.6 ± 1.1* (+134)	53.1 ± 1.4* (+203)	52.6 ± 1.4* (+194)
+ Endosulfan	22.8 ± 0.7* (+30)	27.0 ± 0.11* (+53)	31.3 ± 0.9* (+75)	43.0 ± 1.6* (+142)	46.8 ± 1.5* (+167)	46.3 ± 2.0* (+159)
GPT (x 10^{-3} U/mg)						
Control	8.2 ± 0.4	8.6 ± 0.7	8.4 ± 0.5	8.8 ± 0.9	9.0 ± 0.6	9.0 ± 0.7
+ Carbofuran	8.8 ± 0.4 (+7)	9.4 ± 1.2* (+9)	10.9 ± 2.0* (+30)	14.9 ± 1.7* (+60)	19.9 ± 0.9* (+121)	19.7 ± 1.7* (+119)
+ Endosulfan	10.1 ± 0.8* (+23)	11.4 ± 0.2* (+33)	15.3 ± 1.6* (+82)	20.5 ± 1.4* (+133)	26.5 ± 1.9* (+194)	26.0 ± 2.0* (+189)
Acetylcholinesterase (U/mg)						
Control	0.23 ± 0.01	0.22 ± 0.02	0.22 ± 0.01	0.23 ± 0.01	0.23 ± 0.01	0.24 ± 0.02
+ Carbofuran	0.20 ± 0.01* (-13)	0.17 ± 0.01* (-24)	0.15 ± 0.01* (-32)	0.14 ± 0.01* (-39)	0.10 ± 0.01* (-57)	0.06 ± 0.01* (-75)
+ Endosulfan	0.22 ± 0.02 (-4)	0.21 ± 0.01 (-5)	0.18 ± 0.01* (-19)	0.13 ± 0.03* (-44)	0.12 ± 0.01* (-48)	0.11 ± 0.01* (-54)

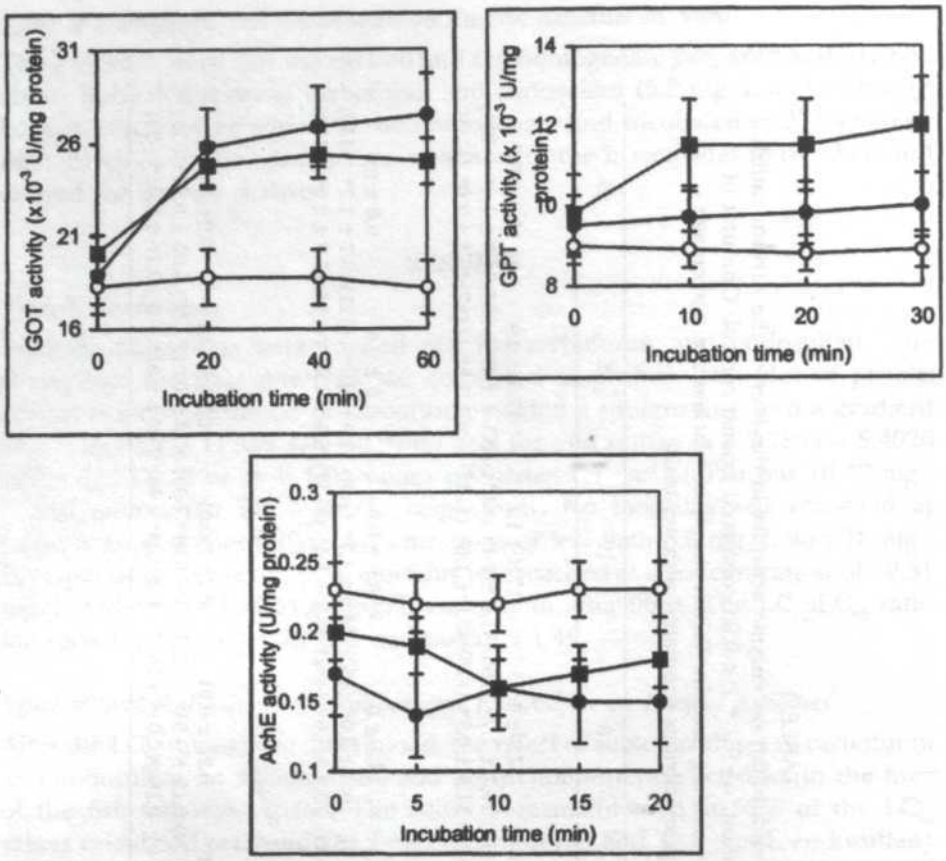

Fig. 1: Effect of carbofuran and endosulfan on GOT, GPT and Acetylcholinesterase activities of fish liver extracts in vitro. Values shown are mean ± standard deviation, n = 9. Controls (o); carbofuran treated (●); endosulfan treated (■). Insecticide treatment carried out at 50% of 96 h LC_{50} value

Liver acetylcholinesterase activity was inhibited immediately by both carbofuran and endosulfan, with carbofuran generally showing greater inhibition of acetylcholinesterase activity than endosulfan.

DISCUSSION

No mortality was recorded for *Clarias gariepinus* at carbofuran and endosulfan concentrations below 5.0 mg/L and 16.0 mg/L, respectively. However, 90% mortality was achieved at 12.51 mg/L carbofuran and 31.62 μg/L endosulfan. The LC_{50} values of carbofuran and endosulfan for the African catfish were calculated from probit analysis to be 10.42 mg/L and 21.67 μg/L, respectively. Endosulfan seemed to be more toxic than carbofuran by about 480-fold. Nevertheless, both insecticides are highly toxic to the African catfish, with the LC_{50}:LC_{90} values of 1:1.20 and 1:1.46 for carbofuran and endosulfan, respectively.

The narrow LC_{50} : LC_{90} values indicated that both these insecticides are highly toxic. The use of these pesticides in areas where there are freshwater fishes should be minimized or avoided (Mathiessen and Roberts 1982).

Carbofuran, a systemic insecticide, belongs to the carbamate group and endosulfan, a cyclodiene organochlorine insecticide, are contact poisons and act primarily by inhibiting cholinesterase activity (Gupta *et al.* 1971; Gupta 1994). Freshwater fish acetylcholinesterase activity was found to be inhibited by both carbofuran and endosulfan at a sub-lethal concentration in the present study. In addition to the anti-acetylcholinesterase activity, both carbofuran and endosulfan also affected amino acid transaminase activities *in vivo* and *in vitro.*

Protein metabolism in freshwater fish has been reported to be affected by insecticides (Murty and Devi 1982; John and Jayabalan 1993; Singh and Sharma 1998). Fish exposed to sublethal dose of the insecticides had reduced protein content in various organs and tissues. Protein expression was also affected by the insecticides. In the gills of *Cyprinus carpio,* the protein profile was altered by insecticide exposure; a number of proteins were depressed while several others were over-expressed (John and Jayabalan 1993).

Both GOT and GPT are markers of amino acid and protein metabolism, particularly in relation to tissue and organ damage. The activities of these enzymes were found to be elevated in fish exposed to the insecticides, indicating damage to tissues and organs of the fish exposed to the insecticides. The increase in enzyme activities in fish exposed to the insecticides was time-dependent. This shows that both carbofuran and endosulfan damage the liver by altering protein expression and increasing marker enzyme activities. Amino acid metabolism was increased in fish exposed to the insecticides leading to reduced protein content in organs and tissues.

The elevated marker enzyme activities is also an indication of stress. Fish exposed to residual and sublethal levels of carbofuran and endosulfan was reported to register reduced growth and protein content in tissues and organs besides a reduction in glycogen (Sastry and Siddiqui 1982; Rajeswari *et al.* 1989). Coupled with the increase in amino acid transaminase activities, it is possible that incorporation of amino acids into proteins was reduced. As a result, the growth rate of the fish will be diminished, leading to a lower production.

Elevated GOT and GPT activities also indicate liver and tissue damage. This had been substantiated by reports that other markers for liver damage such as glutathione S-transferase and cytochrome P_{450} monooxygenases were also increased in fish exposed to endosulfan and polyaromatic hydrocarbons (Rodriguez-Ariza *et al.* 1993; Arnold *et al.* 1995). Thus, although the fish survived after exposure to sublethal doses of carbofuran and endosulfan, damage to organs and tissues had occurred.

Acetylcholinesterase inhibition caused by sublethal doses of insecticides in the present study was observed to be time dependent. By extrapolation, the fish might not survive over a longer period since total inhibition of acetylcholinesterase activity will be achieved. The African catfish would probably

have a low chance of survival even under the sublethal concentrations of carbofuran and endosulfan.

In conclusion, endosulfan is about 480-fold more toxic than carbofuran to the African catfish, *Clarias gariepinus*. The effect of carbofuran on amino acid transaminases and acetylcholinesterase in the fish is similar to endosulfan. Since the African catfish is sensitive to both carbofuran and endosulfan, where possible, applications of these insecticides should be avoided to ensure the survival of the fish.

ACKNOWLEDGEMENTS

This study was funded by IRPA Grant 01-02-04-078.

REFERENCES

ARNOLD, H., H. J. PLULA and T. BRAUNBECK. 1995. Simultaneous exposure of fish to endosulfan and disulfoton *in vivo*: Ultrastructural, stereological and biochemical reaction in hepatocytes of male rainbow trout (*Oncorhynchus mykiss*). *Aquat. Toxicol.* **33**: 17-43.

ELLMAN, J. L., K. D. COURTNEY, I. R. ANDRES and R. M. FEATHERSTONE. 1961. A new and rapid colorimetric determination of acetylcholinesterase activity. *Biochem. Pharmacol.* **7**: 88-95.

GILL, T. S., J. PANDE and H. TEWARI. 1990. Enzyme modulation by sub-lethal concentrations of aldicarb, phosphamidon and endosulfan in fish tissues. *Pestic. Biochem. Physiol.* **38**: 231-244.

GUPTA, P. K. and R. C. GUPTA. 1971. Pharmacology, toxicology and degradation of endosulfan. A review. *Toxicol.* **13**: 115-130.

GUPTA, R. C. 1994. Carbofuran toxicity. *J. Toxicol. Environ. Health.* **43**: 383-418.

JOHN, J. R. and N. JAYABALAN. 1993. Sub-lethal effects of endosulfan on the histology and protein pattern of *Cyprinus carpio* gill. *J. Appl. Ichthyol.* **9**: 49-56.

LIONG, P. C., W. P. HAMZAH and V. MURUGAN. 1988. Toxicity of some pesticides towards freshwater fishes. *Malaysian Agri. J.* **54**: 147-156.

MATHIESSEN, P. and R. J. ROBERTS. 1982. Histopathological changes in liver and brain of fish exposed to endosulfan insecticide during tsetse fly control operations in Botswana. *J. Fish. Dis.* **5**: 153-159.

MUKHOPADHYAY, P. K., A. P. MUKHERJI and P. DEHADRAI. 1982. Certain biochemical responses in the air breathing catfish, *Clarias batrachus* exposed to carbofuran. *Toxicology* **33**: 337-345.

MURTY, A. S. and P. A. DEVI. 1982. The effect of endosulfan and its isomers on tissue protein, glycogen, and lipids in the fish *Channa punctatus*. *Pestic. Biochem. Physiol.* **17**: 280-286.

RAJESWARI, K., S. J. REDDY, G. M. RAFI, S. N. REDDY and D. C. REDDY. 1989. Impact of thiodan (Sic) on the metabolic pathway of the fish *Tilapia mossambica*. *Environ. Ecol.* **7**: 863-866.

REITMAN, S. and S. FRANKEL. 1957. Colorimetric method for the determination of serum transaminase activity. *American. J. Clin. Pathol.* **28**: 56-63.

RODRIGUEZ-ARIZA A., J. PEINADO, C. PUEYO and J. LOPEZ-BAREA. 1993. Biochemical indicators of oxidative stress in fish from polluted littoral areas. *Canadian J. Fish. Aquat. Sci.* **50**: 2568-2573.

SAMUEL, M. K. and V. SASTRY. 1989. *In vivo* effect of monocrotophos on the carbohydrate metabolism of the freshwater snake head *Channa punctatus. Pestic. Biochem. Physiol.* **34**: 1-8.

SASTRY, K. V. and A. A. SIDDIQUI. 1982. Metabolic changes in the snake head fish, *Channa punctatus* chronically exposed to endosulfan. *Water Air Soil. Pollut.* **19**: 133-141.

SINGH, R. K. and B. SHARMA. 1998. Carbofuran-induced biochemical changes in *Clarias batrachus. Pestic. Sci.* **53**: 285-290 .

SUR, R. K. and K. C. GHOSE. 1978. Studies on *in vitro* inhibition of fish brain cholinesterase by some insecticides. *Indian. J. Physiol. Allied. Sci.* **32**: 72-83.

TROTTER D.M. 1991. Aquatic fate effect of carbofuran. *Critical Rev. Environ. Control.* **21**: 137-176.

VERMA, S. R., S. RANI and R. C. DALELA. 1981. Isolated and combined effects of pesticides on serum transaminases in *Mystus vittatus* (African catfish). *Toxicol. Letts.* **8**: 67-71.

ISSN: 0128-7680
Pertanika J. Sci. & Technol. **12(2)**: 235 - 248 (2004)

Tolerance and Accumulation of Cadmium, Copper, Lead and Zinc by Two Different Size Groups of the Green-Lipped Mussel *Perna viridis* (Linnaeus)

Yap, C. K., A. Ismail & S. G. Tan
Department of Biology, Faculty of Science and Environmental Studies, Universiti Putra Malaysia, 43400 UPM, Serdang, Selangor, Malaysia
E-mail: yapckong@hotmail.com

Received: 22 August 2002

ABSTRAK

Dua kumpulan saiz yang berlainan bagi kupang *Perna viridis* dengan panjang cangkerang 3-4 sm (kecil) dan 6-8 sm (besar), telah digunakan untuk menentukan ketahanan dan penimbunan terhadap pelbagai tahap pendedahan kuprum (Cu), kadmium (Cd), plumbum (Pb) dan zink (Zn). Kepekatan 'lethal' logam-logam yang membunuh 50% (LC_{50}) kupang selepas 24-jam pendedahan, dikira untuk kumpulan besar dan kecil adalah: 2.82 dan 1.53 mg/L untuk Cd, 0.61 dan 0.25 mg/L untuk Cu, 5.91 dan 4.22 mg/L untuk Pb dan 5.22 dan 3.48 mg/L untuk Zn, masing-masing. Keputusan-keputusan tersebut menunjukkan kupang adalah paling sensitif terhadap Cu, diikuti Cd, Zn dan Pb walaupun kumpulan saiz kecil adalah lebih sensitif daripada kumpulan saiz besar kerana kumpulan kecil mempunyai nilai LC_{50} yang lebih rendah daripada kumpulan besar. Nilai-nilai LC_{50} bagi Cd, Pb dan Zn yang diperoleh menggunakan 24-jam ujian toksiksiti adalah lebih kurang sama dengan data lain yang dilaporkan sebelum ini yang berdasarkan ujian 'conventional' 48 atau 96-jam. Maka, ini membolehkan kita untuk mencadangkan kegunaan kaedah ini yang lebih efisien bagi kajian yang lebih besar skelnya.

ABSTRACT

Two different size groups of the green-lipped mussel *Perna viridis* (L.) with shell lengths of 3-4 cm (small) and 6-8 cm (large), were used to determine the mussels' tolerance and accumulation at different levels of copper (Cu), cadmium (Cd), lead (Pb) and zinc (Zn) exposures. The lethal concentrations of the metals to kill 50% (LC_{50}) of the mussels after 24-hour exposure, calculated for the small and large size groups were: 1.53 and 2.82 mg/L for Cd, 0.25 and 0.61 mg/L for Cu, 4.22 and 5.91 mg/L for Pb and 3.48 and 5.22 mg/L for Zn, respectively. The results indicated the mussel was most sensitive to Cu, followed by Cd, Zn and Pb although the small size group was more sensitive than the large one since the small group had lower LC_{50} values than the large one. The LC_{50} values for Cd, Pb and Zn which we obtained using the 24-hour toxicity tests were relatively comparable to those reported by others based on the conventional 48 or 96-hour tests, thus enabling us to recommend the use of this more efficient method for large scale studies.

Keywords: Tolerance, accumulation, heavy metals, *Perna viridis*

INTRODUCTION

The intertidal zone is continuously influenced by tidal changes and inputs from riverine systems which are closely associated to inputs from anthropogenic sources. If there was a short period of contamination by heavy metals from these sources, questions such as 'What are the responses and ranges of tolerance for the intertidal inhabitant such as the green-lipped mussel *Perna viridis* (L.)?', arose. Cases of water due to pig farm effluents, industrial and domestic wastes had been reported in local newspapers (*New Straits Times* 1999) which could have caused the death of cultured fish and mussels. From the aquaculture point of view, the ranges of heavy metals which could be tolerated by mussels are important because levels which exceed the threshold may also have serious implications for the other intertidal communities.

In this work, we focused on heavy metals, which are potentially detrimental to most marine bivalves at levels of exposures which are above the minimum thresholds. Their presence in the marine environment has generally increased due to anthropogenic inputs. Therefore, there have been constant efforts to measure the impacts of heavy metals on the marine fauna (Ahsanullah 1976; Bayne *et al.* 1985; Bhat and Vamsee 1993). Toxicity tests such as the acute lethality test is useful for assessing the effects of these elevated and hazardous metal levels on marine life (Abel and Papoutsoglou 1986; Abel 1991). Toxicity tests are also essential in the investigation of pollution incidents, and in some cases, data from lethal toxicity tests can also be used to construct predictive models which are useful in the management and improvement of heavily polluted waters (Abel 1991).

The mussel *P. viridis* filters out food from the water column and has a pumping and filtering mechanism capable of bioaccumulating a wide range of contaminants including heavy metals besides fulfilling most of the recommended criteria for a biomonitor (Phillips 1985; Ismail *et al.* 2000; Yap 2002a, 2002b). Since decades ago, much research had focused on heavy metal levels in marine mussels in response to the international 'Mussel Watch' monitoring programme (Goldberg 1975; Livingstone and Goldfarb 1998; Tanabe 2000). This species is chosen because it is an ecologically and economically important bivalve species in Malaysia (Yap *et al.* 2003a; 2003c) besides the blood cockle *Anadara granosa*. Owing to its wide distribution along the west coast of Peninsular Malaysia, *P. viridis* has been suggested as a potential local biomonitoring agent for heavy metals (Ismail *et al.* 2000).

The objective of this paper is to determine the toxicities of Cd, Cu, Zn and Pb by understanding the tolerance and accumulation of these metals by small (3-4 cm) and large (6-8 cm) size groups of *P. viridis*.

MATERIALS AND METHODS

Mussel samples were collected from an unpolluted mussel aquacultured site at Sebatu, Malacca on 12 August 2000. The mussels were separated from the clumps by carefully cutting the byssus, and then all the barnacles attached to the shell surface were removed. This was done carefully in order to reduce the

mechanical disturbance to the mussel byssus. During the acclimatization period at the Institute of Bioscience's hatchery in Serdang, the mussels were first put into a big tank and they were aerated and acclimatized to laboratory conditions in filtered seawater for 3 days before being put into the experimental aquariums. During this acclimatization period, some mussels, which were seriously mechanically disturbed (injured) during separation from the barnacles, died and were removed. The healthy mussels were fed with monocultured unicellular algae, *Isochrysis galbana*. The seawater was changed daily.

Only mussels of shell lengths 3-4 cm (loading capacity: 0.5-0.8 g/L) and 6-8 cm (loading capacity: 0.8-1.2 g/L) were chosen for experimental study. According to Rand and Petrocelli (1985), the loading capacity for the test organism should not exceeded 0.8 g/L. For the large mussel size group, although the loading capacity was exceeded, stress was not observed within 24 hours in the mussels without metal addition. In addition, the researchers had determined the amount of test seawater suitable for the experiments which would not stress the mussels. Also, we had tried to determine the number of mussels that could be placed in one aquarium. Although the metal concentration was too high when compared to those in the field seawater, it was the objective of this study to determine the tolerance and accumulation of *P. viridis* to the 'very' high levels of metal exposure conducted under laboratory conditions.

The 3-4 cm and 6-8 cm mussels were considered the small and large size groups, respectively, in this preliminary study. The toxicity tests were carried out as described by D'Silva and Kureishy (1978) and Chan (1988). The mussels were not fed for two days before the experiment until the completion of the experiment. About 10-13 healthy test mussels from each size group (3-4 cm and 6-8 cm) were selected. These two significantly different size groups were put together into each experimental aquarium. They were allowed to acclimatize in the aquaria for 2 days to let their byssus attach well to the aquarium walls before the start of the toxicity tests.

Standard solutions of heavy metals (analytical reagent grade Fisher Chemical) (Cd as cadmium nitrate; Cu as copper nitrate; Pb as lead nitrate; Zn as zinc nitrate) were mixed into the aquarium to provide a range of nominal concentrations (mg/L) of metals (0.50, 1.0, 1.5, 3.0 for Cd; 0.05, 0.10, 0.20, 0.30 for Cu; 0.5, 1.5, 3.0, 5.0 for Pb and 0.05, 1.0, 2.5, 5.0 for Zn) in 16 different experimental aquariums after a series of trial and error toxicity tests had been conducted. Also, the basis of selection of metal concentrations for the toxicity tests was the LC_{50} values using 46 or 96-hour tests reported in the literature for *P. viridis*; D'Silva and Kureishy (1978) and Krishnakumar *et al.* (1987a) for Cu, D'Silva and Kureishy (1978), Krishnakumar *et al.* (1987a) and Chan (1988) for Zn, Tan and Lim for Pb and Chan (1988) for Cd. The background levels of dissolved metals in the seawater in these 16 aquariums and one control were measured. The metal concentrations in these aquariums were measured again after additions of the metals.

The test solutions (10 L) were kept static but were constantly aerated and maintained at room temperature (25-28°C), salinity at 25-26ppt, dissolved

oxygen at 6.9-7.8 mg/L (80-90%) during the experimental period. After 24 hours, the mussels which had their shells widely gaped and showed no response to tactile stimulus were considered dead. In practice, when the valves closed partially, after they were pressed, the mussel was transferred to the aquarium filled with filtered and clean seawater to establish whether it was capable of recovery. Mussels that failed to recover were considered dead (Ahsanullah 1976). The life mussels were analysed for their metal concentrations after the 24-hour metal exposure.

All the samples (0.5-0.8 g wet weight for small mussels and 0.8-1.2 g wet weight for large mussels) were digested in concentrated nitric acid (AnalaR grade 69%). They were placed in a hot-block digester first at low temperature (40°C) for 1 hour and then they were fully digested at high temperature (140°C) for at least 3 hours (Yap *et al.* 2003c). The digested samples were then diluted to 40 mL with double distilled water. After filtration, the prepared samples were determined for Cd, Cu, Pb and Zn by using an air-acetylene flame atomic absorption spectrophotometer (AAS) Perkin-Elmer Model 4100. The detection limits of the AAS used were:- Cu: 0.010 mg/g; Cd: 0.007 mg/g; Pb: 0.080 mg/g and Zn: 0.005 mg/g. The data were presented in mg/g wet weight basis. To avoid possible contamination, all glassware and equipment used were acid-washed. For the quality control activity, procedural blanks and quality control samples made from standard solutions of each metal (analytical reagent grade Fisher Chemical), namely Cd as cadmium nitrate; Cu as copper nitrate; Pb as lead nitrate and Zn as zinc nitrate were run through in every 5 samples to check for possible external contamination and metal recoveries. The percentages of metal recoveries were 110% for Cd, 96% for Cu, 92.5% for Pb and 92% for Zn.

The result of the toxicity test for each metal was expressed as the LC_{50} value namely the concentration of a metal killing 50% of the test mussels during the period of exposure (Stephen 1977). A statistical estimation method (Finney 1971) was then used to obtain the best estimate of the LC_{50} values from the concentration-mortality data of metal exposure for each size group and for each metal.

RESULTS

The LC_{50} values of 24-hour exposure for Cd, Cu, Pb and Zn for each size group are shown in Table 1. The LC_{50}/24-hour values in size group 6-8 cm were Cd: 2.82, Cu: 0.61, Pb: 5.91 and Zn: 5.22 mg/L while the values in the size group 3-4 cm were Cd: 1.53, Cu: 0.25, Pb: 4.22 and Zn: 3.44 mg/L. Comparing all the metals studied, Cu recorded the lowest LC_{50} values, followed by Cd, Zn and Pb regardless of the different size groups being analysed.

The percentages of mortality with different metal concentrations are shown in *Figs. 1 (a, b, c* and *d)*. The levels of Cd, Cu, Pb and Zn all showed similar patterns that is, the small size group had higher percentages of mortality than the large size group. *Figs. 1 (e, f, g* and *h)* shows that the smaller mussels accumulated higher metal levels than the larger individuals in their soft tissues.

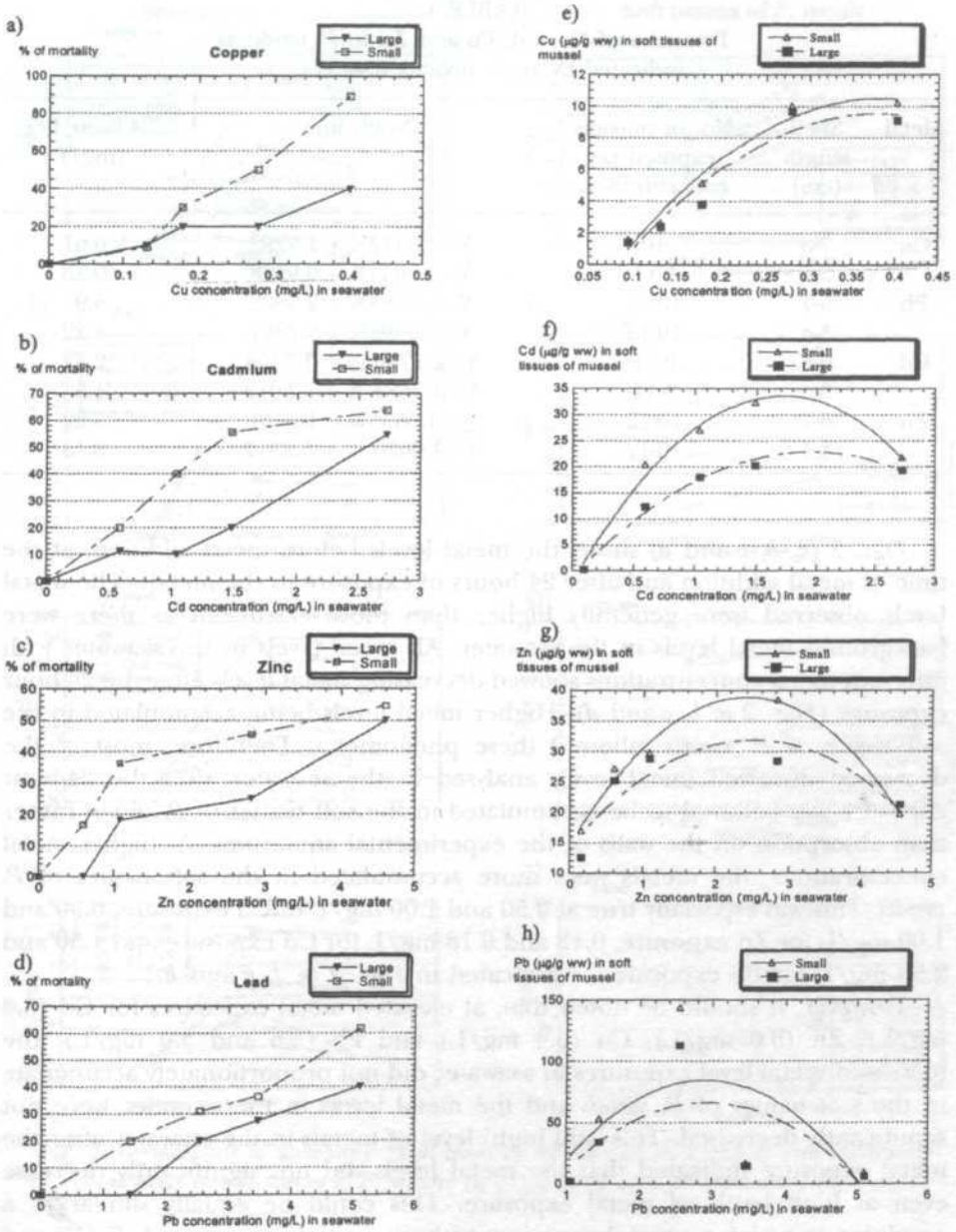

Fig. 1: Comparisons of mortalities (a, b, c and d) and concentrations of Cu (e), Cd(f), Zn(g) and Pb(h) between two different size groups of the green-lipped mussel P. viridis

TABLE 1
Toxicities of Cu, Cd, Pb and Zn to *P. viridis* as indicated by acute toxicity tests (LC_{50})

Metal	Shell length (cm)	No. of mussels exposed per concentration	Probit line	24-hour LC_{50} (mg/L)
Cu	7-8	10	Y= 1.8477X + 1.9292	0.61
	3-4	9-11	Y= 4.6644X – 0.9528	0.25
Pb	5-7	10-11	Y= 2.7353X + 2.9802	5.91
	3-4	10-13	Y= 2.0393X + 3.7251	4.22
Cd	6-8	9-11	Y= 2.1796 X + 1.3408	2.82
	3-4	9-11	Y= 1.7683 X + 2.5019	1.53
Zn	6-7	10-12	Y= 1.6533X + 1.7964	5.22
	3-4	10-12	Y= 1.0020 X + 3.2347	3.48

Figs. 2 (a, b, c and *d)* shows the metal levels before metal addition, at the time of metal addition and after 24 hours of exposure to the metals. The metal levels observed were generally higher than those calculated as there were background metal levels in the seawater. All metal levels in the seawater with different metal concentrations showed decreasing metal levels after the 24-hour exposure (*Figs. 2 a, b, c* and *d*). Higher metal levels being accumulated in the soft tissue of *P. viridis* followed these phenomena. Therefore, most of the decreased dissolved metal levels analysed in the seawater after the 24-hour exposure was believed to be accumulated in the soft tissues of *P. viridis* rather than absorption on the walls of the experimental aquariums. At higher metal concentrations, the metals were more accumulated in the soft tissues of *P. viridis.* This was especially true at 0.50 and 1.00 mg/L of Cd exposure, 0.50 and 1.00 mg/L for Zn exposure, 0.13 and 0.18 mg/L for Cu exposure and 1.50 and 2.50 mg/L for Pb exposure, as indicated in *Figs. 2 (e, f, g* and *h).*

However, it should be noted that, at elevated metal exposures for Cd (3.0 mg/L), Zn (5.0 mg/L), Cu (0.4 mg/L) and Pb (3.5 and 5.0 mg/L), the increased metal level exposures in seawater did not proportionately accumulate in the soft tissues of *P. viridis* and the metal levels in the seawater were not significantly decreased. This 'still high' level of metals in the seawater after the metal exposure indicated that the metal levels did not significantly decrease even at high levels of metal exposure. This could be equally similar to a condition in which a control aquarium without mussels was created. *Figs. 1* and *2 (e, f, g* and *h)* shows that the metal levels in the soft tissues of *P. viridis* only increased proportionately until a threshold level was reached. In the present results, after the 24-hour exposure, at 5.0 mg/L Zn exposure, the total Zn concentration in the soft tissues of *P. viridis* was lower than those under 0.5, 1.0 and 2.5 mg/L of Zn exposures (*Figs. 1f* and *2f*). Similarly for Pb, at 5.0 mg/L Pb (*Figs. 1h* and *2h*), there was only a slight difference from the Pb levels of the control samples.

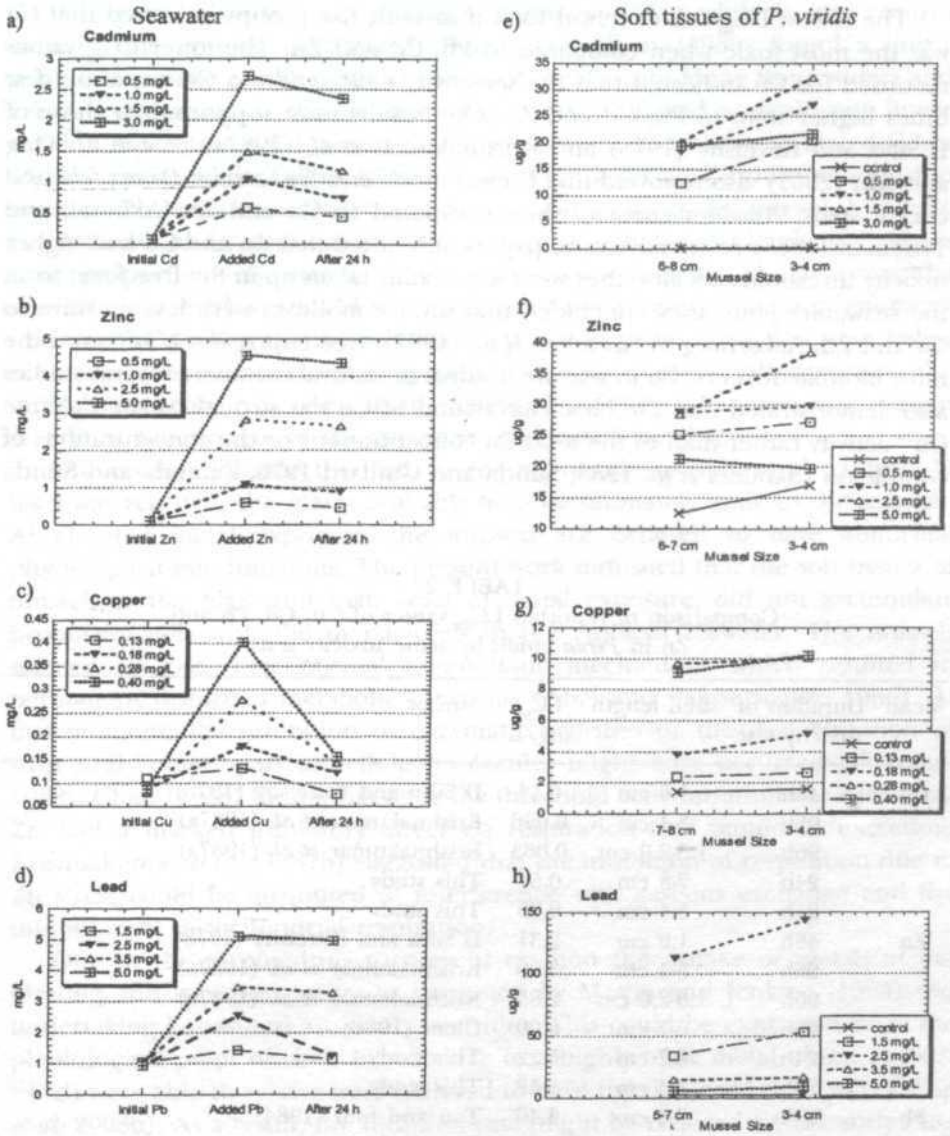

Fig. 2: Comparisons of decreasing metal levels in seawater (a, b, c and d) and increasing metal levels in soft tissues of P. viridis *(e, f, g and h) after 24-hour metal exposure*

DISCUSSION

When compared with other LC_{50} values reported by other authors (Table 2) who used *P. viridis* as test organisms in longer exposure experiments, the present LC_{50} values were relatively close to them although our Cu LC_{50} value was higher. D'Silva and Kureishy (1978) used 48-hour toxicity tests, Krishnakumar *et al.* (1987a) and Chan (1988) 96-hour toxicity tests and Tan and Lim (1984) 196-hour toxicity tests in this species.

The lowest LC_{50} values found for Cu in both size groups indicated that Cu was the most toxic when compared to Pb, Cd and Zn. The lower LC_{50} values recorded for Cu indicated that the sensitivity of *P. viridis* to Cu was also a few times higher than to Pb, Cd and Zn. Our results were supported by those of D'Silva and Kureishy (1978) and Krishnakumar *et al.* (1987a) (Table 2). Ong and Din (2001) also reported that Cu was most sensitive to clam *Donax faba* and cockle spats, *Anadara granosa*, when compared to Cd and Zn. Akberali and Trueman (1985) reviewed several papers and noted that Zn and Cd had higher toxicity thresholds because they were less readily taken up in the free form from the seawater. Thus, they concluded that bivalve molluscs were less sensitive to Cd and Zn. According to Crecelius *et al.* (1982), free cupric ion (Cu^{2+}), was the most biotoxic form of Cu to marine bivalves in natural seawater. Several studies also demonstrated that the bioaccumulation of Cu was strongly related to free Cu^{2+} activity rather than to the total Cu concentrations or the concentrations of complexes (Sanders *et al.* 1983; Sunda and Guillard 1976; Zamuda and Sunda 1982).

TABLE 2
Comparison of reported LC_{50} values of Cu, Cd, Pb and Zn in *Perna viridis* by acute toxicity test

Metal	Duration of toxicity test	shell length	LC_{50} mg/L	Author
Cu	48h	1.6 cm	0.14	D'Silva and Kureishy (1978)
	96h	3-4 cm	0.086	Krishnakumar *et al.* (1987a)
	96h	1.5-2.0 cm	0.063	Krishnakumar *et al.* (1987a)
	24h	7-8 cm	0.61	This study
	24h	3-4 cm	0.25	This study
Zn	48h	1.6 cm	2.31	D'Silva and Kureishy (1978)
	96h	3-4 cm	3.90	Krishnakumar *et al.* (1987a)
	96h	1.5-2.0 cm	2.85	Krishnakumar *et al.* (1987a)
	96h	6-7 cm	6.00	Chan (1988)
	24h	6-7 cm	5.22	This study
	24h	3-4 cm	3.48	This study
Pb	168h	3-4 cm	4.46	Tan and Lim (1984)
	24h	5-7 cm	5.91	This study
	24h	3-4 cm	4.22	This study
Cd	96h	6-7 cm	1.50	Chan (1988)
	24h	6-8 cm	2.82	This study
	24h	3-4 cm	1.53	This study

When exposed to metal levels considered tolerable to mussels, they seemed to establish a different set of steady-state conditions from the pre-exposure period (Mason and Jenkins 1995). In the presence of metal levels below the LC_{50} values, the mussels were capable of withstanding the toxic effects of the metals and accumulated metals to very elevated levels. For example, at 0.5 mg

Cd/L exposure, mussels accumulated 20.45 mg Cd/g while in the control samples, the mussels only had 0.29mg Cd/g. Chan (1988) found a linear relationship between the uptake of Cd by *P. viridis* from Hong Kong waters and Cd concentrations in the medium. Cossa (1988) found a significant linear relationship between Cd concentration in seawater and bioaccumulated Cd in *Mytilus* species while Talbot (1987) found significant equilibrium relationship between Pb levels in seawater and its concentration in the mussel *M. edulis*. Lakshmanan and Nambisan (1989) also reported that metal levels in *P. viridis* were proportionately increased when the concentrations of environmental seawater increased. It should be noted that the above-mentioned phenomena were recorded when the mussels were exposed to metal levels that were below the acute concentrations or LC_{50} values. At these metal level exposures, the mussels probably have developed increased abilities to endure and sustain metabolic functioning in the presence of elevated metal levels.

Our results indicated that with increasing metal exposure until a threshold level was reached, the metal probably became ultimately toxic to the mussels. At elevated metal exposure, the mussels are believed to have abnormal physiological rate functions. The present work indicated that the soft tissues of mussels at the high and toxic level of metal exposure, did not accumulate proportionately with the metal levels in the ambient seawater. The mussels seemed to lose their normal homeostatic mechanisms which resulted in permanent disturbed metabolic functions (Abel and Papoutsoglou 1986). At this moment, the inhibition of enzymatic activities or the destabilization of structural components of cellular molecules might have occurred (Viarengo 1989). Chan (1988) found that once the threshold concentration was exceeded, Zn had a marked inhibitory effect on respiration and ammonia excretion. Krishnakumar *et al.* (1987b) suggested that the inhibition of respiration due to Zn stress could be attributed to interference with gaseous exchange and the inhibition of mitochondrial respiration.

One of the mechanisms to prevent or limit the uptake of metals at the binding and transport stages as suggested by Mason and Jenkins (1995) was undertaking behavioral avoidance activities. This could be explained from the physiological point of view. In response to a highly toxic metal, those mussels which were able to survive were believed to have tightly closed their valves (Yap *et al.* 2003b). As a result, the filtration rate might be reduced significantly (Yap *et al.* 2003b) due to the inhibitory effects of metals on the ciliary actions of the gill surfaces (Viarengo *et al.* 1996) and would reduce the efficiency of the filtration rate (Sunila 1988). Also, minimal surfaces of soft tissues were in contact with the environmental seawater (George 1980). Possibly the mussels under metal-stress could only survive for a short time due to some irreversible metabolic changes. This mechanical avoidance could likely be used as an important physiological response to counter the transient, short-term and adverse environmental changes in metal levels. This phenomenon was supported by Davenport (1977) who showed rapid valve closure in *M. edulis* and recently by (Yap *et al.* 2003b) who showed lowered filtration rate of *P. viridis* in response to elevated external metal concentrations.

From the cellular response point of view, Moore (1985) pointed out four main categories by which the structure and function of organelles and cells can be disturbed by toxic contaminants. One of these categories included membrane disturbances. At elevated and toxic metal levels, cellular membranes might be severely disturbed to cause cell injury which included injury to the lysosomes. Since metallothionein and lysosomes might play inter-related key roles in metal homeostasis, the injury to lysosomes would reduce the metal detoxification process. This detoxification system is effective until the lysosome is overloaded and damaged directly by the accumulated toxic metals. Therefore, this might cause the death of *P. viridis* at elevated metal levels.

More metals were accumulated in the small size group than in the large size group. This phenomenon is well supported by a number of studies that used molluscs species (Williamson 1980; Amiard *et al.* 1986; Martincic *et al.* 1992). Boyden (1977) found that metal concentrations in older mussels were less than in the young ones. Gilek *et al.* (1996) found that the mussel *M. edulis* was influenced by mussel size in which the tissue concentrations decreased with increasing body size and the observed size-dependent differences in bioaccumulation primarily were caused by size-related differences in the uptake rate. In addition, smaller mussels have larger surface area to volume ratios (Jones *et al.* 1992). Recently, Yap *et al.* (2003) reported significant inverse relationships between metal concentration (Cd, Pb and Zn) and size of *P. viridis.*

Although the loading capacity of large mussel as 0.8-1.2 g /L, which is higher than the suggested 0.8 g/L by Rand and Petrocelli (1985), it was found that the data obtained were still useful, valid and were able to give relatively reasonable toxicities namely Cu> Cd> Zn> Pb and this toxicity was well supported by a study reported previously (Yap *et al.* 2003b) that used filtration rate as a physiological endpoint during the toxicity tests of the similar metals. Also, Ong and Din (2001) found metal toxicity as Cu> Cd> Zn using clam *D. faba* as test organism under laboratory conditions. Therefore, the 24-hour duration of toxicity tests on *P. viridis* was found to be a rapid and inexpensive method and it therefore has a wide applicability. Instead of using the conventional 48-hour or 96-hour of duration of toxicity tests which had been used by other workers on bivalves such as mussels, oysters and clams, the 24-hour duration of toxicity tests we used on *P. viridis* is suggested. Since mussels have the highest feeding rate in comparison to clams and oysters (Tenore 1973), the use of the 24-hour toxicity tests is reasonable because effective response (mortality) was observed after the experimental period.

CONCLUSION

The present study indicated that *P. viridis* could directly bioaccumulate Cd, Cu, Pb and Zn from ambient seawater. Although the study was conducted using only a period of 24-hour duration for the toxicity test, the results were able to give a good picture on the metal tolerance and accumulation by two significantly different size groups. The small size group was more sensitive to Cu, Cd, Zn and

Pb than the large size group as indicated by the lower LC_{50} values found in the small size group. Regardless of the size of *P. viridis*, the toxicities of the metals were in the order Cu> Cd> Zn> Pb. These LC_{50} values are useful in the study of sub-lethal tests in which the test mussels are exposed to metals for up to several weeks. Selection of specific size groups in the study of sub-lethal levels can also be made based on our results reported in this paper.

REFERENCES

ABEL, P. D. 1991. Approaches to measuring the toxicity of pollutants to marine organism. In *Ecotoxicology and the Marine Environment*, ed. P. D. Abel and V. Axiak, p. 19-38. New York: Ellis Horwood.

ABEL, P. D. and S. E. PAPOUTSOGLOU. 1986. Lethal toxicity of cadmium to *Cyprinus carpio* and *Tilapia aurea*. *Bull. Environ. Contam. Toxicol.* **37**: 382-386.

AHSANULLAH, M. 1976. Acute toxicity of cadmium and zinc to seven invertebrate species from Western Port, Victoria. *Aust. J. Mar. Freshwat. Res.* **27**: 187-196.

AKBERALI, H. B. and E. R. TRUEMAN. 1985. Effects of environmental stress on marine bivalve molluscs. *Adv. Mar. Biol.* **22**: 102-198.

AMIARD, J. C., C. AMIARD-TRIQUET, B. BERTHET and C. METAYER. 1986. Contribution to the ecotoxicological study of cadmium, lead, copper and zinc in the mussel *Mytilus edulis* I: Field study. *Mar. Biol.* **90**: 425-431.

BAYNE, B. L., D. A. BROWN, K. BURNS, D. R. DIXON, A. IVANOVICI, D. R. LIVINGSTONE, D. M. LOWE, M. N. MOORE, A. R. D. STEBBING and J. WIDDOWS. 1985. *The Effects of Stress and Pollution on Marine Animals*. New York: Praeger Publishers.

BHAT, U. G. and K. VAMSEE. 1993. Toxicity of heavy metals Cu, Cd and Hg to the gammarid amphipod *Parhalella natalensis* (Stebbing). *Sci. Tot. Environ.* Supplement **1993**: 887-897.

BOYDEN, C. R. 1977. Effects of size upon metal contents of shellfish. *J. Mar. Biol. Ass. U. K.* **57**: 675-714.

CHAN, H. M. 1988. Accumulation and tolerance to cadmium, copper, lead and zinc by the green-lipped mussel *Perna viridis*. *Mar. Ecol. Prog. Ser.* **48**: 295-303.

COSSA, D. 1988. Cadmium in *Mytilus* spp. Worldwide survey and relationship between seawater and mussel content. *Mar. Environ. Res.* **26**: 265-284.

CRECELIUS, E. A., J. T. HARDY, C. I. GIBSON, R. L. SCHMIDT, C. W. APTS, J. M. GURTISEN and S. P. JOYCE. 1982. Copper bioavailability to marine bivalves and shrimp: relationship to cupric ion activity. *Mar. Environ. Res.* **6**: 13-26.

D'SILVA, C. and T. W. KUREISHY. 1978. Experimental studies on the accumulation of copper and zinc in the green mussel. *Mar. Poll. Bull.* **9**: 187-190.

DAVENPORT, J. 1977. A study of the effects of copper applied continuously and discontinuously to specimens of *Mytilus edulis* (L.) exposed to steady and fluctuating salinity levels. *J. Mar. Biol. Assoc. U. K.* **57**: 63-74.

FINNEY, D. J. 1971. *Probit Analysis*. 333p. 3rd edition. Cambridge: Cambridge University Press.

GEORGE, S. G. 1980. Biochemical and cytological assessments of metal toxicity in marine animals. In *Heavy Metals in the Marine Environment*, ed. R. W. Furness and P. S., Rainbow, p.123-142. Boca Raton: CRC Press, Inc.

GILEK, M., M. BIORK and C. NAF. 1996. Influence of body size on the polychorinated biphenyl congeners by Baltic Sea blue mussels, *Mytilus edulis. Mar. Biol.* **125**: 499-510.

GOLDBERG, E. D. 1975. The mussel watch - a first step in global marine monitoring. *Mar. Poll. Bull.* **6**: 111.

ISMAIL, A., C. K. YAP, M. P. ZAKARIA, S. TANABE, H. TAKADA and A. R. ISMAIL. 2000. Green-lipped mussel *Perna viridis* (L.) as a biomonitoring agent for heavy metals in the west coast of Peninsular Malaysia. 2000. In *Towards Sustainable Management of the Straits of Malacca, Technical and Financial Options*, ed. M. Shariff, F. M. Yusoff, N. Gopinath, H. M. Ibrahim and A. Nik Mustapha, p. 553-559. Malacca Straits Research and Development Centre (MASDEC), Universiti Putra Malaysia, Serdang, Malaysia.

JONES, H. D., O. G. RICHARDS and T. A. SOUTHERN. 1992. Gill dimension, water pumping rate and body size in the mussel *Mytilus edulis* (L.). *J. Exp. Biol. Ecol.* **155**: 213-237.

KRISHNAKUMAR, P. K., R. DAMADARAN and P. N. K. NAMBISAN. 1987a. Acute toxicity of selected heavy metals to green mussel *Perna viridis* (Linnaeus). *Indian J. Mar. Sci.* **16**: 263-264.

KRISHNAKUMAR, P. K., R. DAMADARAN and P. N. K. NAMBISAN. 1987b. Carotenoid content of green mussel *Perna viridis* (Linnaeus) to acute mercury and zinc toxicity. *Indian J. Mar. Sci.* **16**: 155-157.

LAKSHMANAN, P. T. and P. N. K. NAMBISAN. 1989. Bioaccumulation and depuration of some trace metals in the mussel *Perna viridis* (Linnaeus). *Bull. Environ. Contam. Toxicol.* **43**: 131-138.

LIVINGSTONE, D. R. and P. S. GOLDFARB. 1998. Aquatic environmental biomonitoring: Use of cytochrome P450 1A and other molecular biomarkers in fish and mussels. In *Biotechnology Research Series: Environmental Biomonitoring: The Biotechnology Ecotoxicology Interface*, ed. J. Lynch and A. Wiseman, **6:** 101-129. Cambridge University Press.

MARTINCIC, D., Z. KWOKAL, Z. PEHAREC, D. MARGUS and M. BRANICA. 1992. Distribution of Zn, Pb, Cd and Cu between seawater and transplanted mussel (*Mytilus galloprovincialis*). *Sci. Tot. Environ.* **119**: 211-230.

MASON, A. Z. and K. D. JENKINS. 1995. Metal detoxification in aquatic organisms. In *Metal Speciation and Bioavailability in Aquatic Systems*. ed. A. Tessiers and D. R. Turner, p. 479-608. New York: John Wiley and Sons Limited.

MOORE, M. N. 1985. Cellular responses to pollutants. *Mar. Poll. Bull.* **16**: 134-139.

New Straits Times. 1999. Pig farm effluents polluting river-by Hamidah Atan, 23 April.

ONG, E. S. and Z. B. DIN. 2001. Cadmium, copper and zinc toxicity to the clam, *Donax faba* C., and the blood cockle, *Anadara granosa* L. *Bull. Environ. Contam. Toxicol.* **66**: 86-93.

PHILLIPS, D. J. H. 1985. Organochlorines and trace metals in green-lipped mussels *Perna viridis* from Hong Kong waters: a test of indicator ability. *Mar. Ecol. Prog. Ser.* **21**: 251-258.

RAN, G. M. and S. R. PETROCELLI. 1985. *Fundamental of Aquatic Toxicology: Methods and Applications*. New York: Hemisphere.

SANDERS, B. M., K. D. JENKINS, W. G. SUNDA and J. D. COSTLOW. 1983. Free cupric ion activity in seawater: effects on metallothionein in growth in crab larvae. *Science* **222**: 53-55.

STEPHEN, C. E. 1977. Methods for calculating an LC50. In *Aquatic Toxicology and Hazard Evaluation*, ed. F. L. Mayer and J. L. Hamelink, p. 65-84. American Society for Testing and Materials, Memphis.

SUNDA, W. G. and R. R. GUILLARD. 1976. Relationship between cupric ion activity and the toxicity of copper to plankton. *J. Mar. Res.* **34**: 511-529.

SUNILA, I. 1988. Acute histological responses of the gill of the mussel, *Mytilus edulis*, to exposure by environmental pollution. *J. Invert. Path.* **52**: 137-141.

TALBOT, V. 1987. Relationship between lead concentrations in seawater and in the mussel *Mytilus edulis*: a water quality criterion. *Mar. Biol.* **94**: 557-560.

TAN, W. H. and L. H. LIM. 1984. The tolerance to and uptake of lead in the green mussel, *Perna viridis*. *Aquaculture* **42**: 317-332.

TANABE, S. 2000. Asia-Pacific mussel watch progress report. *Mar. Poll. Bull.* **40**: 651.

TENORE, R. K., J. C. GOLDMAN and J. P. CLARNER. 1973. The food chain dynamics of the oyster, clam and mussel in an aquaculture food chain. *J. Exp. Mar. Biol. Ecol.* **12**: 157-165.

VIARENGO, A. 1989. Heavy metals in marine invertebrates: mechanism of regulation and toxicity at the cellular levels. *Rev. Aquat. Sci.* **1**: 295-317.

VIARENGO, A., M. PERTICA, G. MANCINELLI, B. BURLANDO, L. CANESI and M. ORUNESU. 1996. In vivo effects of copper on the calcium homeostasis mechanisms of mussel gill cell plasma membranes. *Comp. Biochem. Physiol.* **113C**: 421-425.

WILLIAMSON, P. D. 1980. Variables affecting body burdens of lead, zinc and cadmium in a road side population of the snail *Cepaea hortensis* Müller. *Oecologia (Ber.)* **44**: 213-220.

YAP, C. K., A. ISMAIL and S. G. TAN. 2003a. Mercury levels in the green-lipped mussel *Perna viridis* (Linnaeus) from the West Coast of Peninsular Malaysia. *Bull. Environ. Contam. Toxicol.* **71**: 570-576.

YAP, C. K., A. ISMAIL and S. G. TAN. 2003c. Background concentrations of Cd, Cu, Pb and Zn in the green-lipped mussel *Perna viridis* (Linnaeus) from Peninsular Malaysia. *Mar. Poll. Bull.* **46**: 1035-1048.

YAP, C. K., A. ISMAIL, S. G. TAN and H. OMAR. 2002a. Correlations between speciation of Cd, Cu, Pb and Zn in sediment and their concentrations in total soft tissue of green-lipped mussel *Perna viridis* from the west coast of Peninsular Malaysia. *Environ. Int.* **28(1-2)**: 117-126.

YAP, C. K., A. ISMAIL, S. G. TAN and H. OMAR. 2003b. Effects of heavy metals (Cd, Cu, Pb and Zn) on the filtration rate of the green-lipped mussel *Perna viridis* (Linnaeus). *Malaysian Appl. Biol.* **32(1)**: 7-13.

YAP, C. K., A. ISMAIL and S. G. TAN. 2003c. Effects of total soft tissue and shell thickness on the accumulation of heavy metals (Cd, Cu, Pb and Zn) in the green-lipped mussel *Perna viridis*. *Russian J. of Mar. Biol.* **29(5)**: 323-327.

YAP, C. K., S. G. TAN, A. ISMAIL and H. OMAR. 2002b. Genetic variation of green-lipped mussel *Perna viridis* (Linnaeus) from the west coast of Peninsular Malaysia. *Zool. Stud.* **41(4)**: 376-387.

ZAMUDA, C. D. and W. G. SUNDA. 1982. Bioavailability of dissolved copper to the American oyster *Crassostrea virginica*. 1. Importance of chemical speciation. *Mar. Biol.* **66**: 77-82.

ISSN: 0128-7680
Pertanika J. Sci. & Technol. 12(2): 249 - 263 (2004)

Design and Simulation of Three-tier Hierarchical Network for 3rd Generation Mobile System

[1]N. K. Noordin, [1]J. Chong, [1]F. Hashim & [1]S. Khatun
[1]Department of Computer and Communications System Engineering,
Faculty of Engineering,
Universiti Putra Malaysia, 43400 UPM Serdang,
Selangor, Malaysia
E-mail: nknordin@eng.upm.edu.my

Received: 22 August 2002

ABSTRAK

Sewaktu dunia komunikasi bersiap sedia menuju ke arah sistem komunikasi bergerak generasi ketiga (3G), beberapa piawaian termasuk Telekomunikasi Bergerak Antarabangsa-2000 (IMT-2000) telah diberi pertimbangan untuk dilaksanakan. Dalam IMT-2000, sistem tiga-lapisan dicadangkan untuk komunikasi berasaskan selular. Sistem hierarki ini bertujuan meningkatkan kapasiti secara keseluruhan dengan menyediakan laluan alternatif bagi panggilan-panggilan sedia ada. Makalah ini bertujuan menilai prestasi sistem tiga-lapisan dengan melaksanakan pembahagian lapisan mengikut tahap kelajuan kenderaan, iaitu kenderaan dengan kelajuan perlahan, kenderaaan dengan kelajuan sederhana, dan kenderaan laju. Tiga model dengan tiga taburan berbeza disimulasikan dengan model-model ini menentukan interaksi antara lapisan, dan dikenali sebagai model bergerak bebas, model bergerak satu-arah dan model bergerak dwi-arah. Gred perkhidmatan (GoS) bagi sistem ini diukur melalui keberangkalian panggilan dihalang dan juga keberangkalian panggilan terputus secara paksa.

ABSTRACT

As the communication world prepares to move into third generation (3G) mobile communication systems, several standards, including the International Mobile Telecommunication 2000 (IMT-2000) standard, are being considered for implementation. In IMT-2000, a three-tier system is proposed for cellular-based communication. Hierarchical systems will increase overall system capacity by providing alternative routes for existing calls. This paper examines the performance of a three-tier system implementing segregation of different mobile traffic speeds according to tier, namely slow, medium and fast mobile speeds. Three models and three different call distributions are simulated. These models determine the interaction between tiers, and are known as independent model, unidirectional model and bi-directional model. The grade of service (GoS) of a system is measured via the call blocking probability and the forced termination probability.

Keywords: IMT-2000, hierarchical systems, three-tier networks, cellular system, 3G, third generation mobile communication

INTRODUCTION

IMT-2000 stands for International Mobile Telecommunication 2000, a standard being developed by the International Telecommunication Union (ITU) for use with third generation (3G) mobile communication. Even though some European countries and Japan have deployed the system, Malaysia is still at its infancy in awarding spectrum and identifying the right network and service operators. A lot more research is still going on to ensure the system is flawless and will satisfy the customers. IMT-2000 envisions bringing together fixed line, mobile and satellite systems into one harmonious system. To ensure good quality of service network, a three-tier hierarchical architecture has been proposed in IMT-2000, comprising macrocells for suburban areas, microcells for urban areas, and picocells for inside buildings (Callendar 1999; Shafi *et al.* 1997).

The main consideration in using any type of communication system is the network performance (Ganz *et al.* 1997). Some of the previous works basically implement the frequency reuse techniques, prioritised network and also the two-tier cellular network system. A new proposed method to improve resource utilization is the concept of three layers hierarchical (or three-tier) network design. Thus, a teletraffic simulation according to the three-tier system architecture proposed in the IMT-2000 standard is carried out so that the performance between various layers according to mobile speed can be compared. In this hierarchical system, different cell sizes are used. In the initial proposal, there were three types of cells: macrocells, microcells and picocells. The microcells are similar to regular cells in traditional design. Superimposed on this structure are the macrocells, each of which covers the same geographical area as several microcells. Lastly the addition of picocells into each microcell. *Fig. 1* shows an example of the three-tier cellular network architecture.

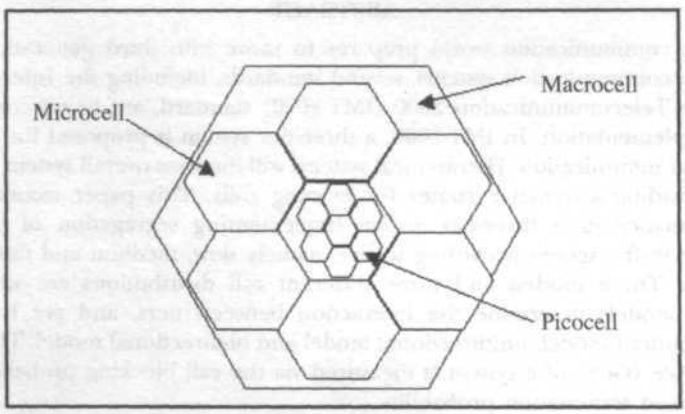

Fig. 1: Three-tier architecture

The proposed architecture is not only to handle cellular telephone systems, but also other wireless devices such as personal digital assistants (PDA), wireless terminals and so on. This is in line with ITU's vision for a global harmonized wireless access system (Callendar 1999).

Ekici (1999) described a two-tier system and gave analytical results for a set of different parameters. He designed a minimum cost two-tier cellular network with call overflow and guard channels that satisfy certain performance constraints. Ali (1999) and Ho (2000) developed a two-tier system that implements fixed channel assignment. They examined the system in terms of network performance. None of the mentioned works present a simulation for three-tier cellular network with different types of call distributions.

The focus of this work is to examine the three-tier cellular network implementing segregation of different mobile traffic speeds according to tier, namely slow, medium and high mobility. In this work, three models and three different call distributions are simulated. These models determine the interaction between tiers, and are known as independent model, unidirectional model and bi-directional model.

In Independent Model, no overflow call is allowed between each layer, whereas in Unidirectional Model, there will be overflow calls from picocell to microcell to macrocell layer. Lastly, Bi-directional Model employs both directions of call overflow; from picocell to microcell to macrocell; and from macrocell to microcell to picocell. *Figs. 2* and *3* show the Unidirectional model and Bi-directional model for three-tier cellular network.

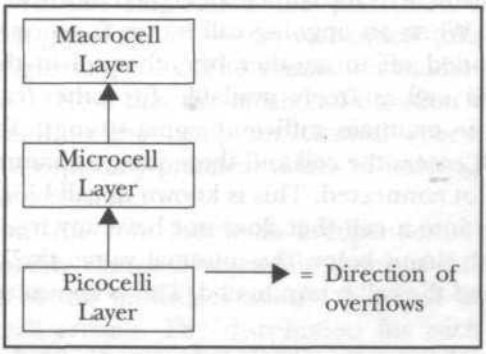

Fig. 2: Unidirectional model

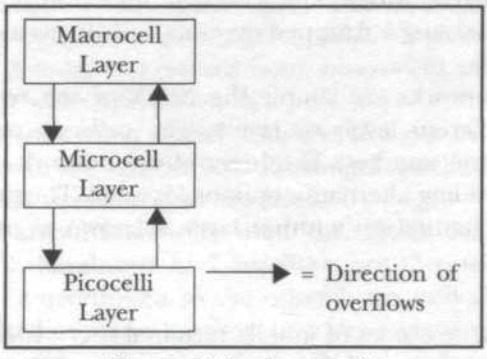

Fig. 3: Bi-directional model

Handoff calls are given higher priority to use any channel available in each layer. If there is no overflow call, then only the new calls can be allocated a channel. Lastly we will compare each type of model in terms of network performance.

The outline of this paper is as follows: in the second section, the design problem is formulated. Then, the objective function that will be used in the solution techniques is described and the calculation methods are presented. The third section explains the solution techniques extensively. In the final section, the results of the computational experiments are presented.

PROBLEM DEFINITION

Cellular Network

Current mobile telecommunication systems are cellular-based systems using the concept of cells and channels. An area of coverage is divided into cells of certain sizes and each cell contains a number of channels, which can support a call. A number of cells are grouped together and is called clusters. Different clusters share the same set of frequency channels. This technique called frequency reuse, allows limited bandwidth to be reused, saving cost and increasing capacity.

When a call is made, a free channel is assigned to the call in order to enable it to communicate. When an ongoing call moves from one cell to an adjacent cell, the call is handed off to another free channel in the new cell and the channel in the old cell is freely available for other calls. This process is necessary in order to maintain sufficient signal strength for call integrity.

When a new call enters the cell and there are no channels available, the call is dropped and is not connected. This is known as call blocking. Likewise, if an ongoing call moves into a cell that does not have any free channels, once the call's signal strength drops below the minimal value, the call will be dropped from the network and the call is terminated. This is known as forced termination (Chong 2001).

The probability of these two events is commonly used as a measure of the efficiency and performance of a cellular system, known as the grade of service (GoS) of the cellular network. The forced termination probability usually has more importance because a dropped ongoing call affects a customer more than a blocked new call.

Hierarchical networks are simply the result of the overlaying cells above each other on different levels or layers. The cells on one layer are usually different in size from another. The hierarchical network increases capacity of the network by providing alternative options for a call. The process of transferring a call to another channel on another layer is known as overflow.

Simulation Model

Here we assume three classes of mobile terminal users: high, medium and slow mobility users. The high mobility class (more than 30km/hr) represents the

vehicular mobile terminals. The low mobility class (lower than 3km/hr) is made up of users that are primarily pedestrians while in between these two types of classes there is the medium mobility class. Since the main target is to provide high performance cellular network that will cover a large area like an entire city, we assume that the distribution of the mobile terminals is even over the entire area, but with different rates. The systems are categorised into three different types of distribution: Type 1 (33%-33%-33%) is for equal distribution between mobile calls, Type 2 (50%-30%-20%) is for a higher population of slow mobile calls and Type 3 (70%-20%-10%) is when slow mobile calls' population is further increased. Furthermore, we also assume that the mobile terminals may move in any direction with equal probability. This assumption is valid both for high, medium and low mobility classes. The mean call duration (420 ns) is assumed to follow exponential distribution. The call duration has the same distribution for the mobility classes. The time spent in a cell, which is called dwell time Ud, depends on the speed and trajectory of the mobile terminal as well as the shape of the cell. The cells are assumed to be hexagonal in general. However, for easy calculation of the dwell time, the cells are assumed to be circles. Besides that the total coverage area is assumed to have two macrocells layer, four microcells layer and eight picocells layer. We used the fixed channel assignment Ekici (1999), Ali (1999) and Ho (2000) for all the cells with 32 channels per cell. We also implement the prioritised network technique (Rappaport 1996) that gives higher priority to handoff calls and overflow calls compared to new originating calls. The simulation model described above is summarised in Table 1. Note that the mean call duration was set at 420 ns to avoid excessive burden to the computer Central Processing Unit (CPU). However the model accepts any practical values of holding time provided the computer memory is sufficient.

The call arrivals to the cells follow an independent Poisson distribution regardless of the mobility classes. The mobile terminal density and the mean call generation rate of the individual mobile terminal users determine the mean rate for the call arrivals. The distribution for each mobility terminal differs only in the mean rates.

The cells of the lowest tier are called picocells and their radii are smaller than those of the cells of the upper layer. The layers above it are called microcells. The microcells cover an integer number of picocells. The top layer cells are macrocells. Similar to previous ones, macrocells will cover an integer number of both microcells and picocells.

Furthermore, the simulation model simulates two systems with different cell sizes. These values are in accordance with the ranges specified in (Nanda 1993). Table 2 shows the cell sizes for each model.

Six different call arrival rates were used: 0.25, 0.33, 0.5, 1, 2 and 4 calls/second. All new calls, handovers and overflows are directed into the system. Only handoff calls are overflowed to the other layers and this occurs only for Unidirectional and Bi-directional models. In Independent model there will be no overflow calls between each layer. New calls do not have this capability in

TABLE 1
Simulation model

Mobility Class	High Medium Low	> 30 km/hr between 3 km/hr to 30 km/hr < 3 km/hr
Types of mobile distribution	Type 1 Type 2 Type 3	Equal distribution of high, medium and low mobility classes (33%:33%:33%) (High 20% : Medium 30% : Low 50%) (High 10% : Medium 20% : Low 70%)
Mean Call Duration	420 ns (for simulation purposes)	
Number of cells	2 macrocells 4 microcells 8 picocells	
Number of channels	32 channels per cell with fixed channel assignment	

TABLE 2
Cell sizes for each type of simulation

	PICOCELL	MICROCELL	MACROCELL
Standard Simulation	100 m	400 m	800 m
Simulation B	100 m	200 m	400 m

order to preserve the GoS of the ongoing calls in the source layer as well as the destination layer. *Fig. 4* shows the algorithms used to implement each model.

The simulation utilized three types of hierarchical relationships between the three layers. Independent Type is where the layers act independently of each other and no overflows to other layers are allowed. The Independent Type model is used as a reference for comparison to the other models. Unidirectional Type allows single directional overflows from picocells upwards to macrocells. Bi-directional Type allows bi-directional overflows among all the layers.

SOLUTION TECHNIQUES

In this section, we describe the details on network performance calculation for each model based on Jabbari and Fuhrman (1992). From *Fig. 1*, we may see that there are three layers in a three-tier system. The largest cell is basically the macrocell. For every macrocell, there is an overlaid layer of M microcells, and for every microcell, there is an overlaid layer of P picocells.

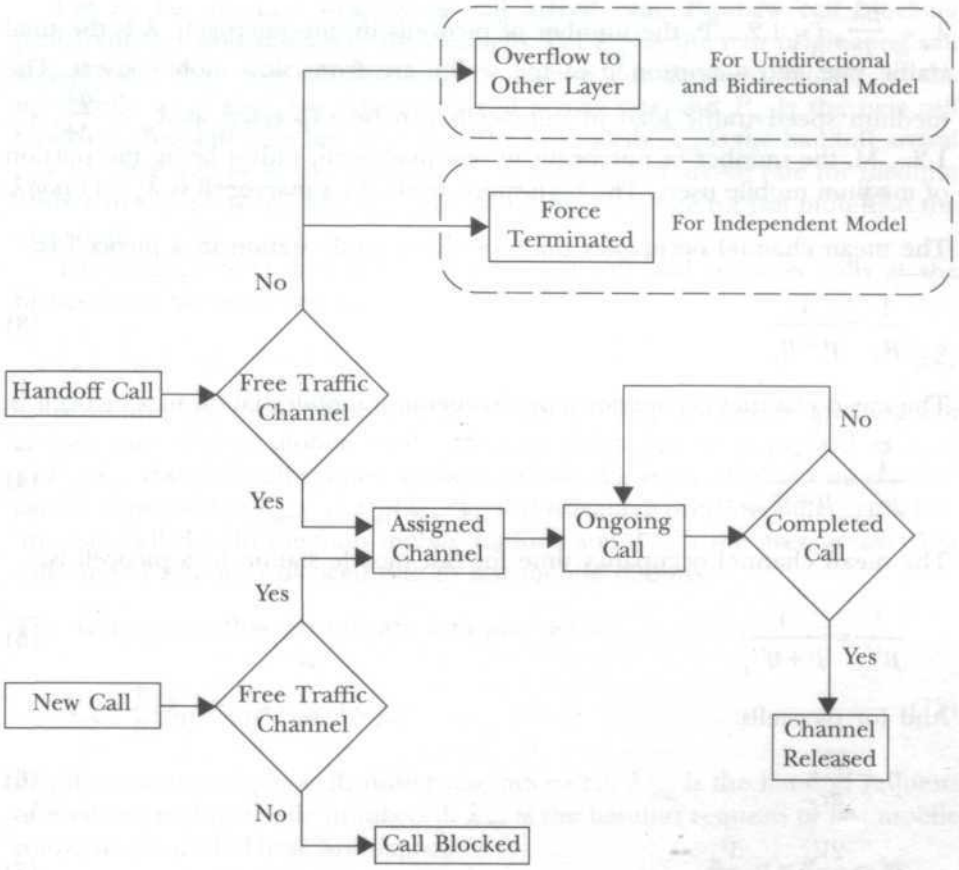

Fig. 4: Algorithm for three-tier cellular system (Chong 2001)

The mobile channel time in a cell is assumed to follow negative exponential distribution, (0 for fast mobile, η_1 for medium mobile and η_2 for slow mobile. The call arrival rates are assumed to be independent and identically distributed random variable with distribution $F_m(t_m)$ and the density function $f_m(t_m)$ with mean $1/\eta$. The call arrival rate is a Poisson random variable, the density function $r_{mi}(t)$ can be derived as:

$$r_{mi}(t) = \eta_i = \eta_i[1 - F_{mi}(t)] \quad (1)$$

The density function is:

$$f_{mi}(\mu) = \frac{\pi_i}{\pi + \pi_i} \quad (2)$$

The new arrival call is assumed to follow Poisson process of parameter λ_s for slow mobile, λ_m for medium mobile and λ_f for fast mobile, which are randomly distributed. Thus, the slow speed traffic load in picocells can be expressed as

$\lambda_{si} = \frac{\rho\lambda}{P}$, i = 1,2.....P, the number of picocells in one microcell. λ is the total traffic rate and a portion ρ of the traffic are from slow mobile users. The medium speed traffic load in microcells can be expressed as $\lambda_{mi} = \frac{q\lambda}{M}$, i = 1,2.....M, the number of microcells in one macrocell, with q being the portion of medium mobile users. The high-speed traffic in a macrocell is $\lambda_{fo} = (1\text{-}\rho\text{-}q)\lambda$.

The mean channel occupancy time for slow mobile station in a picocell is:

$$\frac{1}{\mu_j} = \frac{1}{\mu + \eta_j} \tag{3}$$

The mean channel occupancy time for medium mobile station in a picocell is:

$$\frac{1}{\mu'_j} = \frac{1}{\mu + \eta'_j} \tag{4}$$

The mean channel occupancy time for fast mobile station in a picocell is:

$$\frac{1}{\mu''_j} = \frac{1}{\mu + \eta''_j} \tag{5}$$

And for picocells:

$$\eta_j = \frac{2V_s}{\pi r_j} \tag{6}$$

$$\eta'_j = \frac{2V_m}{\pi r_j} = \eta_j \frac{V_m}{V_s} \tag{7}$$

$$\eta''_j = \frac{2V_f}{\pi r_j} = \eta_j \frac{V_f}{V_s} \tag{8}$$

η_j is the time of slow mobile users crossing picocell boundary, η'_j is the time of medium mobile users crossing picocell boundary and $\eta''j$ is the time of fast mobile users crossing picocell boundary.

Similarly, for picocells, the handoff probability of slow, medium and fast mobile station is given as:

$$P_{hj} = \frac{\eta_j}{\mu + \eta_j} \tag{9}$$

$$P'_{hj} = \frac{\eta'_j}{\mu + \eta'_j} \tag{10}$$

$$P''_{hj} = \frac{\eta''_j}{\mu + \eta''_j} \tag{11}$$

Let λ_{s2} be the new originating call arrival rate, P_{sb2} new call blocking probability for slow mobile in the picocells. Let λ_{m1} be the new originating call arrival rate, P_{mb1} new call blocking probability for medium mobile in the microcells. λ_{f0} is the new originating call arrival rate and P_{fb0} is the new call blocking probability for fast mobile in the macrocells. λ_{sh2} is the handoff arrival rate for slow mobile in the picocell, λ_{mh1} is the handoff arrival rate for medium mobile in the microcell and λ_{fh0} is the handoff arrival rate for fast mobile in the macrocell.

The average total arrival rate of new, handoff and overflow calls at the picocell can be expressed as:

$$\lambda_{t2} = \lambda_{s2} + \lambda_{sh2} + \lambda'_{t2} + \lambda''_{t2} \tag{12}$$

λ_{t2} is the average total arrival rate at the picocell, λ_{s2} the new originating call arrivals rate of slow mobile to the picocell which can be expressed as $\lambda_{s2} = (1\text{-}P_{sb2})\lambda_{s2}$. Handoff call request of slow mobile, λ_{sh2} from neighboring picocell can be expressed as $\lambda_{sh2} = (1\text{-}P_{sb2})\lambda_{sh2}$. λ'_{t2} is the average overflow calls arrival rate into picocell due to medium mobile stations and λ''_{t2} is the average overflow calls arrival rate into picocell due to fast mobile stations.

The average overflow arrival rate into picocell is:

$$\lambda'_{t2} = \frac{1}{P}(\lambda_{t1})P_{mb1} + \lambda'_{mh2} + \lambda'_{fh2} \tag{13}$$

P is the number of picocells under one microcell, λ'_{mh2} is the handoff requests of medium mobile traffic in picocell. λ'_{fh2} is the handoff requests of fast mobile traffic in picocell. These are expressed as:

$$\lambda'_{mh2} = P'_{h2}\left\{\frac{1}{P}(\lambda_{t1})P_{mb1}(1-P_{sb2}) + \lambda'_{mh2}(1-P_{sb2})\right\} \tag{14}$$

$$\lambda'_{fh2} = P'_{h2}\left\{\left(\frac{1}{P}(\lambda_{t1})P_{mb1}(1-P_{sb2})\right) + \lambda'_{fh2}(1-P_{sb2})\right\} \tag{15}$$

The parameters for microcell and macrocell layer can be calculated on the same idea.

Thus, the equation for Erlang B (blocking probability) (Jabbari & Fuhrmann 1992) can be expanded for the three-tier cellular networks.

$$P_{oi} = B(N,A) = \frac{\left(\frac{\lambda_{ti}}{\mu_i} + \frac{\lambda'_{ti}}{\mu'_i} + \frac{\lambda''_{ti}}{\mu''_i}\right)}{N_i!} \Bigg/ \sum_{l=0}^{N} \frac{\left(\frac{\lambda_{ti}}{\mu_i} + \frac{\lambda'_{ti}}{\mu'_i} + \frac{\lambda''_{ti}}{\mu''_i}\right)^l}{l!} \tag{16}$$

P_{oi} is the blocking probability at picocell for $i = 2$, at microcell for $i = 1$, and at macrocell for $i = 0$. λ_i, for $i = 0, 1, 2$ is the total call arrival rate (new and handoff calls) from the same cell-layer, λ'_i and λ''_i for $i = 0,1, 2$ is the handoff requests from different cell layer. μ_i, μ'_i and μ''_i are the channel occupancy times for the different mobiles, where applicable.

Computational Experiments

After running the simulation using MatLab 5.0, the respective graphs were plotted. *Figs. 5* and *6* show the comparison between each model in terms of call blocking probability.

From *Fig. 5*, it is observed that the Bi-directional systems have worse call blocking probability than Unidirectional systems. This is due to the fact that Bi-directional system that allows overflows among all layers suffers from lack of channels after allowing other cells to occupy its channels.

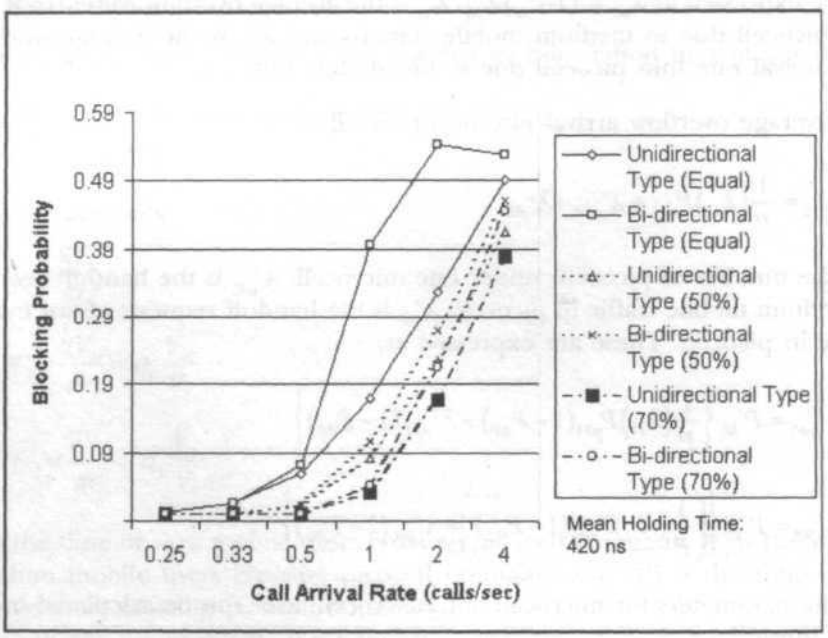

Fig. 5: Comparison of blocking probability

On the other hand, Bi-directional performs better in terms of forced termination probability compared to Unidirectional system as shown in *Fig. 6*. Bi-directional systems generally have more options for handoff calls compared to Unidirectional Type systems in order to reduce the forced termination probability. This, however, reduces the number of free channels available for new calls, hence the higher call blocking probability. The options for new calls are the same as a Unidirectional Type system. A Unidirectional Type system has

better call blocking probability because more channels are available, which were not taken by overflowed calls.

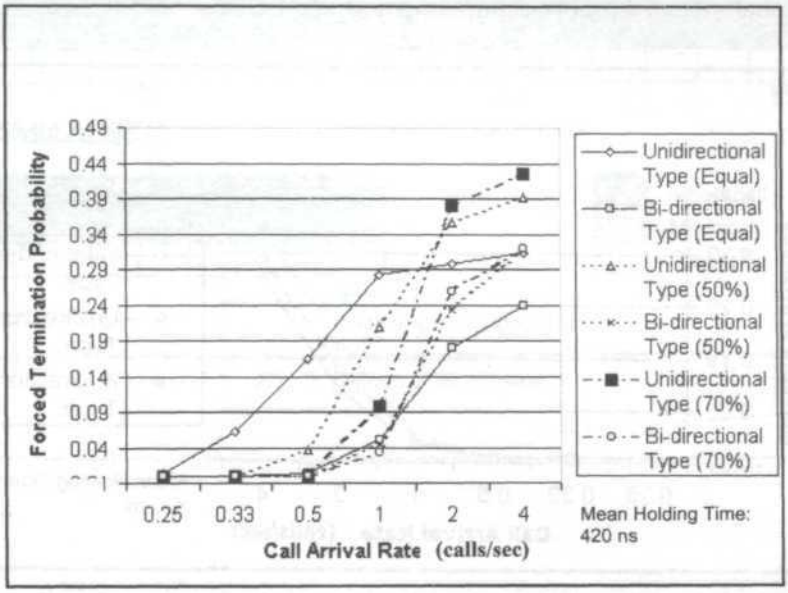

Fig. 6: Comparison of forced termination probability

Figs. 7 and *8* show comparison of forced termination, and blocking probability for all systems respectively. The reference model, which is the Independent Type system has the worst forced termination probability due to the lack of overflow mechanisms. However the higher number of available channels in this non-overflow system allows for lowest call blocking probability. Unidirectional system can be seen to have more balanced system implementations with acceptable call blocking and forced termination probability.

Fig. 9 shows the difference in cell sizes for Standard Simulation and Simulation B. The simulations of big cell size versus small cell size are performed and results are shown in *Figs. 10* and *11* respectively. It can be observed that results obtained from both simulations share similar characteristics but higher values in terms of blocking probability for Simulation B compared to the Standard Simulation. It can be concluded that when smaller cell sizes are used, the system generally shows same characteristics as a larger cell sized system albeit higher blocking probability values.

This is due to the reduced number of total available channels when the number of picocells decreases. The less channels, the less calls can be supported. Smaller cell size also increases the frequency of handovers as more calls reach the boundary of the cells earlier. This also reduces the number of channels for new calls that are available, as more channels are being taken by the handover calls.

Another criteria that is also usually used to decide the system implementation is the system throughput (*Fig. 12*). The bi-directional system model has the highest throughput for all the three slow call ratios. This shows that the bi-directional system should be implemented.

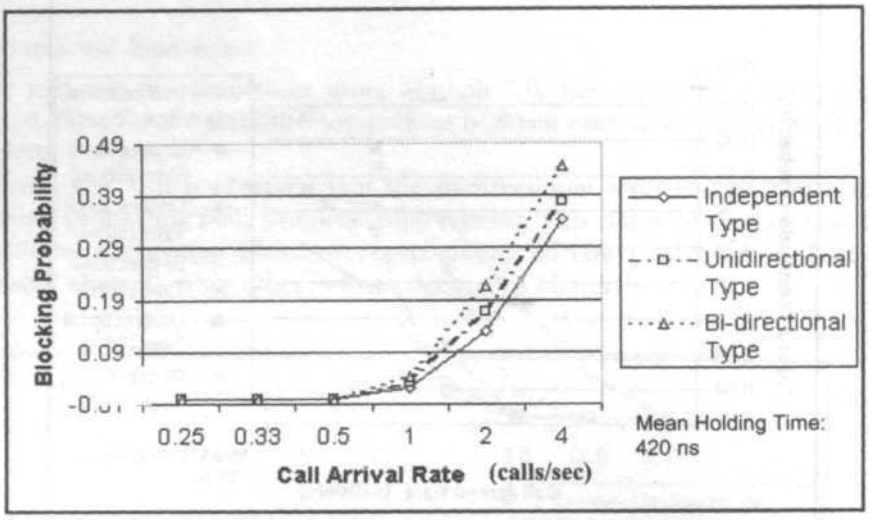

Fig. 7: Overall blocking probability (70%-20%-10% distribution)

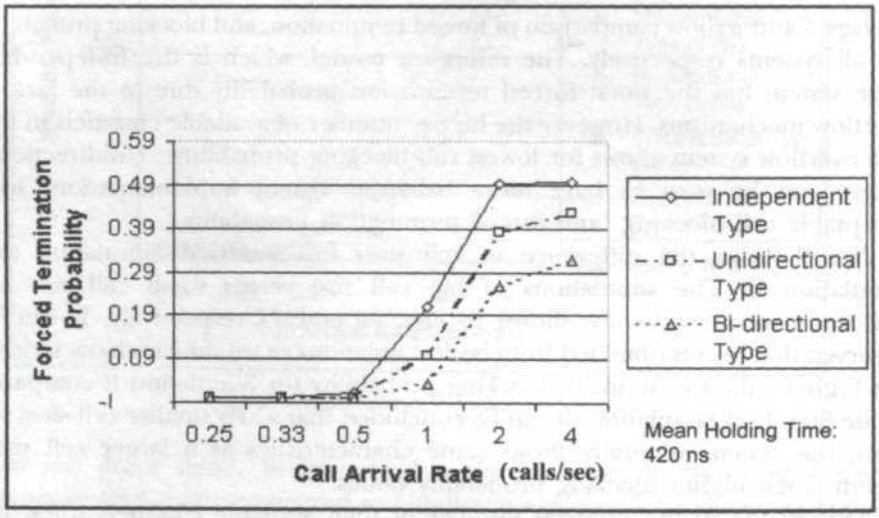

Fig. 8: Overall forced termination probability (70%-20%-10% distribution)

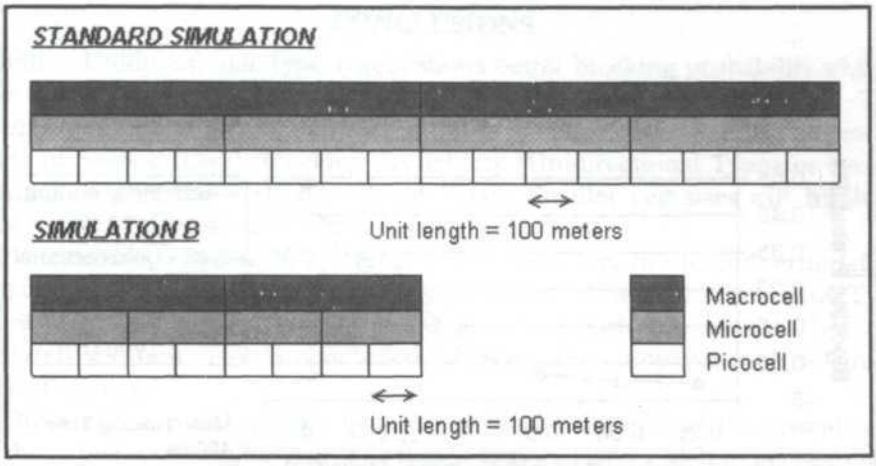

Fig. 9: Difference in cell sizes

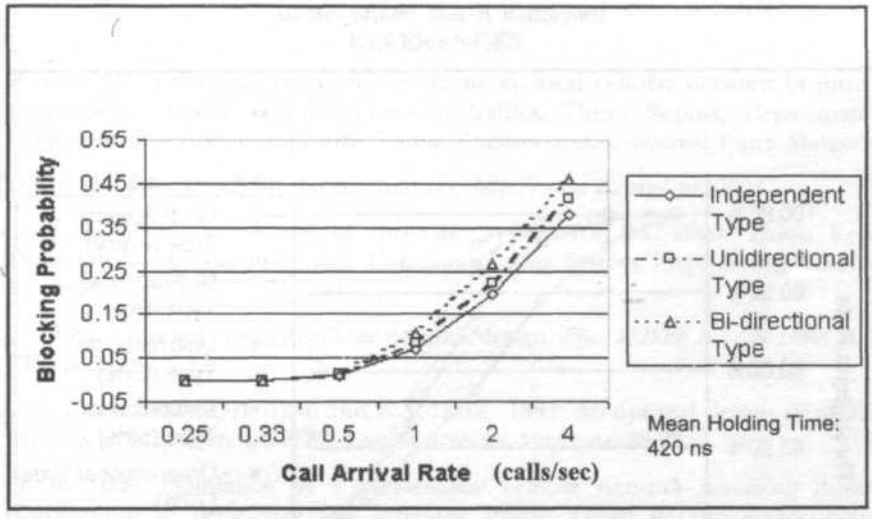

Fig. 10: Overall blocking probability (50%-30%-20% distribution) for standard simulation

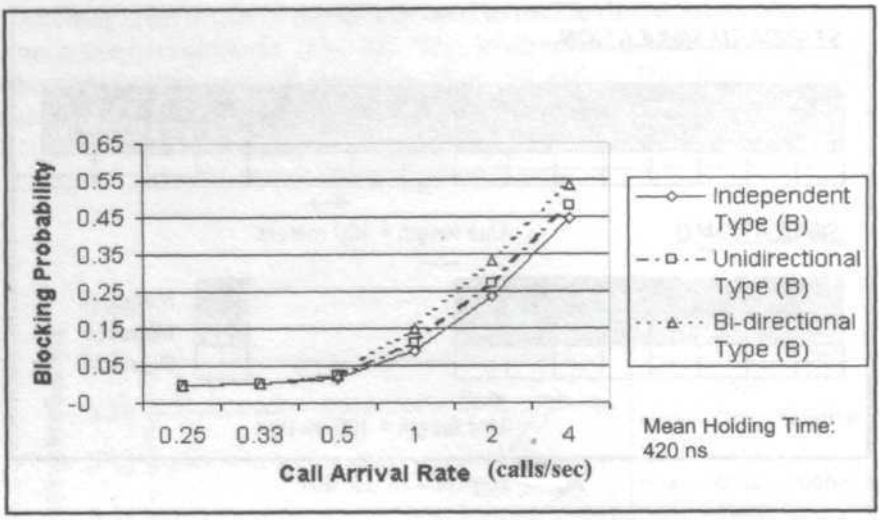

Fig. 11: Overall blocking probability (50%-30%-20% distribution) for simulation B with smaller cell size

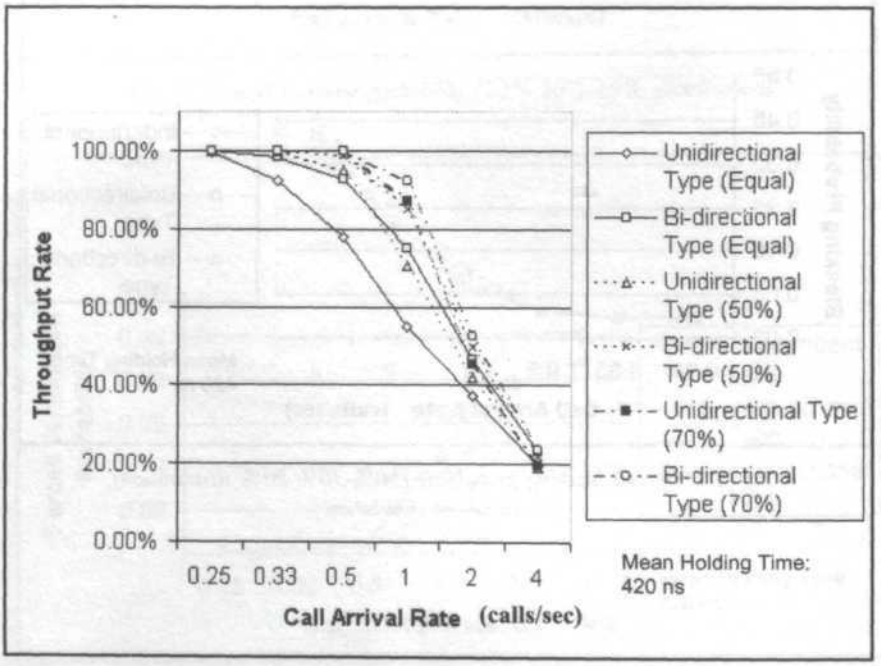

Fig. 12: System throughput

CONCLUSIONS

Overall, a Unidirectional Type system shows better blocking probability while a Bi-directional Type system has better forced termination probability. The system implementation will depend on the preference of the cellular network's Grade of Service (GoS); blocking probability (Unidirectional Type) or forced termination probability (Bi-directional Type). Smaller cell sizes will result in higher forced termination and blocking probability.

To conclude, a Bi-directional Type system shows superior forced termination probability at the expense of blocking probability, while a Unidirectional Type system is generally more well-balanced, good in both probabilities but not absolutely the best. This is concluded based on the comparison of all three types of systems.

The simulation only gives a general practical behaviour of the system, and not the actual system behaviour. For that, additional issues such as propagation, switching, processing, cost, topology and others must be put into consideration when finally deciding on the system that should be implemented.

REFERENCES

ALI, A. H. 1999. Teletraffic performance of hierarchical cellular network in different populations of slow mobile generated traffics. Thesis Report, Department of Computer and Communications System Engineering, Universiti Putra Malaysia.

CALLENDAR M. 1999. IMT2000 standardization, *http://www.itu.org/imt2000/*

CHONG, J. H. 2001. Simulation of three-tier system for IMT-2000. Thesis Report, Department of Computer and Communications System Engineering, Universiti Putra Malaysia.

EKICI, E. 1999. Optimal two-tier cellular network design. *Proc. of IEEE ICCCN 1999*, p. 312-317, Boston.

GANZ, A., C. M. KRISHNA, D. TANG and Z. J. HAAS. 1997. An optimal design of multitier wireless cellular systems. *IEEE Communications Magazine:* 88-93.

HO, Y. K. 2000. Simulation of a hierarchical cellular network assuming different distributions of pedestrian and vehicular traffic. Thesis Report, Department of Computer and Communications System Engineering, Universiti Putra Malaysia.

JABBARI, B. and W. F. FUHRMANN. 1992. Teletraffic modeling and analysis of flexible hierarchical cellular networks with speed-sensitive handoff strategy. *IEEE JSAC* **15(8):** 1539-1548.

NANDA, S. 1993. Teletraffic models for urban and suburban microcells: Cell sizes and handoff rates. In *Wireless Communications - Future Directions*, ed. Jack M. Holtzman and David J. Goodman, p. 157 - 175. Kluwer Academic Publishers.

RAPPAPORT, T. S. 1996. *Wireless Communications - Principles and Practise.* p. 25-63. New Jersey: Prentice Hall PTR.

SHAFI, M., A. HASHIMOTO, M. UMEHIRA, S. OGOSE and T. MURASE. 1997. Wireless communications in the twenty-first century: a perspective. *Proc. of the IEEE* **85(10):** 1622-1639.

ISSN: 0128-7680
Pertanika J. Sci. & Technol. 12(2): 265 - 275 (2004)

Parallel System Using the Log-Linear Exponential Model with Censored Data and Two Covariates

Jayanthi Arasan & Isa Daud
Faculty of Sciences and Environmental Studies
Universiti Putra Malaysia, 43400 UPM, Serdang
Selangor, Malaysia

Received: 30 November 2002

ABSTRAK

Fokus utama kertas ini adalah untuk mengkaji keupayaan model dalam sistem selari dengan data tertapis dan pelbagai kovariat. Kita telah melanjutkan penggunaan model "log-linear-exponential regression" oleh Glasser kepada sistem selari dengan data tertapis jenis II dan dua kovariat. Kajian simulasi juga telah dijalankan untuk mengkaji kesan kadaran dalam data tertapis, saiz sampel dan bilangan komponen selari ke atas ketepatan dan kecekapan penganggar parameter-parameter tersebut.

ABSTRACT

The main focus of this paper is to investigate the performance of a parallel system model with censored data and multiple covariates. We extended the use of the log-linear-exponential regression model of Glasser to a parallel system model with two covariates in the presence of Type II censoring. Simulation studies were carried out to analyze the effect of censoring proportion, sample size and number of parallel components on the bias and efficiency of the parameter estimates.

Keywords: Parallel model, covariates, censoring

INTRODUCTION

The rapid increase in the use of parallel systems in order to achieve higher reliability in the engineering field and the natural existence of these systems in medical and biomedical fields has directly attracted attention to the development of survival models based on them.

The inclusion of prognostic factors or more popularly known as covariates or concomitant variables have become almost an essential in all fields involved with survival studies. Examples of covariates often seen in the medical field are age, duration of the disease, family history of the disease, use of certain drug, gender and race. In fields such as engineering, the covariates may be factors such as temperature or voltage.

Covariates help to reduce variability in the observed data, also known as effect modifiers or control of confounding which helps in achieving more efficiency in statistical inference (Hosmer 1999). Developing survival models that include multiple covariates is very important since it is very common, especially in the medical field, to find at least a few covariates significantly related to survival. Thus, the simultaneous and interactive effect of the covariates

needs to be examined thoroughly in order to obtain an accurate survival model. The main focus of this paper is to investigate the performance of a parallel system model with censored data and multiple covariates. The multiple regression method is well known as the traditional way of examining the relationship between survival time and potential covariates or prognostic variables.

There are many regression models developed by authors in the past to accommodate for covariate adjustment and distribution other than normal and also censored data. Some examples of such models are the log-linear-exponential regression model of Glasser (1967), linear-exponential model by Feigl and Zelen (1965) and the linear-exponential model by Byar (1974). All the above models assume that the underlying survival distribution is exponential. This paper will extend the use of the log-linear-exponential regression model of Glasser to a parallel system model with multiple covariates in the presence of Type II censoring.

Log-Linear Exponential

The log-linear exponential model incorporates the effect of covariates in its hazard function. It assumes that the hazard rate can be expressed as a linear function of the covariates and that the underlying survival distribution is exponential. Suppose there are, i=1,2...,n samples or individuals and p covariates. Then, λ_i, is the hazard rate of the i^{th} sample and can be expressed as

$$\lambda_i = exp(\beta' x_i) \tag{1}$$

where $x'_i = (xi_0, x_{i1},..., x_{ip})$ is the vector of covariate values and $x_{i0} = 1$
$\beta' = (\beta_0, \beta_1,..., \beta_p)$ are unknown parameters.

The survivorship function of the ith sample is then

$$S(t_i, \lambda_i) = e^{-\lambda i t i} \tag{2}$$

The following indicator variables will help us identify whether the data was censored or otherwise.

$$s_i \begin{cases} 1 & \text{if } t_i \text{ uncensored} \\ 0 & \text{if } t_i \text{ censored} \end{cases}$$

The Parallel Model

For a parallel system consisting of m identical and independent components, with exponential failure distribution, the survival of the entire system is equivalent to the probability of at least one component still operating. If t_k is the survival time of component k, where k = 1,2,...,m and unit failures are independent, then time to failure of the entire system, t_s is,

$$t_s = max\{t_1, t_2,..., t_m\} \tag{3}$$

Thus, the survival function of the entire system is,

$$\begin{aligned} S(t) &= P\{max\ t_k > t\} \\ &= [P(t_1 > t)(\ P(t_2 > t) \cup ... \cap\ P(t_m > t)] \\ &= 1-[P(t_1 \le t) \cap P \le t_2(\ t) \cap ... \cap P(t_m \le t)] \\ &= 1-[(P(t_1(\ t)(P(t_2(\ t) \times ... \times P(t_m(\ t)] \\ &= 1-[F(t)]^m \\ &= 1-(1-\ e^{-\lambda t})\, m \end{aligned} \tag{4}$$

Likelihood Function for Parallel Model with Covariates

Assuming that we have n independent observation of time, p covariates and a censoring indicator denoted by (t_i, x_i, s_i), $i = 1,2,...,n$, the likelihood function of the full sample is

$$l(\beta) = \prod_{i=1}^{n} [f(t_i)]^{S_i} [1 - F(t_i)]^{1-S_i} \tag{5}$$

where $F(t_i) = (1-e^{-\lambda_i t_i})\mathrm{m}$ (6)

thus $f(t_i) = m\lambda_i(e^{-\lambda_i t_i})(1-e^{-\lambda_i t_i})^{m-1}$ (7)

Maximized likelihood with respect to the parameters, β, can be obtained more easily by maximizing the log-likelihood function given in (8).

$$L(\beta) = \sum_{i=1}^{n} \{ s_i ln[f(t_i)] + (1-s_i) ln[1-F(t_i)] \} \tag{8}$$

Differentiating the log likelihood function above with respect to the unknown parameter estimates and setting the expressions equal to 0 would give us likelihood equations that can easily be solved using the Newton-Raphson iterative procedure for solving non linear equations, Lee (1992). The steps can be implemented easily using the fortran programming language.

The general form of the $(p+1)$ likelihood equations are as follows:

$$\sum_{i=1}^{n} x_{ij} [s_i A_i - (1-s_i) t_i h_i] = 0 \tag{9}$$

$j=0,1,2,...,p$

$$A_i = 1 - \lambda_i t_i + \frac{(m-1)\lambda_i t_i e^{-\lambda_i t_i}}{1-e^{-\lambda_i t_i}} \tag{10}$$

$$h_i = \frac{f(t)}{1-F(t_i)} \tag{11}$$

Estimator of the variance and covariance of the estimated coefficients can be obtained from the second partial derivatives of the log-likelihood function.

$$\frac{\partial^2 L(\beta)}{\partial \beta_j \beta_k} = \sum_{i=1}^{n} x_{ij} x_{ik} t_i \left[s_i \lambda_i B_i + (1-s_i)\left(A_i h_i + t_i h_i^2\right)\right] \tag{12}$$

$j,k = 0,1,.....p$

$$B_i = \frac{(m-1)e^{-\lambda_i t_i}\left(1-\lambda_i t_i - e^{-\lambda_i t_i}\right)}{\left(1-e^{-\lambda_i t_i}\right)^2} \tag{13}$$

The inverse of the sample information matrix provides us with the estimators for the variance and covariance.

$$\hat{Var}\left(\hat{\beta}\right) = i\left(\hat{\beta}\right)^{-1} \tag{14}$$

where $i\ (\hat{\beta}) = -\frac{\partial^2 L(\beta)}{\partial \beta_j \beta_\kappa}$, given by the negative of equation (11), is a matrix evaluated at the estimated coefficients, $\hat{\beta}$.

Thus, the standard errors of the coefficients can be obtained from the square root of the elements on the main diagonal of the matrix given in equation (14).

Another way to obtain the parameter estimates, which is computationally faster is by using the fact that the exponential regression model can be written in a log-liner form with the error variable having extreme value density. Thus, if $z_i = exp(lnt_i - \beta' X_i)$, then the general form of the $(p+1)$ likelihood equations are as follows:

$$\sum_{i=1}^{n} x_{ij}\left[s_i A_i^* - (1-s_i)h_i^*\right] = 0 \tag{15}$$

$j=0,1,2,...,p$

The second partial derivatives of the log-likelihood function is

$$\frac{\partial^2 L(\beta)}{\partial \beta_j \beta_k} = \sum_{i=1}^{n} x_{ij} x_{ik} \left[-s_i z_i B_i^* + (1 - s_i)\left(A_i^* h_i^* + h_i^{*2} \right) \right] \tag{16}$$

$j, k = 0,1,...,p$

$$A_i^* = 1 - z_i + \frac{(m-1) z_i e^{-z_i}}{1 - e^{-z_i}} \tag{17}$$

$$B_i^* = 1 + \frac{(m-1) e^{-z_i} \left(-1 - z_i + e^{-z_i} \right)}{\left(1 - e^{-z_i} \right)^2} \tag{18}$$

$$h_i^* = \frac{f(z_i)}{1 - F(z_i)} \tag{19}$$

$$F(z_i) = (1\text{-}e^{-z_i})\, m \tag{20}$$

$$f(z_i) = m z_i (e^{-z_i})\, (1\text{-}e^{-z_i})^{m-1} \tag{21}$$

Describing the model using the extreme value distribution helps to simplify the implementation of the Newton-Raphson iterative procedures in Fortran or any other programming languages. It also converges faster and provides estimates that are more efficient than the log-linear exponential regression model. In this paper, all the results for the parameter estimates were obtained by using this model.

Numerical Procedures

In this paper, we used simulated data to study the performance of the parallel model with two covariates. The main focus is to observe the following:

i) The significance of the bias and standard error of the parameter estimates.
ii) How does the number of independent and identical parallel components in the system, m, effect the estimation procedure?
iii) How well this model handles the censoring in data and what the outcome of using different censoring proportions, c, is.
iv) Whether the efficiency and accuracy of the parameter estimates improve with the increase in sample size.

The simulation was performed to obtain 10,000 samples, each with the combinations of different m, n and c given below.

m = 2, 4, 6, 8
n = 20, 40, 60, 80, 100
c = 0.0, 0.1, 0.2, 0.3, 0.4, 0.5

Two covariates were used in the model. The first one was simulated from the Bernoulli distribution, to obtain a dichotomous or binary covariate and the other one was generated from the standard normal distribution using the Tieochew algorithm (Yakowitz 1977). The main reason for choosing these two covariates are due to the fact that they occur more regularly in applied settings especially in fields such as medicine and engineering. Details of the algorithm on the simulation of the Bernoulli variates and the Tieochew algorithm can be obtained from the Computational Probability and Simulation (Yakowitz 1977). The steps for the algorithms can be implemented easily using the Fortran programming language. Simulation of the main variable of interest, time, was performed by using the cumulative distribution function technique. Using the equation of $F(z_i) = (1\text{-}e^{-z})\,m$, we can obtain the ln t_i's from the parallel model given in equation (15). The initial values of the all the parameters were, β_0, β_1, $\beta_2 = 1$, then

$$\ln t_i = \beta' x_i + ln(-ln(1\text{-}U) \qquad (22)$$

After the variable of interest, time, has been simulated, the effect of censoring can be imposed on them to see how this model performs when data is censored. The data was censored by using Type II censoring, where only r smallest observations out of the n were observed and the rest were censored at the r^{th} sample failure time.

Numerical Results

We can clearly see from *Figs. 1-6* and Tables 1 and 2 that both the bias and standard error of all the parameter estimates, $\hat{\beta}$, seem to increase with the increase in the censoring proportion, c. The bias is the lowest when there is no censoring in our data but increases drastically when c is 0.1. The rate of the increase in the bias is very low when c is between 0.1 and 0.3 but higher when c is more than 0.3. Increase in the number of parallel components, m, however, seems to reduce the bias and standard error of the estimates.

Some of the numerical results obtained for the biases and standard errors are given in Table 1, Table 2 and Table 3.

All biases and standard error estimates reduce with the increase in sample size. None of the bias are significant at $\alpha = 0.05$ level of significance as can be seen from the T statistic in Table 3, even though their value tends to be very high when c=0.5.

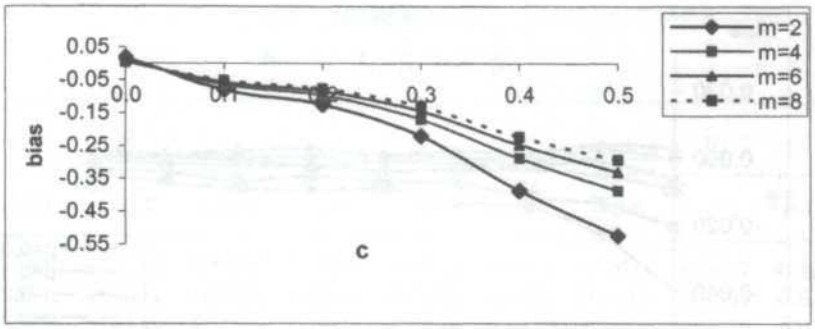

Fig. 1: Bias of $\hat{\beta}_0$ versus censoring proportion, n = 40

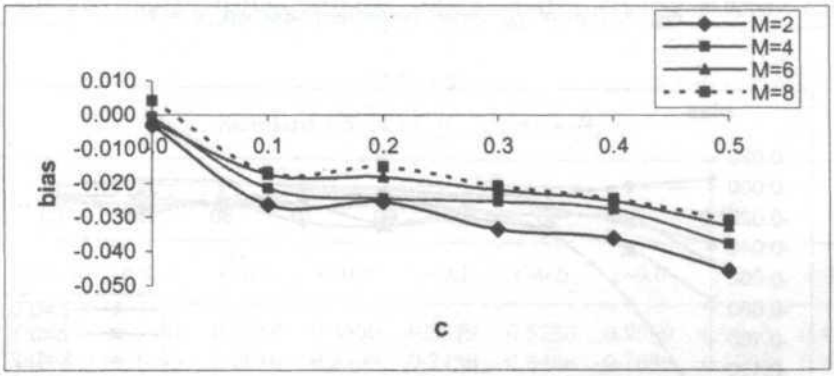

Fig. 2: Bias of $\hat{\beta}_1$ versus censoring proportion, n = 40

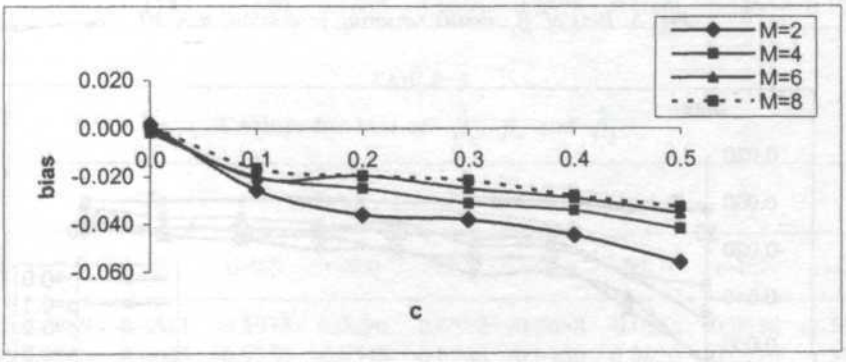

Fig. 3: Bias of $\hat{\beta}_2$ versus censoring proportion, n = 40

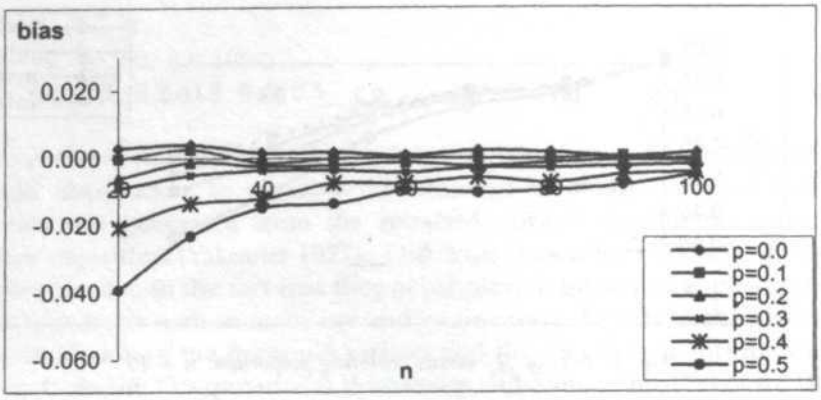

Fig. 4: Bias of $\hat{\beta}_0$ versus censoring proportion, n = 40

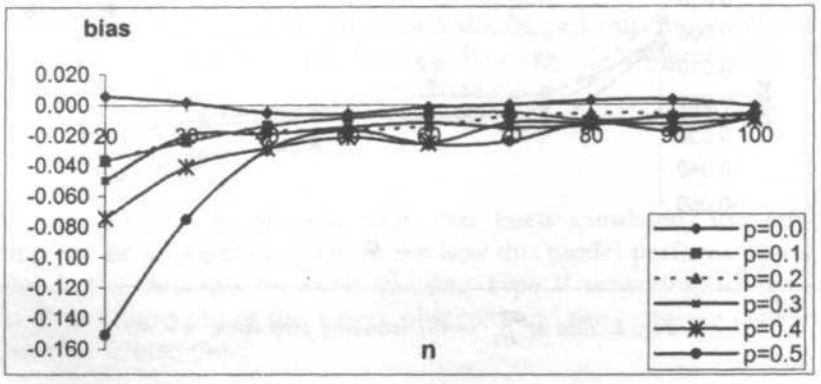

Fig. 5: Bias of $\hat{\beta}_1$ versus censoring proportion, n = 40

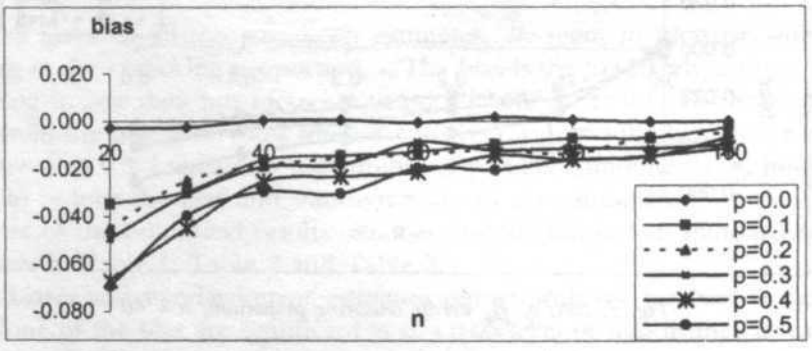

Fig. 6: Bias of $\hat{\beta}_2$ versus censoring proportion, n = 40

TABLE 1

Bias of $\hat{\beta}_0$, $\hat{\beta}_1$ and $\hat{\beta}_2$

		$\hat{\beta}_0$			$\hat{\beta}_1$			$\hat{\beta}_2$		
n	m	c=0.0	c=0.1	c=0.5	c=0.0	c=0.1	c=0.5	c=0.0	c=0.1	c=0.5
20	2	0.0349	0.0268	-0.0430	0.0024	-0.0592	-0.0894	-0.0012	-0.0607	-0.1094
	6	0.0111	0.0031	-0.0448	-0.0018	-0.0369	-0.0451	0.0012	-0.0391	-0.0797
30	2	0.0225	0.0135	-0.0246	-0.0008	-0.0385	-0.0593	-0.0006	-0.0429	-0.0707
	6	0.0076	0.0031	-0.0241	-0.0005	-0.0233	-0.0459	0.0017	-0.0248	-0.0509
40	2	0.0177	0.0099	-0.0202	-0.0030	-0.0265	-0.0458	0.0017	-0.0258	-0.0563
	6	0.0046	0.0018	-0.0188	-0.0022	-0.0174	-0.0328	0.0000	-0.0208	-0.0359

TABLE 2

Standard errors of $\hat{\beta}_0$, $\hat{\beta}_1$ and $\hat{\beta}_2$

		$\hat{\beta}_0$			$\hat{\beta}_1$			$\hat{\beta}_2$		
n	m	c=0.0	c=0.1	c=0.5	c=0.0	c=0.1	c=0.5	c=0.0	c=0.1	c=0.5
20	2	0.2567	0.2661	0.3218	0.3600	0.3879	0.5236	0.2550	0.2845	0.4264
	6	0.1634	0.1695	0.2010	0.2303	0.2436	0.3488	0.1635	0.1763	0.2690
30	2	0.2029	0.2072	0.2471	0.2866	0.3052	0.4230	0.1963	0.2169	0.3163
	6	0.1319	0.1340	0.1541	0.1858	0.1934	0.2719	0.1294	0.1416	0.2084
40	2	0.1716	0.1764	0.2119	0.2453	0.2591	0.3619	0.1661	0.1856	0.2635
	6	0.1123	0.1138	0.1320	0.1603	0.1666	0.2323	0.1082	0.1191	0.1745

TABLE 3

T values for bias of $\hat{\beta}_0$, $\hat{\beta}_1$ and $\hat{\beta}_2$

		$\hat{\beta}_0$			$\hat{\beta}_1$			$\hat{\beta}_2$		
n	m	c=0.0	c=0.1	c=0.5	c=0.0	c=0.1	c=0.5	c=0.0	c=0.1	c=0.5
20	2	0.6089	0.4511	-0.5973	0.0296	-0.6829	-0.7638	-0.0214	-0.9536	-1.1474
	6	0.3030	0.0805	-0.9960	-0.0348	-0.6768	-0.5780	0.0330	-0.9916	-1.3247
	2	0.6068	0.3577	-0.5458	-0.0153	-0.6910	-0.7679	-0.0164	-1.0844	-1.2247
30	6	0.3153	0.1248	-0.8578	-0.0145	-0.6612	-0.9254	0.0722	-0.9575	-1.3376
	2	0.6522	0.3540	-0.6040	-0.0762	-0.6466	-0.8004	0.0654	-0.8792	-1.3505
40	6	0.2590	0.0994	-0.8986	-0.0885	-0.6601	-0.8935	-0.0016	-1.1035	-1.2997

CONCLUSION AND SUGGESTIONS

In general, the results obtained show that the parallel model with two covariates work extremely well especially when data has low censoring proportion, between 0.1-0.3, high m, $m \leq 4$ and sample size at least more than 30. These conditions seem to generate the best set of estimated parameters, with high efficiency and low bias.

The model is less efficient when censoring proportion is too high, usually more than 0.4, m is low, m=2 and small sample sizes. These conditions seems to generate higher biases and standard errors even though none of the biases are significant at (=0.05 level of significance. Thus, it is valid to say that overall, the model is very effective, especially with moderately censored data and large sample sizes.

It is very common in statistics to develop a model based on several conveniently made assumptions. One of such assumptions made in this paper is that the parallel components are functioning independent of each other. As we would have already expected, most of these assumptions will not be suitable when dealing with real data. There are cases where failure of one component may affect the hazard rate of the remaining component, for example kidney failures in the human body.

Apart from that, in this research we were merely concerned in analyzing the performance of the parallel model with censored data and two covariates. There are still several unanswered questions, for example how the model would work if the number of covariates were to be larger than 2.

Thorough investigations on the covariates are extremely necessary, particularly when a large number of covariates is involved. This is due to the fact that some of the covariates might be significantly correlated with each other and decisions such as to exclude or include those needs need to be carefully examined before going further with the analysis.

Apart from that, is also very important to check whether the covariates included in our model have the ability to change over time since the model we discussed does not account for time varying covariates and inclusion of such variables might cause serious error in model fitting.

We should also bear in mind that all the results presented in this paper were obtained from simulated data, which could appear to be rather perfect sometimes. When dealing with real data, the outcome might not be as pleasant due to several factors concerning the data, for example, outliers, heteroscedastisity and missing values. Our current model doesn't automatically deal with these types of data but this might be an interesting area for further research.

Since the parameter estimates and standard error calculations were based on the maximum likelihood method (MLE), it is rather critical that we check further on the validity of these calculations. We know that the MLE method depends heavily on asymptotic properties, thus, for moderate and small sample sizes, the estimates and standard error calculations may not be particularly

good. Therefore, it is important that we obtain alternative ways of calculating the standard errors, especially those methods that do not rely on many assumptions, such as the Bootstrap and Jacknife and compare them with the standard error calculations from the MLE method. Thus, this research would provide a great opportunity for further work by upcoming researchers.

REFERENCES

BAIN, L. J. 1978. *Statistical Analysis of Reliability and Life -Testing Models.* New York: Dekker.

BAKLIZI, A. 1997. Likelihood inference in parallel systems regression models with censored data. Doctoral Dissertation, Universiti Putra Malaysia.

BALAKRISHNAN, N. 1995. *Recent Advances in Life Testing and Reliability.* CRS Press.

BASU, A. and A. EL-MAWAZINY. 1978. Estimates of reliability of k-out-of-m structures in the independent exponential case. *JASA* **73:** 850-854.

BRESLOW, N. 1974. Covariance analysis of censored survival data. *Biometrics* **30:** 139-156.

BYAR, D. P. 1974. Selecting optimum treatment in clinical trials using covariate information. Presented at *Annual Meeting of the American Statistical Association.*

EFRON, B. and R. TIBSHIRANI. 1993. *An Introduction to the Bootstrap.* London: Chapman and Hall.

ELANDT-JOHNSON, R. and N. JOHNSON. 1980. *Survival Models and Data Analysis.* New York: Wiley.

FEIGL, P. and M. ZELEN. 1965. Estimation of exponential survival probabilities with concomitant information. *Biometrics* **21:** 826-838.

GLASSER, M. 1967. Exponential survival with covariance. *Journal of the American Statistical Association* **62:** 561-568.

HAMADA, M. and S. TSE. 1989. When do estimates exist from censored data in industrial experiments. IIQP Research Report RR-89-3.

HOSMER, D. W. and S. LEMESHOW. 1999. *Regression Modeling of Time to Event Data.* New York: Wiley.

KALBFLEISH, J. and R. PRENTICE. 1980. *The Statistical Analysis of Failure Time Data.* New York: Wiley.

KECECIOGLU, D. 1991. *Reliability Engineering Handbook.* **1.** New Jersey: Prentice Hall.

KECECIOGLU, D. 1991. *Reliability Engineering Handbook.* **2.** New Jersey: Prentice Hall.

LAWLESS, J. 1983. Statistical methods in reliability. *Technometrics* **25:** 305-316.

LEE, E. 1992. *Statistical Methods for Survival Data Analysis.* New York: Wiley.

MANN, N., R. SCHAFER and N. SINGPURWALLA. 1974. *Methods for Statistical Analysis of Reliability and Life Data.* New York: Wiley.

YAKOWITZ, S. 1977. *Computational Probability and Simulation.* Addison Wesley, Reading, Mass.

Pertanika J. Sci. & Technol. 12(2): 277 - 290 (2004)
ISSN: 0128-7680

Comparative Evaluation of Composite Forecasting Methods: A Case Study

[1]Abu Hassan Shaari Mohd Nor, [2]Fauziah Maarof & [3]Muslimah Simo
[1]Jabatan Statistik Ekonomi
Universiti Kebangsaan Malaysia,
43600 UKM Bangi, Selangor, Malaysia
E-mail: ahassan@pkrisc.cc.ukm.my
[2]Jabatan Matematik
Fakulti Sains dan Pengajian Alam Sekitar, Universiti Putra Malaysia,
43400 UPM, Serdang, Selangor, Malaysia
E-mail: fauziah@fsas.edu.upm.my
[3]TMnet Sdn. Bhd.
Cyberjaya, Selangor, Malaysia

Received: 19 December 2002

ABSTRAK

Beberapa kajian lepas telah menunjukkan bahawa kaedah telahan gabungan mengatasi sebarang kaedah telahan individu. Sepanjang tiga puluh tahun lalu, para penyelidik telah mencadangkan banyak teknik telahan komposit. Dalam kajian ini, lima kaedah telahan komposit dipertimbangkan dan teknik tersebut digunakan ke atas data hasil jualan TMnet. Kajian menunjukkan kelima-lima kaedah menghasilkan nilai ramalan yang lebih baik berbanding kaedah individu yang terbaik, dan kaedah Dickinson menghasilkan punca min kuasa dua ralat (RMSE) terkecil.

ABSTRACT

A number of previous studies have shown that combinations of forecast method outperform any individual forecasts. During the past thirty years, researchers have proposed a wide variety of composite forecast techniques. In this study, five methods of composite forecast are considered and the techniques are applied on the TMnet sales data. The study shows that all the five methods give better prediction values compared to the best of individual methods, and amongst them, Dickinson's method produce the lowest Root Mean Square Error (RMSE).

Keywords: Combination of forecasts, combined forecast, individual forecast, forecast accuracy, root mean square error (RMSE)

INTRODUCTION

When two or more forecasts are available, one possibility is simply to select one of them. This choice could be based on the analyst's experience and judgement. However, very often it will not be possible to arrive at such a conclusion with any great confidence. Some guidance may be provided by historical data of competing approaches, so that the procedure that performed best in the recent past can be chosen. This is certainly an attractive possibility if a single forecast

can be chosen. However, the available data will be quite short so that it will be difficult to ascertain whether an apparently superior performance among the competing approaches is due to chance or an inherently better forecast-generating process.

Even if one has a high confidence that, for a given problem, a particular forecasting approach is likely to outperform its competitor, it does not necessarily follow that this approach should be used to the exclusion of the others. Two competing forecasts will generally be based on different assumptions about the process generating the quantity to be forecasted. Therefore, even if one method is clearly superior, it may be possible to incorporate the information in the inferior forecast to produce a combined forecast that performs better than both individual forecasts.

The basic idea in combined or composite forecast is that instead of choosing a single forecasting method, it is more appropriate to consider aggregating information by generating forecasts from several methods and then combining these forecasts (Makridakis and Winkler 1983). In this manner, the ultimate forecast should contain more information than when only one method is used. This could provide more accurate forecast and improved decisions based on these forecasts.

The work of Bates and Granger (1969) on combining forecasts has made other researchers construct several different schemes. Crane and Crotty (1967), Reinmuth and Geurts (1976) and Granger and Ramanathan (1984) propose, for instance, the use of regression methods for combining several different forecasts. In theory the best forecasting model makes use of all available information, but this ideal model never exists in practice (Granger and Newbold 1977). In the situation where different systematic techniques are applied to the same time series, the premise of composite forecasting model is to extract different predictive factor from the same data (Nelson 1973).

As Bates and Granger (1969), Newbold and Granger (1974), and De Menzes, Bunn and Taylor (2000) have demonstrated, combining the forecast of different models usually yields prediction that is more accurate than either (or any) of the separate predictions. Hence, the most important motive to combine forecasts from different models is the fundamental assumption that the true process cannot be identified exactly, but different models play a complementary role in the approximation of the data-generating process.

In the first part of this paper, four individual forecasting models for the TMnet sales data were developed using naïve method, double moving average, double exponential smoothing, and ARIMA Box and Jenkins method with intervention adjustment. In the next section five techniques of combining forecasts ranging from Equal Average Method, Dickinson's method, Granger and Ramanathan's Ordinary Regression Based Weight, Weighted Inversely proportional to Sum of Square and Least Absolute Value (LAV) Regression method were considered. A study to compare the accuracy of forecasts between individual and combined forecasts is also given. Three criteria for assessing the accuracy of both individual and combined forecasts are used.

METHODOLOGY

Individual Forecasts

Four different individual forecasting models are used on TMnet data and the one-step ahead forecasts are produced. The models used are as follows:

1. Naïve model

$$\hat{Y}_{t+1} = Y_1$$

2. Double Moving Average of length nine, for a p- step ahead forecast

$$\hat{Y}_{t+p} = 2SMA_t - DMA_t + p * \left(\frac{SMA_t - DMA_t}{4} \right)$$

where SMA_t denotes single moving average

3. Double Exponential Smoothing, at time t for a p- step ahead forecast

$$\hat{Y}_{t+p} = \hat{T}_t(t) + p * \hat{B}_1(t)$$

where $\hat{T}_t = \hat{Y}_t(t-1) + 1.526e_t$

denotes the updated 'permanent component'

$$\hat{B}_1(t) = \hat{B}_1(t-1) + 1.526 * 0.009e_t$$

denotes the updated 'trend component'

$$e_t = Y_t - \hat{Y}_t(t-1)$$

and e_t is the one-step-ahead forecast error, while the values 1.526 and 0.009 refer to the smoothing constants. Please refer to Bowerman and O'Connell (1993) for further details.

4. ARIMA (1,1,0) with intervention adjustment

$$(1 - \varphi_1 B)\ \Delta Y_t = \mu + \beta_1 D_1 + \beta_2 D_2 + a_t$$

where B is the backshift operator,
ΔY_t is the first difference of TMnet sales data,

D_1 and D_2 are dummy variables assigned to observation 39 and 40 (intervention periods), respectively,
and a_t is white noise series.

Combined Forecasts

Five techniques for combining the four individual forecasts are presented in this section. Data from TMnet is used to obtain and evaluate the forecast values using the five techniques discussed below.

1. Equal Average Method

One of the best known and simplest methods of combining forecasts is the simple average approach. With this method, a combined forecast for period t (denoted by F_t) is generated by taking the arithmetic mean of two or more component forecasts for period t. Suppose we have f_1, f_2, ..., f_p, a set of p individual forecasting techniques. Then the combined forecast is given by

$$F_t = \sum_{i=1}^{p} \frac{f_i}{p} \tag{1}$$

where f_i a forecast obtained using the i^{th} individual forecasting technique and p is the number of individual forecasts to be combined. In this study, there are four individual forecasts namely Naïve, Double Moving Average (DMA), Double Exponential Smoothing (DES) and ARIMA. For p= 1,2,..,4 we took all the ${}^4C_p$ possible combinations of forecasting method and the average forecast value for each combination is calculated using Equation (1). This approach does not take into account the relative accuracy of the individual method.

2. Dickinson's Weighted Average Method

Dickinson (1972) extended the technique due to Bates and Granger (1969) to more than two individual forecasts. Let f_1, f_2, ..., f_n, be the individual forecasts. The Dickinson combining model can be written as follows

$$f_c = \sum_{i=1}^{n} w_i f_i \tag{2}$$

where w_i is the weighting factor for the i^{th} individual forecast and is calculated using the following formula

$$w = \Sigma^{-1} I_n (I_n \Sigma^{-1} I_n)^{-1}$$

where $w = (w_1, w_2, ..., w_n)'$ is an nx1 vector of weights, Σ is nxn covariance matrix of the individual forecast errors and $I_n = (1,1,...,1)'$.

Bates and Granger and Dickinson have proven that the minimum error variance of the combined forecast, $\sigma^2_{(c)} = (I_n \Sigma^{-1} I_n)^{-1}$ is always less than min ($\sigma^2_{(1)}$, $\sigma^2_{(2)}$,..., $\sigma^2_{(n)}$). This makes the combined forecast attractive.

3. Regression Weights

The third method of combining individual forecasts that is considered is by using regression weights. The approach by Granger and Ramanathan(1984) for using regression-based weights is given by

$$X_t = \alpha + \beta_1 f_{1t} + \beta_2 f_{2t} + \ldots + \beta_k f_{kt} + \varepsilon_t \quad (3)$$

where $\alpha,\beta_1,\ldots\beta_k$ are the regression parameters that are used as weights in combining the individual forecast, f_{1t},..., f_{kt}.

The regression model in Equation (3) is estimated using the Ordinary Least Square (OLS) method yielding the following regression equation estimate

$$\hat{X}_t = \hat{\alpha} + \hat{\beta}_1 f_{1t} + \ldots + \hat{\beta}_k f_{kt} \quad (4)$$

Hence, the values for the combined forecasts using regression weights are obtained by putting the estimated regression parameters into Equation (4). A general model of regression combined forecast is as follows

$$f_c = \alpha + \beta_1 f_1 + \beta_2 f_2 + \ldots\ldots + \beta_n f_n + \varepsilon \quad (5)$$

where f_c denotes the combined forecast, f_i denotes the individual forecast, and α and β_i are the regression coefficients. The estimates of α and β_i denoted as a and b are obtained by regressing the actual values (y_t) with the individual forecast, f_i using equation

$$b = (X' X)^{-1} X' y$$

where X is the matrix of individual forecast, b is a vector of estimates and y is the vector of actual values.

4. Weighted Inversely Proportional to Sum of Square (WIPS)

Let X_{t-j} be the original observation at time t-j and f_{t-j} be the j^{th} one-step ahead forecast, then

$$e_{i,t-j} = X_{t-j} - f_{i,t-j} \qquad j = 1,\ldots,n$$

is the error made in individual forecasting. The larger the magnitude of the errors made, the poorer the performance of a particular forecasting method. One way to assess the quality or accuracy of forecast is through the sum of squared forecast errors. These SSE for k individual forecast methods over the last n observations are given by the following equation:

$$SSE_i = \sum_{j=1}^{n} \left(X_{t-j} - f_{i,t-j}\right)^2 = \sum_{i=1}^{k} \sum_{j=1}^{n} e_{i,t-j}^2 \quad (6)$$

Then the combined forecast is obtained by using the weight attached to forecasts from the k^{th} method inversely proportional to the sum of squared errors achieved by individual forecasts over the n most recent time periods. With some simplification, the weights can be written as:

$$w_i = \left(\sum_{j=1}^{n} e_{i,t-j}^2\right)^{-1} \Big/ \left[\left(\sum_{j=1}^{n} e_{1,t-j}^2\right)^{-1} + \ldots + \left(\sum_{j=1}^{n} e_{k,t-j}^2\right)^{-1}\right] \quad i = 1, 2, \ldots k \quad (7)$$

Hence, the combined forecast can be obtained using the equation shown below:

$$f_{ct} = w_1 f_{1t} + w_2 f_{2t} + \ldots + w_n f_{nt}, \text{ with } \sum_{i=1}^{n} w_i = 1 \quad (8)$$

5. Least Absolute Value (LAV) Regression

De Menzes *et al.* (2001) reported that the regression approach is an optimal model because it can give an unbiased combined forecast. However, Narula and Korhonen (1988) have argued that OLS regression model may not be the best regression approach in some instances. The OLS model "implicitly assumed that the loss function is proportional to the square of error and it is known that in many situations the quadratic loss function is inappropriate". The result of OLS is reported in term of relative percentage error, which is based on the absolute value of the ratio of the error term to the observed value. Thus, they concluded that it is more appropriate to consider loss function proportional to the absolute value of error rather than the squared of errors. They recommend that least absolute value (LAV) regression be considered as an alternative to OLS regression. LAV regression find coefficients and constant term that minimize the sum of absolute values of the error term of Equation (6). LAV is one of the robust techniques that reduce the effect of outlier/intervention on the estimates of the OLS.

Forecasting Performance Criteria

The criteria for a good forecasting model depends very much on how the model is able to reproduce the data that are already known. There are many criteria for measuring the accuracy of forecast but in this paper we are only considering Mean Square Error(MSE) or Root Mean Square Error (RMSE), Mean Absolute Percentage Error (MAPE) and Theil's U Statistics. If Y_t is the actual observation and f_t is the forecast value at time t, then

i) MSE $= \Sigma (Y_t - f_t)^2 / n$

ii) RMSE = sqrt(MSE)

iii) MAPE $= \Sigma |(Y_t - f_t) / Y_t| / n * 100\%$

iv) Theil's U = $\text{sqrt}\{\Sigma ((Y_{t+1} - f_{t+1}) / Y_t)^2 / (\Sigma ((Y_{t+1} - Y_t) / Y_t)\}$

Theil's U accommodates for large error and provides a relative comparison with the naïve method of forecasting. The smaller the U value, the better the formal forecasting method is relative to the naïve (base) method. The ranges of the U – statistics can be summarized as:

U=1 : the naïve method is as good as the formal forecasting techniques.

U<1 : the forecasting technique used is better than the naïve method. U>1 : the naïve method is better than the forecasting technique used.

Comparisons among the competing models are done using in-sample and out-of-sample statistics of the above mentioned criteria. Four data points are allocated for the out-of-sample analysis (validation).

CASE STUDY

Competition within the Internet service provider (ISP) in Malaysia has increased dramatically during the past two years especially with the increase in the number of competitors. The first Internet service was provided by Jaring. In 1996 Telekom Malaysia launched its Internet service to the public. Ensuring a good service to stay competitive in the market is actually started with good planning that relates to a reliable demand forecast. This is where the importance of reliable and accurate forecast plays its role.

Data Source

All the four individual methods and five composite forecast methods are applied to monthly sales data from August 1997 to August 2001 provided by TMnet Bhd. The series consists of 49 observations and is plotted in *Fig. 1.* From the time plot, it can be seen that the series is not a "well behaved" series.

Stage 1: Development of the individual forecast

Preliminary study shows that the series has a linear trend and has no seasonal effect. Two peak values (intervention) are also detected in the data set. The analysis begins with the naïve forecast which uses the most recent observation as a forecast for the subsequent values of the series. A search to determine the smoothing constant for double exponential smoothing with trend adjustment was done to ensure the greatest accuracy. Double moving average is considered to handle the existence of linear trend. Finally, the Box and Jenkins model with

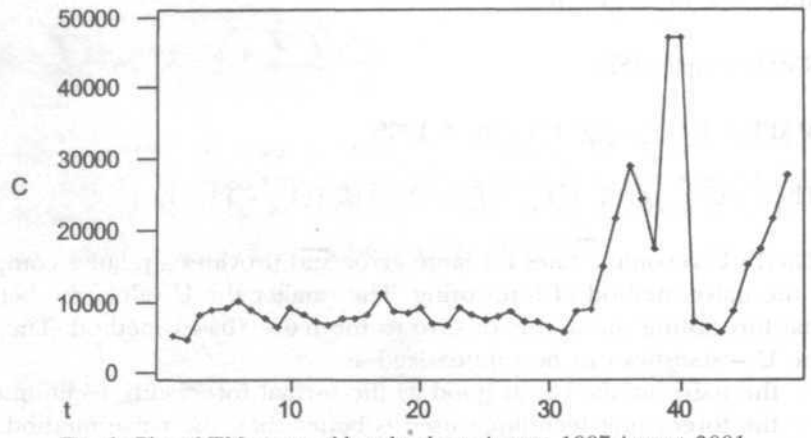

Fig. 1: Plot of TMnet monthly sales data; August 1997-August 2001

an adjustment on the interventions (two peak values) is also used. All the four individual forecasting models used in the next stage is significant at the 5% level.

Stage 2: Development of the composite forecasts

Each model developed in Stage 1 was used to fit the series of monthly sales data using methods described earlier. The best model in Stage 1 using the suggested criteria is then used as the benchmark of the performance of the composite forecast method.

RESULTS AND DISCUSSION

The Individual Forecast

Table 1 below gives the two forecasting accuracy criteria for four individual forecasting methods. Among the individual forecasts, the Box-Jenkins ARIMA(1,1,0) with intervention adjustment appears to be the best model as indicated by the lowest RMSE. This is supported by the lowest value of Theil's U statistics which is 0.886.

The simplest method (naïve) slightly outperformed the DMA. However, DMA is still considered in the composite forecast to show that even the worst model contributes to the improvement of the composite forecast. The rank of the forecast performance (in descending order) is ARIMA(1,1,0), DES, and lastly DMA.

TABLE 1
Accuracy of individual forecasting methods (NAÏVE as the benchmark)

CRITERIA	NAÏVE	DMA	DES	**ARIMA**
RMSE	10843	11976	10493	**9603**
THEIL'S U	1.0	1.104	0.968	**0.886**

Comparison between the Individual and Composite Forecast Models

The main aim in forecasting is to produce forecasted figures with high accuracy and reliability. This section is important because it evaluates the worthiness of doing extra jobs in forecasting activities, which can be done by comparing the forecast accuracy of the composite methods to the individual methods. Theil's U statistics fit this purpose to compare the 'best' and the 'worst' of individuals to the composite models and the result is given in Table 2. ARIMA (1,1,0) with intervention adjustment is the 'best' among the individual methods while DMA is the 'worst'.

TABLE 2
Theil's U statistics of composite forecast models

Composite Method	Theil's U statistics (Compared to ARIMA)	Theil's U statistics (Compared to DMA)
Equal Weight	0.74	0.6
Dickinson	**0.73**	**0.59**
Regression	0.95	0.76
WIPS	0.86	0.69
LAV	0.83	0.67

Table 2 shows that the composite forecast is superior to the 'best' of individual methods. The result is more pronounced when Dickinson's method is used. This indirectly implies that the composite forecasts outperform other individual methods. The use of OLS regression-based weight was somewhat less successful. Another way of accessing the accuracy of the composite forecasts is by calculating the percentage improvement gained in terms of RMSE and MAPE. Table 3 summarizes the percentage improvement gained from the composite forecast, both for in-sample and out-of-sample (based on the last four observations).

The results in Table 3 show that maximum improvement gained was 36% in reducing MAPE and 28% in reducing RMSE from in-sample perspective. In terms of out-of-sample performance, the percentage gain RMSE and MAPE are 24% and 14%, respectively. These percentage improvements are considered significant as more accurate forecast values will lead to better business planning and strategy.

Evaluation of Forecasting Accuracy for the Composite Method

For the overall comparisons among all the methods, the following ranking procedure is adopted:

A rank of 1 is given to the best composite method, and a rank of 5 to the worst. Both in-sample and out-of-sample performances are evaluated. Table 4 gives the summary of the ranking process.

TABLE 3
In-sample percentage improvement gained by composite forecast methods

Composite Method	% improvement in RMSE as compared to ARIMA		% improvement in MAPE as compared to ARIMA	
	In-sample	Out-of-sample	In-sample	Out-of-sample
Equal Weight	26%	18%	5%	none
Dickinson	**28%**	**11%**	**17%**	**9%**
Regression	5%	11.1%	16%	none
WIPS	14%	none	16%	14%
LAV	17%	24%	36%	%

TABLE 4
Total points obtained by composite forecast models

Composite Method	In-sample	Out-sample
	Rank	Rank
Equal Weight	3	4
Dickinson	**1**	**2.5**
Regression	5	5
WIPS	4	1
LAV	2	2.5

In terms of in-sample forecast performance, the Dickinson's composite method outperforms the other four methods. LAV Regression appears second, followed by Equal Weight method, while OLS Regression is in the last position. In terms of out-of-sample forecast performance (based on four observations), composite method using WIPS is the best. Dickinson's and LAV Regression are both equally good at second place, while Regression method has the lowest rank.

Comparing OLS Regression with LAV Regression, the difference in forecast accuracy is quite significant. One possible explanation is that LAV Regression can be written as a linear programming model and therefore the sensitivity analysis can be used to determine the effect of an outlier or intervention on model parameter. When intervention exists in the data set, LAV is capable of giving better prediction as compared to OLS Regression.

The superior performance of weights based on the inverse of the sum of square errors (WIPS) compared to OLS regression-based approach is consistent with the finding by Newbold and Boss (1973) and Bunn(1985). They concluded that the OLS regression-based approach is likely to be preferable when one or more of the individual methods is inferior to the other. In such cases, it is better to discard the inferior forecast when using OLS regression. Another

possibility is OLS regression-combined forecast is subject to instability of weighting factor due to collinearity.

Forecast of Future TMnet Sales

The results shown in Table 2, Table 3 and Table 4 suggest that the Dickinson's composite forecast is the superior method. Hence, using the Dickinson's composite forecast method, the 14-months ahead point forecast of TMnet sales for the period from September 2001 to October 2002 is calculated and presented in Table 5. The plot of these forecasts is presented in *Fig. 2.* The forecasted values show an upward trend, indicating that the TMnet sales are expected to have a positive growth.

TABLE 5
Forecast of TMnet sales account

Month	Year 2001	Year 2002
	Dickinson	Dickinson
January	-	37475
February	-	38530
March	-	39585
April	-	40640
May	-	41694
June	-	42749
July	-	43803
August	-	44858
September	28939	45912
October	33056	46967
November	35365	-
December	36421	-

CONCLUSION

As clearly indicated by the Theil's U statistics, Root Means Square, and MAPE, all of the five composite forecast methods outperform the best of the individual forecast. Applying the five composite forecast methods to the TMnet sales data result in the following rank (descending order) in terms of forecast accuracy.

1. Dickinson's Method
2. Weighted Inversely proportional to SSE
3. Equal Weight
4. LAV Regression
5. OLS Regression

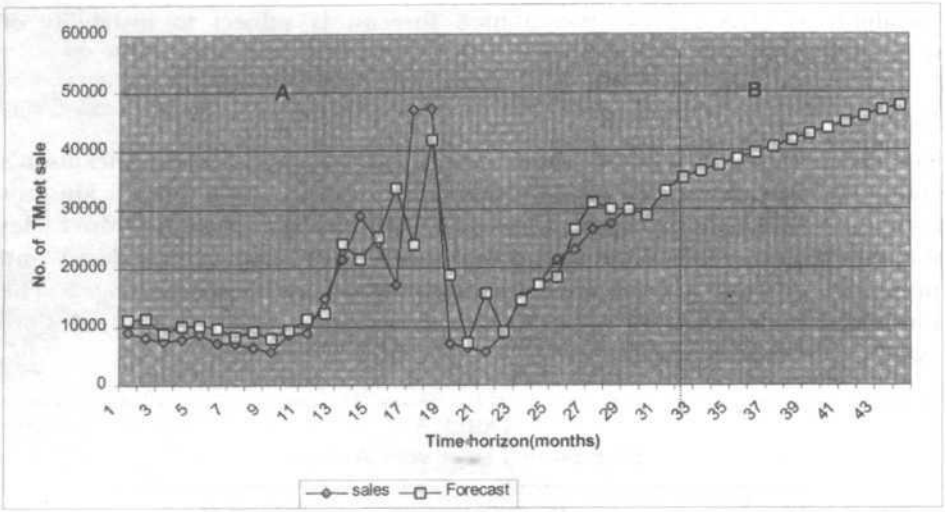

Fig. 2: Plot of Dickson's composite forecasts
(Note: A - Estimation period B - Forecast horizon)

In conclusion, the composite forecast method has improved the forecast accuracy of the TMnet sales data from the lowest of 5 percent to the highest of almost 30 percent.

REFERENCES

BATES, J.M. and C.W. GRANGER. 1969. The combination of forecast. *Operational Research Quarterly* **20:** 451-468.

BOWERMAN, B. L. and R. T. O'CONNELL. 1993. *Forecasting and Time Series: An Applied Approach.* 3rd edition. Duxbury Press.

CLEMEN, R. T. and R. H. WINKLER. 1992. Sensitivity of weights in combining forecast. *Operational Research* **40(3)** May-June.

CRANE, D. B. and J. R. CROTTY. 1967. A two-stage forecasting model: exponential smoothing and multiple regression. *Management Science* **13B:** 501-507.

DE MENZES, L., D. BUNN and J. TAYLOR. 2000. Review of guidelines for the use of combined forecast. *European Journal of Operational Research* **120:** 190-204.

GAYLORD, J.M. and M.S. JOANNE. 2001. An LAV methodology for forecast combination in service forecasting. *Production and Operations Management Society*, POM – 2001, March 30-2001.

GRANGER, C.W.J and P. NEWBOLD. 1977. *Forecasting Economic Time Series.* London: Academic Press.

GRANGER, C. W. J and R. RAMANATHAN. 1984. Improved methods in combining forecast. *Journal of Forecasting* **3:** 197-204.

MAKRIDAKIS, S. and R. L. WRINKLER. 1983. Averages of forecast: some empirical result. *Management Science* **29:** 987-996.

NARULA, S. and P. KORHONEN. 1994. Multivariate multiple regression based on the minimum sum of absolute error criterion. *European Journal of Operational Research* **73:** 70-75.

NELSON, C.R. 1973. *Applied Time Series for Managerial Forecasting.* San Francisco: Holden-Day.

NEWBOLD, P. and C. W. J. GRANGER. 1974. Experience with forecasting univariate time series and the combination of forecasts. *Journal of Royal Statistical Society A* **137:** 131-165.

NEWBOLD, P. and T. Bos. 1994. *Introductory Business & Economic Forecasting.* Second edition. Cincinnati, Ohio: South-Western Publishing Co.

APPENDIX

Results from the Composite models

1. Equal Weights for p=4

$$f_c = 0.25^* \textit{Naive} + 0.25^* \textit{DES} + 0.25^* \textit{ARIMA}$$

2. Dickinson's Method

$$f_c = -0.526^* \textit{Naive} + 0.105^* \textit{DMA} + 0.789^* \textit{DES} + 0.0526^* \textit{ARIMA}$$

3. Regression weights

$$f_c = -2593.61 + 0.14^* \textit{Naive} - 0.322^* \textit{DMA} + 0.301^* \textit{DES} + 0.682^* \textit{ARIMA}$$

4. LAV Regression

$$f_c = -4068.98 + 0.459^* \textit{Naive} + 0.233^* \textit{DMA} - 0.043^* \textit{DES} - 0.00056^* \textit{ARIMA}$$

5. Weighted Inversely Proportional to SSE (WIPS)

$$f_c = 0.186^* \textit{Naive} + 55^* \textit{DMA} + 0.917^* \textit{DES} + 0.216^* \textit{ARIMA}$$

ISSN: 0128-7680
Pertanika J. Sci. & Technol. 12(2):291 - 294 (2004)

Microwave Dielectric Permittivity of Water from 10°C to 50°C - Tabulated

Jumiah Hassan, Kaida Khalid & W. Mohammad Daud Wan Yusoff
Department of Physics
Faculty of Science and Environmental Studies
Universiti Putra Malaysia
43400 UPM, Serdang, Selangor, Malaysia

Received: 19 December 2002

ABSTRAK

Sifat dielektrik air iaitu pemalar dielektrik dan faktor kehilangan dielektrik disenaraikan pada julat frekuensi 0.2 GHz - 20 GHz dan suhu 10°C - 50°C. Pengukuran dibuat dengan menggunakan penduga talian sepaksi terbuka di hujung dan penganalisis rangkaian automatik. Keputusan yang diperoleh dibandingkan dengan laporan yang terdahulu dan perbezaan $|\Delta\varepsilon'|$ adalah dalam lingkungan 0.1- 1.8 dan $|\Delta\varepsilon''|$ dalam julat 0.0 - 1.9.

ABSTRACT

The dielectric properties of water, namely the dielectric constant and the dielectric loss factor were tabulated in the frequency range of 0.2 GHz - 20 GHz and temperatures 10°C - 50°C. Measurements were made using the open-ended coaxial line sensor and automated network analyzer. Results obtained were compared with previous reports and the difference of $|\Delta\varepsilon'|$ is within 0.1- 1.8 and that of $|\Delta\varepsilon''|$ is in the range 0.0 - 1.9.

Keywords: Water, dielectric constant, dielectric loss factor, sensor, frequency, temperature

INTRODUCTION

The dielectric properties of a substance are interpreted in terms of its electric dipole moments, both permanent and induced. The water molecule, H_2O possesses a permanent dipole moment and polarizability. The dipole moment arises from a fixed positive and negative charge separated by a certain distance while polarizability is when additional dipole is induced by an electric field (Hasted 1973). The dielectric properties of a sample are represented by its complex permittivity $\varepsilon^* = \varepsilon' - j\varepsilon''$ where ε' is the dielectric constant and ε'' is the dielectric loss factor. At microwave frequencies, dipoles play an important role in determining the dielectric properties of a solution because how much it can be polarized determines the dielectric constant and how much energy is dissipated in the process contributed to the dielectric loss factor. A sample with more moisture has a higher dielectric constant whereas water (100% moisture) has the highest dielectric constant. Water is used as a reference or standard in measuring other solutions and it is one of the three standards used in calibrating the open-ended coaxial probe attached to the network analyzer (HP8720B).

The purpose of this paper is to collect the data on the complex permittivity of water in the microwave frequency which is scattered in various journals and reports, and present it in such a way for comparison or general reference purposes. The data which has been accumulated started with the early work of Cook (1952), Hasted and El Sabeh (1953), Buchanan and Grant (1955) and Pottel (1973) at frequencies 2.0 GHz to ~ 18 GHz and temperatures 10 to 50°C.

MATERIALS AND METHODS

In this study deionised water was used as the sample and dielectric measurements were made using a 4-mm open-ended coaxial line probe attached to an automated network analyzer and a computer. Standard calibration procedures (Krazewski *et al.* 1983) was employed which involved three standards: air, a metal short and deionised water. Water bath was used to warm the water as reported (Hassan *et al.* 1997). Measurements of the complex permittivity of water were made at 0.2 - 20 GHz and temperatures 2 - 50°C.

RESULTS AND DISCUSSION

The results of the dielectric permittivity obtained in this study and those previously reported are tabulated in Table 1. $|\Delta\varepsilon'|$ and $|\Delta\varepsilon''|$ are derived from the maximum difference from the results already reported and the experimental results. The maximum difference showed that $|\Delta\varepsilon'|$ is within 0.1 to 1.8 where the former refers to the difference in the results by Pottel (1973) at 25°C (17.23 to 17.43 GHz), Buchanan and Grant (1955) at 30°C (9.31 to 9.39 GHz) and Cook (1952) at 40°C (4.56 to 4.63 GHz) while the latter refers to the difference in the results by Pottel (1973) at 50°C (17.23 to 17.43 GHz). The maximum difference in $|\Delta\varepsilon''|$ is within 0.0 to 1.9. The 0.0 difference refers to the difference in the results by Pottel (1973) at 25°C (17.23 to 17.43 GHz) while 1.9 refers to the difference in the results by Pottel (1973) at 50°C (17.23 to 17.43 GHz). It can be seen that the experimental results obtained at 25°C gives the minimum of the maximum difference for both ε' and ε''. This suggests that at this temperature the water molecules are very stable with no extra thermal agitation introduced by heating and measurements are easily made with minimum errors involved. From these results, it is clear that the method of measuring the dielectric properties of water is reliable and this method could be employed to measure the dielectric properties of other solution samples.

CONCLUSION

The dielectric properties of water in the temperature range of 10°C to 50°C resulted in the difference of $|\Delta\varepsilon'|$ and $|\Delta\varepsilon''|$ within 0.1- 1.8 and 0.0 - 1.9 respectively compared to the works of Cook (1952), Hasted and El Sabeh (1953), Buchanan and Grant (1955) and Pottel (1973). This showed that the method employed is reliable and could be used to measure the dielectric properties of other solution samples.

TABLE 1
Microwave dieletric data for liquid H2O; Cook (1952), Hasted and El Sabeh (1953), Buchanan and Grant (1955), Pottel (1973) and Experimental

Temp. (°C)	Frequency (GHz)	Cook (1952)		Hasted and El Sabeh (1953)		Buchanan and Grant (1955)		Pottel (1973)		Experimental		Maximum $\Delta\varepsilon'_{literature} - \Delta\varepsilon'_{exp}$	
		ε'	ε''	ε'	ε''	ε'	ε''	ε'	ε''	ε'	ε''	ε'	ε''
10	2.97 to 3.25	79.4	17.5	79.3	19.4	-		-		78.9	18.0	0.5	1.4
	4.56 to 4.63	74.3	25.2	-		-		-		73.9	25.5	0.4	-0.3
	9.31 to 9.39	54.4	37.1	-		54.0	37.8	-		55.1	37.6	-1.1	-0.5
20	2.97 to 3.25	77.7	13.0	77.8	13.9	-		-		77.1	12.9	0.7	1.0
	4.56 to 4.63	74.0	18.8	-		-		-		74.2	18.9	-0.2	-0.1
	9.31 to 9.39	61.5	31.6	-		62.0	32.0	-		61.9	31.3	-0.4	0.7
25	17.23 to 17.43	-		-		-		45.8	36.1	45.9	36.1	-0.1	0.0
30	2.97 to 3.25	75.3	9.9	75.8	10.2	-		-		74.7	9.6	1.1	0.6
	4.56 to 4.63	73.1	14.6	-		-		-		72.8	14.3	0.3	0.3
	9.31 to 9.39	64.8	25.6	-		65.0	26.4	-		64.9	25.6	0.1	0.8
40	2.97 to 3.25	72.6	7.6	73.0	8.4	-		-		71.7	7.4	1.4	1.0
	4.56 to 4.63	70.7	12.0	-		-		-		70.6	11.2	0.1	0.8
	9.31 to 9.39	65.5	20.9	-		65.2	21.2	-		65.3	20.8	0.2	0.1
50	2.97 to 3.25	69.7	6.0	69.7	6.5	-		-		68.6	6.0	1.1	0.5
	4.56 to 4.63	68.5	9.4	-		-		-		67.8	9.0	0.7	0.4
	9.31 to 9.39	64.6	17.0	-		64.5	17.0	-		63.8	16.8	0.8	0.2
	12.47 to 12.50	-		-		-		61.5	21.4	60.3	20.8	1.2	0.6
	17.23 to 17.46	-		-		-		56.3	27.2	54.5	25.3	1.8	1.9

ACKNOWLEDGEMENTS

This work was supported by Universiti Putra Malaysia (UPM) research grant (50205-93-14). The authors wish to thank technical staff, En. Roslim Mohd., of Applied Electromagnetic Laboratory, Department of Physics for his invaluable help.

REFERENCES

BUCHANAN, T. J. and E. H. GRANT. 1955. *Brit. J. Appl. Phys.* **6**: 64.

COOK, H. F. 1952. A comparison of the dielectric behaviour of pure water and human blood at microwaved frequencies. *Brit. J. Appl. Phys.* **3**: 249.

HASSAN, J., K. KHALID and W. M. D. WAN YUSOFF. 1997. Microwave dielectric properties of hevea rubber latex in the temperature range of -30°C to 50°C. *Pertanika J. Sci. Technol.* **5(2)**: 179.

HASTED, J. B. 1973. *Aqueous Dielectrics.* London: Wiley.

HASTED, J. B. and S. H. M. EL SABEH. 1953. The dielectric properties of water in solutions. *Trans. Faraday Soc.* **49**: 1003.

KRAZEWSKI, A. 1983. Guidelines for measuring permittivity using open-ended coaxial line sensors and the HP 8410B automated network analyser. Laboratory Application Notes, Department of Electrical Engineering, University of Ottawa.

POTTEL, R. 1973. *Water. A. Comprehensive Treatise.* **11**. New York - London: Plenum Press.

Pertanika J. Sci. & Technol. 12(2): 295 - 310 (2004)
ISSN: 0128-7680

Synergic Extraction of Zirconium (IV) with the New Solvent Tri-iso-amyl Phosphate (TAP) and Thenoyltrifluoroacetone (TTA)

Syed Hadi Hasan
Department of Applied Chemistry,
Institute of Technology Banaras Hindu University,
Varanasi - 221 005, India
E-mail: hasanitbhu@yahoo.co.in

Received: 22 July 2002

ABSTRAK

Pengekstrakan Zr (IV) daripada larutan asid hidroklorik akueus dikaji secara mendalam dengan menggunakan tiga sistem pelarut yang berlainan dengan *thenoyltrifluoroacetone* (TTA), menggunakan pelarut baru dan yang disediakan secara asli *tri-iso-amyl phosphate* (TAP) dan akhir sekali campuran TTA dan TAP ke dalam benzene (vol/vol). Dengan demikian satu optimum 93.24% Zr (IV) diekstrak dengan 2.50% TTA dan satu ekstrak 95.50% Zr (IV) dapat dicapai dengan 18% TAP. Walau bagaimanapun, satu kesan sinergi yang signifikan diperhatikan walaupun apabila separuh kepekatan daripada dua bahan pengekstrak digunakan, iaitu satu campuran 1.25% TTA dan 8% larutan TAP diekstrak sebanyak 99.0% Zr (IV) daripada larutan HCI akueus. Bagi semua ketiga-tiga sistem di atas [Zr (IV)] dan [HCI] masing-masing dikekalkan pada 1.0 x 10-3 mol l-1 dan 7.70 mol l-1. Dapatan juga menunjukkan bahawa walaupun Zr (IV) membentuk bukan solvat apabila digunakan dengan TTA dan TAP secara berasingan, satu solvat yang bercampur 1:1 terbentuk apabila sistem campuran TTA-TAP digunakan. Sehubungan itu disimpulkan bahawa TTA bersekutu dalam bentuk tak disosiasinya dengan ion logam pusat Zr (IV). Pengolahan matematik ketiga-tiga sistem pengekstrakan menunjukkan bahawa nilai purata log Kex untuk ketiga-tiga sistem adalah 2.97 (TTA); 1.85 (TAP) dan 3.68 (sistem sinergi TTA-TAP). Dapatan juga menunjukkan bahawa nilai yang diperhatikan untuk sistem solvat yang bercampur adalah 9.31 kali lebih daripada nilai yang diber penilaian secara statistik untuk sistem pelarut yang bergabung.

ABSTRACT

The extraction of Zr (IV) from its aqueous hydrochloric acid solutions was investigated in detail, by using three different solvent systems viz., with thenoyltrifluoroacetone (TTA), using a new and indigenously prepared solvent tri-iso-amyl phosphate (TAP) and finally a mixture of TTA and TAP into benzene (vol/vol). Thus, an optimum of 93.24% Zr (IV) was extracted with 2.50% TTA and an extraction of 95.50% Zr (IV) could be achieved with 18% TAP. However, a significant synergic effect was observed even when half concentration of the two extractants were employed, i.e., a mixture of 1.25% TTA and 8.0% TAP solution extracted as much as 99.0% of Zr (IV) from its aqueous HCl solutions. For all the above three extraction systems [Zr (IV)] and [HCl] were maintained at 1.0x10-3 mol l-1 and 7.70 mol l-1 respectively. It has also been shown that whereas Zr (IV) forms a disolvate when used with TTA and TAP individually but a 1:1 mixed solvate is formed when the TTA-TAP

mixed system was used. It has further been concluded that TTA is associated in its undissociated form with the central metallic ion Zr (IV). The mathematical treatment of the three extraction systems has shown that the average value of log Kex for the three systems are 2.97 (TTA); 1.85 (TAP) and 3.68 (TTA-TAP synergic system). It has also been shown that the observed value for the mixed solvate system is 9.31 times more than the statistically evaluated value for the combined solvent systems.

Keywords: Synergic extraction, zirconium, TAP, TTA

INTRODUCTION

Zirconium metal has come into prominence because of its applications in the nuclear installations. However, the initial development of zirconium metallurgy was largely prompted by the requirement of an appropriate structural material for the core components for a UO_2-fuelled reactor. Zirconium and its alloy offer a potentially unique combination of attractive properties with respect to low neutron absorption, good ductility, strength and good corrosion resistance at high temperatures of water and are found to be best materials for fuel cladding and coolant nuclear reactors (Sundaram and Subramanyam 1986).

The hydrometallurgical techniques viz. the solvent extraction and ion exchange methods are generally employed for the recovery and purification of zirconium metal. Since ion exchange process suffers from certain disadvantages e.g. poisoning of the resistance, lately the solvent extraction techniques has come to the forefront specially for nuclear plant processing (Prakash and Sundaram 1956).

The term synergism implying the formations of a synergistic adduct has now become a rather well-established phenomenon in the solvent extraction of metals. Basically it refers to an enhancement of the extraction of a formally uncharged metal chelate formed with a ligand such as alkyl phosphoric acids, β-diketones, oximes, etc. and a neutral adduct with a coordinating solvent viz. organophosphorus esters, an alcohol, sulphoxide, heterocyclic base or a phenol (Taketatsu and Bauks 1966; Sekine and Dyrssen 1967a; Sekine and Dyrssen 1967b). The TTA complexes have shown an exceptionally large tendency to form adducts with various neutral ligands (Sekine and Dyrssen 1967a). It was also reported that ligand with a $\rightarrow$ P = O donor groups have larger adduct formation constant with the TTA chelate than with any other donor (Sekine and Dyrssen 1967b). Various extractions of Zr (IV) including the synergic extractions from aqueous acidic solutions have been reported in the literature from systems such as methyl-iso-butyl ketone (MIBK), tri-n-octyl phosphine oxide (TOPO) and n-tributyl phosphate (TBP) (Marcus and Kertes 1969; Nandi, Das and Bhattacharya 1983; Komatsu 1980).

The potentialities of the TAP solvent prepared by the researchers utilising an indigenous byproduct of the Indian Alcohol Industry have been reported during the past few years (Pandey and Rupainwar 1979; Jaiswal and Rupainwar 1984; Singh, Hasan and Rupainwar 1986; Hasan and Rupainwar 1987). Further, it was considered worthwhile to test the potentialities of this new solvent as an

extractant for the Zr (IV)-HCl-TTA-TAP system and the results are described in this paper.

MATERIALS AND METHODS

Preparation of Tri-iso-amyl Phosphate (TAP)

Fuel oil obtained from Indian Alcohol Industry was fractionally distilled and the fraction at 131°C was collected as isoamyl alcohol, which was redistilled. In a three-necked flask (1 l) 137 grams (3 moles) of pure and dried pyridine and 138 mL of benzene were dried over sodium wire. The reaction mixture was subjected to mechanical stirring at low temperature (-5°C). A total volume of 46 mL (1 mol) of dry phosphorus oxychloride (B.P. 107°C) was gradually and carefully added through a dropping funnel at such a rate (complete time of addition is nearly 8 hours) so that the temperature of the reaction mixture did not exceed 5°C. The reaction mixture was then refluxed for two hours, cooled and 200-300 mL water was added to it to dissolve the white precipitate of pyridine hydrochloride. The mixture was then transferred into a separating funnel and the organic layer containing mainly crude TAP was separated, washed several times with water and kept overnight over anhydrous sodium sulphate. Benzene and other unreacted materials were removed by distillation at low pressure (20 mm Hg) till the temperature of the evaporating vapours reached 90°C. The ester TAP was then collected at 160°c/4 mm Hg as a colourless liquid. Analysis of the product showed 58.5% C and 10.6% H compares with theoretical values of 58.4% C and 10.77% H for C15H33O4P. The density of 0.9476 and yield of 75% confirmed the purity of the ester. The TAP ester is freely miscible with all the common organic solvents.

TAP thus prepared was diluted with thiophene free benzene for the extraction experiment.

Preparation of Zr (IV) and Thenoyltrifluoroacetone Solution

The stock solution of Zr (IV) was prepared by dissolving zirconyl chloride (Analytical Grade) in 8 mol l^{-1} hydrochloric acid and used as such after desired and appropriate dilution.

Thenoyltrifluoroacetone solution was prepared by dissolving TTA (Analytical Grade) in benzene. Further, the solution was diluted by benzene for required concentration.

(i) Extraction Procedure

Extraction procedure has been investigated by the following three stages:
(i) Zr (IV) - HCl - TTA (benzene)
(ii) Zr (IV) - HCl - TAP (benzene)
(iii) Zr (IV) - HCL - TTA + TAP (benzene)

For all the above systems 15 mL of properly diluted extractant was equilibrated for 15 minutes with an equal volume of aqueous layer containing desired acidity but having no Zr (IV).

10 mL of this pre-equilibrated solvent was then equilibrated with an equal volume of an aqueous solutions containing 1.0 x 10-3 mol of Zr (IV).

There was no change in the volume of the two layers on standing. The concentration of the hydrogen ion in all these experiments was determined by potentiometric titration (Sandel 1958). It had also been previously ascertained that the diluent benzene itself does not extract Zr (IV) from its hydrochloric acid solutions.

(ii) Determination of Zr (IV) in Aqueous/Organic Layer

To the solution of Zr (IV) enough hydrochloric acid was added to make its acidity 0.5-mol l-1 when the overall solution would be finally diluted up to 25 mL. Then 5 mL of alcohol and 3.0 mL of quercetin (0.10% in ethyl alcohol) was added and the overall solution was made up to 25 mL in a volumetric flask. The absorbance of the solution was measured against reference solution at 440 nm with spectrophotometer [Spectronic-20 and SicoSpec-200GL] (Vogel 1978).

The Zr (IV) from the organic phase was back extracted by shaking the organic layer with several small portions of diluted HCl (1 mol l-1) solution till all the Zr (IV) was back extracted and the amount of Zr (IV) thus back extracted was determined by the above mentioned method.

(iii) Distribution Coefficient, D

The distribution ratio was determined experimentally as the ratio of the total amount of Zr (IV) in the organic and aqueous phases.

$$D = \frac{\Sigma[Zr]org}{\Sigma[Zr]aq} \tag{1}$$

Thus, the percentage extraction

$$\%E = \frac{Dx100}{D + V_w / V_o} \tag{2}$$

Where V_w is the volume of aqueous phase and V_o is the volume of organic phase.

RESULTS AND DISCUSSION

For the synergic system under investigation the extraction of Zr (IV) has been studied in three stage systems as stated in the extraction procedure. The discussion of the three systems, therefore, has also been presented separately in the following pages. Nevertheless, overall discussions of the systems, the synergic effect, the mathematical treatment and the evaluation of the extraction constants have also been given. The effect of various other parameters viz. acid concentration, extractant concentration, metal ion concentration and the diluents on the extraction system has also been discussed.

Extraction of Zr (IV) from Hydrochloric Acid Medium with TTA-Benzene

Thus in the first system viz. Zr (IV)-HCl-TTA (benzene) the key parameter is the initial hydrogen ion concentration of the aqueous phase maintained by the addition of hydrochloric acid.

However, the concentration of Zr (IV) for all the experiments was kept constant at 1.0x10-3 mol l-1 in view of the formation of polymeric and inextractable species at higher metal concentration (Maya and Bopp 1977).

To find out the optimum acidity for the extraction of Zr (IV), experiments were performed at an arbitrary and fixed TTA concentration of 2.0 (v/v) and varying the initial HCl concentration. The results revealed a proportional and gradual increase in the percentage extraction with a maximum of 90.31% extraction achieved at 7.70 mol l^{-1} HCl concentration. However, a further increase in the aqueous acidity beyond 7.70 mol l^{-1} shows a decrease in the percentage extraction which is attributed to the formation of inextractable anionic zirconium (IV) chloride complexes (Connick and McVey 1949; Bases and Mesmer 1976). Consequently, all subsequent experiments were performed at an initial acidity of 7.70 mol l^{-1}.

The solvation number of the extracted species was evaluated by investigating the effect of TTA on the distribution ratio of Zr (IV). Thus, experiments were performed at 7.70 mol l-1 acid concentrations by varying concentrations of TTA. The results summarized in Table 1 reveal that the maximum extraction

TABLE 1
Effect of variation of TTA concentration on the distribution coefficient (D) of Zr(IV) from aqueous hydrochloric acid solutions

[HCl] = 7.70 mol l-1
[Zr(IV)] = 1.0 x 10-3 mol l-1
vol. of aqueous layer = vol. of organic layer = 103 mL

S. No.	[TTA]%	Amount in 5 mL aliquot 10-2 mg		D	%E	*Log Kex
		[Zr(IV)]aq	[Zr(IV)]org			
1	0.50	29.23	16.38	0.56	35.89	2.97
2	0.75	20.18	25.43	1.26	55.75	2.97
3	1.00	14.34	31.27	2.18	68.55	2.96
4	1.25	10.02	25.59	3.55	78.02	2.98
5	1.50	07.58	38.03	5.01	83.36	2.97
6	1.75	05.57	39.74	6.76	87.11	2.97
7	2.00	04.69	40.92	8.71	89.70	2.95
8	2.25	03.73	41.88	11.22	91.81	2.96
9	2.50	03.08	42.53	13.80	93.24	2.96
10	2.75	03.08	42.53	13.80	93.24	-
11	3.00	03.08	42.53	13.80	93.24	-

* Average value of log Kex = 2.97 ± 0.0083.

of 93.24% was obtained at TTA of 2.5%. A plot of log D against log CTTA (*Fig. 1*) gives a straight line with a slope of nearly 2 indicating the association of two moles of TTA in the extracted moiety of Zr (IV).

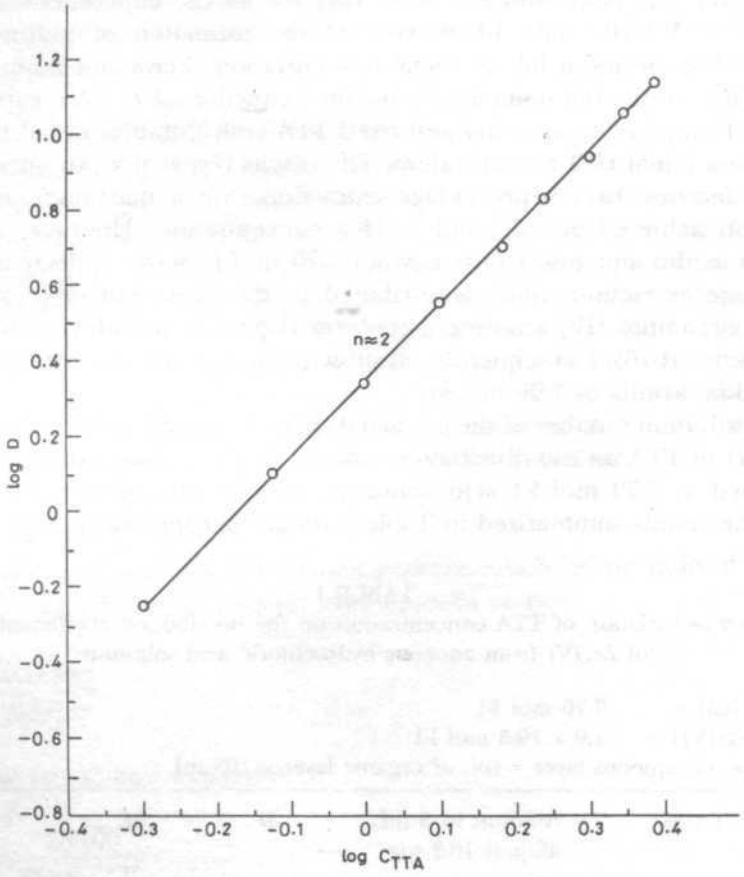

Fig. 1: Effect of variation of TTA concentration on the distribution coefficient (D) of Zr (IV) from its hydrochloric acid solutions [HCL] = 7.70 mol l^{-1} [Zr(IV)] = 1.0 ¥ 10^{-3} mol l^{-1}

It was predicted by earlier workers (Huffman and Beaufait 1949) that the TTA reacts in the dissociated form and the following equation represents the extraction process:

$$ZrCl_4 + 2HTTA \leftrightarrow (TTA)_2\ ZrCl_2 + 2HC_1 \qquad (3)$$

Further, it was also assumed by these workers that a proton was liberated from TTA molecule when the mixed complex extracted.

The fact that the percentage extraction increases on increasing the hydrogen ion concentration also indirectly rules out the possibility that the proton was being liberated from TTA or in other words TTA is combined with the metal

in an undissociated form. This observation is further substantiated by the literature reports for an analogous Ti (IV) extraction system (Komatsu1980; Stardy and Hladsky 1963).

Though for all these experiments benzene was used as a diluent, the role of other diluents such as carbon tetrachloride, toluene and chloroform was also investigated and it was found that maximum values of D are obtained when the non-polar benzene is employed as a diluent.

Extraction of Zr (IV) from Hydrochloric Acid Medium with TAP

Extraction of Zr (IV) from hydrochloric acid medium by TAP has been reported (Hasan and Rupainwar 1990).

However, the relevant and significant data is given in Table 2, which shows that an optimum of 95.5% Zr (IV) is extracted from its 1x10-3 mol l-1 aqueous hydrochloric acid solution by 18% TAP in benzene (v/v) at an acidity of 7.70

TABLE 2

Effect of variation of TAP concentration on the distribution coefficient (D) of Zr(IV) from aqueous hydrochloric acid solutions

[HCl] = 7.70 mol l-1
[Zr(IV)] = 1.0 x 10-3 mol l-1
vol. of aqueous layer = vol. of organic layer = 10 mL

S. No.	[TAP]%	Amount in 5 mL aliquot 10-2 mg		D	%E	*Log K_{ex}
		[*Zr*(IV)]aq	[*Zr*(IV)]org			
1	2.00	35.63	9.98	0.28	21.93	1.87
2	4.00	21.01	24.60	1.17	53.91	1.89
3	5.00	17.14	28.47	1.66	62.40	1.85
4	6.00	12.99	32.62	2.51	71.50	1.85
5	8.00	8.35	37.26	4.46	81.68	1.86
6	10.00	5.87	39.74	6.77	87.12	1.86
7	11.50	4.70	40.91	8.70	89.69	1.84
8	12.50	4.06	41.55	10.23	91.09	1.84
9	14.00	3.36	42.25	12.58	92.63	1.83
10	15.00	2.95	42.66	14.46	93.53	1.83
11	16.00	2.59	43.02	16.61	94.32	1.84
12	16.50	2.48	43.13	17.39	94.56	1.83
13	17.00	2.27	43.34	19.09	95.02	1.84
14	17.50	2.17	43.44	20.01	95.24	1.84
15	18.00	2.04	43.57	21.35	95.50	1.84
16	19.00	2.04	43.57	21.35	95.50	-
17	20.00	2.04	43.57	21.35	95.50	-
18	25.00	2.04	43.57	21.35	95.50	-

* Average value of log Kex = 1.85 ± 0.0161.

mol l^{-1}. The effect of diluents showed that the highest value of distribution ratio was obtained when non-polar benzene was used as a diluent.

The formula of the extracted moiety was evaluated by the slope of graph (log *CTAP* vs log D) and is $ZrCl_4$.2TAP (*Fig. 2*).

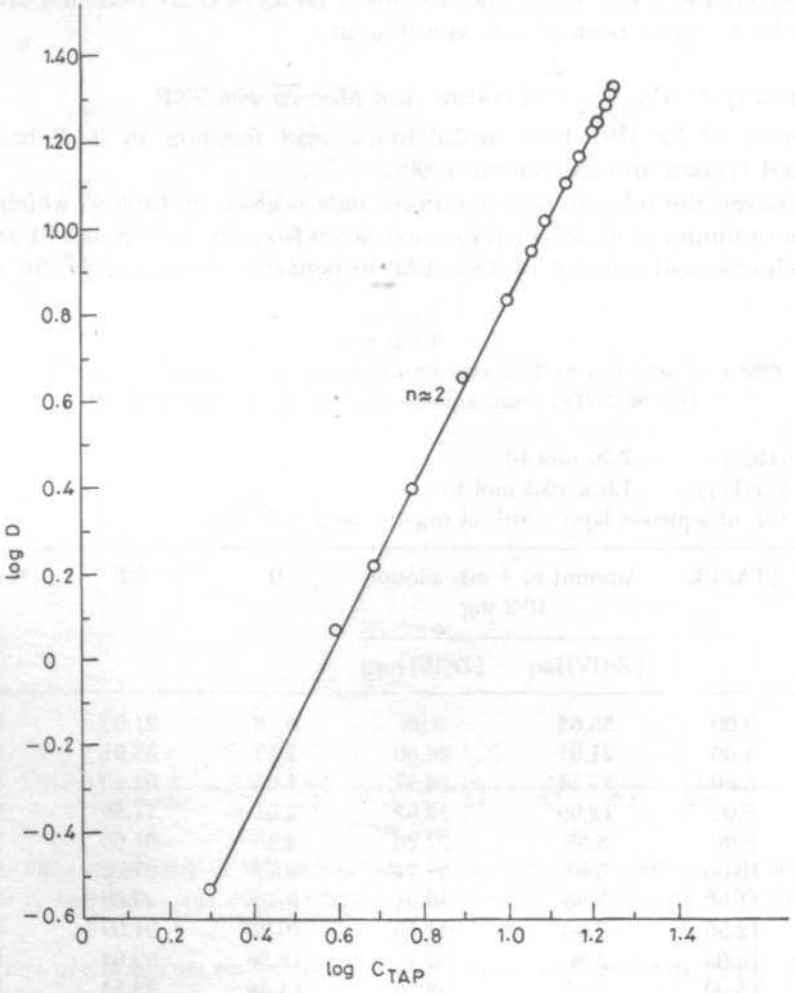

Fig. 2: Effect of variation of TAP concentration on the distribution ratio of Zr (IV) from its hydrochloric acid solutions [HCL] = 7.70 mol l^{-1} [Zr(IV)] = 1.0 ¥ 10^{-3} mol l^{-1}

The Synergic Extraction of Zr (IV) from Hydrochloric Acid with a Mixture of TAP and TTA

After establishing the extraction of Zr (IV) from hydrochloric acid medium in the presence of individual ligands viz. TAP and TTA, the extraction of Zr (IV) from hydrochloric acid medium was then performed by using a mixture of TAP and TTA so as to see the effect of the combined ligands. The acidity of the aqueous solution and the [Zr (IV)] were fixed at 7.70 mol l^{-1} and 1.0×10^{-3} mol

l^{-1} respectively in accordance with the earlier observations. Since the two extractants are being used, the concentration of one of the extractants was kept constant while varying the concentration of the other. Consequently, in the first series of experiments TAP was fixed at 5.0% (v/v) (in benzene) and the TTA concentration was varied from 0.5-1.5% (v/v). The results given in Table 3 show that 97.85% extraction of Zr (IV) was achieved even when the concentrations of TTA was 1.25%. At greater concentrations of TTA (>1.25%) the values of the distribution coefficient are leveled off. Thus, for further experiment TTA was fixed at 1.25% and TAP was varied in the range of 0.5 to 10.0%; the results given in Table 4 show that extraction increases significantly, i.e., up to 99.0% at TAP concentration of only 8.0%.

This enhancement of the extraction of Zr (IV) by using a mixture of TTA and TAP at concentrations much lower than those used for individual ligands clearly reflect the synergic effect of the TTA. Further, the TAP concentration used is decreased to a much less extent, i.e., only 8.0% in place of 18% for TAP alone and the extraction increases from 95.5% to 99.0%. This is attributed to the adduct formation of Zr (IV) with TTA and TAP. The system was then further investigated to evaluate the number of moles of TAP used in the adduct formation. Thus, log D was plotted against log TAP from the data in Table 4. The results as depicted graphically in *Fig. 4* give a straight line with a slope of nearly one. It can be inferred that one mole of TAP is utilised in the adduct

TABLE 3

Effect of variation of TTA concentration on the distribution coefficient (D) of Zr (IV) when TAP concentration is constant

[HCl] = 7.70 mol l-1
[TAP] = 5% TAP (vol/ vol) benzene
[Zr(IV)]= 1.0 x 10-3 mol l-1
vol. of aqueous layer = vol. of organic layer = 10 mL

S. No.	[TTA]%	Amount in 5 mL aliquot 10-2 mg		D	%E
		[Zr(IV)]aq	[Zr(IV)]org		
1	0.50	5.10	40.51	7.94	88.81
2	0.60	4.60	41.01	8.91	89.90
3	0.70	3.89	41.72	10.71	91.46
4	0.80	2.95	42.66	14.45	93.52
5	0.90	2.32	43.29	18.62	94.90
6	1.00	1.74	43.87	25.12	96.17
7	1.10	1.40	44.21	31.62	96.93
8	1.20	1.11	44.50	39.81	97.55
9	1.25	0.97	44.64	45.71	97.85
10	1.30	0.97	44.64	45.71	97.85
11	1.50	0.97	44.64	45.71	97.85

TABLE 4
Effect of variation of TAP concentration on the distribution coefficient (D) of Zr(IV) from aqueous hydrochloric acid solutions

$[HCl]$ = 7.70 mol l^{-1}, [Zr(IV)]= 1.0 x 10-3 mol l^{-1}
vol. of aqueous layer = vol. of organic layer = 10 mL

S. No.	[TAP]%	Amount in 5 mL aliquot 10-2 mg		D	%E	*Log Kex
		[Zr(IV)]aq	$[Zr(IV)]_{org}$			
1	0.50	8.18	37.43	4.57	82.04	3.64
2	0.60	7.74	37.87	4.89	83.02	3.65
3	0.70	7.02	38.59	5.49	84.59	3.63
4	0.80	6.48	39.13	6.03	85.77	3.61
5	0.90	5.87	39.74	6.76	87.11	3.61
6	1.00	5.53	40.08	7.24	87.86	3.59
7	1.25	4.41	41.22	9.33	90.31	3.60
8	1.50	3.57	42.04	11.77	92.16	3.61
9	2.00	2.64	42.97	16.27	94.20	3.63
10	2.50	2.08	43.53	20.89	95.43	3.63
11	3.00	1.60	44.01	27.54	96.49	3.69
12	3.50	1.33	44.28	33.11	97.06	3.69
13	4.00	1.12	44.49	39.71	97.54	3.71
14	4.50	0.97	44.64	45.71	97.87	3.72
15	5.00	0.85	44.76	52.65	98.13	3.73
16	5.50	0.74	44.87	60.26	98.37	3.73
17	6.00	0.68	44.93	66.07	98.50	3.73
18	6.50	0.63	44.98	71.59	98.61	3.73
19	7.00	0.54	45.07	83.17	98.81	3.76
20	7.50	0.50	45.11	90.22	98.90	3.77
21	8.00	0.45	45.16	100.35	99.00	3.77
22	8.50	0.45	45.16	100.35	99.00	-
23	9.00	0.45	45.16	100.35	99.00	-
24	10.00	0.45	45.16	100.35	99.00	-

* Average value of log $K_{ex_{mix}}$ = 3.68 ± 0.0595.

formation. Since it has already been concluded (*Fig. 1*) that Zr (IV) forms a 1:2 complex with TTA, the ratio of Zr:TTA:TAP is now definitely 1:1:1 when both the ligands are used in combination.

Thus the extraction systems can be mathematically represented as follows:

$$ZrCl_4 + 2TAP \xleftrightarrow{K_{ex}} ZrCl_4.2TAP \qquad (4)$$

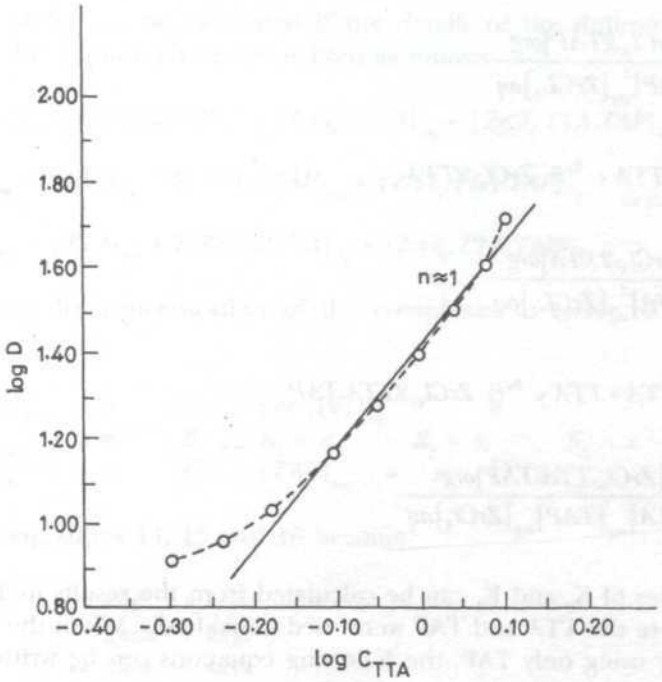

Fig. 3: Effect of variation of TTA concentration on distribution ratio of Zr (IV) at fix tap concentration [HCL] = 7.70 mol l^{-1} [Zr(IV)] = 1.0 × 10^{3} mol l^{-1} [TAP] = 5% in benzene

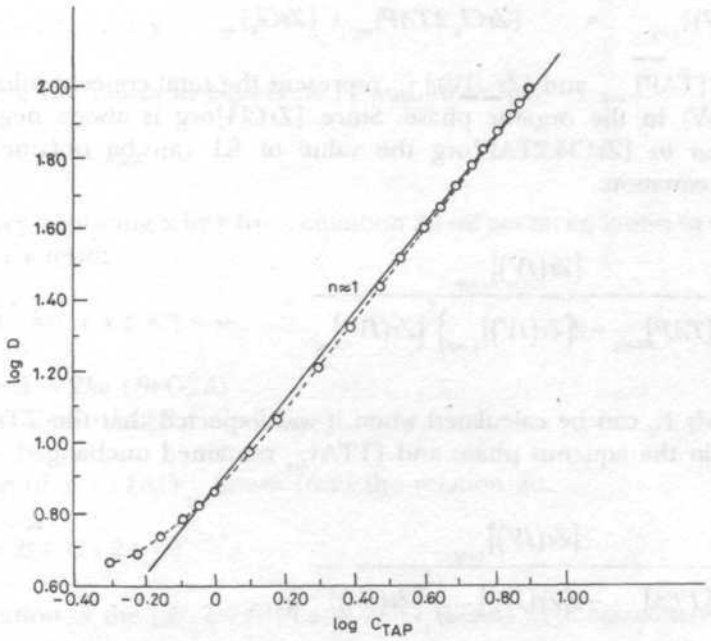

Fig. 4: Effect of variation of TAP concentration on the coefficient (D) of Zr (IV) when TTA concentration is constant [TTA] = 1.25% (vol./vol) in benzene [HCL] = 7.70 mol l^{-1} [Zr(IV)] = 1.0 × 10^{3}

$$K_1 = \frac{[ZrCl_4.2TAP]org}{[TAP]^2_{org}[ZrCL_4]aq} \quad (5)$$

$$ZrCl_4 + 2TTA < {}^{K_2}\text{fi } ZrCl_4.2TTA \quad (6)$$

$$K_2 = \frac{[ZrCl_4.2TTA]org}{[TTA]^2_{org}[ZrCL_4]aq} \quad (7)$$

$$ZrCl_4 + TTA + TTA < {}^{K_3}\text{fi } ZrCl_4.2TTA.TAP \quad (8)$$

$$K_3 = \frac{[ZrCl_4.TTA.TAP]org}{[TTA]_{org}[TAP]_{org}[ZrCl_4]aq} \quad (9)$$

The values of K_2 and K_1 can be calculated from the results in Table 1 and Table 2 where the TTA and TAP were used individually. When the Zr (IV) was extracted by using only TAP, the following equations can be written:

$$[TAP]_{t.org} = [TAP]_{org} + [ZrCl_4.2TAP]_{org} \quad (10)$$

$$[Zr\ (IV)]_{t.org} = [ZrCl_4.2TAP]_{org} + [ZrCl_4]_{org} \quad (11)$$

where $[TAP]_{t.org.}$ and $[Zr\ (IV)]_{t.org}$ represent the total concentration of TAP and Zr (IV) in the organic phase. Since [ZrCl4]org is always negligible in comparison to [ZrCl4.2TAP]org the value of K1 can be obtained by the following equation:

$$K_1 = \frac{[Zr(IV)]_{t.org}}{\left([TAP]_{t.org} - 2[Zr(IV)]_{t.org}\right)^2 [Zr(IV)]_{aq}} \quad (12)$$

Similarly K_2 can be calculated when it was expected that the TTA was not dissolved in the aqueous phase and $[TTA]_{org}$ remained unchanged.

$$K_2 = \frac{[Zr(IV)]_{t.org}}{\left([TTA]_{t.org} - 2[Zr(IV)]_{t.org}\right)^2 [Zr(IV)]_{aq}} \quad (13)$$

The value of K_3 can be calculated if the details of the different complexes formed in the organic phase are written as follows:

$$[Zr\ (IV)]_{t.org} = [ZrCl_4.2TAP]_{org} + [ZrCl_4.2TTA]_{org} + [ZrCl_4.TTA.TAP]_{org} \quad (14)$$

$$[TAP]_{t.org.} = [TAP]_{org} + 2[ZrCl_4.2TAP]_{org} + [ZrCl_4.TTA.TAP]_{org} \quad (15)$$

$$[TTA]_{t.org.} = [TTA]_{org} + 2[ZrCl_4.2TTA]_{org} + [ZrCl_4.TTA.TAP]_{org} \quad (16)$$

Replacing the concentration of the complexes in terms of the stability constant.

$$[Zr\ (IV)]_{t.org} = A \quad [Zr\ (IV)]_{aq.} = k$$
$$[TAP]_{t.org} = B \quad K_1 = a, \quad K_2 = b, \quad K_3 = z$$
$$[TTA]_{t.org} = C \quad [TAP]_{org.} = x, \quad [TTA]_{org.} = y$$

The above equations 14, 15 and 16 become

$$A = kax^2 + kby^2 + kxyz \quad (17)$$
$$B = x + 2kax^2 + kxyz \quad (18)$$
$$C = y + 2kby^2 + kxyz \quad (19)$$

Combining these equations in the manner of (18) + (19) - 2 x (17)

$$B + C - 2A = x + y \quad (20)$$

Thus using the values in equations 17 and 18 we get

$$A - B = kby^2 - kax^2 - x \quad (21)$$

Further, replacing x by y from equation 20 we get an equation to the second degree in y term;

$$y^2\ (kb - ka) + y\,\varepsilon + \gamma = o \quad (22)$$

where $\varepsilon = 1 + 2ka\ (B+C-2A)$

$\gamma = A - C - ka\ (B + C - 2A)^2$

The value of $x = (TAP)_{org}$ drawn from the relation 20

$$x = m\ B + C - 2A - Y$$

concentration of the $[ZrCl_4.2TAP]$ and $[ZrCl_4.2TTA]$ were calculated from their respective extraction constants.

$$[ZrCl_4.2TAP]_{org} = K_1\ [TAP]^2[Zr(IV)]_{aq.} = kax^2$$
$$[ZrCl_4.2TTA]_{org.} = K_2\ [TTA]^2[Zr(IV)]_{aq.} = kby^2$$

Thus the concentration of the adduct formed in the statements 14, 15 and 16 can be calculated by the following equations:

$$[ZrCl_4.TTA.TAP]_{org.} = [TAP]_{t.org.} - [TAP]_{org.} - 2[ZrCl_4.2TAP]_{org.} \quad (23)$$

Finally K_3 can be calculated from its definition

$$z = K_3 = \frac{Bxx - 2kax^2}{kxy} \quad (24)$$

or

$$K_3 = \frac{[TAP]_{t.org.} - [TAP]_{org.} - 2[Zr(IV)]_{aq.} K_1 [TAP]^2_{org.}}{[Zr(IV)]_{aq.} [TAP]_{org.} [TTA]_{org.}} \quad (25)$$

with the help of equations 12, 13 and 25 the extraction constants were evaluated and given in the last columns of Tables 2, 3 and 4.

The average value for log K_{ex} (*TTA*) and log K_{ex} (*TAP*) are 2.97 and 1.85; the statistical value and the observed value for $K_{ex(mix)}$ are represented as in Table 5.

TABLE 5
Comparison of observed value and statistical value of Kex(mix)

Ligands	Log $K_{ex(mix)}$ Statistical	Log $K_{ex(mix)}$ observed
TTA + TAP	2.39	3.19

It can further be emphasized that the observed value of Kex for TTA-TAP mixed ligand species was 9.30 times more than the statistical value. Our results are also supported by the earlier work of Sekine and Dyrssen (1964) for the extraction of similar mixed chelate complexes of divalent metals with TTA and other ligand wherein it has been concluded that the extraction proceeds to a greater extent than the statistically evaluated values for the same ligands used separately. Further, these workers have also evaluated the statistical extraction constant for divalent ion with the two ligands HA and HB using the relationship.

$$K_{(ex)_{(mix)}} = 2\sqrt{K_{exA} X K_{exB}} \quad (26)$$

where K_{exA} is the extraction constant for HA and K_{exB} is that for *HB*; the same statistical treatment has been used to evaluate the log $K_{ex(mix)}$ (Stat.).

ACKNOWLEDGEMENTS

The authors are thankful to the Head, Department of Applied Chemistry and Director, Institute of Technology, Banaras Hindu University for providing the laboratory facilities.

REFERENCES

BASES, C. F. and R. E. MESMER. 1976. *The Hydrolysis of Cations.* New York: John Willey.

CONNICK, R. E. and W. H. MCVEY. 1949. The aqueous chemistry of zirconium. *J. Am. Chem. Soc.* **71**: 3182-3191.

HUFFMAN, E. H. and L. J. BEAUFAIT. 1949. The fractional separation of zirconium and hafnium by extraction with thenoyltrifluoroacetone. *J. Am. Chem. Soc.* **71**: 3179-3182.

HASAN, S. H. and D. C. RUPAINWAR. 1987. Extraction of titanium (IV) from acidic thiocynate solution by tri-iso-amyl phosphate (TAP). *J. Ind. Chem. Soc.* **64**: 249-250.

HASAN, S. H. and D. C. RUPAINWAR. 1990. Extraction of zirconium (IV) from its hydrochloric acid solution with tri-iso-amyl phosphate (TAP). *Acta Chim. Hung.* **121**: 65-75.

JAISWAL, S. and D. C. RUPAINWAR. 1984. Extraction of thorium (IV) from aqueous nitric acid solution by tri-iso-amyl phosphate (TAP). *Acta Chim. HUng.* **115(3)**: 261-267.

KOMATSU, YU. 1980. The extraction behaviour of Ti (IV) in concentrated hydrochloric acid with TBP and β-diketones. *J. Inorg. Nucl. Chem.* **42**: 265-268.

MARCUS, Y. and A. S. KERTES. 1969. *Ion Exchange and Solvent Extraction of Metal Complexes.* p. 333. New York: Wiley Inter-Science.

MAYA, L. and C. D. BOPP. 1977. Extraction of zirconium from nitric acid media by butyl lauryl phosphoric acid in dodecane. *J. Inorg. Nucl. Chem.* **40**: 1149.

NANDI, B., N. R. DAS and S. N. BHATTACHARYA. 1983. Review; solvent extraction of zirconium and hafnium. *Solv. Ext. & Ion Exch.* **1(1)**: 141-202.

PRAKASH, B. and C. V. SUNDARAM. 1956. The present status of zirconium metallurgy. *Proc. U.N. Int. Conf. Peaceful Uses at Energy,* **8**: 554-568. Geneva.

PANDEY, B. D. and D. C. RUPAINWAR. 1979. Extraction of Iron (III) with a new and indigenously prepared solvent tri-iso-amyl phosphate (TAP). *J. Inorg. Nucl. Chem.* **41**: 337-338.

SUNDARAM, C. V., R. B. SUBRAMANIYAM and R. S. BABU. 1986. Development of zirconium process metallurgy in India. *Trans. of Indian Instt. of Metals.* **39**: 23-40.

SEKINE, T. and D. DYRSSEN. 1964. Solvent extraction of metal ions with mixed ligands. *J. Inorg. Nucl. Chem.* **26**: 1727-1732.

SEKINE, T. and D. DYRSSEN. 1967a. Solvent extraction of metal ions with mixed ligands. *J. Inorg. Nucl. Chem.* **29**: 1457-1473.

SEKINE, T. and D. DYRSSEN. 1967b. Solvent extraction of metal ions with mixed ligands. *J. Inorg. Nucl. Chem.* **37**: 217-226.

SINGH, J. P., S. H. HASAN and D. C. RUPAINWAR. 1986. Extraction of Vanadium (IV) from its aqueous chloride solution by tri-iso-amyl phosphate (TAP). *Ind. J. Tech.* **24**: 169-170.

SANDEL, E.B. 1958. *Colorimetric Determination of Traces of Metals.* p. 968-981. New York: Interscience.

STARDY, J. and E. HLADSKY. 1963. Systematic study of the solvent extraction of metal β-diketones. *Anal. Chim. Acta.* **28**: 227.

TAKETATSU, T. and C. V. BAUKS. 1966. Spectrophotometric investigation and analytical application of the synergic solvent extraction of rare earths with mixture of TTA and Tri-n-octyl phosphine oxide. *Anal. Chem.* **38**: 1524-1525.

VOGEL, A. I. 1978. *A Textbook of Quantitative Inorganic Analysis.* 4th ed. London: Longman.

Pertanika J. Sci. & Technol. 12(2): 311 - 327 (2004)
ISSN: 0128-7680

Analysis of Drum Brake Squeal Using Finite Element Method

Zahrul Fuadi & Zaidi Mohd. Ripin
School of Mechanical Engineering
Engineering Campus, Universiti Sains Malaysia
14300 Nibong Tebal, Seberang Perai Selatan, Pulau Pinang, Malaysia

Received: 6 May 2003

ABSTRAK

Fenomena kebisingan brek telah dikaitkan dengan ketidakstabilan dinamik sistem disebabkan penggandingan nilai eigen komponen dengan pekali geseran. Model unsur terhingga brek gelendong motosikal telah dibangunkan untuk analisis ini dan ketidakstabilan sistem telah dianggarkan dengan menggunakan analisis nilai eigen kompleks. Redaman telah diambil kira dalam analisis ini yang dianggap berkadaran dengan matriks kekukuhan. Keputusan analisis menunjukkan ketidakstabilan utama sistem berlaku dalam lingkungan 1200 Hz. Analisis parametrik telah dijalankan untuk mencari kesan pekali geseran dan juga kekukuhan pelbagai komponen brek. Keputusan menunjukkan ketidakstabilan bermula apabila nilai pekali geseran μ=0.3 dan tahap ketidakstabilan bertambah seiring pertambahan nilai pekali geseran. Pengukuhan gelendong dan plat di belakang kasut boleh meningkatkan kestabilan sistem. Peningkatan yang paling menonjol untuk kestabilan sistem dicapai dengan mengukuhkan rusuk pada belakang plat brek gelendong.

ABSTRACT

The phenomenon of brake squeal has been associated with the dynamic instability of the system that is caused by the coupling between eigenvalues of the components in the presence of friction. A finite element model of a motorcycle drum brake has been developed in the present analysis and the instability of the system predicted using the complex eigenvalue analysis. Damping was included in the analysis and assumed to be proportional to the stiffness matrix. The analysis results showed that the main instability of the system occurred in the vicinity of 1200 Hz. Parametric analysis was conducted on effect of friction coefficient and the stiffness of various brake components. The results showed that instability started at the value of friction coefficient μ=0.3 and the level of instability increased with the increase in the coefficient of friction. Stiffening the drum brake and the shoe back plate improves the stability of the system. The most significant improvement for the system stability was achieved by stiffening the brake drum back plate ribs.

Keywords: Drum brake squeal, complex eigenvalue analysis, finite element method

INTRODUCTION

Squeal is associated with noise generated by friction-induced vibration. Generally found in brakes, it occurs at certain levels of vibration with frequency ranges

from 1-15 kHz (Nishiwaki 1993; Pappiniemi *et al.* 2002). The squeal noise in the frequency region of 1 kHz to 6 kHz is the most annoying to the human ear (Hulten 1995; Lang and Smales 1983). For instance, noise from city buses' brakes is very disturbing, because of frequent stops in densely populated areas. Studies of brake squeal have been associated more with convenience rather than safety. Customer complaints result in significant warranty costs yearly (Liles 1989).

There have been a considerable number of studies on brake squeal and this has been collated in a relatively comprehensive overview (Crolla and Lang 1991; Pappiniemi *et al.* 2002). Since then there have been remarkable improvements in the understanding of the cause of drum brake squeal particularly when the problem is treated as a stability problem associated with the complex eigenvalue of the brake system (Hamabe *et al.* 1999; Liles 1991; Ripin *et al.* 1995). A number of studies have been conducted to analyze the cause and the mechanism of squeal. From those analyses, it reveals that squeals occurred as the effect of dynamic instabilities between the parts of the brake system, also known as self-excited vibration (Liles 1989; Murakami *et al.* 1984; Nishiwaki 1993; Ripin *et al.* 1995). One of the causes of this dynamic instability is the coupling between eigenvalues of particular mode shapes of the brake components which has become the focus of many researchers in the study of brake squeal (Chung *et al.* 2001; Hamabe *et al.* 1999; Kung *et al.* 2000; Ripin *et al.* 1995). The coupling between two initially separated eigenvalues is caused by the presence of coefficient of friction at the interface between the brake pad and the rotor (Okamura and Nishiwaki 1989; Lang 1994).

Although many recommendations have been given for suppressing the occurrence of brake squeal, it is still difficult to predict the occurrence of brake squeal in practice (Pappiniemi *et al.* 2002). Nowadays, finite element method is widely used for analysis in structural mechanics and other disciplines. Once a model is developed, analysis can be conducted and modifications carried out to see the effects of parameters to the model. This can save time and cost, as the cost experimentation is very high. The powerful modern computers facilitated the application of finite element method in the analysis of brake squeal. A recent study showed that a complex eigenvalue analysis of a finite element model was effective in analyzing the squeal problem of drum brake (Hamabe *et al.* 1999).

This paper presents the analysis of squeal propensity of a typical motorcycle drum brake (*Fig. 1*) using the finite element method. The objectives of this research are to establish a condition of squeal between the brake drum and brake shoes using the complex eigenvalue analysis and to study the relationships between parameters such as coefficient of friction and stiffness of the brake components to the squeal propensity of the drum brake system. The importance of this work lies in the fact that unlike disc, the drum brake assembly is relatively more complex and asymmetry already existed due to the design of drum brake assembly. In addition, none of the previous studies on drum brake squeal have been conducted for motorcycle brake drum system.

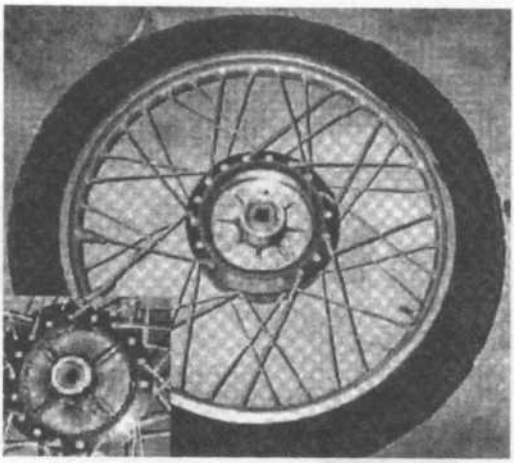

Fig. 1: Typical motorcycle drum brake used in this analysis

METHODOLOGY

The rear drum brake of a motocycle (typically with engine displacement less than 125 cc) used in the present analysis is shown in *Fig. 1*. The diameter of the drum is 130 mm. The drum brake and the shoe back plate are made of cast aluminium alloy with modulus of elasticity of 69 GPa and density of 2720 kg/m^3. The lining interface of the drum brake that is in contact with shoe lining is made of steel with modulus of elasticity of 207 GPa and density of 7800 kg/m^3. The shoe lining's modulus elasticity is taken as 8 GPa with density of 2500 kg/m^3.

Interface elements representing the contact stiffness are modeled along the surface of the interaction between the linings and the drum. The interface element will take into account the nodal contact stiffness, kc, and the coefficient of friction, μ. The braking forces from the actuator that act at both shoe-ends are modeled by spring-damper elements. The elements will connect the nodes where braking forces are applied with ground nodes with a value of contact support, ks. The finite elements model of the drum brake and the shoes is shown in *Fig. 2*. There are two major idealizitions made here, the first is the omission of the spokes from the flanges and second is the bearing assumed to be forced to slide in the inner bore and does not contribute to the stiffness of the drum.

Modeling of Interface Elements

The sliding interface modeling is conducted based on the work of Ripin *et al.* (1995). The mating surface of the shoe and the drum is assumed to have some flexibility in which they can move relative to each other. The sliding interface model is shown in *Fig. 3*.

The active forces on the interface can be arranged in the form of:

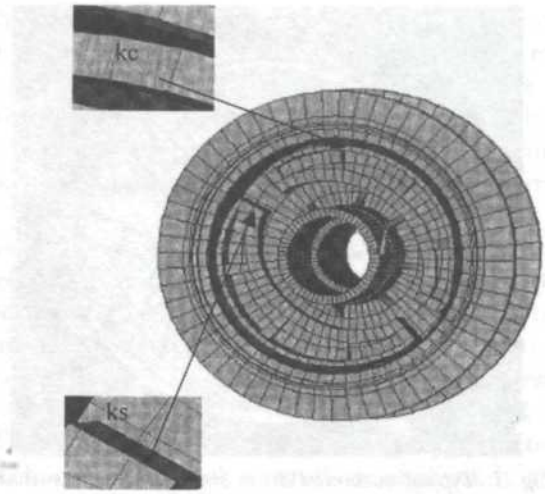

Fig. 2: Finite element model of the drum brake-shoe

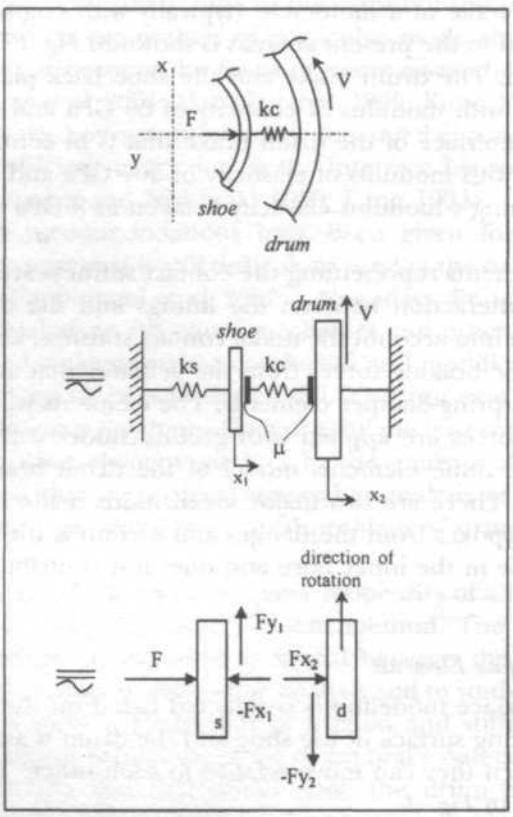

Fig. 3: Sliding interface model

$$\begin{Bmatrix} Fx_1 \\ Fy_1 \\ Fx_2 \\ Fy_2 \end{Bmatrix} = \begin{bmatrix} -k_c & 0 & k_c & 0 \\ \mu k_c & 0 & -\mu k_c & 0 \\ k_c & 0 & -k_c & 0 \\ -\mu k_c & 0 & \mu k_c & 0 \end{bmatrix} \begin{Bmatrix} x_1 \\ y_1 \\ x_2 \\ y_2 \end{Bmatrix} \quad (1)$$

or,

$$\{F\} = [Kf]\{Q\} \quad (2)$$

where $\{F\}$ is the force vector, $[K_f]$ is the friction interface matrix, and $\{Q\}$ is the vector of displacement.

Complex Eigenvalue Analysis

The equation of motion of a vibrating system can be written as

$$[M]\ddot{Q}(t)+[C]\dot{Q}(t)+[K]Q(t)=F(t) \quad (3)$$

where $[M]$, $[C]$, and $[K]$ are mass, damping and stiffness matrices respectively and $\{Q\}$ is the displacement vector. For friction-induced vibration, it is assumed that the force function is mainly contributed by friction force between the mating surfaces of the linings. Introducing the friction force of Equation 2 into the equation of motion, we get

$$[M]\ddot{Q}(t)+[C]\dot{Q}(t)+[K]Q(t)=[K_f]\{Q\}(t) \quad (4)$$

Rearranging the equation into the left side,

$$[M]\ddot{Q}(t)+[C]\dot{Q}(t)+[K-K_f]Q(t)=0 \quad (5)$$

The stiffness matrices of Equation 5 become asymmetry because of the presence of friction interface matrix K_f. The solution of Equation 5 can be written in the form of a complex eigenvalue problem:

$$([M]s^2 + [C]s + [K - K_f])\ \{U\} = 0 \quad (6)$$

which will result in a complex number having both real and imaginary parts:

$$\lambda_i = \sigma_i \pm \omega j \quad (7)$$

where $j = \sqrt{-1}$ and i =1,2,3,...,n, being the order of eigenvalue

Stability of the homogeneous system in Equation 6 can be analyzed by evaluating the complex eigenvalue. For the stable case, the real part of the

eigenvalue will have the negative sign, indicating that the response of the system will decay with time. On the other hand, positive sign of the real part of the eigenvalue indicates that the response of the system will grow, thereby causing the system to be unstable. For the particular study of the brake drum, positive value of the real part of the eigenvalue indicates the occurrence of self-excited vibration, or squeal.

Damping is included in this analysis. Damping matrix is provided in the form of $C = \beta K$, or also known as beta damping (ANSYS 2001). Beta damping provides a damping ratio that is linearly related to frequency and tends to affect higher-frequency content, which is proportional to stiffness matrix. Beta damping can be calculated from the damping ratio, ξ, by the relation of $\beta = 2\xi/\omega$, where ω is angular frequency.

The following additional assumptions are also applied in this analysis, which are:

1. The material properties are linear elastic and homogeneous.
2. The coefficient of friction between the lining interfaces is assumed to be constant.
3. It is assumed that the contact stiffness is uniformly distributed among the contact nodes at the lining interface.

Stability Analysis

The stability analysis is conducted for contact stiffness value Kc from 70 MN/m to 450 MN/m with the increment of 20 MN/m. Beta damping value is set at (=3.14E-6 which gives a damping ratio of 0.15% of critical damping at 6000 Hz and the coefficient of friction is set to 0.4. The stability analysis showed three unstable mode shapes occurring at different values of contact stiffness indicated by the positive real part of the eigenvalues. These complex eigenvalues are given in *Fig. 4* for values of Kc = 70 MN/m up to Kc = 270 MN/m and *Fig. 5* for values of Kc = 310 MN/m up to Kc = 430 MN/m.

Fig. 4 shows one persistent unstable mode with positive real part even though the contact stiffness varies from 70 MN/m to 270 MN/m. This particular mode has positive real part in the range of 10 to 30. It can be seen also that the imaginary part which represents the frequency of the mode does not change with the values of the contact stiffness. This unstable mode is labeled as mode A. *Fig. 5* extends the values of contact stiffness from Kc = 310 MN/m to Kc = 430 MN/m. In this figure there are two major clusters of unstable modes. The first occurs around the frequency of about 1200 Hz and will be labeled as mode B. The second cluster is around the frequency of about 2800 Hz and labeled as mode C. The mode shapes of these unstable modes are shown in *Fig. 6.*

The results of the unstable modes are plotted against the contact stiffness for both its frequency components (the imaginary parts) and the instability (the real part). *Fig. 7* shows the development of the complex eigenvalues with the contact stiffness for mode A. Unstable mode A occured at the value of contact stiffness Kc between 90 MN/m and 230 MN/m in the frequency range of 1214

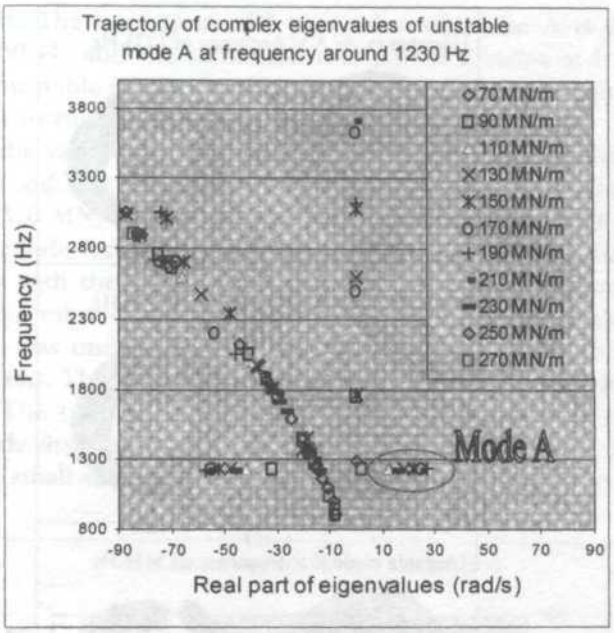

Fig. 4: Complex eigenvalue for different values of contact stiffness of Kc = 70 MN/m to Kc = 270 MN/m (μ=0.4 and β=3.14E-6)

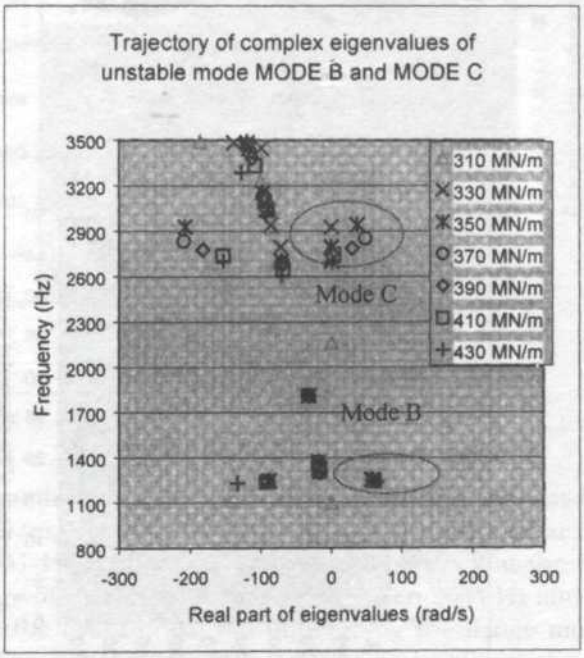

Fig. 5: Complex eigenvalue for different values of contact stiffness of Kc=310 MN/m to Kc=450 MN/m ((μ=0.4 and β=3.14E-6)

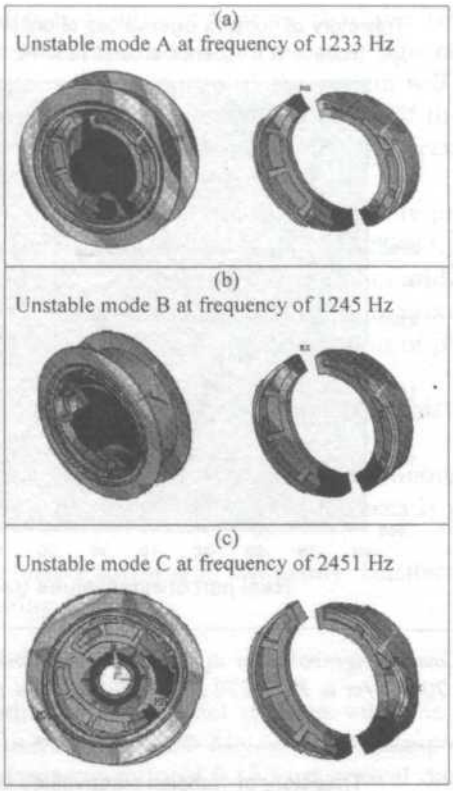

Fig. 6(a)-(c): Mode shapes of unstable modes A, mode B, and mode C

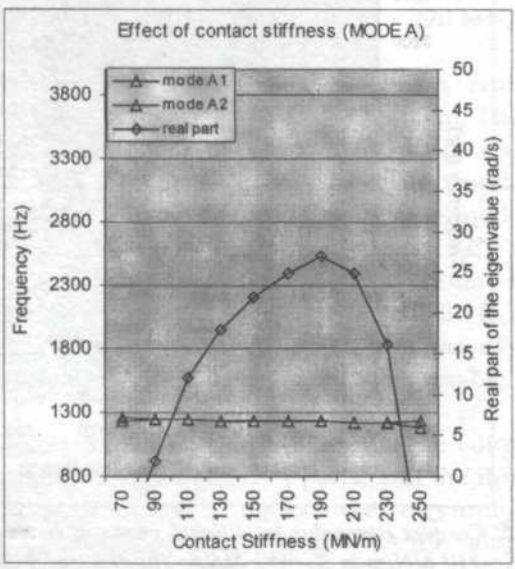

Fig. 7: Effect of contact stiffness for unstable mode A ($(\mu=0.4)$

Hz and 1241 Hz. The maximum real part value of mode A is 27 rad/s at frequency of 1230 Hz and the minimum real part is 2 rad/s at frequency of 1241 Hz. In this unstable mode, the shoes were undergoing the combination of the bending and twisting mode shape as shown in *Fig. 6.*

Fig. 8 shows the variation of the real and imaginary part of mode B and C with the contact stiffness. Mode B occured at the value of contact stiffness starting at Kc = 310 MN/m with the real part and frequency of 54 ± 1266 Hz. The real part of mode B reaches the maximum at the value of contact stiffness Kc = 430 MN/m with the value of real part 64 (64 ± 1242 Hz) but suddenly disappeared at the value of contact stiffness Kc = 450 MN/m. In this unstable mode, the drum was undergoing the first radial mode shape but with lower flange displacement. The shoes were undergoing different mode shape in this unstable mode. The trailing shoe underwent the combination of the twisting and bending mode shape with larger displacement at the abutment. Meanwhile, there was only a small displacement of the leading shoe (refer to *Fig. 6b*).

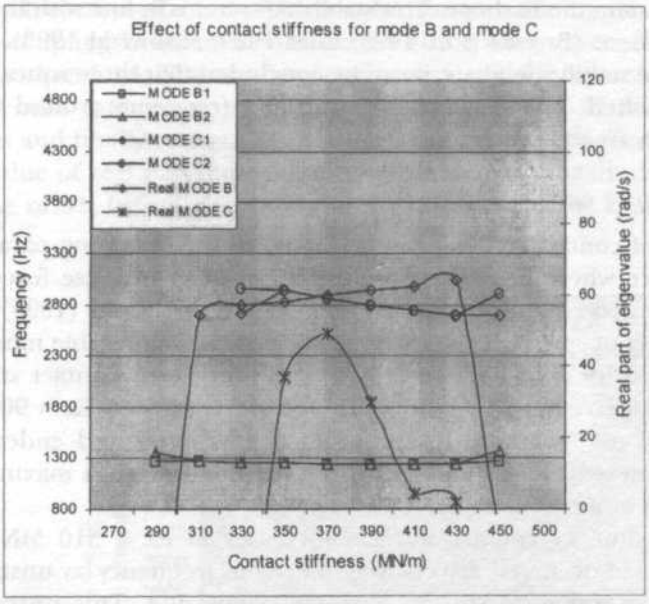

Fig. 8: Effect of contact stiffness for unstable mode B and mode C ((=0.4)

The unstable mode C occurred at a value of contact stiffness between 350 MN/m to 450 MN/m. The maximum value of real part is 49 at frequency of 2851 Hz (49 ± 2851 Hz) and the minimum real part is 2 at the frequency of 2694 Hz. The range of this unstable mode is between 2694 Hz and 2940 Hz. In unstable mode C, the drum brake was undergoing the flange mode shape in radial direction. The radial mode of the flange acted almost the same as the second radial mode of the drum but only at higher frequency. At the same time, the shoe undergoes the second bending mode shape as shown in *Fig. 6c.*

All of these unstable modes indicate an important trend which involves the convergence of two initially separate and distinct modes to coalesce to form a pair of one unstable mode and another stable mode at a common frequency. This similar trends was also reported by other workers (Ripin *et al.* 1995; Ghesquire and Castel 1992; Hamabe *et al.* 1999).

The effect of damping on the stability of the system was investigated by the inclusion of stiffness proportional damping, or also known as beta damping. In this case damping ratio of 0.15% is taken with the equivalent beta value $\beta = 3.14$ E-6. The result from the complex eigenvalue analysis with the inclusion of damping for the particular value of contact stiffness Kc = 150 MN/m is given in *Fig. 9.* As indicated by the arrow, an unstable mode still occurs as damping is included, although the magnitude of its real part did decrease.

Damping is found to be effective in decreasing the value of the real part of the three unstable modes obtained but does not totally suppress them. The main advantage of the damping application is that it can suppress most of the resulting complex eigenvalues except the one that belongs to the unstable highly consistent mode shape. This stablizing trend is in line with the observation made elsewhere (Brooks *et al.* 1993; Liles 1989; Nishiwaki 1993).

From the stability analysis, it can be concluded that three squeal modes have been established. The first two occurred at a frequency around 1230 Hz and another at a frequency around 2450 Hz.

Effect of Contact Stiffness

The effect of contact stiffness can be linked to the operating parameter of the applied force where increased stiffness is linked to increase force applied on the brake based on the work of Sheriff (1993) and Ripin (1995).

The effect of contact stiffness on the occurance of unstable modes A is given in *Fig. 7* and for modes B and C *Fig. 8* for different contact stiffness value. Unstable mode A started at the value of contact stiffness Kc = 90 MN/m with the value of real part and frequency of 2 ± 1230 Hz and ended at value of contact stiffness Kc = 250 MN/m. Unstable mode A has a maximum value of real part 27 at a frequency of 1230 Hz.

As the value of contact stiffness increases to Kc = 310 MN/m, another unstable mode occurred at relatively the same frequency as unstable mode A but at higher value of real part of the eigenvalue. This unstable mode is considered as mode B. Mode B started at the value of contact stiffness Kc = 310 MN/m with the real part and frequency 54 ± 1266 Hz and disappeared at the value of contact stiffness Kc = 450 MN/m. The maximum real part value of unstable Mode B is 64 at a frequency of 1242 Hz.

One more unstable mode shape occurred as the value of contact stiffness reached 350 MN/m. This unstable mode occurred at the value of real part and frequency of 37 ± 2940 Hz. This unstable mode shape is further considered as mode C. At this value of contact stiffness, the real part eigenvalue of mode B becomes 58 at frequency of 1251 Hz (58 ± 1251 Hz).

As the value of contact stiffness Kc reaches 450 MN/m, both mode B and mode C disappeared. The effect of contact stiffness for the occurance of unstable mode shapes mode B and mode C is given in *Fig. 8.* Mode C started at contact stiffness Kc = 350 MN/m with the value of real part and frequency of 37 ± 3940 Hz and ended at the value of contact stiffness Kc = 430 MN/m with the real part and frequency of 2 ± 2694 Hz.

The Effect of Friction Coefficient

The effect of coefficient of friction for the squeal propensity of the present drum brake system is analyzed by applying a range of friction coefficient value from 0.1 to 0.7 with the increment of 0.1. The analysis is conducted at the value of contact stiffness Kc=190 MN/m and Kc=370 MN/m. At the value of contact stiffness Kc=190 MN/m, unstable mode A occurred with maximum value of real part (27 (1230 Hz). At the value of contact stiffness Kc=370 MN/m, unstable mode B and unstable mode C occurred with the real parts and frequencies of 49 ± 2851 Hz and 60 ± 1247 Hz, respectively.

The effect of coefficient of friction for the unstable mode A is given in *Fig. 10.* The coupling between modes started at the value of coefficient of friction between 0.3 and 0.4. The two frequencies were initially separated (1371 Hz and 358 Hz) and came close to each other as the value of friction coefficient increases and finally converged at the value of μ =0.4 with the real part 29 rad/s. The value of real part increases afterwards to reach maximum at μ =0.6, with the value of 51, before decreasing to 30 at value of μ =0.7.

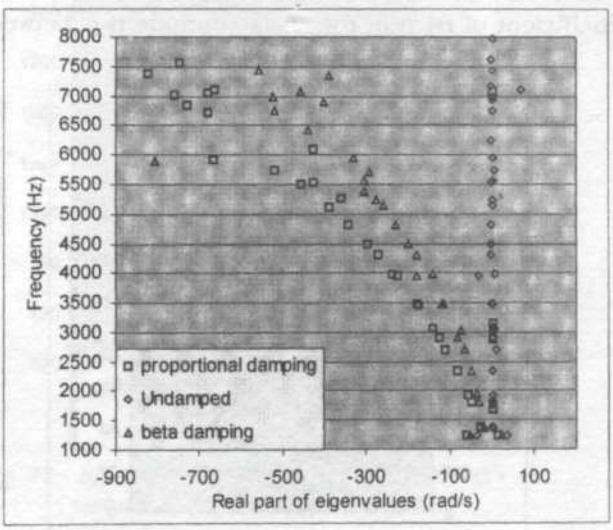

Fig. 9: Effect of damping for complex eigenvalues at Kc = 150 MN/m

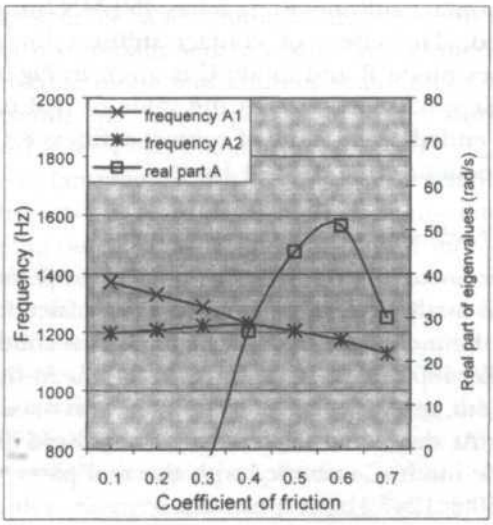

Fig. 10: Effect of friction coefficient for unstable mode A at Kc=190 MN/m (μ=0.4)

The effect of coefficient of friction for the unstable mode B and unstable mode C is given in *Fig. 11.* The unstable mode B at the value of contact stiffness Kc=370 MN/m occurred at the value of friction coefficient between 0.2 and 0.3. As the coefficient of friction is increased, the two frequencies converged at one frequency of 1273 Hz with real part of 29 rad/s at friction coefficient of 0.3. The critical coefficient of friction for unstable mode B is between 0.2 and 0.3

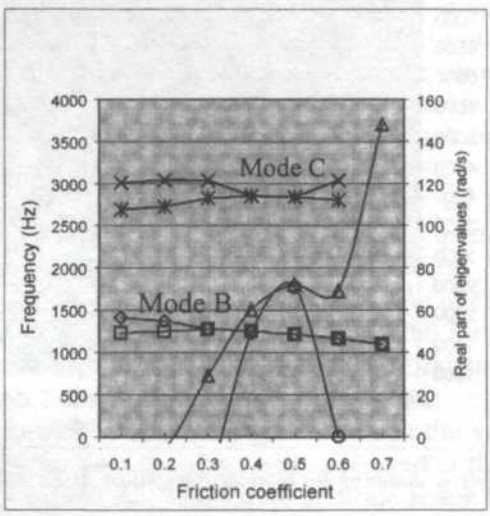

Fig. 11: Effect of coefficient of friction for unstable mode B and mode C at Kc=370 MN/m (μ=0.4)

Unstable mode C consists of drum brake undergoing flange deformation in the radial direction and brake shoes undergoing second bending mode. The two frequencies converged at a value of friction coefficient 0.4 with real part and frequency of 37 ± 2851 Hz. The two frequencies then separated at the value of friction coefficient 0.6, indicating that the modes become stable again.

Effect of Shoe Stiffness

The effect of shoe stiffness is analyzed by changing the shoe back plate with the material having Young's modulus of 207 GPa and density of 7800 kg/m^3. The material is similar to steel (AISI C1020).

The effect of contact stiffness for different shoe back plate stiffness is given in *Fig. 12*. One unstable mode occurred starting at a value of contact stiffness Kc=270 MN/m at a frequency of 1332 Hz with the value of real part 12 rad/s. This unstable mode consists of drum undergoing the first radial mode shape and the trailing shoe undergoing bending mode shapes. However, the mode shapes of the leading shoe was not very clear as the amplitude of the displacement of the leading shoe was hardly noticeable. This unstable mode reached maximum at the value of contact stiffness Kc=350 MN/m with the value of real part and frequency 26 ± 1338 Hz. This unstable mode still exists up to the values of contact stiffness Kc=470 MN/m with the real part and frequency of 13 ± 1338 Hz.

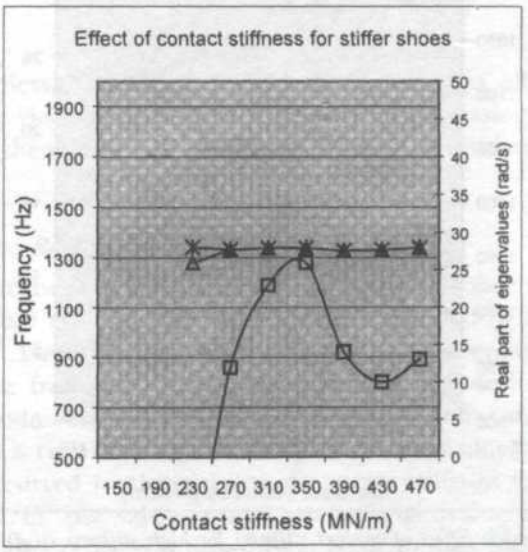

Fig. 12: Effect of contact stiffness for higher Young's modulus of shoe back plate (μ=0.4)

The analysis showed that changing the stiffness of the shoe back plate with higher Young's modulus material has resulted in the number of unstable mode reduces from three to only one. This unstable mode is different from any of those occurring with the initial value of shoe back plate modulus of elasticity

and occurs in a quite wide range of contact stiffness values. Increasing the stiffness of the shoe back plate has also decreased the instability level. The improvement of the system stability is indicated by the relatively lower real part of the occurring unstable mode eigenvalues. On the other hand, the instability occurred in a relatively wider value of contact stiffness.

Effect of Drum Stiffness

The effect of drum stiffness for the occurrence of instability in the coupled drum-shoe is conducted by changing the material of the drum with the material similar to steel of AISI C1020 having Young's modulus of 207 GPa, density of 7800 kg/m^3, and Poison ratio of 0.29.

The result of the analysis is shown in *Fig. 13*. One unstable mode occurred in the range contact stiffness from 110 MN/m to 430 MN/m. The unstable mode occurred in the vicinity of 1200 Hz. The unstable mode consists of drum undergoing the first radial mode shape and shoe brake undergoing bending mode shape. The highest value of the real part of the unstable mode is 25 rad/s at a frequency of 1215 Hz.

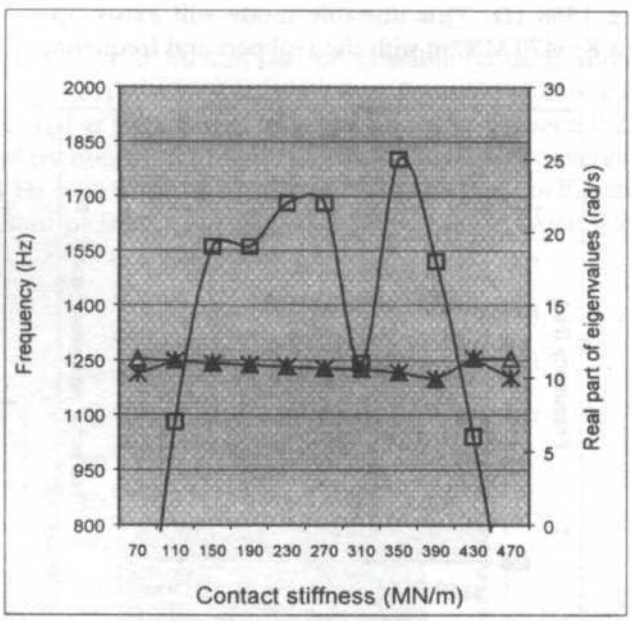

Fig. 13: Effect of contact stiffness for high stiffness (μ=0.4)

In the condition where the drum has lower stiffness (69 GPa), the unstable mode in the vicinity of 1200 Hz occurred within two contact stiffness ranges, between 90 MN/m and 230 MN/m and between 310 MN/ m and 410 MN/m. In the case where the drum stiffness is increased (E=207 GPa), the unstable mode in this vicinity occurred continuously in the range of contact stiffness from 110 MN/m to 430 MN/m.

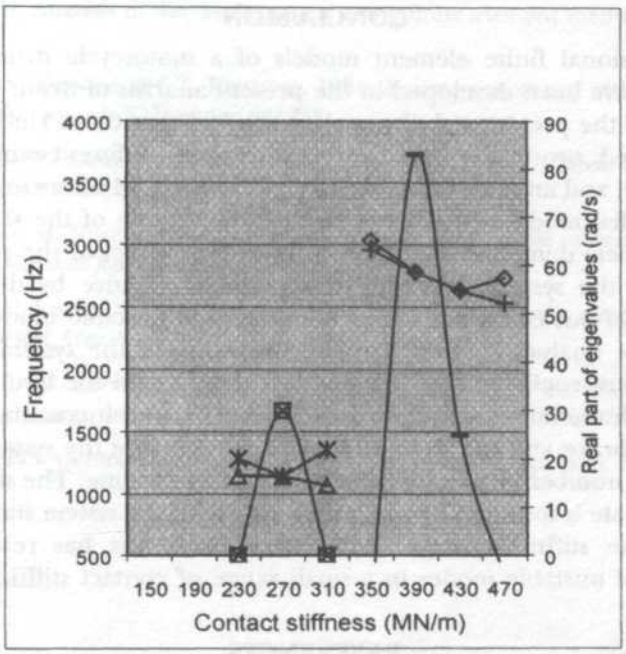

Fig. 14: The effect of contact stiffness for stiffer back plate ribs (μ=0.4)

Nevertheless, increasing the drum stiffness has eliminated one unstable mode in the vicinity of 2800 Hz. In addition, increasing the drum stiffness has also caused the occurring unstable mode to have a relatively lower value of real part.

Effect of Drum Back Plate Ribs Stiffness

The result of the stability analysis with stiffer back plate ribs is shown in *Fig. 14*. The back plate ribs modulus of elasticity is changed to 207 GPa with density of 7820 kg/m^3. Two unstable modes occurred at the frequency of 1141 Hz and the other in the frequency range between 2630 Hz and 2770 Hz. Both of the unstable modes occurred within a relatively small range of contact stiffness value but at a relatively higher real part of eigenvalues. The unstable mode at 1141 Hz occurred in the vicinity of contact stiffness value of 270 MN/m. At Kc=270 MN/m, the value of real part of eigenvalue is 30 rad/s. The other unstable mode occurred within the range of contact stiffness value between 350 MN/m and 470 MN/m. The highest value of real part of the unstable mode shape eigenvalue is 83 rad/s at contact stiffness of 390 MN/m.

Increasing the stiffness of the drum back plate ribs has significantly improved the system stability. Although two unstable modes still existed, they occurred at relatively small ranges of contact stiffness value.

CONCLUSION

Three-dimensional finite element models of a motorcycle drum brake and brake shoe have been developed in the present analysis of drum brake squeal. The result of the present stability analysis showed that three kinds of unstable mode occurred, two in the vicinity of 1230 Hz with different range of contact stiffness value, and another in the vicinity of 2140 Hz. All of the unstable modes consist of radial mode of the drum and bending mode of the shoes. The use of damping beta damping was found to have little effect of the occurrence of instability of the system. Damping was partially effective by decreasing the instability level but could not totally eliminate the unstable modes.

Parametric analysis showed that the instability of the system started at a value of friction coefficient, μ, between 0.3 and 0.4 and the level of instability increased with the increase in the coefficient of friction. Increasing the stiffness of the drum brake and the shoe back plate can improve the system stability by reducing the number of unstable modes from three to one. The stiffness of the drum back plate is found to be the most sensitive to the system stability because increasing the stiffness of the drum back plate ribs has resulted in the occurrence of unstable modes in a small range of contact stiffness value.

REFERENCES

ANSYS Theory References Version 6.0. 2001. Houston, USA: Swanson Analysis Inc.

Brooks, P. C, D. A. Crolla, A. M. Lang and D. R. Schafer. 1993. Eigenvalue sensitivity analysis applied to disc brake squeal. *Proc. I.Mech.E Conf. on Braking of Road Vehicle.* Paper C444/04/93. London.

Chung, C. H., W. Steed, K. Kobayashi and H. Nakata. 2001. A new analysis method for brake squeal part I: Theory for modal domain formulation and stability analysis. SAE paper 2001-01-1600.

Crolla, D. A. and A. M. Lang. 1991. Brake noise and vibration - The state of the art. *Vehicle Tribology*, Leeds-Lyon 17, Tribology series 18. p. 165 - 174. Elsevier Science Pub.

Ghesquire, H. and L. Castel. 1992. Brake squel noise and prediction. In *Proc. I.Mech.E. Conf. Autotech* paper C389/257.

Hamabe, T., I. Yamazaki, K. Yamada, H. Matsui and S. Nakagawa. 1999. Study of a method for reducing drum brake squeal. SAE Paper 99010144.

Hulten, J. 1995. Some drum brake squeal mechanisms. Sweden: Chalmer University of Technology.

Kung, S. W., K. B. Dunlap and R. S. Ballinger. 2000. Complex eigenvalue analysis for reducing low frequency brake squeal. SAE paper 00-01-0444.

Lang, A. M. 1994. An investigation into heavy vehicle drum brake squeal. Ph.D Thesis, Loughborough University of Technology, Loughborough, England.

Lang, A.M. and H. Smales. 1983. An approach to the solution of dics brake squeal problems. In *Proc. I.Mech.E. Conf. on Braking of Road Vehicle*, Loughborough, paper C37/83.

LILES, G.D. 1989. Analysis of disc brake squeal using finite element method. SAE paper 891150.

MURAKAMI, H., N. TSUNADA and T. KITAMURA. 1984. A study concerned with a mechanism of disc-brake squeal. SAE paper 841233.

NISHIWAKI, M. 1993. Generalized theory for brake noise. *Proc. I. Mech. E* **207**, Part D: *Journal of Automotive Engineering*. 195-202.

OKAMURA, H. and M. NISHIWAKI. 1989. A study on drum brake noise - drum brake squeal. *JSME International Journal Series III* **32:** 206-214.

PAPINNIEMI, A., C. JOSEPH, S. LAI, J. ZHAO and L. LOADER. 2002. Brake squeal: a literature review. *Applied Acoustic* **63:** 391-400. Elsevier Science Ltd.

RIPIN, Z. B. M., D. C. BARTON and D. A. CROLLA. 1995. Analysis of disc brake squeal using the finite element method. *I. Mech. E. Autotech 95*, paper C498/12/074.

SHERIF, H. A. 1993. Geometric induced instability in drum brakes. SAE Paper 93-30-72.

Pertanika J. Sci. & Technol. 12(2): 329 - 342 (2004)
ISSN: 0128-7680

Effect of Rare-Earth Sm Substitution and Heat Treatment on Superconducting Properties of $Bi_{1.6}Pb_{0.4}Sr_2(Ca_{1-x}Sm_x)_2Cu_3O_d$ Ceramics

[1]A. I. Malik, [2]S. A. Halim, [3]K. Khalid & [3]Z. A. Hassan

[1]Faculty of Engineering, Multimedia University,
Jalan Multimedia, 63100 Cyberjaya, Selangor, Malaysia
[2]Institute for Mathematical Research, Universiti Putra Malaysia,
43400 Serdang, Selangor, Malaysia
[3]Department of Physics, Faculty of Science and Environmental Studies,
Universiti Putra Malaysia, 43400 UPM Serdang, Selangor, Malaysia

Received: 8 July 2003

ABSTRAK

Satu siri sampel $Bi_{1.6}Pb_{0.4}Sr_2(Ca_{1-x}Sm_x)_2Cu_3O_d$, ($0 \leq x \leq 0.10$) yang didopkan dengan Sm telah disediakan melalui kaedah tindak balas keadaan pepejal lazim. Mikrostruktur, sifat elektrik dan magnet dikaji. Keputusan pembelauan sinar-X menunjukkan yang pecahan isi padu bagi fasa tinggi- T_c(2223) berkurangan dan fasa rendah- T_c(2212) bertambah apabila kepekatan Sm meningkat. Rawatan haba lanjutan pada suhu 830°C meningkatkan pecahan isi padu bagi fasa tinggi- T_c(2223) di dalam sampel. Pengukuran rintangan dan kerentanan AU menunjukkan penurunan berterusan bagi $T_{c(R=0)}$ dan $T_{c(onset)}$ apabila kepekatan Sm bertambah. Ketumpatan arus kritikal antara butiran bagi sampel dikaji dengan menggunakan model Bean. Parameter kekuatan pengepinan dan ketumpatan arus kritikal yang tinggi pada daerah suhu rendah diperoleh pada sampel yang kandungan Smnya tinggi.

ABSTRACT

A series of Sm substituted $Bi_{1.6}Pb_{0.4}Sr_2(Ca_{1-x}Sm_x)_2Cu_3O_d$, samples with $0 \leq x \leq 0.10$ have been prepared by the conventional solid state reaction method. Microstructure, electrical and magnetic properties were investigated. X-ray diffraction results show that the volume fraction of the high-T_c(2223) phase decreases and the low-T_c(2212) phase increases as Sm concentration increases. Extended heat treatment at 830°C increases the volume fraction of the former phase in the samples. The resistance and AC susceptibility measurements reveal that the $T_{c(R=0)}$ and the $T_{c(onset)}$ continue to decrease with increasing Sm content. The intergranular critical current density of the samples was investigated using the Bean's model. Higher pinning strength parameter and higher critical current densities at low temperature region were obtained in the samples with higher Sm content.

Keywords: High-temperature superconductor, pinning strength parameter, Sm substitution

INTRODUCTION

Since the discovery of high-T_c superconductivity in the Bi-Sr-Ca-Cu-O system (Maeda *et al.* 1988), a great number of studies have been published regarding

the preparation, the superconducting properties and the structure of these compounds. It is now well established that Bi-based cuprates belong to the homologous series $Bi_2Sr_2Ca_{n-1}Cu_nO_{2n+4+d}$ with specific transition temperatures ranging from 20K (2201 phase), 85K (2212 phase) and 110K (2223 phase), for n=1, 2 and 3, respectively. The difference between two consecutive phases is the addition of CuO_2-Ca-CuO_2 slab packed along the *c*-axis parameter. The *a*-and *b*-axis parameters remain almost unchanged. However, the highest T_c(2223) phase in the series is not easy to prepare in a single phase form. Partial substitution of Pb for Bi was found to increase the growth rate of the 2223 phase (Sastry *et al.* 1989, Ibrahim *et al.* 2000). It was also found that substitution or addition of elements having different character could change the properties of (BiPb)-Sr-Ca-Cu-O material (Zhigaldo *et al.* 1998, Halim *et al.* 1999). Thus the superconducting properties of the material are enhanced, suppressed or destroyed depending on the amount and the outcome of the substituent in the structure. Satyavathi *et al.* (1996) systematically studied the effect of Nd substitution on $Bi_{1.7}Pb_{0.3}Sr_2Ca_{1-x}Nd_xCu_3O_y$ system. They have found that the material exhibits superconductivity in the range $0.0 \leq x \leq 0.10$, and that the measured critical temperatures, $T_{c(R=0)}$ and $T_{c(onset)}$ were found to decrease with Nd content. Further, they found that T_c improved by vacuum annealing. It was also shown that substitution of Dy^{3+} for Ca^{2+} as well as appropriate annealing at moderate temperatures allowed optimization of the critical temperature of the 2212 phase for low doping ($x \leq 0.2$). Koyama *et al.* (1989) reported that on substitution of rare earth (RE=Pr, Nd), for Ca in $Bi_2Sr_2CaCu_2O_{8+d}$, the occurrence of superconductivity in the system depended strongly on the hole concentration. Furthermore, the decrease in T_c with increasing RE concentration (RE=Pr, Gd, Y, Ce), in 2212 phase was explained with reference to the insulating nature of Bi-O layers and a decrease in O 2p hole concentration in the Cu-O planes (Awana *et al.* 1993).

Although there have been extensive publications on rare earth element substitution for Ca in Bi-based systems, they have been focused mainly on the 2212 phase system. For the 2223 phase, Singh *et al.* (1998) and Sastry *et al.* (1994), have shown that substitution of (RE=Y, La, Pr, Nd, Sm, Eu, Gd and Tm), for Ca in (BiPb)-2223 system leads to the formation of RE-doped (BiPb)-2212 as a stable phase. They observed that the latter phase grows continuously with increasing RE. The T_c and the normal-state resistivity values were strongly dependent on the amount of RE. Kishore *et al.* (1993) explained the effect of Sm doping in $Bi_{1.7}Pb_{0.3}Sr_2Ca_{2-x}Sm_xCu_3O_d$ system $0 \leq x \leq 0.10$, on the basis of granular superconductivity. Recently, Khan *et al.* (1999) reported the effect of (RE=Eu, Yb) substitution for Ca in $Bi_{1.7}Pb_{0.3}Sr_2Ca_{1-x}RE_xCu_3O_d$ system. They also explained their results on the basis of possible variation of hole concentration with trivalent rare earth ion substitutions. In this paper, the results of a systematic study of the effect of Sm doping and heat treatment on the superconducting properties of (BiPb)-Sr-Ca-Cu-O ceramics are reported and compared with data available in the literature.

TABLE 1
List of $Bi_{1.6}Pb_{0.4}Sr_2(Ca_{1-x}Sm_x)_2Cu_3O_\delta$ samples with some fitting parameters

x	0.0	0.01	0.02	0.05	0.10
J_{cm0}(A/cm^2)	3.46×10^3	5.31×10^3	4.02×10^3	6.21×10^3	5.94×10^3
T_{cm}(K)	103.09	101.04	100.57	82.46	80.58
n	1.5045	1.6228	1.6219	1.7198	1.7655
$T_{c(onset)}$(K)	108.50	107.63	107.67	87.75	83.40

EXPERIMENT

The samples with nominal composition $Bi_{1.6}Pb_{0.4}Sr_2(Ca_{1-x}Sm_x)_2Cu_3O_\delta$ were prepared by means of the conventional solid state reaction route, with $0 \le x \le 0.10$. Stoichiometric amounts of Bi_2O_3, PbO, $SrCO_3$, $CaCO_3$, CuO and Sm_2O_3 of purity up to 99.9% were used as starting materials. The required quantities of the materials were weighed using a digital balance of 10^{-4}gm accuracy. The weighed powders were mixed and ball-milled in an alcohol medium for 24 hours. The mixture was dried in an oven at 120°C for 6 hours. To ensure homogeneity, the mixture was first calcined at 800°C for 20 hours. The second and the third calcination steps were made at 820 and 840°C for 10 and 5 hours with intermediate grinding. The resulting powder was ground and pulverized using a standard sieve of 25μm. 1.2 gram of the homogeneous powder was pressed into disc-shaped pellets and sintered in air at 855°C for 150 hours. A further annealing step was done at 830°C for 30 hours and then the pellet samples were cooled in air at a rate of 2°C/minute to the ambient temperature.

X-ray diffraction measurements were made using a SIEMENS model D-5000 X-ray diffractometer with CuK_α radiation (λ = 1.5418 Å). Electrical resistance was measured by standard four-point probe technique with silver epoxy as electrodes. AC susceptibility of the samples was measured with a commercial Lake Shore susceptometer model 7000. The dimensions ($2a \times 2b \times c$) of the samples for AC susceptibility measurements were 1.80mm × 2.10mm × 12.30mm. The sample was mounted in such a way that its length (c) was parallel to the direction of the magnetic field. The temperature adjustment was enhanced by using a closed cycle helium cryostat equipped with a temperature controller. The signals due to the in-phase and out-of-phase magnetization were recorded simultaneously.

RESULTS AND DISCUSSION

Figs. 1(a-f) show the room temperature X-ray diffraction patterns for the samples with x=0.0, 0.01 and 0.10, sintered at 855°C for 150h (*Figs. 1(a), (c), (e)*), and annealed at 830°C for 30h (*Figs. 1(b), (d) (f)*), respectively. The d-spacing values and the intensity ratios of the high-T_c(2223) and the low-T_c(2212) peaks were found to be in a good agreement with the data reported in the literature. It can be seen from *Fig. 1 (a)* that in the Sm-free sample, the high-T_c phase reflections are predominant compared with the low-T_c phase reflections. After annealing

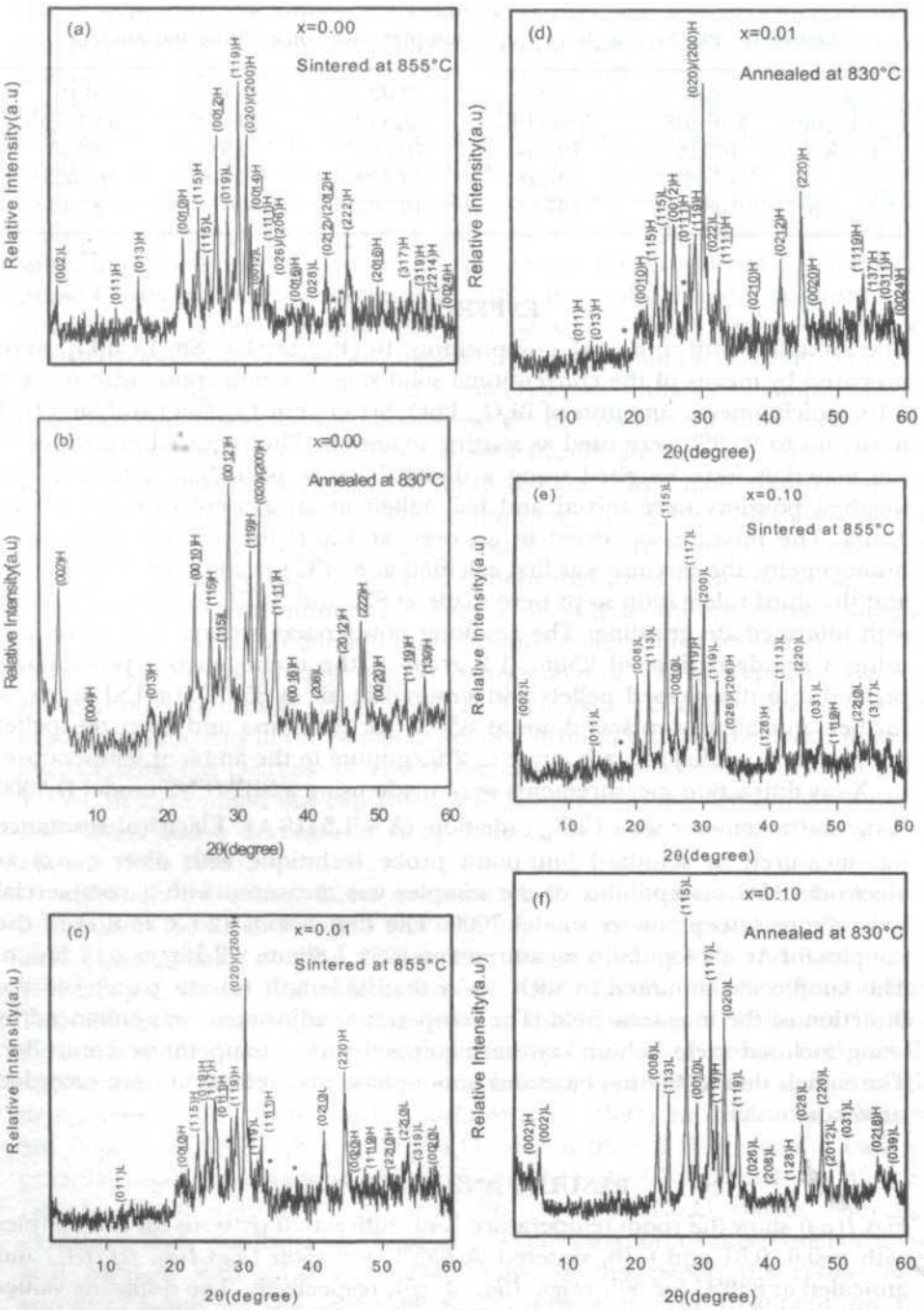

Fig. 1: (a-f) X-ray diffraction patterns for the $Bi_{1.6}Pb_{0.4}Sr_2(Ca_{1-x}Sm_x)_2Cu_3O_d$ samples with x=0.0, 0.01, and 0.10, sintered at 855°C for 150h (a), (c), (e), and annealed at 830°C for 30h (b), (d), (f). The indices H and L in the assignments of the peaks denotes the high-T_c(2223) and the low-T_c(2212) superconducting phases, respectively

(*Fig. 1b*), the intensities of the peaks corresponding to the high-T_c phase increase and there are no unidentified phases. Similar observations can be made from *Figs.1(c)* and *(d)* for the sample with an initial Sm content x=0.01. However, at the highest Sm concentration, the low-T_c reflections are predominant and the annealing step further increases the presence of this phase as shown in *Figs.1 (e)* and *(f)*.

To determine the volume fraction of the present phases, the following general expressions were used

$$Bi-2223(\%) = \{\Sigma I(2223)/[\Sigma I(2223) + I(2212) + I(other]\}x100 \quad (1)$$
$$Bi-2212(\%) = \{\Sigma I(2212)/[\Sigma I(2223) + I(2212) + I(other]\}x100$$

where I is the intensity of the phases present. The ratio of Bi-2223:Bi-2212 phases in the phase mixture for the sintered and annealed samples are given in *Fig.2* as a function of Sm content for all samples. The volume fraction of the high-T_c phase decreases with increasing Sm content while the volume of the low-T_c phase increases. It is interesting to observe from *Fig. 2* that annealing the samples at 830°C for 30h increased the volume fraction of the high-T_c phase throughout the doping range. Unit cell dimensions *a, c* for the annealed samples were refined by using the least square techniques. The samples with x=0.0, 0.01 (*Figs. 1 (b)* and *(d)*), have lattice parameters $a = 5.40$ Å and $c = 37.12$ Å while the lattice constants of the sample with x=0.10 are $a = 5.40$ Å and

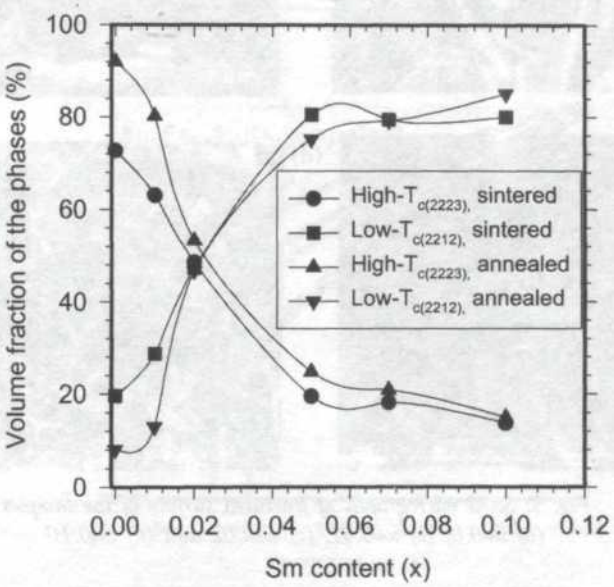

Fig. 2: The volume fraction (%) of the high-T_c(2223) and low-T_c(2212) phases as a function of Sm content x. Solid lines are to guide the eye only

c = 20.70 Å. The *c*-parameter of the low-T_c phase decreases with Sm content while the parameter *a* remains unchanged. Lattice parameters of the high-T_c phase do not show any systematic change, in agreement with previous results (Kishore *et al.* 1993; Khan *et al.* 1999). Hence it can be concluded that beyond x = 0.02, the solubility of Sm in the 2223 phase has reached its limit.

The morphologies of fractured surface of the annealed samples (x=0.0, 0.01, 0.02, 0.10) are shown in *Figs. 3 (a-d)*. For homogeneity and grain shape, each pellet was broken into two pieces and the area along the thickness was examined by a scanning electron microscope. In *Figs. 3 (a-c)*, thicker platelet-like layers with grain sizes of 10-30μm are observed. These well-compacted layers of high density consisting of empty cavities suggest that the final product of the material was formed through a liquid phase process. This observation is consistent with the specific structure reported for Bi-2223 phase (Azzouz *et al.* 2001). However, a slight change in the microstructure is observed in samples with higher Sm concentration as shown in *Fig. 3 (d)*. The layers are now less compact with a decrease in grain size and an increase in porosity.

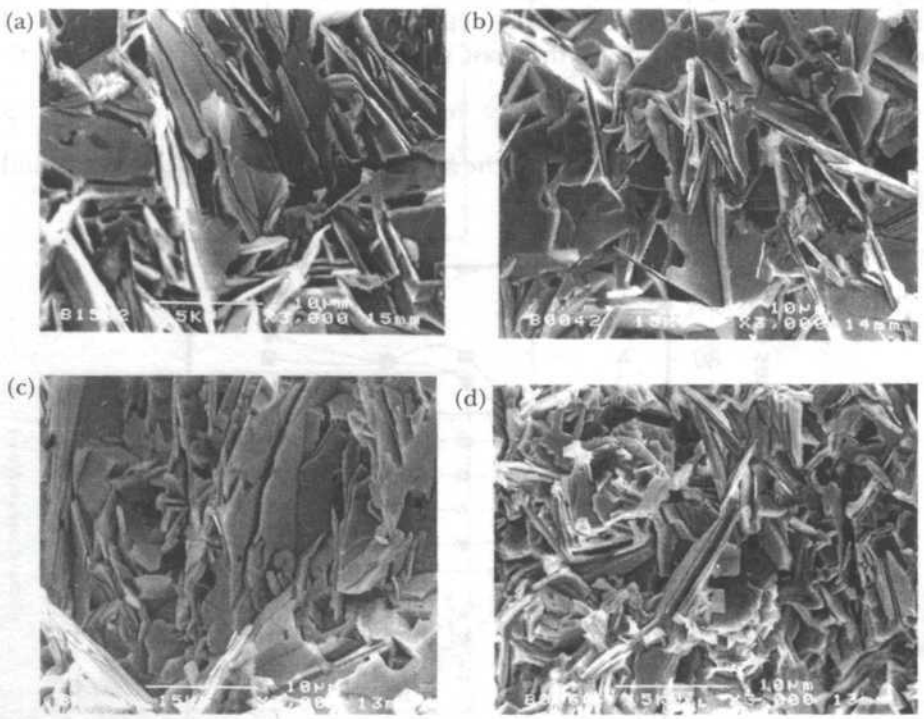

Fig. 3: SEM micrographs of fractured surface of the samples (a) x=0.0, (b) x=0.01, (c) x=0.02 and (d) x=0.10

Fig. 4 (b) shows the normalized resistance versus temperature, R(T) plots as a function of temperature and Sm content for all samples annealed at 830°C for 30h. The transition temperature $T_{c(R=0)}$ decreases and the metallic behavior of the samples increases with increasing Sm content. For the samples with x=0.0, 0.01, and 0.02, $T_{c(R=0)}$ is about 101.1, 98.7 and 98.0K, respectively, and their metallic behavior in the normal conducting state is almost the same. However, for the samples with x=0.05, 0.07 and 0.10, the values of $T_{c(R=0)}$ are 79.0, 78.0 and 76.0K, respectively. The transition width ΔT_c ($T_{c(onset)}$-$T_{c(R=0)}$), was around (9-12K) for the samples with x≤0.02, while it was 18K for the samples with higher Sm content. Similar behavior was previously observed for Sm doping in the Bi-2223 system. It is suggested that the sudden drop in T_c and the corresponding increase in ΔT_c for Sm concentration higher than x=0.02 is due

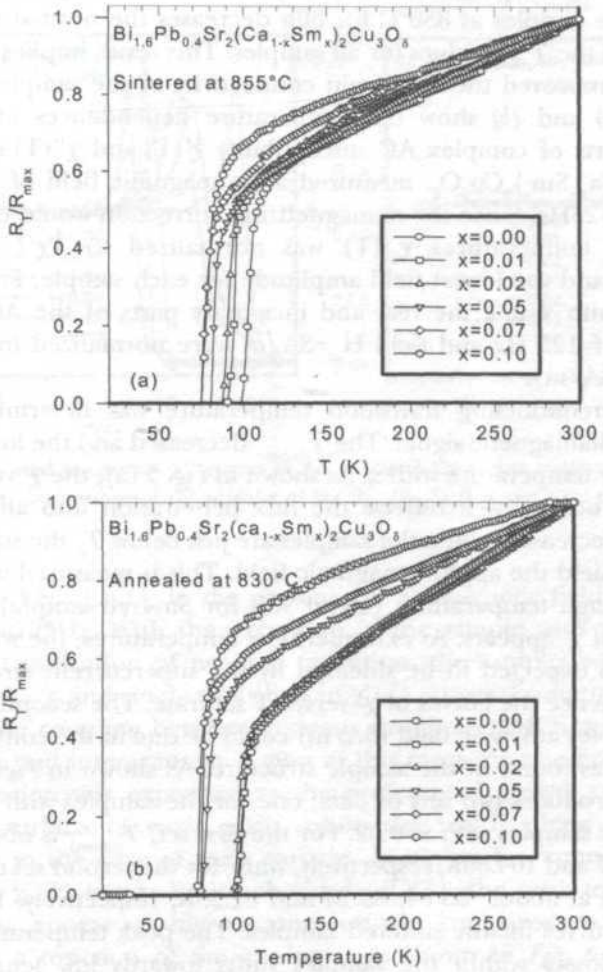

Fig. 4: The temperature dependence of normalized resistance for the sintered (a) and annealed (b) samples of the $Bi_{1.6}Pb_{0.4}Sr_2(Ca_{1-x}Sm_x)_2Cu_3O_d$ system (x=0.0-0.10)

to the attainment of the samarium solubility limit in the 2223 phase. It should be noted that the completion path of the superconducting transition $T_{c(R=0)}$ depends generally on the microstructure and phase composition of the multiphase polycrystalline samples. Therefore, the small kink in the resistance curve for the sample with x=0.07 indicates the presence of a small amount of 2223 phase, in agreement with X-ray diffraction results. A convincing explanation for the decrease of T_c and the change in X-ray data from 2223 phase to a majority of 2212 phase was given by numerous reports. Kishore *et al.* (1993) and Khan *et al.* (1999) have concluded that substitution of Ca^{2+} by (Sm^{3+}, Eu^{3+}, Yb^{3+}) provides additional electrons which in turn decrease the hole carrier concentration, leading to a decrease of T_c and of other superconducting properties of 2223 phase. The present observation is in agreement with this conclusion. For comparison, it is clearly evident from *Fig.4 (a)* and *4(b)* that annealing the samples at 830°C for 30h decreases the normal state resistance and increases the $T_{c(R=0)}$ values for all samples. This result implies that annealing process has improved the intergrain connectivity of the samples.

Figs. 5 (a) and *(b)* show the temperature dependences of the real and imaginary parts of complex AC susceptibility $\chi'(T)$ and $\chi''(T)$ of the sintered $Bi_{1.6}Pb_{0.4}Sr_2(Ca_{1-x}Sm_x)_2Cu_3O_\delta$, measured at ac magnetic field of 8A/m and the frequency f=125Hz. Since the demagnetizing correction would cause $\chi' = -1$ for low enough temperatures, $\chi_{ac}(T)$ was normalized to $|\chi'|$ at the lowest temperature and the lowest field amplitude for each sample. For example, for the sample with x=0.0, the real and imaginary parts of the AC susceptibility measured at f=125 Hz and field H_{ac}=8A/m were normalized to $|\chi'_{27}|$ (where T=27K, H_{ac}=8A/m).

The superconducting transition temperature was determined from the onset of the diamagnetic signal. The $T_{c(onset)}$ decreased and the loss peaks shifted towards lower temperature with x. As shown in *Fig. 5* (a), the χ' versus T displays a two-step process which reflects the flux penetration into and between the grains, as T decreases. When the samples are just below T_c, the superconducting grains first shield the applied magnetic field. This is measured as a negative χ'. At a low enough temperature; (about 95K for Sm-free sample), intergranular component of χ' appears. At extremely low temperatures, the whole volume of the sample is expected to be shielded by the supercurrent circulating in the sample and hence the curves of χ' versus T saturate. The second step transition in these samples at low ac field (8A/m) could be due to the contribution of the low-T_c phase as found in the sample structure. As shown in *Figs. 5 (a)* and *(b)*, Sm doping produces two sets of data; one for the samples with x=0.0-0.02, the other one for samples with x>0.02. For the first set, $T_{c(onset)}$ is observed at about 107.84, 105.77 and 104.80K, respectively, while for the second set the diamagnetic signal started at about 85.84, 83.20 and 82.53K, respectively. In *Fig. 5 (b)* we show $\chi''(T)$ curves for the sintered samples. The peak temperature T_p that is a measure of losses within the samples shifts towards low temperatures with increasing Sm content x. In *Figs. 5(c)* and *(d)* we present the temperature variation of the AC susceptibility $\chi'(T)$ and $\chi''(T)$ curves of the annealed

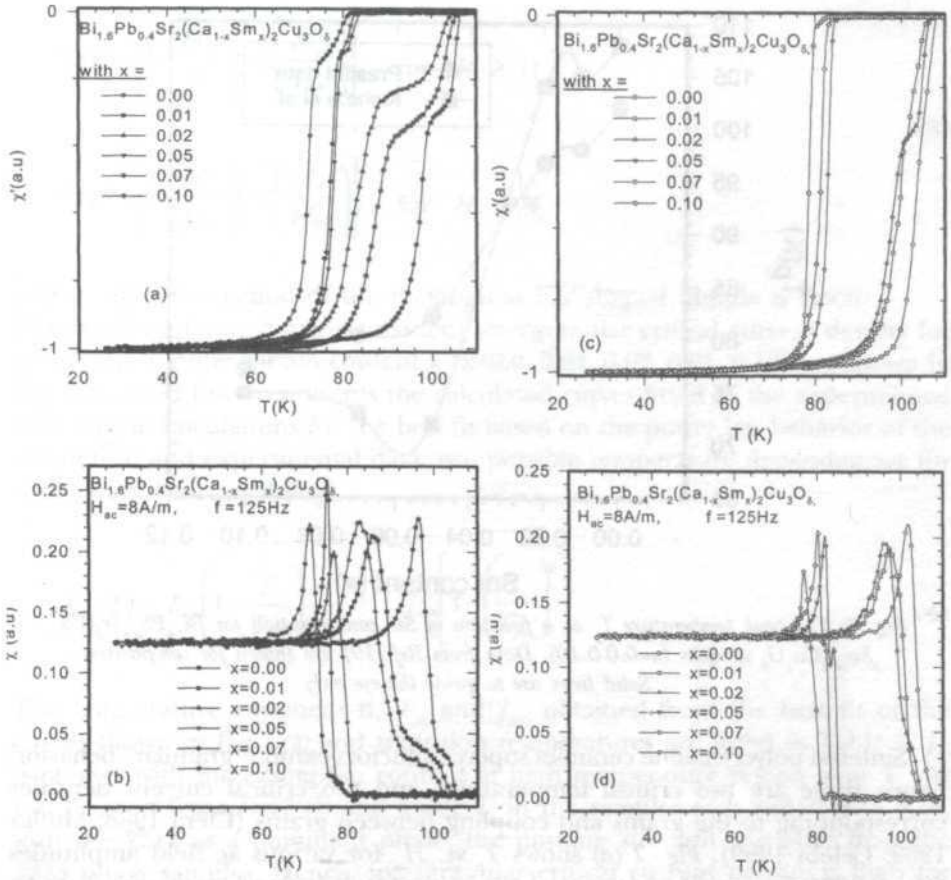

Fig. 5: Real χ' and imaginary χ'' curves of AC susceptibility versus temperature for some sintered (a) and annealed (b) samples of the $Bi_{1.6}Pb_{0.4}Sr_2(Ca_{1-x}Sm_x)_2Cu_3O_d$ system

$Bi_{1.6}Pb_{0.4}Sr_2(Ca_{1-x}Sm_x)_2Cu_3O_d$ in the presence of ac magnetic field 8A/m at the frequency of f=125Hz. With the exception of the sample with x=0.01, which exhibits a faint indication of two-step transition, the samples with x=0.0 and 0.02 exhibit a sharp and single transition in $\chi'(T)$ curves. From this, it could be inferred that the coupling between grains is strong enough not to distinguish between grains and intergranular region at this measuring ac field amplitude. Similar observation was explained as the preferential growth of the high-T_c phase at the surface of each grain, while the low-T_c phase seems to be predominantly in the core of each particle. At higher Sm concentration, the second step in $\chi'(T)$ curves is also absent. In $\chi''(T)$, the peak temperature T_p for all samples appear at higher temperatures compared to the sintered samples. T_p as a function of Sm content x is shown in *Fig. 6* for annealed samples together with the data of Kishore *et al.* (1993). Contrary to T_p values at low Sm content ($x \leq 0.02$), our T_p values are high at higher Sm content. We attribute these differences to the slight difference in our preparation process.

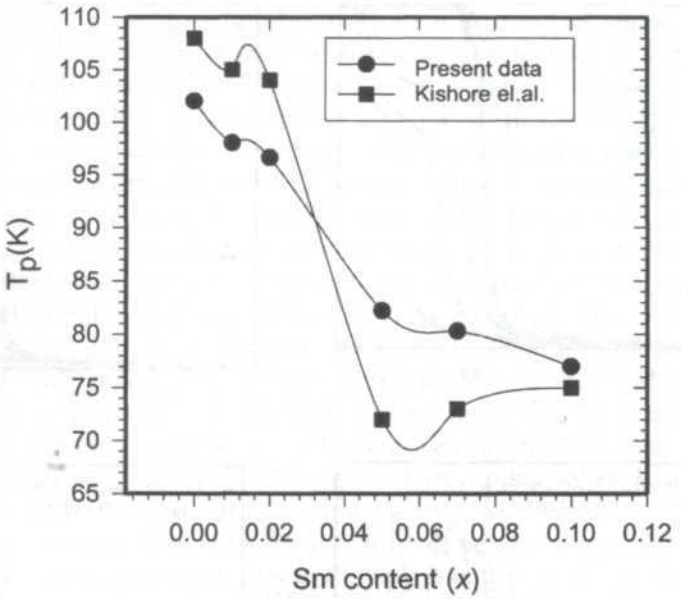

Fig. 6: The peak temperature T_p as a function of Sm concentration for $Bi_{1.6}Pb_{0.4}Sr_2(Ca_{1-x}Sm_x)_2Cu_3O_d$ samples (x=0.0-0.10). Data from Ref.[19] are shown for comparison. Solid lines are to guide the eye only

Sintered polycrystalline ceramics superconductors exhibit "granular" behavior; hence there are two critical temperatures and two critical current densities corresponding to the grains and coupling between grains (Clem 1988; Muller 1989; Çelebi 1999). *Fig. 7 (a)* shows T_p vs. H_{ac} for various ac field amplitudes (H_{ac}=8-800A/m (rms)) for some selected samples. It is clearly seen that T_p shifts to a lower temperature with a small increase in H_{ac}. This is the characteristic feature of intergranular region where its critical current density J_c is less compared to the superconducting grains. Therefore, the low temperature peak T_p is attributed to intergranular flux penetration of intergranular critical current density J_{cm} (matrix) in the sample. The amount of the shift as a function of ac field amplitude is proportional to the magnitude or strength of the pinning force. The larger the shift in the maxima of χ'', the weaker the pinning and hence the smaller J_{cm} will be. When the flux lines fully penetrate the sample, i.e., when H_m (H_m corresponds to $\sqrt{2}\ H_{ac}$(rms)) is equal to the first full penetration field H_* the losses reach a maximum. Consequently, one can estimate the temperature dependence of the intergranular critical current density using the Bean model (Bean 1964). According to the Bean model, the critical current density at the peak temperature T_p of the imaginary part of the AC susceptibility for cylindrical geometry can be written as

$$J_c(T_p) = H_*/a \approx H_* / \sqrt{ab} \qquad (2)$$

$$3\pi\chi'' = \left[\left(4\frac{H_m}{H_*}\right) - 2\left(\frac{H_m}{H_*}\right)\right] \quad \text{for} \quad H_* \geq H_m$$

$$3\pi\chi'' = \left[\left(4\frac{H_*}{H_m}\right) - 2\left(\frac{H_*}{Hm}\right)\right] \quad \text{for} \quad H_* \leq H_m \tag{3}$$

where the cross section of the rectangular bar shaped sample is 2a×2b .
The resulting temperature-dependent intergranular critical current density for samples with different Sm content x (x=0.0, 0.01, 0.02, 0.05, 0.10) are shown in *Fig. 7(b)*. Solid lines represents the calculated curves fitted to the experimental data. In the calculations for the best fit based on the power law behavior of the theoretical and experimental data, two possible temperature dependencies for $J_{cm}(T)$ have been exploited

$$J_{cm}(T) = J_{cm}\left(1-\frac{T}{T_{cm}}\right) \qquad J_{cm}\left[1-\left(\frac{T}{T_{cm}}\right)^2\right] \tag{4}$$

The temperature exponent n, T_{cm} and J_{cm0} obtained from the best fit of the curves shown in *Fig.7 (b)* and transition temperatures are listed in Table 1. J_{cm} decreases with increasing Sm content at high temperature region near T_c. As can be seen from *Fig.7 (b)* and Table 1, in the samples with x=0.05 and 0.10, with the 2212 as a dominant phase, the pinning strength is higher than the 2223 phase samples. Hence, intergranular critical current density is high for these samples at low temperature region. Thus higher Sm content may contribute to the formation of 2212 phase and also increases the intergranular pinning strength. We noted in our previous articles (Çelebi *et al.* 2002; Malik *et al.* 2002) that J_{cm} dependence of Nd contents in Nd-doped BPSCCO have some crossover temperatures. The same behavior can also be seen in *Fig. 7 (b)*. Such a behavior may be attributed to the multiphase granular structure of these samples.

CONCLUSIONS

Samples with (x=0.0-0.10) Sm at Ca position in the nominal composition $Bi_{1.6}Pb_{0.4}Sr_2(Ca_{1-x}Sm_x)_2Cu_3O_\delta$ system have been prepared by means of the solid state reaction method. Microstructure, electrical and magnetic properties were measured for the sintered and subsequently annealed samples. Substitution of Sm for Ca was found to change the superconducting properties of the system drastically. The volume fraction of the high-T_c decreases and that for the low-T_c phase increases through the substitution range. The c-axis parameter decreased with Sm from 37.12 Å to 30.80 Å. The electrical resistance and AC susceptibility

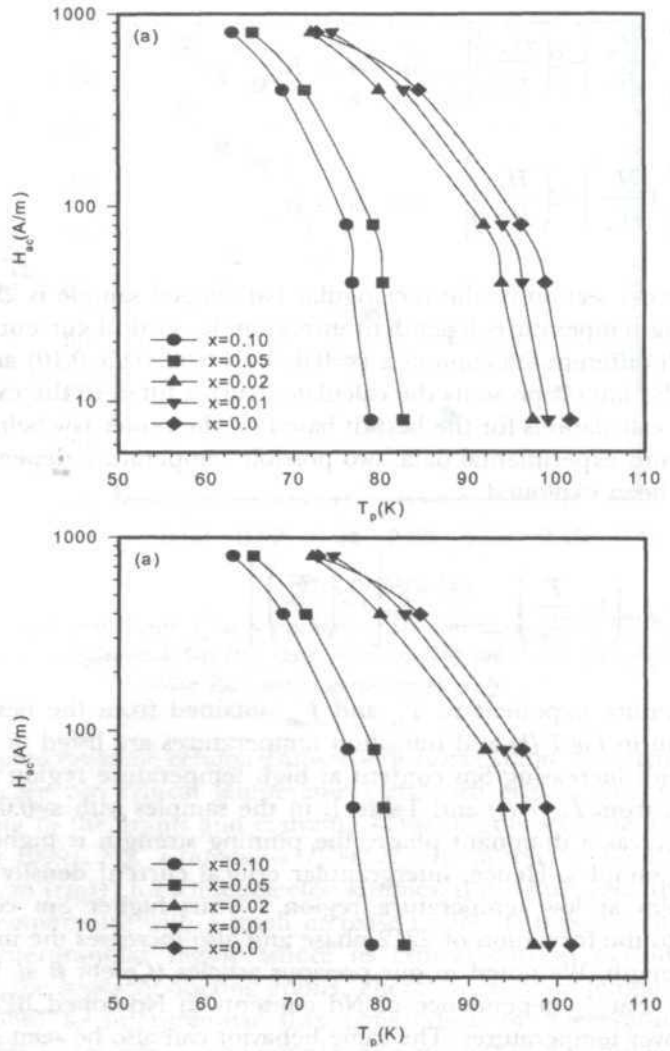

Fig. 7: The peak temperature T_p versus applied magnetic field H_{ac} for the samples with x=0.0, 0.01, 0.02, 0.05 and 0.10 (a) and the temperature dependence of the intergranular critical current density J_{cm} at T_p for the samples with different Sm content x (b)

measurements show that the $T_{c(R=0)}$ and $T_{c(onset)}$ are less affected with Sm content up to x=0.02, whereas these transition temperatures are seen well below 90K at higher Sm content. Annealing at 830°C results in an improvement in the volume fraction of the high-T_c phase and the intergrain superconductivity of the samples. This fact is proved by the decrease of the normal state resistance of the R(T) curves, the single step transition and the shift of the loss peak temperature T_p to higher temperatures in $\chi_{AC}(T,H_{ac})$ curves.

Despite Sm contribution to the formation of the 2212 phase in the samples, the effect of Sm substitution on the intergranular properties of the samples was

found to increase the pinning strength and hence the intergranular critical current density at low temperature region.

ACKNOWLEDGEMENTS

This work was supported by the Ministry of Science, Technology and Environment, Malaysia under the IRPA vote: 4-07-05-026. One of the authors (AIM) gratefully appreciates fruitful discussions with Professor S. ÇELEBI at the Department of Physics, Faculty of Science and Arts of Karadeniz Technical University, Turkey on the pinning behavior of the samples.

REFERENCES

AWANA, V. P. S., S. K. AGARWALL, A. V. NARLIKAR and M. P. DAS. 1993. Superconductivity in Pr-doped $Bi_2CaSr_2Cu_2O_y$ systems. *Phys. Rev. B* **48**: 1211-1216.

AZZOUZ, F. B., A. MCHIRGUI, B. YANGUI, C. BOULESTEIX and M. B. SALEM. 2001. Synthesis, microstructural evolution and the role of substantial addition of PbO during the final processing of (Bi,Pb)-2223 superconductors. *Physica C* **356**: 78-96.

BEAN, C. P. 1964. Magentization of high-field superconductors. *Rev. Mod. Phys.* **36**: 31-39.

CLEM, J. R. 1988. Granular and superconducting-glass properties of the high-temperature superconductors. *Physica C* **153**: 50-55.

ÇELEBI, S. 1999. Comparative AC susceptibility analysis on Bi-(Pb)-Sr-Ca-Cu-O high-T_c superconductors. *Physica C* **316**: 251-256.

ÇELEBI, S., A. I. MALIK and S. A. HALIM. 2002. Study of Nd substitution in Bi-(Pb)-Sr-Ca-Cu-O high-Tc superconductors. *J. Alloys and Compounds* **337**: 237-242.

HALIM, S. A., S. B. MOHAMED, S. A. KHAWALDEH and H. A. A. SIDEK. 1999. Effect of barium doping in Bi-Pb-Sr-Ca-Cu-O ceramics superconductors. *Physica C* **312**: 78-84.

IBRAHIM, M. M., S. M. KHALIL and A. M. AHMED. 2000. Effect of Pb addition on thermoelectric power and microhardness of Bi-Pb-Sr-Ca-Cu-O superconductors. *J.Phys. Chem. of Solids.* **61**: 1553-1560.

KHAN, M. N. and M. KHIZAR. 1999. Effect of rare-earth (Eu, Yb and Ag) substitutions on superconducting properties of the $Bi_{1.7}Pb_{0.3}Sr_2Ca_{2-x}R_x$(R= Eu, Yb, and Ag)$Cu_3O_y$ system. *J. Mater. Sci.* **34**: 5833-5838.

KISHORE, K. N., M. MURALIDHAR and V. H. BABU. 1993. Effect of rare-earth Sm^{3+} substitution on the superconducting properties of the $Bi_{1.7}Pb_{0.3}Sr_2Ca_{2-x}Sm_xCu_3O_y$ system. *Physica C* **204**: 299-304.

KOYAMA, K., S. KANNO and S. NOGUCHI. 1989. Electrical, magnetic and superconducting properties of the high-T_c superconductor $Bi_2Sr_2Ca_{1-x}RE_xCu_2O_{8+d}$ (RE= Nd and Pr). *Jpn. J. Appl. Phys.* **28**: 1354-1357.

MAEDA, H., Y. TANAKA, M. FUKUTOMI and T. ASANO. 1988. A new high-T_c superconductor without a rare earth element. *Jpn. J. Appl. Phys.* **27**: L209-210.

MALIK, A. I., S. ÇELEBI and S. A. HALIM. 2002. AC susceptibility study in Bi1.6Pb0.4Sr2$(Ca_{1-x}Nd_x)$2Cu3Od ceramic superconductors. *Physica C* **377**: 421- 430.

MULLER, K. H. 1989. AC susceptibility of high temperature superconductors in a critical state model. *Physica C* **159**: 717-726.

SINGH, R., A. GUPTA, S. K. AGARWAL, D. P. SINGH and A. V. NARLIKAR. 1998. Superconductivity in Pr-doped $Bi_2Ca_2Sr_2Cu_3O_y$. *Supercond. Sci. Technol.* **11**: 311-314.

SASTRY, P.V. P.S. S., J. V. YAKHMI and R. M. IYER. 1989. Towards the synthesis of the single-phase Bi-2223 superconductor from stoichiometric $(Bi,Pb)_2Ca_2Sr_2Cu_3O_y$ compositions. *Physica C* **161**: 656-660.

SASTRY, P. V. P. S. S., J. V. YAKHMI and R. M. IYER. 1994. Instability of Y-and rare earth-substituted Bi(Pb)-2223 phase. *J. Mater. Chem.* **4**: 1077-1079.

SATYAVATHI, S., K. N. KISHORE, V. H. BABU and O. PENA. 1996. Systematics of the physical properties of $Bi_{1.7}Pb_{0.3}Sr_2(Ca,Nd)_1Cu_2O_y$ compounds. *Supercond. Sci. Technol.* **9**: 93-98.

ZHIGADLO, N. D., V. V. PETRESHKO, YU. A. SEMENKO, C. PANAGOPOULOS, J. R. COOPER and E. K. H. SALJE. 1998. The effects of Cs doping, heat treatments on the phase formation and superconducting properties of (Bi,Pb)-Sr-Ca-Cu-O ceramics. *Physica C* **299**: 327-337.

Pertanika J. Sci. & Technol. 12(2): 343 - 356 (2004)
ISSN: 0128-7680

Mapped Coordinate Transformation for Numerical Solution of Transient Natural Convection

Rimfiel B. Janius & [1]Bryan M. Jenkins[1]
Department of Biological and Agricultural Engineering
Faculty of Engineering
Universiti Putra Malaysia
43400 UPM, Serdang, Selangor, Malaysia
[1]Department of Biological and Agricultural Engineering
University of California Davis
California 95616, USA

Received: 9 July 2003

ABSTRAK

Satu kaedah transformasi telah dibangunkan bagi pengiraan ciri-ciri bendalir dalam olakan tabie transien dalam satu kepongan yang bersempadan tidak sekata. Rantau kepongan ditransformasikan kepada satu domain kiraan segi empat sama dengan menggunakan kaedah koordinat padanan sempadan. Transformasi koordinat fizikal kepongan tak sekata kepada koordinat kiraan dilakukan menerusi satu teknik pemetaan dalam mana kenyataan transformasi diberi dalam bentuk persamaan pembezaan separa. Kaedah transformasi yang dibangunkan memberi hasil transien yang hampir sama dengan hasil karya lain, dan pada keadaan mantap keputusan yang didapati adalah bersamaan tepat. Penggunaan kaedah tersebut pada olakan tabie dalam geometri berbentuk gabel dibincangkan.

ABSTRACT

A transformation scheme is developed for the numerical calculation of the properties of fluid in transient natural convection in an enclosure with irregular boundaries. The enclosure region is transformed to a square computational domain using the boundary fitted coordinate method. Transformation of the physical coordinates of the irregular enclosure into computational coordinates is done through a mapping technique in which the transformation expressions are given in the form of partial differential equations. The transformation method developed gives very close agreement for transient values as compared to the literature and when a steady state is reached, the results concur. Application of the method to natural convection in a gable-shaped geometry is discussed.

Keywords: Irregular geometry, mapped coordinate, natural convection

INTRODUCTION

The equations governing natural convection are the continuity, momentum (the full Navier-Stokes equations) and energy equations and are well documented in any heat transfer or fluid flow texts. Numerical solution of transient natural convection requires the simultaneous solution of these equations due to the

Nomenclature

Roman symbols:

g = gravitational acceleration, ms^{-2}
H = characteristic length
= width of greenhouse, m
p = pressure, Pa
t = non-dimensional time
T = temperature, K
u = horizontal velocity, ms^{-1}
v = vertical velocity, ms^{-1}
x = horizontal coordinate direction of physical domain
y = vertical coordinate direction of physical domain
Gr = Grashof number
Pr = Prandtl number = $\frac{\nu}{\alpha}$
X_ξ = $\frac{\partial X}{\partial \xi}$; similar notations for X_η, Y_ξ, Y_η, F_x, F_y

Greek symbols:

α = thermal diffusivity, m^2s^{-1}; also transformation relation defined below
θ = temperature (non-dimensional)
ξ = horizontal coordinate direction of computational domain
η = vertical coordinate direction of computational domain
ρ = density, kgm^{-3}
τ = time, s
μ = dynamic viscosity, Nsm^{-2}
ν = kinematic viscosity, m^2s^{-1}
ψ = stream function (nondimensional)
ω = vorticity (non-dimensional)
α = partial differential operator
Φ = viscous dissipation function
ξ_x = $\frac{\partial \xi}{\partial X}$; similar notations for x_y, η_x, η_y

coupling of the momentum equation to the energy equation via the body force term. As a result, the calculation becomes very tedious and time-consuming and many computational studies were almost always made on regular geometries such as rectangles, squares, cuboids, circles, cylinders, spheres and annuli. Irregularly shaped geometries were little considered because of the difficulty in defining the coordinates of the boundaries. In practice, however, most fluid flow problems occur in or around irregularly shaped geometries. The mapped coordinate transformation allows for the solution of fluid flow problems involving irregularly shaped geometries. By this method the computational simplicity of finite difference approaches is combined with the geometric flexibility of finite-element techniques.

Natural convection is evaluated at constant fluid thermo-physical properties except for the density in the body-force term of the vertical momentum equation. This last quantity is the driving force behind natural convection. The governing equations are simplified through the application of the Boussinesq approximation and the assumption of incompressible fluid, constant pressure and negligible viscous dissipation. By further non-dimensionalizing the variables as follows;

$$X=\frac{x}{H},\ Y\frac{y}{H},\ U\frac{uH}{\alpha},\ V\frac{vH}{\alpha},\ \theta=\frac{T-T_r}{\Delta T},\ t=\frac{\tau\alpha}{H^2} \qquad \text{(1a,b,c,d,e,f)}$$

and then rewriting the resulting equations in terms of the vorticity-stream function formulation through the use of the following definitions:

$$U=\frac{\partial \psi}{\partial Y},\ V=-\frac{\partial \psi}{\partial X},\ \omega=\frac{\partial V}{\partial X}-\frac{\partial U}{\partial Y} \qquad (2a,b,c)$$

the final set of equations to be solved simultaneously, with the unknown field variables being the stream function, ψ, vorticity, ω, and temperature, θ, are:

a) the stream function equation

$$\frac{\partial^2 \psi}{\partial X^2}+\frac{\partial^2 \psi}{\partial Y^2}=-\omega \qquad (3)$$

b) the vorticity equation

$$\frac{\partial \omega}{\partial t}+U\frac{\partial \omega}{\partial X}+V\frac{\partial \omega}{\partial Y}=Pr\left(\frac{\partial^2 \omega}{\partial X^2}+\frac{\partial^2 \omega}{\partial Y^2}\right)+Gr\,Pr^2\frac{\partial \theta}{\partial X} \qquad (4)$$

c) the energy equation

$$\frac{\partial \theta}{\partial t}+U\frac{\partial \theta}{\partial X}+V\frac{\partial \theta}{\partial Y}=\frac{\partial^2 \theta}{\partial X^2}+\frac{\partial^2 \theta}{\partial Y^2} \qquad (5)$$

Transformation of the Governing Equations

To overcome the difficulties associated with irregular boundaries, a mapped coordinate transformation is used. In this transformation the irregular physical domain is transformed to a regular computational domain whose shape can either be rectangular or square. All calculations are carried out on the computational domain. Results of the calculations are then transformed back to the physical domain. The governing equations therefore must be transformed from the X,Y independent variables of the physical domain to the (ξ,η) independent variables of the computational domain. Each point (ξ,η) in the computational domain corresponds to a point (X,Y) in the physical domain. The corresponding X-coordinate of (ξ_1,η_1) is X (ξ_1,η_1) while that of Y is Y (ξ_1,η_1). This relation is shown in *Fig. 1.* A grid generation routine computes the values of the corresponding X,Y coordinates of the physical domain at each ξ,η grid point in the computational domain. For convenience in the calculation of the field variables ψ, ω and θ in the computational domain, the grid spacing of the domain $\delta\xi$ and $\delta\eta$ were both taken to be equal to unity. Therefore, if the number of grid points used in the δ and η directions is the same, the computational domain is a square.

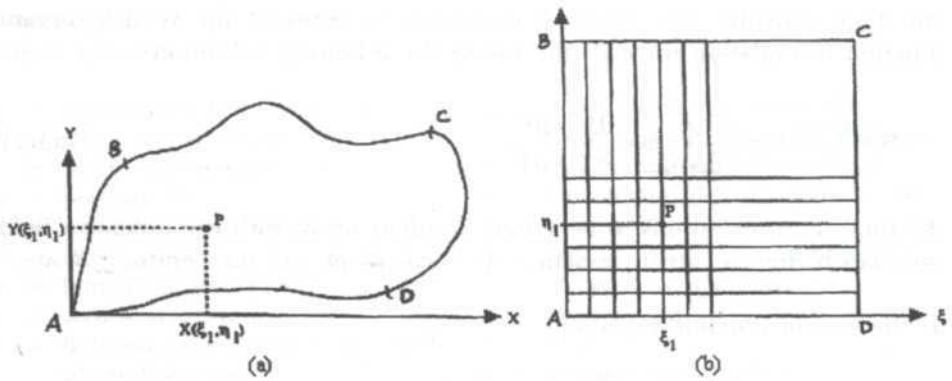

Fig. 1: Corresponding locations of points P in (a) physical and (b) computational domains

Thompson *et al.* (1985) gives the transformation relations for the first derivatives of any function, F, with respect to the independent variables, X and Y, as:

$$F_X = \frac{1}{J}\left\{(Y_\eta F)_\xi - (Y_\xi F)_\eta\right\} \tag{6a}$$

$$F_Y = \frac{1}{J}\left\{-(X_\eta F)_\xi + (X_\xi F)_\eta\right\} \tag{6b}$$

where

J = $(X_\xi Y_\eta - X_\eta Y_\xi)$, the Jacobian of the transformation.

The stream function equation, (3) is an elliptic Poisson equation. In deriving the transformation of the Laplacian part of the equation, the transformation of the second derivatives is obtained by using the transformation relations of the first derivatives above and the chain rule of differentiation. Hence:

$$\nabla^2 F = \frac{1}{J^2}\left\{\alpha F_{\xi\xi} - 2\beta F_{\xi\eta} + \gamma F_{\eta\eta}\right\} + PF_\xi + QF_\eta \tag{7}$$

where:

$\nabla^2 F \equiv F_{XX} + F_{YY}$ $\qquad$ $\alpha = X_\eta^2 + Y_\eta^2$

$\beta = X_\xi X_\eta + Y_\xi Y_\eta$ $\qquad$ $\lambda = X_\eta^2 + Y_\xi^2$

$P = \nabla^2\xi$ = grid control function. $\qquad$ $Q = \nabla^2\eta$ = grid control function.

Grid control functions enable the coordinate lines and to be concentrated towards a specific coordinate line or about a specific point. In this study, grid control is not employed and P and Q in equation (7) are set to zero. In transforming the governing partial differential equations (3), (4) and (5), the derivatives with respect to the X and Y variables are transformed. Velocities U and V are derivatives of ψ with respect to the X and Y variables as shown in equations (2a,b) and therefore need to be transformed.

Following from (7), the transformation of the stream function equation, (3), ($F = \psi$), is:

$$\frac{\alpha}{J^2}\psi_{\xi\xi} - \frac{2\beta}{J^2}\psi_{\xi\eta} + \frac{\gamma}{J^2}\psi_{\eta\eta} = -\omega \tag{8}$$

The vorticity equation (4) is transformed to:

$$\frac{\partial\omega}{\partial t} + \frac{1}{J}\left(\psi_\eta\omega_\xi - \psi_\xi\psi_\eta\right) - \frac{Pr}{J^2}\left(\alpha\omega_{\xi\xi} - 2\beta\omega_{\xi\eta} + \gamma\omega_{\eta\eta}\right) \tag{9}$$

$$-\frac{Gr\,Pr^2}{J}\left(Y_\eta\theta_\xi - Y_\xi\theta_\eta\right) = 0$$

The energy equation (5) is transformed to:

$$\frac{\partial\theta}{\partial t} + \frac{1}{J}\left(\psi_\eta\theta_\xi - \psi_\xi\theta_\eta\right) - \frac{1}{J^2}\left(\alpha\theta_{\xi\xi} - 2\beta\theta_{\xi\eta} + \gamma\theta_{\eta\eta}\right) = 0 \tag{10}$$

Equations (8), (9) and (10) are the final transformed field equations describing natural convection. The coupling of the energy equation to the vertical momentum equation is retained in the final transformed form above whereby the energy equation (10) is coupled to the vorticity equation (9) via the temperature terms. A numerical procedure employing the fully implicit method of discretisation is used. The velocities in the two nonlinear convection terms in the vorticity and energy transport equations are lagged by one time step to linearise the terms. To illustrate the linearisation process, the convective terms of the vorticity equation at time level n+1 are treated thus:

$$\frac{1}{J}\left(\psi_\eta\omega_\xi - \psi_\xi\omega_\eta\right)^{n+1} \tag{11}$$

$$= \frac{1}{J}\left(\psi_\eta^{n+1}\omega_\xi^{n+1} - \psi_\xi^{n+1}\omega_\eta^{n+1}\right)$$

$$= \frac{1}{J}\left(\psi_\eta^{n}\omega_\xi^{n+1} - \psi_\xi^{n}\omega_\eta^{n+1}\right)$$

To obtain a physically realistic and stable solution, especially at higher Grashof number, two-point upwinding is applied to these velocities (Roache 1972; Patankar 1980). In the two-point upwinding scheme the value of the velocity at any point is taken to be equal to that of the upstream point. Janius (1996) gives a detailed description of this lengthy scheme. The code developed is validated against and found to agree with the works of Kublbeck *et al.* (1980) and Hyun and Lee (1989).

RESULTS AND DISCUSSION

Verification of Solution Method

The validity of the solution code for equations (8), (9) and (10) was verified by running it on two problems with known solutions. Works of Kublbeck *et al.* (1980) and Hyun and Lee (1989) were used as reference cases. Both modeled empty square cavities without partitions and employed Boussinesq approximation, neglected viscous dissipation and gave rigid no-slip boundaries at all walls. No-slip boundaries are a source of vorticities and the elliptic stream function equation was used to obtain the vorticities at the boundaries. Thus, all discretised boundary equations for stream function, vorticity and temperature apply to both Kublbeck *et al.* (1980) and Hyun and Lee (1989).

The square cavity of Kublbeck *et al.* (1980) had differentially-heated side walls and adiabatic top and bottom walls. The left wall was at a non-dimensional temperature of zero with the right wall at 1. The simulation was run on a 21 by 21 mesh with a non-dimensional time step equivalent to 2 s for both air and water as was done by Kublbeck *et al.* (1980). Table 1 compares the maximum values of the stream function for air and water obtained with the solution code against those of Kublbeck *et al.* (1980).

In Table 2 the minimum and maximum values of the vorticity for air (Pr=0.733) are compared, while Table 3 compares those of water (Pr=6.983). The difference in the values before reaching steady state can be attributed to

TABLE 1
Comparison of maximum stream function values, Gr=2E04

time, s	Air (Pr = 0.733)		Water (Pr = 6.983)	
	Kublbeck *et al.* (1980)	Validation	Kublbeck *et al.* (1980)	Validation
200	0.366	0.319	12.8	13.1
400	0.801	0.691	25.0	25.7
800	1.812	1.563	31.8	30.9
1600	4.253	3.623	17.0	17.0
2500	6.966	6.236	15.7	15.7
5000	6.930	7.460	15.2	15.1
10000	6.299	6.282	15.2	15.2
20000	6.270	6.271	15.2	15.2

TABLE 2
Comparison of minimum and maximum vorticity values for air (Pr=0.733), Gr=2E04

time, s	Minimum		Maximum	
	Kublbeck *et al.* (1980)	Validation	Kublbeck *et al.* (1980)	Validation
200	-164	-151	44	41
400	-238	-223	67	64
800	-327	-330	92	88
1600	-435	-414	128	121
2500	-514	-489	150	143
5000	-567	-582	160	166
10000	-545	-544	152	151
20000	-545	-545	152	152

TABLE 3
Comparison of minimum and maximum vorticity values for water (Pr=6.983), Gr=2E04

time, s	Minimum		Maximum	
	Kublbeck *et al.* (1980)	Validation	Kublbeck *et al.* (1980)	Validation
200	-2767	-2791	733	740
400	-3418	-3431	915	912
800	-3642	-3626	824	824
1600	-3214	-3216	775	773
2500	-3203	-3202	783	784
5000	-3202	-3202	797	799
10000	-3202	-3202	797	799
20000	-3202	-3202	797	799

the different differencing scheme and method of solution used. At time=20,000 seconds when steady-state conditions are achieved, both the results of the solution code and of Kublbeck *et al.* (1980) are in excellent agreement.

Figs. 2a-2c and *Figs. 3a-3c* show the results of the solution code for air and water respectively running under the same conditions as those of Kublbeck *et al.* (1980) at time=20,000 seconds. The temperature, vorticity and stream function plots produced by the solution code for each fluid as shown agree with the published results.

Hyun and Lee (1989) also had differentially-heated side walls and adiabatic top and bottom walls. The left wall was at a non-dimensional temperature of -0.5 and the right 0.5. The time step used was not mentioned, thus, verification was

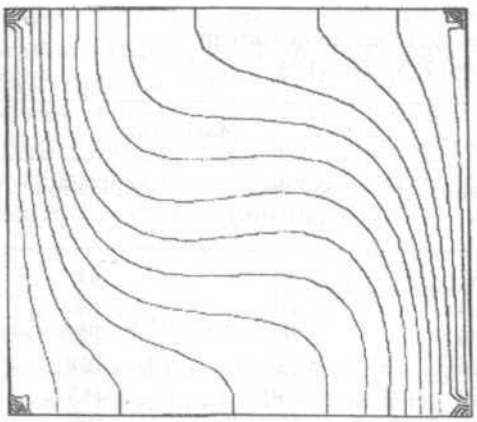

Fig. 2a: Verification of Kublbeck et al. (1980) Temperature contours, Pr = 0.883, Gr = 2E04, time = 20,000 s. Min = 0, max = 1, interval = 0.075

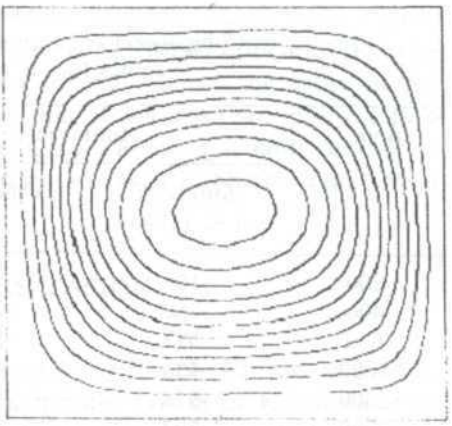

Fig. 2b: Verification of Kublbeck et al. (1980) Stream function contours, Pr = 0.733, Gr = 2E04, time = 20,000 s. Min = 0, max = 6.27, interval = 0.5

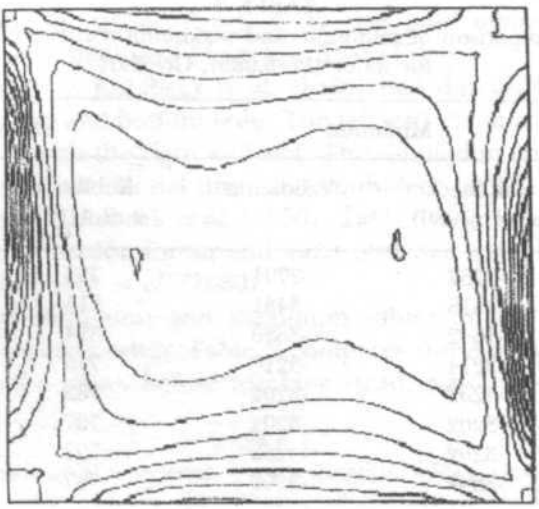

Fig. 2c: Verification of Kublbeck et al. (1980) Vorticity contours, Pr = 0.733, Gr = 2E04, time = 20,000 s. Min = -545, max = 152, interval = 60

made using a reasonably small non-dimensional time step of 0.001. A 31 by 31 mesh as used by Hyun and Lee (1989) was employed. The temperature variations with time at points specified by them were also plotted for comparison. The location of these points in the square domain are shown in *Fig. 4*; they are A (16,18), B (16,22), C (16,26), D (18,16), E (18,22) and F (18,26).

Figs. 5a-5b show the verification results of the solution code for points A, B, C, D, E and F running under the same conditions as those of Hyun and Lee

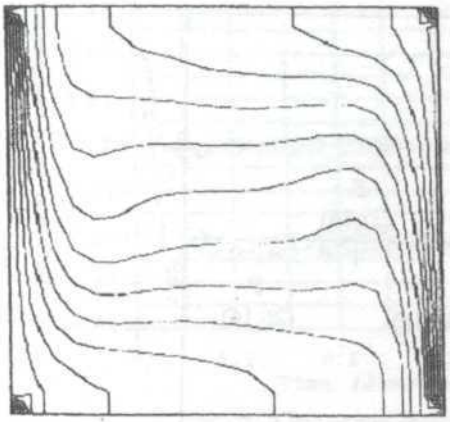

Fig. 3a: Verification of Kublbeck et al. (1980) Temperature contours, Pr = 6.893, Gr = 2E04, time = 20,000 s. Min = 0, max = 1, interval = 0.075

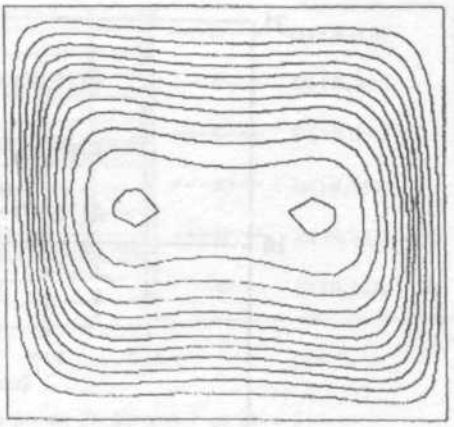

Fig. 3b: Verification of Kublbeck et al. (1980) Stream function contours, Pr = 6.893, Gr = 2E04, time = 20,000 s. Min = 0, max = 15.2, interval = 1.25

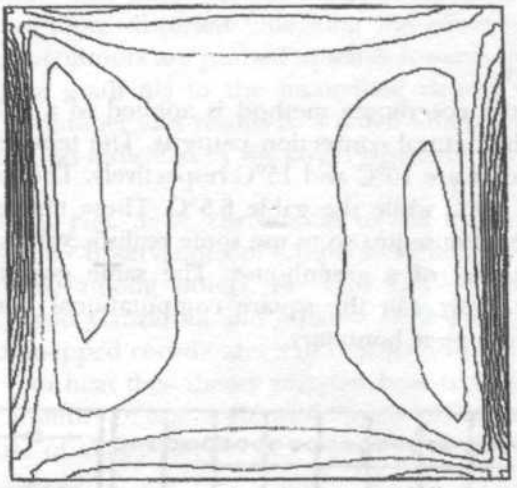

Fig. 3c: Verification of Kublbeck et al. (1980) Vorticity contours, Pr = 6.893, Gr = 2E04, time = 20,000 s. Min = -3202, max = 799, interval = 400

(1989). Values of Hyun and Lee (1989) are indicated by HL in the legend. Exact comparisons of transient condition results could not be made because the data of Hyun and Lee (1989) was presented in small figures and the steep gradients in the transient parts made accurate reading difficult. However, all steady-state results of the solution code clearly agree excellently, overlapping those of Hyun and Lee (1989).

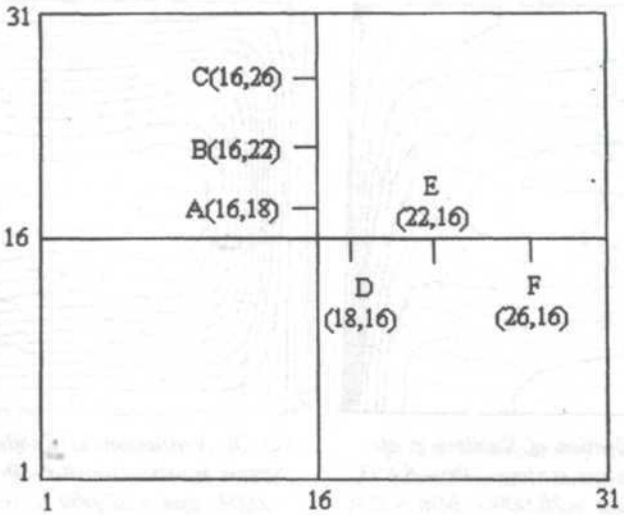

Fig. 4: Location of sample points A, B, C, D, E and F in the square domains used by Hyun and Lee (1989)

Gabled-top Geometry

The boundary-fitted coordinate method is applied to a gabled-top geometry (*Fig. 6*) to describe natural convection patterns. The temperatures on the left and right boundaries are 16°C and 15°C respectively. The lower boundary has a temperature of 30°C while the gable 6.5°C. These temperatures are taken from a typical greenhouse just so to use some realistic values for the geometry, which is actually that of a greenhouse. The same governing equations as described earlier apply. On the square computational domain the gable is represented by the upper boundary.

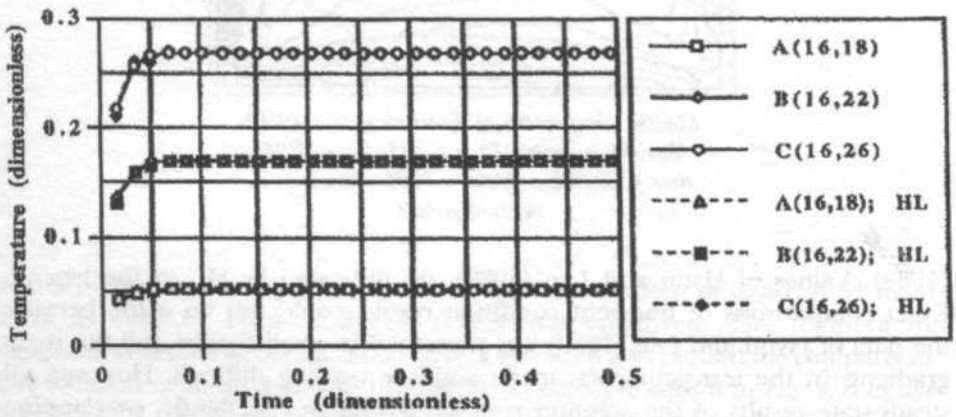

Fig. 5a: Temperature change for points A, B, and C at Pr = 1 and Gr = 1E06. The modeled and HL values overlap

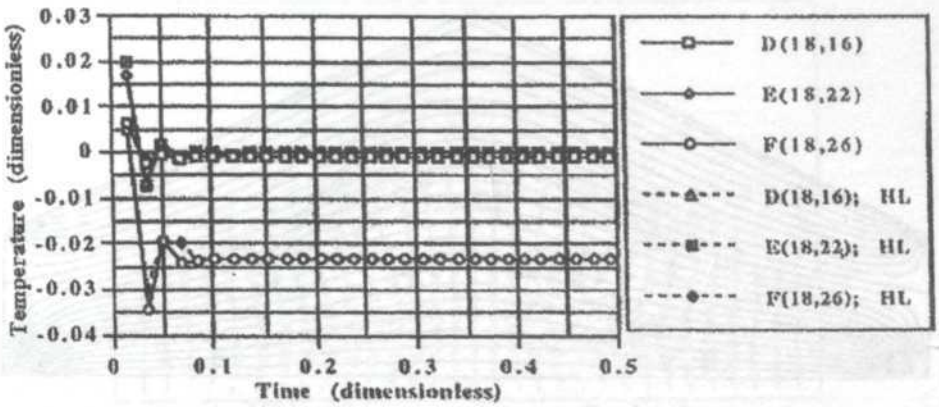

Fig. 5b: Temperature change for points D, E, and F at Pr = 1 and Gr = 1E06. The modeled and HL values overlap

Temperature distribution patterns are shown in *Figs. 7a-7c.* At Gr=10^4 the temperature contours are regularly spaced and parallel to the gable indicating primarily conduction heat transfer. Increasing the Grashoff number results in the contours being more distorted indicating the effect of convection. The higher temperature contours are pushed upwards towards the gable producing steeper temperature gradients in the immediate vicinity of the gable. The increased Grashoff number also results in a much lower temperature gradient in the central region as indicated by the larger distances between contour lines in that area.

Air flow patterns, *Figs. 8a-8c,* correspond to the temperature distribution patterns above. Similar observations of temperature and air flow patterns have also been noted by, among others, de Vahl Davis (1983), Markatos and Pericleous (1984), and Ganzarolli and Milanez (1995) working on enclosures without the use of mapped coordinates and transformed equations. The results are in accordance to heat flow theory whereby heat transfer is by conduction up to a Grashoff number of about 10^4 while the onset of convection occurs at a Grashoff number of about 10^5.

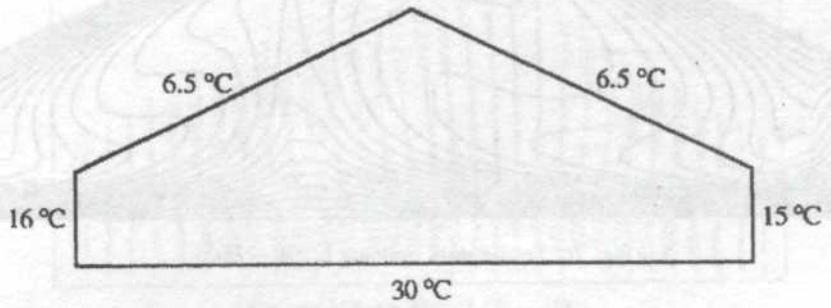

Fig. 6: Boundary temperature for the gabled-top geometry. All temperature plots for this geometry are at 1 degree C interval with the contour line immediately below the gable being at 7 degrees C

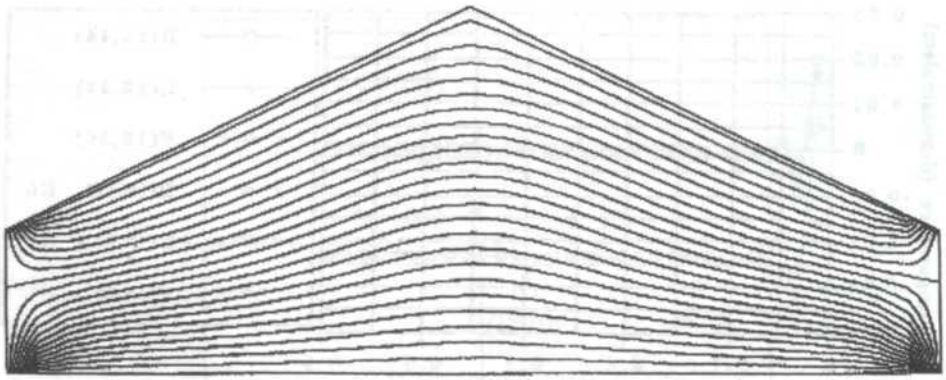

Fig. 7a: Temperature contours at Gr = 1E04

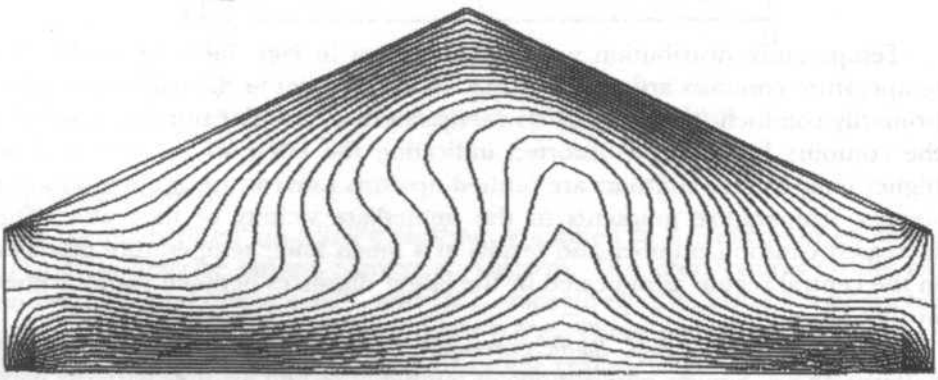

Fig. 7b: Temperature contours at Gr = 1E05

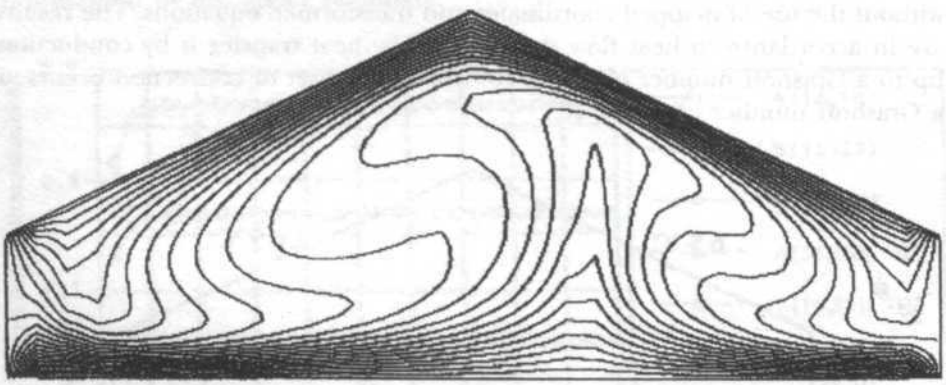

Fig. 7c: Temperature contours at Gr = 1E06

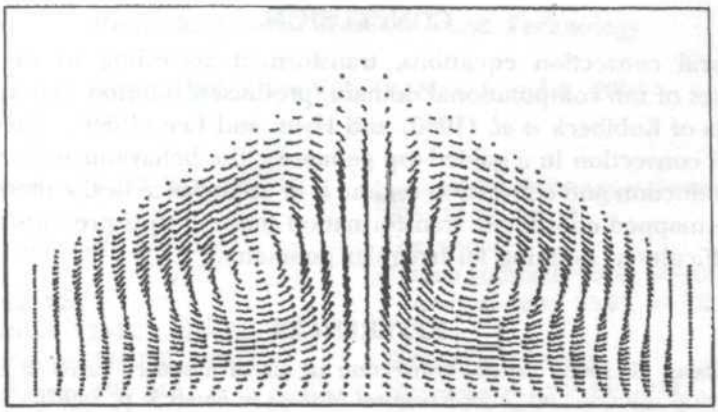

Fig. 8a: Velocity plot at Gr = 1E04

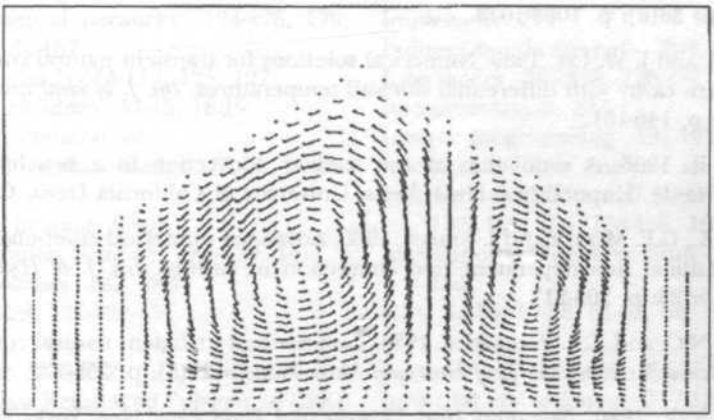

Fig. 8b: Velocity plot at Gr = 1E05

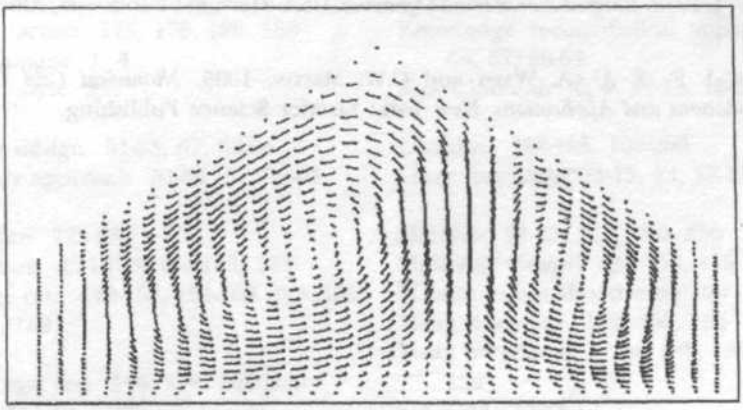

Fig. 8c: Velocity plot at Gr = 1E06

CONCLUSION

The natural convection equations, transformed according to the mapped coordinates of the computational domain, produce a solution that agrees with the results of Kublbeck *et al.* (1980) and Hyun and Lee (1989). When applied to natural convection in a gabled-top geometry, the behaviour of laminar flow in the conduction and convection regime is in accordance to the theory of heat flow. The mapped coordinate transformation method thus presents a solution to the difficulty in defining an irregular geometry.

REFERENCES

De Vahl Davis, G. 1983. Natural convection of air in a square cavity: a benchmark numerical solution. *Int. J. for Numerical Methods in Fluids* **3:** p. 249-264.

Ganzarolli, M. M. and L. F. Milanez. 1995. Natural convection in rectangular enclosures heated from below and symmetrically cooled from the sides. *Int. J. of Heat and Mass Transfer* **38(6):** p. 1063-1073.

Hyun, J. M. and J. W. Lee. 1989. Numerical solutions for transient natural convection in a square cavity with differential sidewall temperatures. *Int. J. of Heat and Fluid Flow* **10(2):** p. 146-151.

Janius, R. B. 1996. A simulation of the laminar convection in a bench-top heated greenhouse. Unpublished Ph.D thesis, University of California Davis, California.

Kublbeck, K., G.P. Merker and J. Straub. 1980. Advanced numerical computation of two-dimensional time-dependent free convection in cavities. *Int. J. of Heat and Mass Transfer* **23:** p. 203-217.

Markatos, N.C. and K.A. Pericleous. 1984. Laminar and turbulent natural convection in an enclosed cavity. *Int. J. of Heat and Mass Transfer* **27(5):** p. 755-772.

Patankar, S. V. 1980. *Numerical Heat Transfer and Fluid Flow.* New York: Hemisphere Publishing Corporation.

Roache, P. J. 1972. *Computational Fluid Dynamics.* USA: Hermosa Publishers, Albuquerque, NM.

Thompson, J. F., Z .U. A. Warsi and C.W. Mastin. 1985. *Numerical Grid Generation. Foundations and Applications.* New York: Elsevier Science Publishing.

Pertanika Journal of Science and Technology

Subject Index for Vol. 12, Nos. 1 and 2, 2004

Pertanika Journal of Science & Technology

Author Index for Volume 12, Nos. 1 & 2, 2004

ACKNOWLEDGEMENTS

The Editorial Board acknowledges the assistance of the following reviewers in the preparation of Volume 12, Numbers 1 & 2 of this journal

Dr. Abu Bakar Mohamad
Prof. Dr. Abdul Halim Shaari
Prof. Dr. Abdul Kariem Arof
Dr. Ahmad Md. Noor
Prof. Dr. Anuar Kassim
Dr. Ashaari Abd. Jalil
Dr. Chong Fai Kait
Assoc. Prof. Dr. Desa Ahmad
Dr. F. Faez Osuna
Dr. Harbant Singh
Dr. Hishamudin Zainudin
Assoc. Prof. Dr. Husaini Omar
Assoc. Prof. Dr. Ibrahim Jantan
Dr. Jumiah Hassan
Assoc. Prof. Dr. Karen Badri
Prof. Dr. Karsono Ahmad Dasuki
Assoc. Prof. Dr. Khairudin Omar
Dr. Mohd. Khazani Abdullah
Assoc. Prof. Dr. Khoo Khay Huat
Assoc. Prof. Dr. Khozirah Shaari
Dr. Lee Pat Moi
Ir. Dr. Lee Teang Shui
Prof. Dr. Liew Kong Yong
Assoc. Prof. Dr. Lim Poh Eng
Assoc. Prof. Dr. Mat Johar Abdullah
Prof. Dr. Mohamad Ridza Wahidin
Assoc. Prof. Dr. Mohd. Alaudin Mohd Ali
Assoc. Prof. Dr. Mohd. Amin Mohd. Som
Assoc. Prof. Dr. Mohd Jelas Haron
Assoc. Prof. Dr. Mohd. Radzi Abas
Assoc. Prof. Dr. Mohd. Zaizi Desa
Assoc. Prof. Dr. Muhamad Deraman
Prof. Dr. Muhammad Mat Salleh
Prof. Dr. Muhammad Yahya
Assoc. Prof. Dr. Noriah Bidin
Assoc. Prof. Dr. Ir. Norman Mariun
Assoc. Prof. Dr. Othman Karim
Dr. Rosalina Abdul Salam
Assoc. Prof. Dr. Salim Said
Assoc. Prof. Dr. Salmijah Sarif
Assoc. Prof. Dr. Tan Guat Huat
Assoc. Prof. Dr. Tan Wee Tee
Dr. Thamer Ahmed
Assoc. Prof. Dr. Wan Azlina Ahmad
Assoc. Prof. Dr. Yousif Khalid
Assoc. Prof. Dr. Zainal Abidin Talib
Assoc. Prof. Dr. Zulkarnain Zainal

Preparation of Manuscript

General
The manuscript, including footnotes, tables, and captions for illustrations, should be typewritten double spaced on paper 210 x 297 mm in size, with margins of 40 mm on all sides. Three clear copies are required. Typing should be on one side of the paper only. Each page of the manuscript should be numbered, beginning with the title page.

Title page
The title of the paper, name of author and full address of the institution where the work was carried out should appear on this page. A short title not exceeding 60 characters should be provided for the running headline.

Abstract
Abstracts in Bahasa Melayu and English of not more than 200 words each are required for full articles and communications. No abbreviation should appear in the abstract. Manuscripts from outside of Malaysian may be submitted with an English abstract only.

Keywords
Up to a maximum of ten keywords are required and they should be placed directly below the abstract.

Footnotes
Footnotes to material in the text should not be used unless they are unavoidable. Where used in the text, footnotes should be designated by superscript Arabic numerals in serial order throughout the manuscript. Each footnote should be placed at the bottom of the manuscript page where reference to it is made.

Equations
These must be clearly typed, triple-spaced and should be identified by numbers in square brackets placed flush with the right margin. In numbering, no distinction is made between mathematical and chemical equations. routine structural formulae can be typeset and need not be submitted as figures for direct reproduction but they must be clearly depicted.

Tables
Tables should be numbered with Arabic numerals, have a brief title, and be referred to in the text. Columns headings and descriptive matter in tables should be brief. Vertical rules should not be used. Footnotes in tables should be designated by symbols or superscripts small italic letters. Descriptive materials not designated by a footnote may be placed under a table as a *note.*

Illustrations & Photographs
Illustration including diagrams and graphs are to be referred to in the text as 'figures' and photographs as 'plates' and numbered consecutively in Arabic numerals. All photographs (gloosy black and white prints) should be supplied with appropriate scales.

Illustrations should be of print quality; outputs from dotmatrix printers are not acceptable, Illustrations should be on separate sheets, about twice the size of the finished size in print. All letters, numbers and legends must be included on the illustration with the author's name, short title of the paper, and figure number written on the vereso. A list of captions should be provided on a separate sheet.

Unit of Measure
Metric units must be used for all measurements.

Citations and References
Items in the reference list should be referred to in the text by inserting, within parentheses, the year of publication after the author's name. If there are more than two authors, the first author should be cited followed by '*et al*'. The names of all authors, however, will appear in the reference list.

In the case of citing an author who has published more than one paper in the same year, the papers should be distinguished by addition of a small letter, e.g. Choa (1979a); Choa (1979b); Choa (1979c).

In the reference list, the names should be arranged alphabetically according to the name of the first author. Serials are to be abbreviated as in the *World List of Scientific Periodicals.*

The abbreviation for Pertanika Journal of Science and Technology is *Pertanika J. Sci. Technol.*

The following reference style is to be observed:

Monograph
Alefed, G. and J. Herzberger. 1983. *Introduction to Interval Computations.* New York: Academic Press.

Chapter in Edited Book
Muzzarell, R.A.A. 1980. Chitin. In *Polymers in Nature,* ed. E.A. MacGregor and C.T. Greenwood, p. 417-449. New York: John Wiley.

Serials
Kamaruzaman Ampon. 1991. The effect of attachment of hydrophobic imidoesters on the catalytic activity of trypsin. *Pertanika* **14(2)**: 18-185.

Proceedings
Mokhtaruddin, A.M. and L.M. Maene. 1981. Soil erosion under different crops and management practices. In *Agricultural Engineering in National Development,* ed. S.L. Choa, Mohd Zohdie Bardaie, N.C. Saxena and Van Vi Tran, p. 245-249. Serdang, Malaysia: Universiti Pertanian Malaysia Press.

Unpublished Materials (e.g. theses, reports & documents)

Sakri, 1. 1990. Proper construction set-up of Malaysian Fish Aggregating Devices (Unjam). Ph.D. Thesis, Universiti Pertanian Malaysia, Serdang, Selangor.

Pertanika Journal of Science & Technology

Volume 12 No. 2, 2004

Contents

ISSN 0128-7680

07

9 770128 768083